School of Physical Sciences

MARCH-TYPE MODELS FOR THE DESCRIPTION OF TEXTURE IN GRANULAR MATERIALS

Husinsyah Sitepu

PGradDipAppPhys, MAppSc (Curtin)

This thesis is presented as part of the requirements for
the award of the Degree of Doctor of Philosophy
of the
Curtin University of Technology

October 1998

ABSTRACT

Texture in crystalline materials, *i.e.* preferred orientation (PO), is of interest in terms of texture-property relationships and also in X-ray diffraction science because PO can cause serious systematic errors in quantitative phase analysis using diffraction data. The single-parameter, pole-density distribution function (PDDF), proposed by March (1932) to represent PO in diffraction analysis, is used widely in Rietveld pattern-fitting following a suggestion by Dollase (1986). While the March model is an excellent descriptor of PO for gibbsite [$Al(OH)_3$] x-ray powder diffraction (XRPD) data (O'Connor, Li and Sitepu, 1991), the model has proved to be deficient for Rietveld modelling with molybdite [MoO_3], calcite [$CaCO_3$] and kaolinite [$Al_2O_3.2SiO_2.2H_2O$] XRPD data (Sitepu, 1991; O'Connor, Li and Sitepu, 1992; and Sitepu, O'Connor and Li , 1996). Therefore, the March model should not be regarded as a general-purpose PDDF descriptor.

This study has examined the validity of the March model using XRPD and neutron powder diffraction (NPD) instruments operated, respectively, by the Curtin Materials Research Group in Perth and by the Australian Nuclear Science and Technology Organisation at the HIFAR reactor facility at Lucas Heights near Sydney. Extensive suites of XRPD and NPD data were measured for uniaxially-pressed powders of molybdite and calcite, for which the compression was systematically varied. It is clear from the various Rietveld refinements that the March model becomes increasingly unsatisfactory as the uniaxial pressure (and, therefore, the level of PO) increases.

The March model has been tested with a physical relationship developed by the author which links the March *r*-parameter to the uniaxial pressure via the powder bulk modulus, *B*. The agreement between the results obtained from directly-measured values of *B* and from Rietveld analysis with the March model are promising in terms of deducing the powder bulk modulus from the March r-parameter.

An additional test of the March model was made with NPD data for specimens mounted, first, parallel to the instrument rotation axis and, then, normal to the axis.

The results have provided some further indication that the March model is deficient for the materials considered in the study.

During the course of the study, it was found that there are distinct differences between the direction of the near-surface texture in calcite, as measured by XRPD, and bulk texture characterised by NPD. The NPD-derived textures appear to be correct descriptions for the bulk material in uniaxially-pressed powders, whereas the XRPD textures are heavily influenced by the pressing procedure.

An additional outcome of the NPD work has been the discovery, made jointly with Dr Brett Hunter of ANSTO, that the popular LHPM Rietveld code did not allow for inclusion of PO contributions from symmetry-equivalent reflections. Revision of the code by Dr Hunter showed that there is substantial bias in Rietveld-March *r*-parameters if these reflections are not factored correctly into the calculations.

Finally, examination of pole-figure data has underlined the extent to which the March model oversimplifies the true distributions. It is concluded that spherical harmonics modelling should be used rather than the March model as a general PO modelling tool.

ACKNOWLEDGEMENTS

From the bottom of my heart, I would like to express my greatest gratitude to my principal supervisor Professor Brian Henry O'Connor for his encouragement, consistent support, advice and tremendous knowledge that he has shared with me, not only in crystallography, but in all aspects of life have made this PhD thesis possible. Also for his patience and endless efforts in reviewing and polishing the many drafts of the thesis.

Special thanks are also due to Professor Deyu Li, Associate Supervisor, for his expert advice on diffraction science and on Rietveld analysis. Thanks to Dr Brendan McGann for his assistance and efforts as thesis committee chairperson.

Thanks also to Dr Chris Howard, Dr Brett Hunter and Dr Ross Piltz of the Australian Nuclear Science and Technology Organisation (ANSTO) Neutron Scattering Group for their assistance in the design of the neutron diffraction experiments and for their invaluable contribution in interpreting data. I also thank Dr Shane Kennedy and Dr Margaret Elcombe of ANSTO for discussions and advice on many matters in conducting Rietveld refinements and for the support given to me throughout my PhD thesis. Thanks to Mr Peter Baxter and Mr Merv Perry of ANSTO for their technical assistance.

The financial support provided by the Curtin University Postgraduate Scholarship (CUPS), Alcoa of Australia Limited (Supplement Scholarship), de Laeter Trust Fund (Supplement Scholarship), the Australian Institute of Nuclear Science and Engineering (AINSE) Grants No. 95/11, 96/145 and 97/143, respectively ANSTO and Curtin University of Technology during the course of this PhD project are greatly acknowledged.

Thanks to Mrs Linda Cole, Ms Delia Rogers and Ms Tania Lerch the of Scholarships Office for administering the scholarship awarded to me for this study.

The author thanks Dr Gerald Roach, Mr John Cornell and Mr Nick Pearson of Alcoa for providing advice on x-ray diffraction data collections methods.

Dr Chris Howard and Dr Brett Hunter of the ANSTO Neutron Scattering Group are gratefully acknowledged for their provision of LHPM software which has

included the symmetry-equivalent reflections into their Rietveld code during the course of this study.

Thanks to Professor Wayne A. Dollase of UCLA, USA for his help in showing on how to prove the March-Dollase function for preferred orientation correction factors as shown in Appendix 1. Special thanks are also given to Professor Gerhard Oertel of UCLA, USA for his advice on the March model. Thanks are also to Professor H.R. Wenk of UCLA and Professor M. Humbert and Professor S. Matthies of University of Metz, France for discussion and advice on ODF analysis. Special thanks are also due to Dr R.B. Von Dreele of Los Alamos Laboratory, USA for his advice on the March model and the symmetrised harmonics method.

I also would like to acknowledge the following colleagues at the Curtin Department of Applied Physics who have given me considerable assistance and advice during my PhD study: Prof. John de Laeter, Prof. Kevin Rosman, Dr Ian Bailey, Dr Arie van Riessen, Dr Jim Low, Mrs Carmel McManus, Miss Tiffany Car, Mr James Browne, Mr Glen Lawson, Mr Rob Skala, Mr Stephen Cook, Mr Paul Hamilton-Brown, Ms Elaine Miller and Ms Phe Man Suherman. Thanks to Mr Graeme Burton for proof reading the manuscript.

I would like to thank everyone once again, and also to anyone that I have forgotten to mention, whom in one way or another have helped me make this thesis possible. It has been tremendous experience completing my PhD program. Thank you very much from the bottom of my heart.

Lastly, I would like also to thank my parents and my father and mother in-law. This PhD study would not be possible without them. They have provided me with love, understanding and some financial support that I required throughout all these years during my PhD. I would like to say thanks to my wife, Ella, and may adorable daughters, Rebecca and Alexandra, for their everlasting love, understanding, and support during my study.

MARCH-TYPE MODELS FOR THE DESCRIPTION OF TEXTURE IN GRANULAR MATERIALS

TABLE OF CONTENTS

LIST OF SYMBOLS AND ABBREVIATIONS

The following abbreviations are used extensively in the thesis :

ADF	: angular density distribution frequency
ANSTO	: Australian nuclear science and technology organisation
ESD	: estimated standard deviation
FWHM	: full-width at half-maximum
GOFI	: goodness-of-fit index
HIFAR	: high flux Australian reactor
HRPD	: high resolution neutron powder diffractometer
JCPDS	: joint committee for powder diffraction standards
LAC	: linear attenuation coefficients
NPD	: neutron powder diffraction
ODF	: orientation distribution function
PDDs	: pole-density distributions
PDDFs	: pole-density distribution functions
PO	: preferred orientation
PSDs	: particle size distributions
QPA	: quantitative phase analysis
RLV	: reciprocal lattice vector
RD	: rolling direction
ROD	: random orientation distribution
SE	: series expansion
TD	: transverse direction
XRPD	: x-ray powder diffraction

ASSUMED BACKGROUND FOR THESIS

It is assumed that the readers have a basic understanding of crystallography and diffraction principles at the level of the text *"Elements of X-ray Diffraction"*, authored by B.D. Cullity (1978), 2nd edition - Addition-Wesley.

List of Figures

List of Figures (Continue)

List of Figures (Continue)

List of Figures (Continue)

List of Figures (Continue)

List of Figures (Continue)

List of Figures (Continue)

List of Figures (Continue)

List of Figures (Continue)

List of Figures (Continue)

List of Figures (Continue)

List of Figures (Continue)

List of Figures (Continue)

List of Figures (Continue)

List of Tables

List of Tables (Continue)

CHAPTER 1

INTRODUCTION

1.1 Preferred Orientation (Texture) in Polycrystalline Materials

The single crystals comprising polycrystalline materials are seldomly found to be randomly oriented. Most polycrystalline materials have at least some *preferred orientation* (designated in the thesis as PO) which involves one or more crystallographic directions being preferentially oriented in space. For example, uniaxial-pressing of a powder with 'platy' grains will result in the plate surface tending to align normal to the direction of compression. In keeping with the literature, the term *texture* is used frequently in the thesis as an alternative to PO.

PO in polycrystalline materials has been investigated for many years, particularly in relation to metals, rocks and minerals. Metals have been the most intensively studied class of materials and their characterisation has formed the basis of most of the theoretical work in the field. Rocks and minerals, which have received less attention principally due to the greater complexity of their crystal structures, can now be studied more readily using the powerful texture computational procedures which have been developed (Weiss and Wenk, 1985).

There are various possible physical origins of texture formation in powders: (i) rigid particle rotation due to particle shape anisotropy, (ii) plastic deformation caused by crystallographic gliding, (iii) twinning, and (iv) crystal fracture as well as combinations of two or more of these processes. PO development will also depend on the particular method of sample treatment, *e.g.*, sedimentation and uniaxial compaction. Further, interaction between particles of different phases may also occur. Since the resulting PO may be dependent on the phase content, PO modelling is especially important in quantitative phase analysis (QPA) with diffraction data.

Texture modelling is mainly conducted using the *orientation distribution function* (ODF) formalism proposed initially by Bunge (1965) and Roe (1965) - see

also the review by Bunge (1982). The ODF $f(\mathbf{g})$ represents the volume fraction of crystallites in the sample having the crystal orientation $\mathbf{g}$:

$$\frac{dV}{V} = f(\mathbf{g}) \cdot d\mathbf{g} \tag{1.1a}$$

In order to describe the ODF of a polycrystalline sample it is necessary to define (i) *a sample coordinate system* K_A to which orientation is to be referred, and (ii) *a crystal coordinate system* K_B for each crystallite - see Figure (1.1). Both the sample and crystal coordinate systems are assumed to be (i) right-handed cartesian coordinate systems and (ii) adapted to symmetry, *i.e.* crystal and sample symmetries.

The orientation of a crystallite in a sample is determined by the rotation $\mathbf{g}$ which transforms the sample coordinate system into the crystal coordinate system, as described by Bunge (1982) :

$$K_B = \mathbf{g} \cdot K_A \tag{1.1b}$$

In the Bunge notation, the crystal orientation is defined by *Eulerian angles* :

$$\mathbf{g} = (\varphi_1, \phi, \varphi_2) \tag{1.1c}$$

see Figure (1.1a). In rolled metal sheets, the specimen coordinate system is defined by the rolling direction (RD), the transverse direction (TD), and the normal to the plane of sheet. The crystal coordinate system is normally defined by the principal directions [100], [010], and [001] - see Figure (1.1b).

By an appropriate definition of the orientation element $d(\mathbf{g})$ it is possible to normalise the ODF function $f(\mathbf{g})$ such that the function integral over all of angular space is

$$\int f(\mathbf{g}) \cdot d\mathbf{g} = 1 \tag{1.1d}$$

The ODF function cannot be measured directly. However it can be derived from diffraction data comprising several measured *pole-figures*. Such measurements require a multi-axis, pole-figure diffractometer, normally comprising a *Eulerian cradle* fitted to a 2-circle diffractometer. A pole-figure is the angular distribution of a chosen crystal direction $\mathbf{h}$[1] with respect to the sample coordinate system. The $\mathbf{h}$ *pole-density distribution* (PDD) is defined by the volume fraction dV/V of crystallites

[1] The terms **h** and hkl are used here interchangeably.

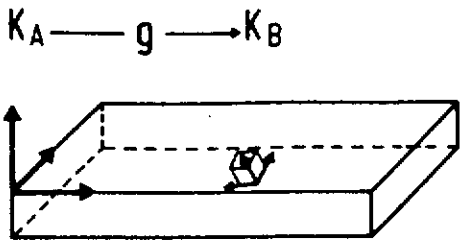

(a)

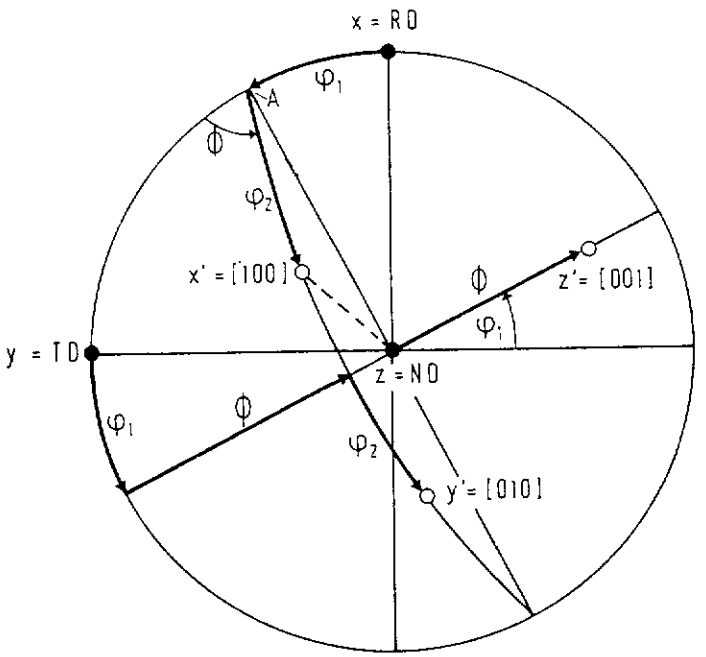

(b)

Figure 1.1. (a) The orientation of a crystallite in a polycrystalline sample is determined by the rotation **g** which transforms a sample coordinate system K_A into the crystal coordinate system K_B - see equation (1.1b). (b) The Euler angles $(\varphi_1, \phi, \varphi_2)$ of a crystal define rotation **g**. After Bunge (1982).

having direction **h** parallel to a specific sample direction **y**

$$\frac{dV(\mathbf{y})}{V} = \frac{1}{4\pi} P_{hkl}(\mathbf{y}) \cdot d\mathbf{y} \tag{1.2}$$

The key aspects of PDD measurement are shown schematically in Figure (1.2a). Functional representations of the PDD are designated *pole-density distribution functions* (PDDFs) in the thesis. The PDDF P_{hkl} is normalised such that :

$$\int P_{hkl}(\mathbf{y}).d\mathbf{y} = 4\pi \tag{1.3}$$

The PDD can be determined by x-ray powder diffraction (XRPD), by neutron powder diffraction (NPD) or by electron diffraction using a monochromatic beam. As shown schematically in Figure (1.2a), an incident beam will be reflected by all crystallites with **h** directions parallel to the bisector between the incident and reflected beam (within the solid angular element dΩ) provided that angle 2θ between these beams fulfils the Bragg-reflection condition

$$\lambda = 2 \cdot d_{hkl} \cdot \sin\theta_{hkl} \tag{1.4}$$

The measured intensity of the reflected beam is :

$$I_{hkl}(\mathbf{y}) = I_o \cdot R_{hkl} \cdot \frac{dV(\mathbf{y})}{V} \tag{1.5}$$

where I_o is the intensity of the incident beam and R_{hkl} is the crystallite reflectivity which depends on the material under consideration and the reflecting lattice plane **h**. Substituting equation (1.2) into equation (1.5) yields :

$$I_{hkl}(\mathbf{y}) = \frac{I_o \cdot R_{hkl}}{4\pi} \cdot d\Omega \cdot P_{hkl}(\mathbf{y}) \tag{1.6}$$

Factor $(\frac{I_o \cdot R_{hkl}}{4\pi} \cdot d\Omega)$ is usually unknown. Also, term dΩ makes the factor dependent on the experimental conditions, *viz.* the beam apertures. Equation (1.6) can be written in the form

$$I_{hkl}(\mathbf{y}) = N_{hkl} \cdot P_{hkl}(\mathbf{y}) \tag{1.7}$$

where N_{hkl} is the normalising factor.

During pole-figure measurement, diffraction vector **h** is made parallel, successively, to selected sample directions **y**. This process generates the **h** PDD or **h** pole-figure. The pole-figure does not involve a rotation of the crystallites about the diffraction vector. A PDDF at **y**, representing the PDD, is the integral of the

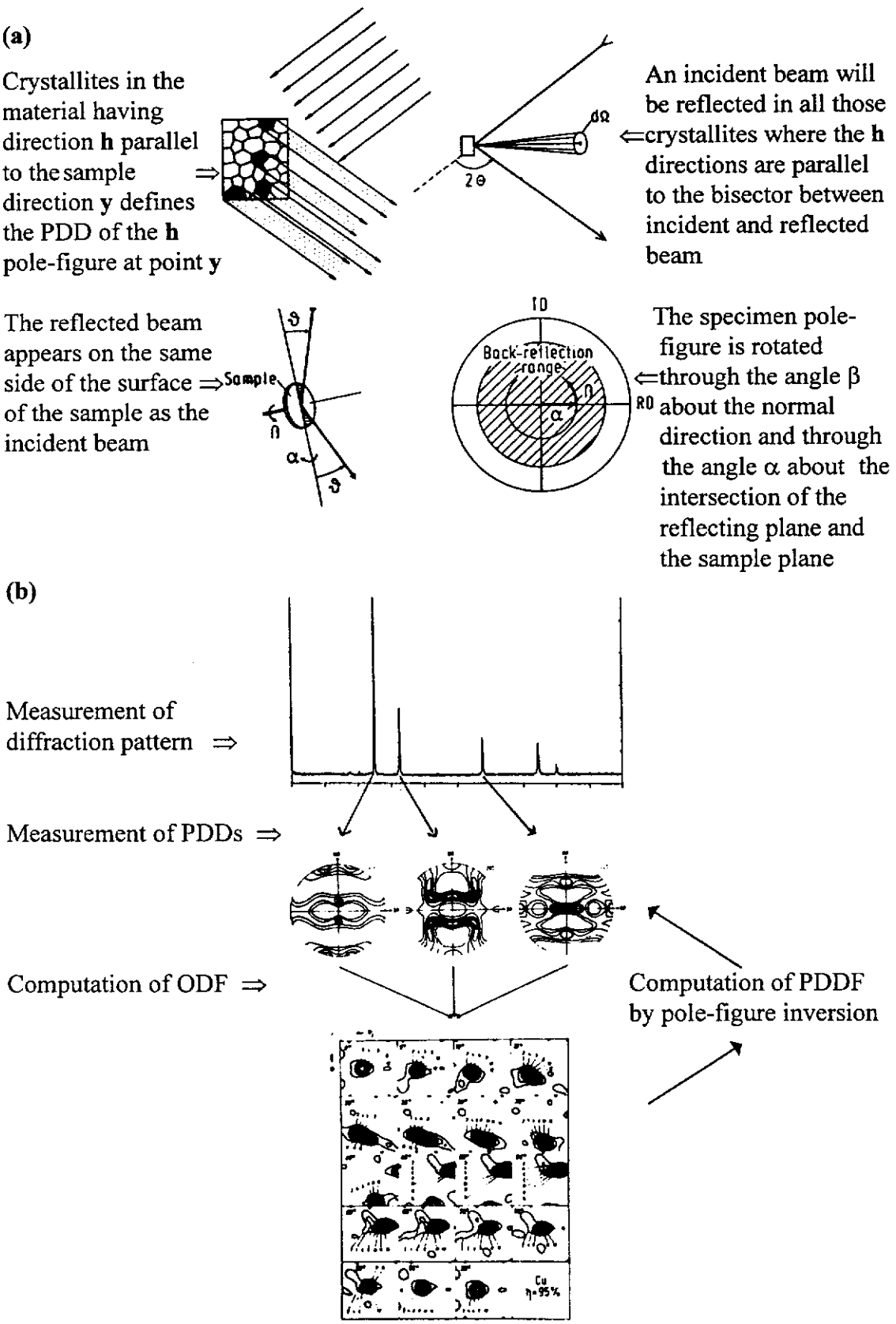

Figure 1.2. Schematic diagrams illustrating (a) pole-figure measurements for determining PDDs, and (b) PDDF calculation from the ODF by pole-figure inversion - see Section (1.1) for explanation. The axes for the ODF diagram in Figure 1.2(b) are the Euler angles $(\varphi_1, \phi, \varphi_2)$ - see equation 1.1(c). Based on Bunge (1982).

ODF $f(\mathbf{g})$ taken over a certain path in the Euler space, which is defined by the condition $\mathbf{h} \| \mathbf{y}$:

$$P_{hkl}(\mathbf{y}) = \frac{1}{4\pi} \int_{\mathbf{h}\|\mathbf{y}} f(\mathbf{g}) \cdot d\chi \tag{1.8}$$

where χ represents a rotation of the crystal about the common **h**, **y** direction. *The pole-figure is thus a 2D ODF.* It is seen from equation (1.8) that the ODF is not completely determined by one pole-figure. The missing information can be provided from other pole-figures which are themselves integrals over the ODF but along different paths. Bunge (1982) showed that function $f(\mathbf{g})$ is uniquely determined only by an infinite set of pole-figures *i.e.* the pole-figures of all crystallite directions **h**. Equation (1.8) is regarded as the *fundamental relation of texture analysis*. The solution of equation (1.8) for $f(\mathbf{g})$ is called *pole-figure inversion*, see Figure (1.2b).

Texture analysis consists of solving equation (1.8) for the unknown function $f(\mathbf{g})$ using known PDDFs $P_{hkl}(\mathbf{y})$ which have been extracted from measured pole-figures. For the solution of equation (1.8), essentially four different mathematical approaches have been described in the literature, see Table (1.1). Each of the methods has advantages and disadvantages. The harmonic method, which provides a concise mathematical description using a small number of coefficients, is of considerable value in calculating physical properties. This method has been employed in the present study.

Table 1.1

Mathematical Approaches Proposed in the Literature for Solving the *Fundamental Relation of Texture Analysis, Equation (1.8)*

Mathematical Approach	**Method**	**References**
Discretisation	*Vector*	Williams (1968); Ruer and Baro (1977).
Integral transformation	*Inversion*	Matthies (1979).
Probabilistic	*WIMV*	Imhof (1977); Matthies and Vinel (1982).
Series expansion	*Harmonic*	Roe (1965); and Bunge (1965).

The *vector method* was proposed by Williams (1968) for analysis of biaxial pole-figures, and subsequently refined by Ruer (1976; pp. 139-147), Ruer and Baro (1977), and Vadon (1981). The most attractive feature of the *vector method* is the simple crystallographic description of orientation relations in the pole-figure, which conforms with the view that a polycrystal is the sum of individual grains. This simple geometrical concept leads to mathematical analysis by linear algebra and optimisation. A minimal amount of experimental data is required to obtain a reasonable approximation to the true ODF. The vector method demonstrates that a single pole-figure contains much information about the orientation distribution.

The *inversion method,* introduced by Matthies (1979), provides a direct inversion formula for equation (1.8). The method makes use of Abel's integral transformation formula (Muller, Esling and Bunge; 1981). This procedure provides a straightforward solution to the pole-figure inversion problem. However, it has not been applied to numerical calculation of $f(\mathbf{g})$, see Bunge (1982).

The *WIMV method,* named after the method developers, was proposed originally by Imhof (1977), and then, described in more detail by Matthies and Vinel (1982). Subsequently, Matthies and Wenk (1985; pp. 139-147) showed that the method (i) provides an efficient approach to calculating the true ODF from experimental pole-figures, (ii) does not use spherical harmonics and is, therefore, free of termination of errors and (iii) does not require manipulation of large matrices because the ODF value for each **g** is calculated separately.

The *series expansion method* [see Section (2.2) for more details], which is employed in the thesis, uses harmonic functions which are defined to be invariant with respect to crystallite as well as sample symmetry (Bunge, 1982), according to:

$$f(\mathbf{g}) = \sum_{l=0}^{\infty} \sum_{m=-l}^{+l} \sum_{n=-l}^{+l} C_l^{mn} \cdot T_l^{mn}(\mathbf{g}) \tag{1.9}$$

$$P_{\mathbf{h}}(\mathbf{y}) = \sum_{l=0}^{\infty} \sum_{m=-l}^{+l} \sum_{n=-l}^{+l} C_l^{mn} \cdot \frac{4\pi}{2\lambda+1} \cdot K_l^{n}(\mathbf{y}) \cdot K_l^{*n}(\mathbf{h}) \tag{1.10}$$

with $T_l^{mn}(\mathbf{g})$ being *generalised harmonics*, and $K_l^{n}(\mathbf{y})$ and $K_l^{*n}(\mathbf{h})$ are *surface harmonics*. The texture is then completely described by the set of coefficients C_l^{mn}. The positivity of the PDDFs $P_{hkl}(\mathbf{y})$, defined in equation (1.10), is helpful for the

calculation of the ODF $f(\mathbf{g})$ with a minimum of experimental data. A comprehensive ODF analysis program, developed by LM2P[2] and SOCABIM[3] on this basis, has been employed in this study. The program can automatically construct ODFs if pole-figure data are available. The data are generally collected as XRPD back-reflection pole figures as depicted in Figure (1.2a).

1.2 Diffraction Methods for Characterising Texture

The most common way of directly evaluating the form and extent of PO is to measure the pole-figures for several crystallographic directions with an x-ray pole-figure instrument [see Section (3.3) for more details]. The pole-figure is the intensity of a particular Bragg diffraction line plotted as a function of the 3D orientation of the specimen. It is determined with a *'Eulerian cradle'* texture diffractometer which is essentially a single-crystal diffractometer fitted with appropriate collimators for the incident and diffracted beams. The instrument rotates the specimen through a broad range of orientations while monitoring the intensity of a selected Bragg reflection. The intensity distribution is normally displayed as a pole-figure in 2D stereographic projection form.

PO effects may also be observed in XRPD patterns measured with diffractometers such as the popular *Bragg-Brentano* instrument. It is possible to extract PO information from such patterns if the pattern for a randomly-oriented specimen can be modelled, or simulated, from a knowledge of the crystal structure parameters and various other factors (*e.g.* line broadening) which influence the pattern.

NPD data may be used to complement XRPD measurements on the texture character of materials [see Section (3.3)]. The pertinent attribute of NPD in relation to texture is the small attenuation coefficients of neutrons for most materials relative to x-ray absorption. Therefore NPD texture information is gained from the bulk of the sample [*ca.* several cm for most materials], whereas the XRPD response is typically from the near-surface [*ca.* tens of μm in oxide materials]. Thus, XRPD and

[2] University of Metz, Laboratorie de Metallurgie des Materiaux Polycrystallins (LM2P), Ile du Saulcy, 57045 METZ Cedex, France.
[3] SOCABIM, 9 bis villa du Bel-Air, 75012 Paris, France.

NPD are *excellent complementary tools* for characterising texture from the near-surface into the bulk of the material.

While powder diffraction instruments and diffraction pattern modelling procedures have been improved dramatically in recent years, specimen preparation techniques for diffraction measurements have not reached the same stage of development. Smith and Barrett (1979) considered specimen preparation methods for reducing PO in powders for XRPD analysis. Although such methods may be effective in reducing PO, there is no guarantee that the sample will be randomised. Calvert, Sirianni, Gainsford and Hubbard (1983) used side-drifted mounting procedures in which molybdite (MoO_3) powder was mixed with silica gel with the aim of reducing PO. It was demonstrated that the relative intensities for side-drifted powders agreed well with the calculated values derived from the MoO_3 crystal structure (Kihlborg, 1963) assuming random orientation

Suortti and Jennings (1977) showed that such special techniques to reduce the effect of PO cannot be used in the case of compact polycrystalline samples, and also that the inhomogeneity of packing of the crystallites in a loosely pressed specimen will cause uncontrollable variation in the intensity distribution, thus making accurate intensity measurements impossible. Carefully prepared and sufficiently hard specimens with a smooth surface should be prepared for accurate intensity measurements. On the other hand, sufficient compression produces a homogeneous sample with a smooth surface and reduced porosity effects, but enhanced PO of the crystallites then becomes apparent. Various mathematical forms have been proposed for the application of PO corrections to diffraction pattern data [see Sections (1.3) and (1.4) below and Chapter 2].

1.3 Texture Modelling in Powder Diffraction Analysis

Powder patterns include convolved information on crystal structure (*e.g.* atom positions) and bulk character (*e.g.* phase composition levels) which may be severely biased when extracted from the pattern if PO is ignored or is modelled incorrectly. Texture modelling has become an important aspect of contemporary powder diffraction analysis as the effect is present in almost all specimens.

A Bragg intensity for direction **y** in the sample may be written as :

$$I_{hkl}(\mathbf{y}) = I_{hkl}^{random} \cdot P_{hkl}(\mathbf{y}) \tag{1.11}$$

where I_{hkl}^{random} is the ideal random orientation intensity for the defined reciprocal lattice vector (hkl), and $P_{hkl}(\mathbf{y})$ is the *PO correction factor* - see equation (1.7). The correction factor may be extracted from the ODF [see Section (1.1)], the ODF being obtainable from pole-figure measurements for which the sample is tilted while keeping the same reflection diffracting. Use of equation (1.11) with non-tilt diffractometer data is simplified by spinning the specimen. Then the ODF can be represented by a 2D function using the *symmetrised harmonic method*, which represents pole-figures by *spherical harmonic* functions and may be applied to specimens with *cylindrically-symmetric* PO (Jarvinen *et al.*, 1970; and Jarvinen, 1993). The most commonly-used texture models are simple analytical forms which can be applied to powder diffraction data produced using a sample spinner

A cylindrically-symmetric form of $P_{hkl}(\mathbf{y})$, based on the work of March (1932), was proposed by Dollase (1986) to describe the PDDF in a powder sample [see Sections (1.5) and Section (2.1) for more details]. The March-Dollase function was subsequently introduced into the popular Rietveld (1969) refinement computer program LHPM (Hill and Howard, 1986) to correct for the effects of PO in powder diffraction data [see Section (3.4)]. The March model has been extensively employed to describe the texture resulting from packing effects in Bragg-Brentano powder diffraction samples. A partial implementation of a *spherical-harmonic* model (see below) for the texture in a Rietveld refinement program was reported in which the sample symmetry was assumed to be cylindrical (Ahtee *et al.*, 1989; Berar and Garnier, 1992; and Popa, 1992). Ferrari and Lutterotti (1994) described a similar approach which also covered cylindrical sample symmetry but included a parametrisation of the diffraction-line shifts that frequently occur in textured samples from residual strain effects. They suggested that generalisation of the texture problem to other sample symmetries is possible.

A method was proposed by Wenk, Matthies and Lutterotti (1994) which combines the Rietveld method with ODF calculations. Subsequently Matthies, Lutterotti and Wenk (1997) tested the method with the experimental neutron time-of-flight diffraction data for deformed calcite limestone. The results showed that the

approach worked well with low symmetry materials and composites which have complicated diffraction patterns.

Von Dreele (1997) described the use of *generalised spherical-harmonics* for modelling in the Rietveld refinement program GSAS written by Larson and Von Dreele (1986). Von Dreele tested the method using neutron time-of-flight data taken from a standard calcite sample previously used in the round-robin PO study coordinated by Wenk (1991). The results showed that the generalised spherical harmonic method gave texture results similar to those obtained from individual pole-figures, and that the procedure yielded a quantitative description of the texture simultaneously with the crystal structure.

Jarvinen *et al.* (1970) investigated the use of *symmetrised harmonics* in applying texture corrections for axially-symmetric distribution functions. In their approach, the **h** PDDF is represented by an expansion of symmetrised harmonics:

$$P_{hkl}(\alpha) = \sum_{ij} C_{ij} \cdot Y_{ij}(\vartheta_{hkl}, \varphi_{hkl}) \cdot P_i(\cos\alpha) \qquad (1.12)$$

where i and j are integers, $P_i(\cos\alpha)$ is the *Legendre polynomial,* angle α is the angle between **h** and the PO direction [see Figure (1.3)], $(\vartheta_{hkl}, \varphi_{hkl})$ are the *spherical coordinates* of the normal to plane **h**, Y_{ij} are the *symmetrised harmonics*, and the C_{ij} are *texture parameters.* Jarvinen (1993) showed that PO can be successfully modelled in Rietveld refinements if the crystal structure of the textured material is precisely known or if pole-figure measurements are available. In principle, the

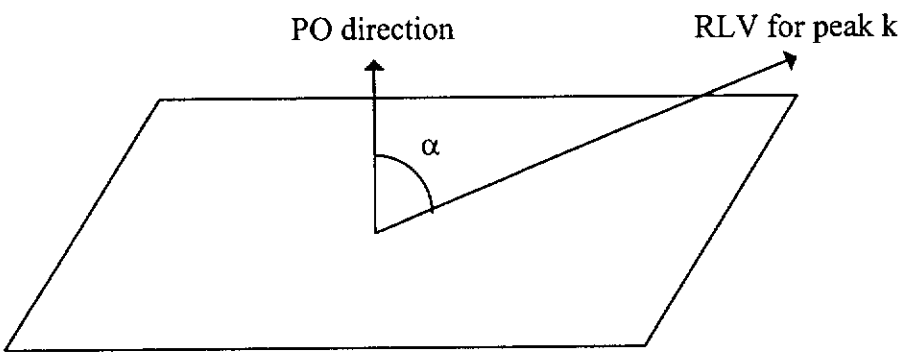

Figure 1.3. Orientation angle, α, between crystallographic direction **h** and the PO direction.

parameters C_{ij} involved in the series expansion can be determined from a least-squares analysis of a set of pole-figure observations (Valvoda, 1987). However the number of coefficients required becomes too large to be practically applicable if the texture is strong. Jarvinen (1995) used this approach with a surface-layer texture model for PO corrections with XRPD data for NH_4Cl powder specimens.

Jarvinen *et al.* (1970) showed that well-developed PO can be characterised by several parameters when a specimen spinner is used to make the measurements. The ODF of crystallites can be expanded in site-symmetrised harmonic functions, where the coefficients can be determined from the pole-figures of several reflections. The axially-symmetric ODF can be expressed as a series expansion of Legendre polynomials and symmetrised harmonic functions possessing the Laue symmetry of the crystal, provided that the polar-axis density possesses the Laue symmetry of the crystal structure (Jarvinen, 1993).

Rietveld analysis with powder diffraction data, using texture corrections according to the harmonic model [equation (1.12)], was tested by Ahtee *et al.* (1989) with samples of Ni, Mg and $NaNO_3$. The results demonstrated that the whole-pattern fit improved substantially when such texture corrections were employed in the refinement. Recently, the symmetrised harmonics method has been applied to QPA using diffraction data measured by Bragg-Brentano powder diffractometry (Valvoda; 1986, 1987 and 1992). The spherical harmonics approach, while very powerful, may produce false texture descriptions in Rietveld analysis as the function is purely mathematical and may therefore be influenced by systematic errors in the diffraction data other than PO.

In Rietveld analysis, PO may be modelled with relatively-simple, axially-symmetric PDDFs involving one variable [polar angle α - see Figure (1.3)] and one or two refineable parameters. Use of such models, rather than the multi-parameter harmonic approach, is clearly appealing for PDDFs which closely mimic the PO in the material under examination. The following two sections outline the simple cylindrically-symmetric PO models which have been proposed in the literature.

1.4 Cylindrically-Symmetric PDDFs

Various mathematical forms have been proposed for the application of PO corrections for materials with cylindrically-symmetric distributions, see Table (1.2). The models make use of the *orientation angle* for direction **h**, α [see Figure (1.3)], between **h** and the PO direction.

It is desirable that these distributions have one, perhaps several at most, refineable parameters. Ideally, models should have some physical basis related to the mechanism causing the PO. The attributes of models should include :

1. Integral of the function for a given **h** over all orientations is unity.
2. Symmetric across $\alpha = 0$ and $\alpha = \pi/2$.
3. Smooth across $\alpha = 0$ or $\alpha = \pi/2$, *i.e.* $(\partial P/\partial\alpha) = 0$ at these angles.
4. General agreement in form with measured pole-densities.

Acceptable models should reasonably describe two general distribution types representing (i) maximum for $\alpha = 0$ and minimum for $\alpha = \pi/2$, and (ii) minimum for $\alpha = 0$ and maximum for $\alpha = \pi/2$. Materials which may be modelled with these functions will fall into one of the above categories depending on whether the crystallite shapes may be represented by disc or rod shapes and also on the sample consolidation procedure (compaction or extension) and the sample geometry (flat-plate or capillary).

The following review of functions proposed in the literature includes comments on a useful evaluative method developed by Altomare *et al.* (1994) who considered a statistical procedure involving an analysis of *normalised structure-factor* moduli to obtain information on PO distribution for a powder sample. The *normalised intensities* $|E'_{hkl}|^2$ are defined as

$$E'_{hkl} = s \cdot F_{hkl} / [\varepsilon_{hkl} \sum_{j=1}^{N} f_i^{\,2}]^{1/2}$$

where s and F_{hkl} are the scale factor and structure factor, respectively, ε_{hkl} is the Wilson statistical weight and f_j is the scattering factor for the jth atom (thermal vibration included). By definition,

$$\left\langle |E'_{hkl}|^2 \right\rangle = 1$$

Table 1.2
Attributes of Cylindrically-Symmetric PDDFs Reported in the Literature

#	Form	Norm-alisati-on	Symmetry		Smoothness, $\frac{\partial P}{\partial \alpha} = 0$		Consistency with Measured Pole-figures	References
			$\alpha = 0$	$\alpha = \pi/2$	$\alpha = 0$	$\alpha = \pi/2$		
1a	$\exp(-G\alpha^2)$	No	Yes	No	Yes	No	Poor	Uda (1967); and Rietveld (1969)
1b	$\exp[-G(\pi/2-\alpha)^2]$		Yes	Yes	No	Yes		
2a	$\exp[G(\pi/2-\alpha)^2]$	No	Yes	Yes	No	Yes	Poor	Parrish and Huang (1983); and Will, Parrish and Huang (1983)
2b	$\exp(G\alpha^2)$		No	Yes	Yes	No		
3a	$\exp(-G\sin^2\alpha)$	No	No	No	Yes	Yes	Sound	Capkova and Valvoda (1974)
3b	$\exp(-G\cos^2\alpha)$		No	No	Yes	Yes		
4a	$\exp[-G(1-\cos^3\alpha)]$	No	No	No	Yes	Yes	Sound	Capkova and Valvoda (1974)
4b	$\exp[-G(1-\sin^3\alpha)]$		No	No	Yes	Yes		
5a	$b+(1-b)\exp(-G\alpha^2)$	No	No	No	No	Yes	Poor	Sasa and Uda (1976); and Toraya and Marumo (1981)
5b	$b+(1-b)\exp(-G(\pi/2-\alpha)^2)$		No	No	No	Yes		
6	$(r^2\cos^2\alpha + r^{-1}\sin^2\alpha)^{-3/2}$	Yes	Yes	Yes	Yes	Yes	Sound	March (1932); and Dollase (1986)
7	$\exp(G\cos 2\alpha)$	Yes	Yes	Yes	Yes	Yes	Sound	Altomare *et al.* (1994)
8	$\exp(-G(1-\cos^n\alpha))$	Yes	Yes	Yes	Yes	Yes	Sound	Cerny, Valvoda and Chladek (1995)

where the average value is calculated for the complete set of reflections.

Plots of $\left\langle \left| E_{hkl}^{'} \right|^2 \right\rangle$, derived for the measured data, versus off-set angle α are constructed for a selection of possible PO directions. These plots are then compared with plots constructed using the PDDF function under test. Figure 1.4(a) shows a set of plots prepared with PbS_2O_3 powder data. The method is applicable to flat-plate diffractometer data in reflection mode, where the crystallites are disc-shaped and the ODF has cylindrical symmetry.

The following summary describes the functions which have been reported in the literature. These are summarised in Table (1.2), and compared graphically in Figures 1.4(b) and (c). The functions represent two general PO categories depending on whether the PO factor is a maximum or minimum at $\alpha = 0$, and vice-versa at $\alpha = \pi/2$.

❶ *Gaussian function* proposed by Uda (1967) and Rietveld (1969) :

Function 1a (max. at $\alpha = 0$) $\quad P_{hkl}(\alpha) = \exp(-G \cdot \alpha^2)$ *(1.14a)*

The function is not symmetric or smooth at $\alpha = \pi/2$, and is not normalisable. Also, Sasa and Uda (1976) and Toraya and Marumo (1981) pointed out that PDDFs calculated with this function disagree considerably with measured distributions.

Function 1b (min. at $\alpha = 0$) $\quad P_{hkl}(\alpha) = \exp[G(\pi/2 - \alpha)^2]$ *(1.14b)*

The function is not smooth or symmetric at $\alpha = 0$, and also provides PDDFs which are too low at high-angle α values (Sasa and Uda, 1976; Toraya and Marumo, 1981).

❷ Profiles investigated by Parrish and Huang (1983) and by Will, Parrish and Huang (1983)

Function 2a (max. at $\alpha = 0$) $\quad P_{hkl}(\alpha) = \exp[G(\pi/2 - \alpha)^2]$ *(1.15a)*

Function 2b (min. at $\alpha = 0$) $\quad P_{hkl}(\alpha) = \exp(G \cdot \alpha^2)$ *(1.15b)*

They found that these expressions gave lower crystallographic figures-of-merit for Si, α-SiO_2 and α-Al_2O_3 powders compared with those observed using the Gaussian function 1.14(a).

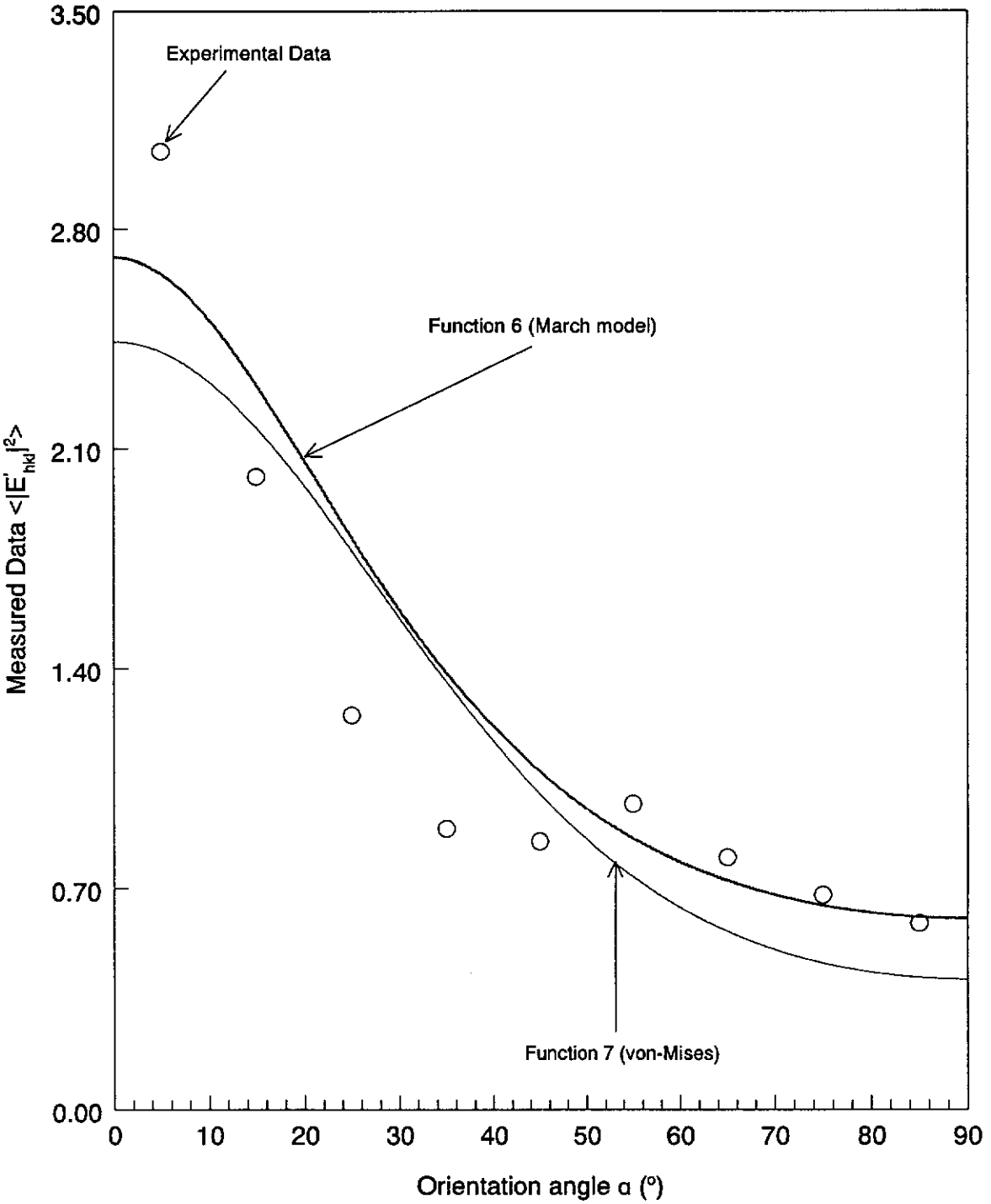

Figure 1.4(a). Variation of the distribution of PbS_2O_3 experimental data $\left\langle \left| E'_{hkl} \right|^2 \right\rangle$ versus orientation angle α for the plane (002). The best-fitting von-Mises function shown in the diagram has a G-parameter of 0.893; and the best-fitting March-Dollase function has a PO r-parameter of 0.717. After Altomare *et al.* (1994).

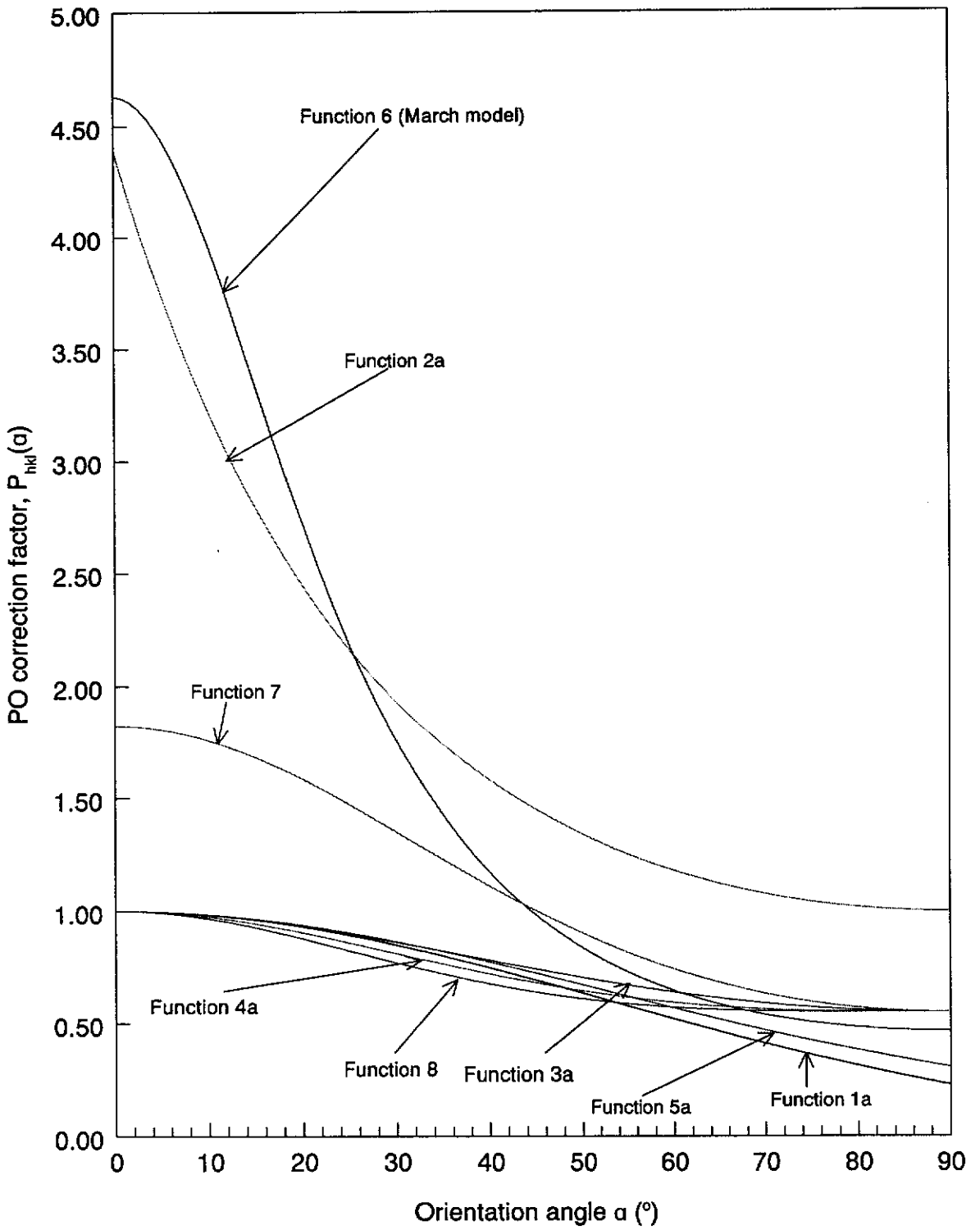

Fig. 1.4(b). Variation of single-parameter PDDFs with orientation angle α - *distributions with maximum at* $\alpha = 0$, *minimum at* $\alpha = \pi/2$, see functions (1) - (8) in Table (1.2). Plots given for the PO parameter of 0.60.

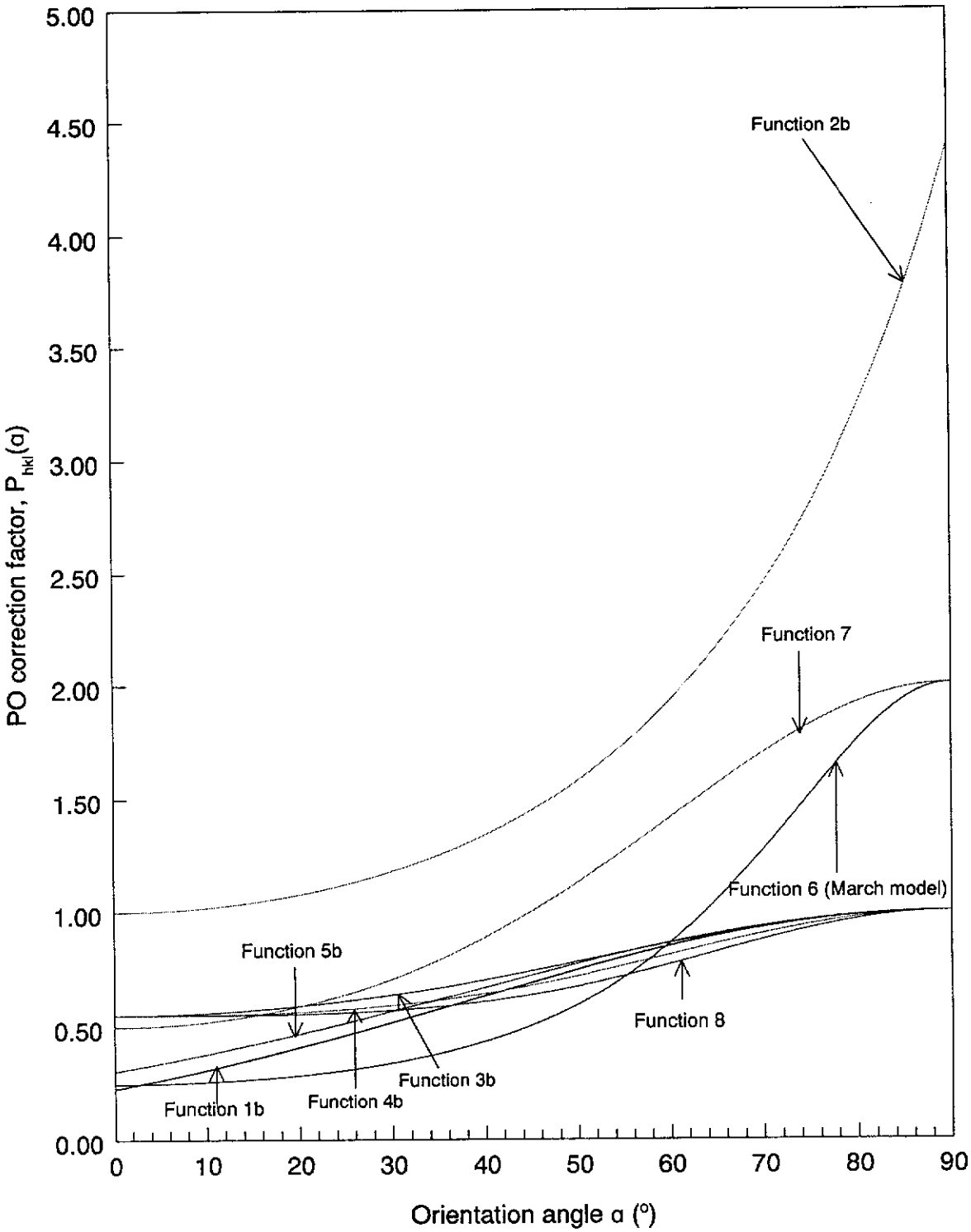

Fig. 1.4(c). Variation of single-parameter PDDFs with orientation angle α - *distributions with minimum at $\alpha = 0$, maximum at $\alpha = \pi/2$*, see functions (1) - (8) in Table (1.2). Plots given for the PO parameter of 0.60 for functions (1) - (5) and (8), whereas the plots for functions (6) and (7) are for parameter values 1.59 and -0.70, respectively.

Function (2a) is not symmetric or smooth at $\alpha = 0$ whereas (2b) is not smooth at $\alpha = \pi/2$. These functions are not normalisable and do not mimic published pole-figures.

❸ Functions proposed by Capkova and Valvoda (1974)

Function 3a (max. at $\alpha = 0$) $P_{hkl}(\alpha) = \exp(-G \cdot \sin^2 \alpha)$ *(1.16a)*

Function 3b (min. at $\alpha = 0$) $P_{hkl}(\alpha) = \exp(-G \cdot \cos^2 \alpha)$ *(1.16b)*

❹ Functions proposed by Capkova and Valvoda (1974)

Function 4a (max. at $\alpha = 0$) $P_{hkl}(\alpha) = \exp[-G(1 - \cos^3 \alpha)]$ *(1.16c)*

Function 4b (min. at $\alpha = 0$) $P_{hkl}(\alpha) = \exp[-G(1 - \sin^3 \alpha)]$ *(1.16d)*

By direct measurement of the orientation distributions in Mg and Mg_3Cd powder samples, obtained from texture goniometer measurements, it was found that a cylindrically-symmetric, needle-type texture was present in the samples. The data were modelled with the functions 1.16(a) and (c).

Functions 3(a), (b) and 4(a) and (b) have zero derivatives at $\alpha = 0$ and $\alpha = \pi/2$, but are non-symmetric across $\alpha = 0$.

❺ Gaussian-related functions proposed by Sasa and Uda (1976) and Toraya and Marumo (1981)

Function 5a (max. at $\alpha = 0$) $P_{hkl}(\alpha) = b + (1 + b) \cdot \exp[-G\alpha^2]$ *(1.17a)*

Function 5b (min. at $\alpha = 0$) $P_{hkl}(\alpha) = b + (1 + b) \cdot \exp[G(\pi/2 - \alpha)^2]$ *(1.17a)*

With these expressions, the value of b becomes indeterminate as PO parameter G approaches 0. The functions are non-symmetric at $\alpha = 0$ and $\pi/2$, and not smooth at $\alpha = 0$. They do not match published pole-figures.

Functions (6) and (7), see following outline, are generally superior to functions (1) - (5) in that they

1. may represent distributions which have either a maximum or minimum at $\alpha = 0$,
2. may be normalised, and
3. are symmetric and smooth across $\alpha = 0$ and $\alpha = \pi/2$.

❻ The currently-popular function developed by March (1932) for modelling the grain rotation mechanism producing PO, and proposed by Dollase (1986) for correction of powder diffraction intensities

Function 6 $$P_{hkl}(\alpha) = [r^2 \cos^2 \alpha + r^{-1} \sin^2 \alpha]^{-3/2} \qquad (1.18)$$

where r is the single parameter controlling distribution shape. This function, which enjoys widespread use in Rietveld analysis, is considered in Section (1.5).

❼ The *von Mises distribution function* proposed by Altomare *et al.* (1994)

Function 7 $$P_{hkl}(\alpha) = \exp[G \cdot \cos(2\alpha)] \qquad (1.19)$$

which can provide distributions similar to those for the March type (function 6) although the function does not have a physical basis.

Both the March-Dollase and the von Mises profiles were tested by Altomare *et al.* (1994) with PbS_2O_3 XRPD data. The Rietveld crystallographic figures-of-merit results obtained with the two functions agreed well. Peschar, Schenk and Capkova (1995) showed that Rietveld-von Mises calculations for $CaCO_3$, $NaNO_3$, $CaMg_3(CO_3)_4$, ZnF_2, Mg and YBC gave excellent results with XRPD data. Subsequently, Altomare *et al.* (1996) considered function (7) in terms of possible complications caused by reflection overlap. The Rietveld refinement results showed that direct methods analysis was successful when the von Mises function was employed for PO corrections. Similarly, Lasocha and Schenk (1997) found that agreement between calculated and measured XRPD patterns improved dramatically when the von Mises function was employed in Rietveld refinements with Bragg-Brentano XRPD data for $ZnMo_3.O_{10}.3.75H_2O$, $(NH_4)_2.Mo_3.O_{10}.H_2O$ and $K_2.Mo_3.O_{10}.H_2O$.

❽ Cerny, Valvoda and Chladek (1995) generalised PO into the following normalised form

Function 8 $$P_{hkl}(\alpha) = A \cdot \exp[-G\{1 - \cos^n \alpha\}] \qquad (1.20)$$

where α is the angle between the Bragg RLV and the PO axis, G and n are free parameters and A is a normalisation constant. Rietveld analysis results obtained by Cerny *et al.* (1995) for a heavily-textured $Mg(OH)_2$ specimen showed that the

agreement between the calculated and measured XRPD patterns improved dramatically when function (8) was employed.

The March (1932) PO model, function (6), proposed by Dollase (1986) for PO modelling with diffraction data, has proved to be the most popular of the simple cylindrically-symmetric models described in the literature. In view of the significance of the function for PO modelling, and the emphasis on the model in the thesis, the function is overviewed separately in the following section.

1.5 The March Model for Cylindrically-Symmetric PDDFs

The March model, function (6) - equation (1.18), is based on the rotation of isolated, rigid, planar "marker" grains in an inert, homogeneous matrix, in response to a volume-conserving, axially-symmetric compression [see Section (2.1) for further details]. Parameter r is an index of the extent of PO rather than a representation of the fractional measure of crystallite random orientation in the material, see Figure (1.5).

The model is applicable to crystals of any symmetry and does not require use of data acquired with a multi-axis diffractometer. The two assumptions implicit in the model are:

(i) the distribution function describing the orientation of crystallites is axially-symmetric (this assumption is usually satisfied for pressed powder samples and can be ensured by spinning the flat-plate sample about its cylindrical axis during data collection); and

(ii) the crystallites are assumed to be disc-shaped. In a (pressed) flat powder sample, every crystallite in the sample, with any orientation with respect to the sample surface, can be arbitrarily rotated around its prominent direction (*i.e.* around the normal to the planar surface of crystallite).

The March model has an important advantage over other PO mathematical models which have been proposed [see Table (1.2)], in that the function $P_{hkl}(\alpha)$ is normalisable over the full angular range of α :

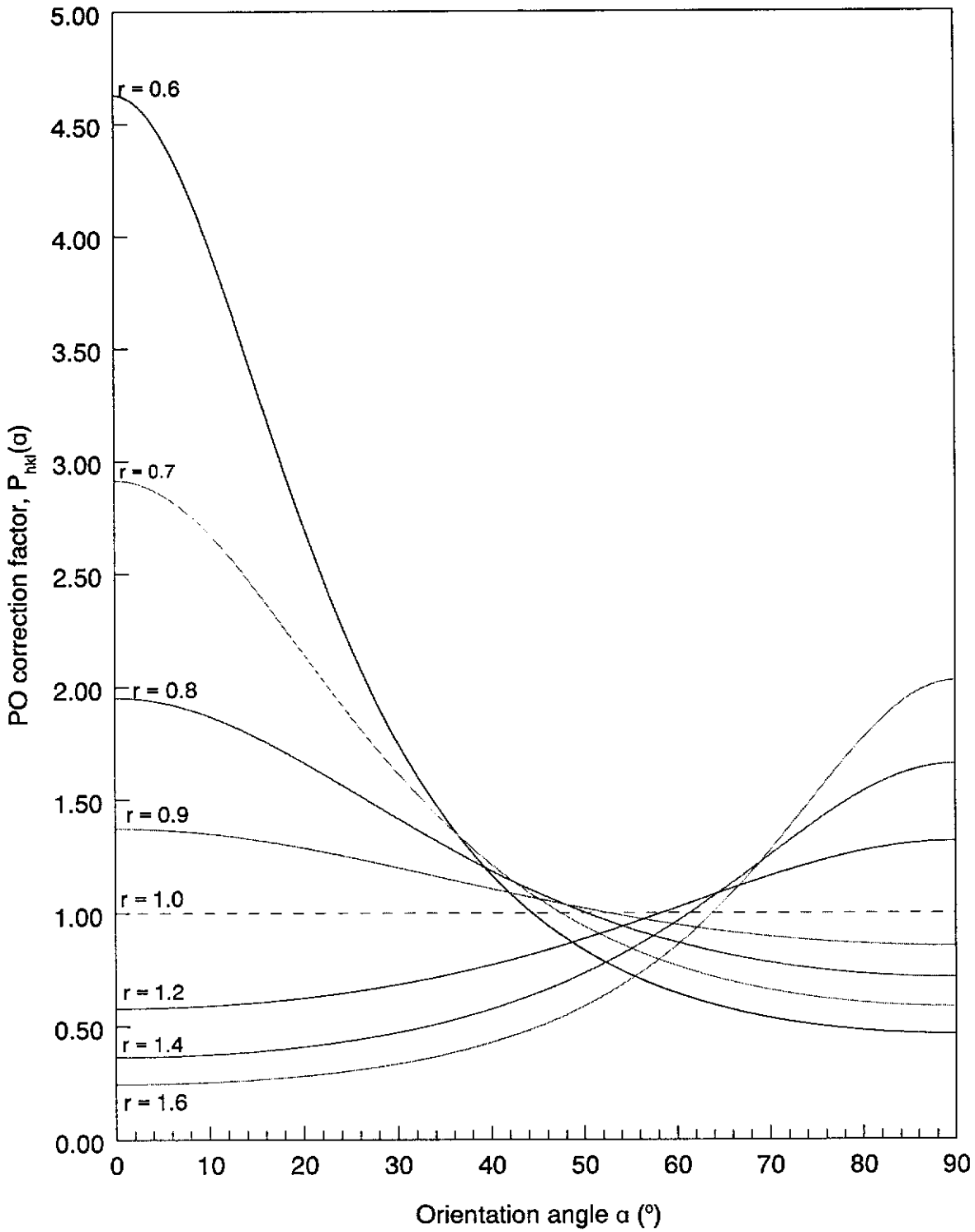

Fig. 1.5. The variation of the March-Dollase PO factor (function 6) with orientation angle α for different values of March r-parameter. The March PDDF value ranges from r^{-3} at $\alpha = 0^{\circ}$ to $r^{3/2}$ at $\alpha = 90^{\circ}$ according to the amount of sample deformation and also depends on particle morphology.

$$\int_0^{\pi/2} P_{hkl}(\alpha) \cdot d\alpha = 1 \tag{1.21}$$

whereas the other functions are unnormalised. The normalisation property is important in that changes in the PDDF shape conserves the total intensity within the diffraction pattern. Therefore, scale factors obtained by Rietveld refinement with the March model should be more reliable than those obtained using unnormalised PO models, and scale factors derived with the March model should be more reliable for absolute phase composition analysis.

Dollase (1986) described Rietveld evaluations of the March model using XRPD data sets for calcite [$CaCO_3$] and huntite [$CaMg_3(CO_3)_4$] powders. The degree of PO for the calcite powders was too weak to demonstrate any superiority of the March formula over the other expressions [see Table (1.2)]. However refinements conducted with two huntite specimens, corresponding to both low- and high-orientations, clearly demonstrated the superiority of the March formula. The low-orientation and high-orientation huntite samples gave substantially superior matches between calculated and observed patterns when the March model was employed.

Li, O'Connor, Roach and Cornell (1990) and O'Connor, Li and Sitepu (1991) described a line ratio PO correction method, based on the March model, for applying PO corrections to XRPD Bragg intensities, which was evaluated with gibbsite [$Al(OH)_3$] data. They concluded from this study that the March model is an excellent descriptor of PO in gibbsite. Sitepu (1991); O'Connor, Li and Sitepu (1992); and Sitepu, O'Connor and Li (1996) subsequently extended the earlier work on gibbsite to other materials [molybdite (MoO_3), calcite ($CaCO_3$) and kaolinite ($Al_2O_3.2SiO_2.2H_2O$)]. *The results indicated that the model has some deficiencies for Rietveld modelling.*

Judson *et al.* (1994) showed that the Rietveld-March calculations for barium copper yttrium oxide (YBa_2CuO_{7-x}) superconductor thin films with strong single-pole orientation provided excellent results with XRPD data. Similarly, Iyengar and Percec (1994) found that agreement between the observed and calculated patterns improved dramatically when the March model was employed in Rietveld refinements with Bragg-Brentano XRPD data for high-density polyethylene.

1.6 Study Objectives

The objective of the thesis study was to extend the work of Li *et al.* (1990); O'Connor, Li and Sitepu (1991, 1992); Sitepu (1991); and Sitepu, O'Connor and Li (1996) on the general applicability of the March (1932) model for modelling PO with both XRPD and NPD powder data, with reference to :

- the reliability of the March model,
- its use in correcting powder diffraction intensities for PO bias.

1.7 Research Plan

In order to fulfil the objectives of this study, the following broad research plan was formulated :

1. Investigate differences between (i) PO correction factors derived from diffraction pattern data and (ii) PO correction factors for selected powders obtained from texture diffractometry.
2. Examine the validity of the March PO model for powder diffraction characterisation of materials.

The study was to be conducted using uniaxially-pressed powders for which the pressure would be varied systematically. X-ray and neutron powder diffractometry would be used in order to obtain near-surface and bulk information, respectively.

1.8 Thesis Structure

Chapter 1 summarises the literature on powder diffraction PO modelling methods for use in materials characterisation. Fully-general methods for modelling PO, which require many-parameter computations, are first surveyed and then the simple single- or several-parameter functions for cylindrically-symmetric PO distributions are considered. Particular attention is given to the March-Dollase formula for modelling cylindrically-symmetric distributions. The Chapter concludes with a statement of study objectives and the associated research plan.

Chapter 2 reviews in considerably greater detail than Chapter 1 the literature on the aspects of PO which are of central importance to the thesis. In particular, the Chapter focuses on (i) PO modelling with the March model and (ii) modelling PO

with texture diffractometry data. The material on the March model includes a discussion on an important aspect of Rietveld modelling with the March model which emerged during the course of the thesis, *viz.* the need for Rietveld programs to factor symmetry-equivalent Bragg reflections into the computations.

Chapter 3 contains an overview of experimental design, followed by a rationale for materials selection, the powder diffraction and pole-figure methods, the methods for Rietveld analysis of diffraction data, and the PO mathematical modelling determination. The Chapter also describes the rationale adopted in comparing PDDFs derived from the texture measurements using Eulerian cradle and obtained from Rietveld-March calculated data sets of molybdite and calcite specimens. The Chapter outlines a method developed during the study whereby the March r-parameter may be used to quantify the bulk modulus of a powder.

Chapter 4 considers the diffraction pattern experiments for molybdite and calcite powders, with particular reference to the validity of the March model and the directly-measured PDDFs.

Chapter 5 describes texture diffractometry experiments from similar perspective to those considered in Chapter 4.

Finally, Chapter 6 gives an overview of the results with reference to the objectives.

CHAPTER 2

ASSESSMENT OF PREFERRED ORIENTATION WITH DIFFRACTION DATA

Following the general review provided in Chapter 1, this chapter considers in detail the basis of the two texture modelling procedures applied in the thesis - use of the March formula to extract texture information from powder pattern data, and the direct measurement of pole-figures by texture diffractometry.

2.1 March Model

2.1.1 Model Features

The March (1932) model was introduced and considered briefly in Section (1.5). Further details, including a summary of the mathematical derivation of the March model provided in Appendix (1), are considered here.

Four features of the March PDDF were noted by Dollase (1986). First, the March model has a valid theoretical basis related to the major mechanism (grain rotation) that produces PO. The second feature is that the model has a true probability distribution with unit integral which means that a change in PO parameter, r, should not produce a change in the Rietveld scale factor [see Section (3.4)]. Third, the model applies to both platy and acicular grains. Fourth, the model has a single variable parameter, r, the March coefficient, that characterises the strength of the PO. Even for samples developing PO due to mechanisms other than compaction and grain settling, fitting a March model allows estimation of an intuitively-simple, specimen-compaction correction which is useful for quantitative comparison of samples.

The value of the PDDF for the model ranges from r^{-3} to $r^{3/2}$ according to the amount of sample deformation. The same expression is used for a PDDF maximum at $\alpha = 0$ ($r < 1.0$) or a PDDF maximum at $\alpha = \pi/2$ ($r > 1.0$). Because the orientations of platy and acicular crystallites are differently defined relative to their respective morphologies, there is a different relationship between the March parameter, r, and

the sample compaction or extension for the two limiting crystallite shapes. In the case of platy crystallites :

$$r = \frac{d}{d_o} \tag{2.1}$$

where d is the sample thickness after axial extension or compaction, and the form

$$r = \frac{d_o}{d} \tag{2.2}$$

applies to acicular crystallites.

Application of the model requires two assumptions to be made (Dollase, 1986), *viz.*:

- The distribution function of the pole HKL, representing the preferentially-oriented direction, has its maximum normal to the specimen surface for symmetric diffraction. This requirement can be satisfied by rapidly spinning a flat-plate specimen around the diffraction vector.
- The distribution is axially-symmetric, corresponding to so-called disc- or rod-shaped behaviour. In a flat sample, the discs will have their prominent faces more or less aligned parallel to the sample surface.

2.1.2 Derivation of the March-Dollase PO Correction Factor

The March model treats the development of PO in a homogeneously deformed medium according to the reorientation of linear and planar indicators. Because deformation is homogeneous, the effect of deformation is to reorient lines and planes.

Owens (1973) used a geometrical approach in his development of the March model according to the movement of linear markers. This approach has the virtue of avoiding the complex tensor mathematics described in the March paper and of making the deformation more evident. Chen (1991) modified the analysis of angular density distribution frequency (ADF), described by Owens (1973), which showed that the pre- and post-deformational ADF of linear and planar elements in a specimen (f and F, respectively) are related by the quadratic elongation, λ^2, of the strain, ε, [see Appendix (1)]

$$F = (\lambda^2)^{3/2} f \tag{2.3}$$

assuming a constant-volume strain, *i.e.* strain normalised to unit volume. Term λ^2 is calculated from the transposed inverse of the strain, ε.

In the following derivation, equation (2.3) is extended in sample coordinates, ${}^{S}X_i$, and reference coordinates, ${}^{R}X_i$, which coincide with the principal axes, E_i, of a strain, ε. The sample and reference coordinates are related to each other by Euler angles $(\varphi_1, \phi, \varphi_2)$- see Figure (2.1). Initial reference coordinates, ${}^{R}X_i''$, are parallel to the sample coordinates, ${}^{S}X_i$, and auxiliary axes, ${}^{R}X_1'$, facilitate the Euler angle operation. The square symbol in the figure represents the maximum principal direction of ADF, the circle represents the intermediate principal direction of ADF, the triangle is the minimum principal direction of ADF; and the filled circles represent the auxiliary coordinate axes.

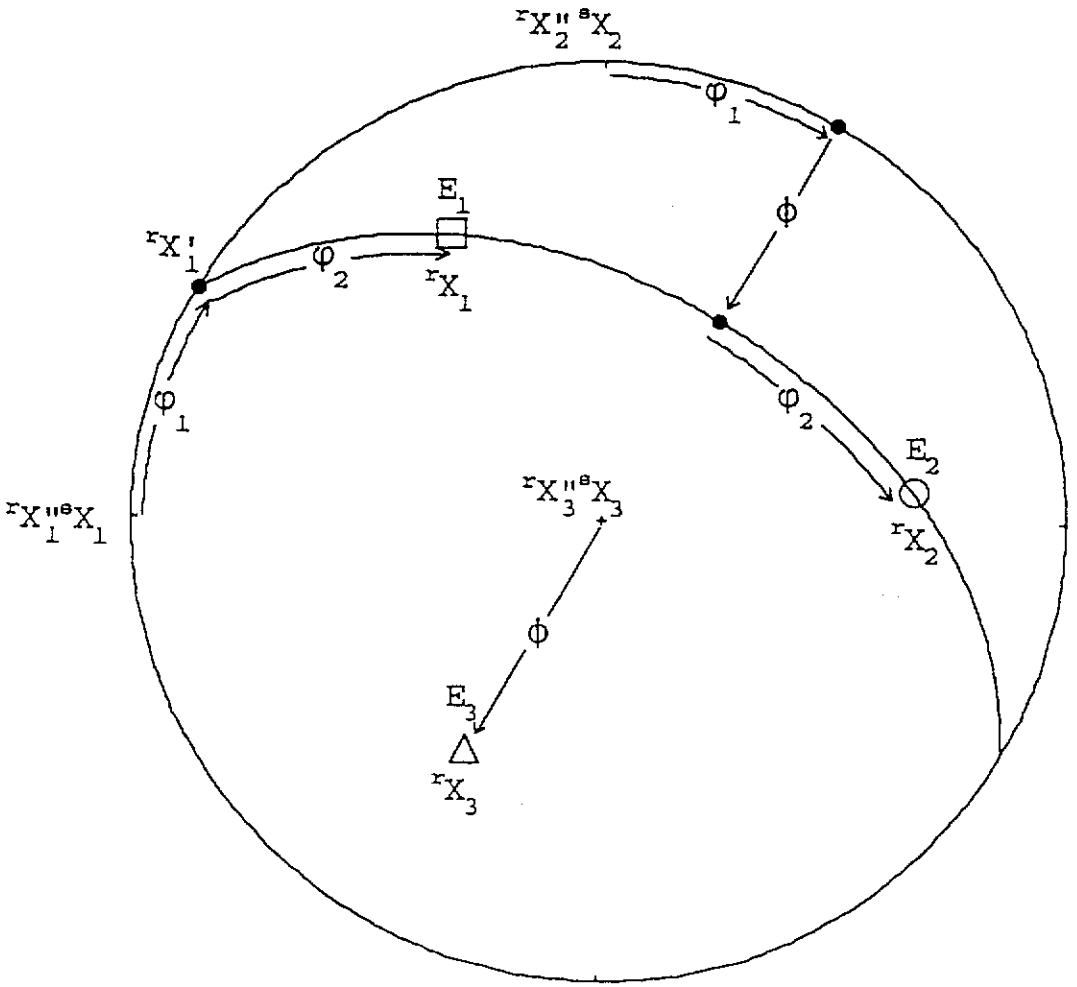

Figure (2.1) A lower hemisphere equal-area projection illustrates the interrelations between the sample coordinates, ${}^{s}X_i$, the reference coordinates, ${}^{r}X_i$, and the principal axes of the ADF, E_i, by the Euler angles, $(\varphi_1, \phi, \varphi_2)$. After Chen (1991).

The observed x-ray intensity I should be proportional to the pole-distribution frequency of the strain markers, and the distribution frequencies F and f can be replaced by x-ray intensities I and q, respectively, and augmented by a background level, B. As a result,

$$I = \left(\lambda^2\right)^{3/2} q + B \tag{2.4a}$$

or

$$I = \left[\frac{1}{{}^{S}R^{T} A^{T} ({}^{R}S)^{2} A\ {}^{S}R}\right]^{3/2} q + B \tag{2.4b}$$

where ${}^{S}R$ is the unit vector representing the direction of an angular pole-density in the sample coordinates; A is the transformation matrix relating the principal stretch axes to sample coordinate [see Appendix (1)]; ${}^{R}S$ is the stretch tensor in reference coordinates which coincide with its principal axes; and q is the x-ray intensity of a hypothetical, randomly-distributed undeformed sample.

Equation (2.3) indicates that the strain tensor and the ADF of a specimen share principal directions. Thus, the principal directions of the strain tensor can be pre-determined by visual inspection. This procedure reduces the number of unknowns from seven to four and one can express equation (2.4b) in reference coordinates which coincide with principal axes (Chen, 1991):

$$I_k({}^{R}\theta_k, {}^{R}\phi_k) = \left[S_1^2 \sin^2{}^{R}\theta_k \cos^2{}^{R}\phi_k + \left(\frac{\sin^2{}^{R}\theta_k \sin^2{}^{R}\phi_k}{S_1^2 S_3^2}\right) + S_3^2 \cos^2{}^{R}\theta_k\right]^{-3/2} q + B \tag{2.5}$$

where $({}^{R}\theta_k, {}^{R}\phi_k)$ are the spherical coordinates, with respect to sample orientation, for the orientation (β_k,τ_k) of the goniometer sample stage (Wenk, 1985); and S_1 and S_3 are the maximum and minimum March stretches, respectively.

Consider a planar powder diffraction sample formed by a volume conserving, cylindrically-symmetric, flattening such that the initial sample thickness d_o is reduced to a thickness d. Assuming that the initial grain orientation was random, what is the degree of PO in the sample? This is precisely the March model for producing PO in a powder diffraction sample.

As the sample flattening is axially symmetric about the sample normal, the stretch tensor axial lengths in the sample plane are equal,

$$S_1 = S_2 \tag{2.6}$$

and the stretch tensor axial length along the sample normal,

$$S_3 = \frac{d}{d_o} = r \tag{2.7}$$

Since,

$$S_1 S_2 S_3 = 1, \tag{2.8}$$

substituting equations (2.6) and (2.7) into equation (2.8) gives :

$$S_1 = S_2 = r^{-1/2} \tag{2.9}$$

and substituting equations (2.7) and (2.9) into equation (2.5) yields :

$$I_k({}^R\theta_k, {}^R\phi_k) = \left[r^{-1}\sin^{2R}\theta_k(\cos^{2R}\phi_k + \sin^{2R}\phi_k) + r^2\cos^{2R}\theta_k\right]^{-3/2} q + B \tag{2.10}$$

Since,

$$(\cos^{2\,R}\phi_k + \sin^{2\,R}\phi_k) = 1,$$

equation (2.10) yields :

$$I_k({}^R\theta_k, {}^R\phi_k) = \left[r^{-1}\sin^{2\,R}\theta_k + r^2\cos^{2\,R}\theta_k\right]^{-3/2} q + B \tag{2.11}$$

Thus, the PO intensity correction factor is,

$$P_k = \left[r^{-1}\sin^{2\,R}\theta_k + r^2\cos^{2\,R}\theta_k\right]^{-3/2} \tag{2.12}$$

where θ_k is the angle between the diffracting plane normal and the sample normal - denoted as α in equation (6) of Table (1.2).

If the grain shape is axially-symmetric, as often applies for hexagonal and trigonal grains, the polar axis density **P** also can be looked upon as axially-symmetric, with regard to the z-axis - see Figure (2.2) which shows the intensity measurement for a flat, rotating specimen using the conventional Bragg-Brentano measuring geometry. If the sample is inclined so that the angle between the polar axis and the scattering vector is α [Figure (2.2b)], only grains whose scattering vector is on the circle O(hkl,α) will contribute to the reflection (hkl). O(hkl,α) is a circle on the unit sphere, whose center is in the direction of the plain normal N^{hkl} and whose radius corresponds to the pole angle α.

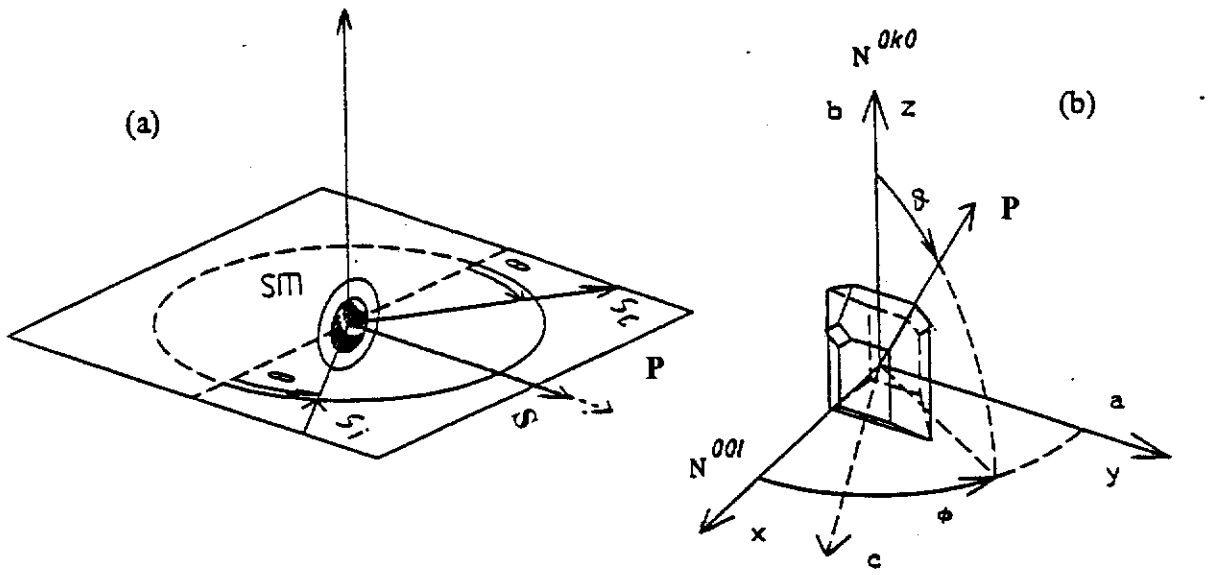

(a) **(b)**

Figure 2.2(a). (a) Bragg-Brentano geometry. Flat sample rotated around polar axis **P** coinciding with scattering vector **S**. (b) Direction of polar axis **P** in crystallographic coordination system of a grain (monoclinic case). After Jarvinen (1993).

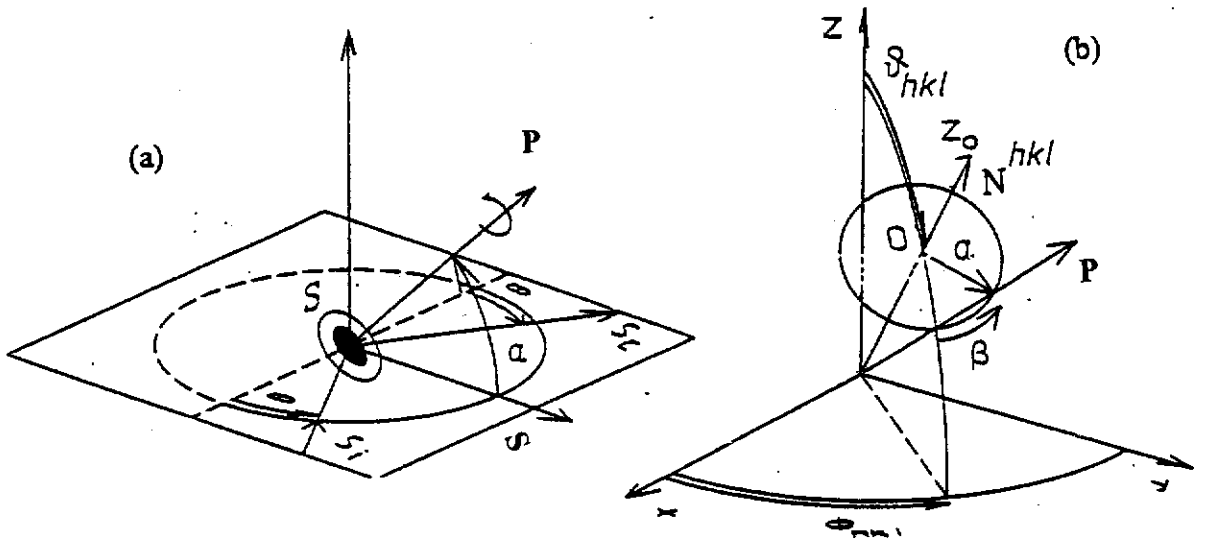

(a) **(b)**

Figure 2.2(b). (a) The sample is inclined from the upright position at an angle α. (b) Orientation of the polar axis **P** in the grain coordinate system. After Jarvinen (1993).

2.1.3 PO Correction Procedures

Two key aspects of PO computation with the March model are considered here - definition of PO direction and the inclusion of reflection symmetry equivalence.

Choice of PO Direction

The PO direction is usually taken from the literature according to the cleavage plane of the material. If there is no cleavage information available, then the PO plane may be determined by trial and error - see, for example, the work of Will, Parrish and Huang (1983) and Will, Belloto, Parrish and Hart (1988) in which the plane giving the lowest Bragg R-factor was used as the PO direction.

An additional aspect of PO direction, which emerged in this study, is that the PO directions for XRPD and NPD data for the same material may be different [see Sections (4.3.2) and (4.4.2)].

Reflection Symmetry-Equivalence

For PO direction [HKL], the intensity I_{hkl} of a single reflection hkl, making an angle α with the preferentially-oriented planes (HKL), will be modified according to:

$$I_{hkl} = s\, L_P\, |F_{hkl}|^2\, P_{HKL}(\alpha) \qquad (2.13)$$

where s is the scale factor, L_P is the combined Lorentz, polarisation and monochromator factors, $|F_{hkl}|^2$ is the absolute square of structure factor and $P_{HKL}(\alpha)$ is the PO correction factor as shown in equation (2.12).

The total intensity resulting from a set of m symmetry-equivalent planes can be denoted

$$I_{2\theta} = s\, L_P\, |F_{hkl}|^2\, m_{hkl}\, P_{HKL}(\alpha) \qquad (2.14)$$

in which m_{hkl} is the multiplicity of the reflection hkl.

Except for special PO directions [equation (2.13)], symmetry-equivalent reflections will contribute in different ways to the total intensity observed at 2θ. It is possible that each reflection plane $(hkl)_j$ from a set of m symmetry-equivalent planes {hkl} makes a different angle α_j with the PO plane (HKL). As a result, the total intensity resulting from a complete set of m symmetry-equivalent planes, taking into account the PO, becomes :

$$I_{2\theta} = s\, L_P\, |F_{hkl}|^2 \sum_{j=1}^{m_{hkl}} P_{HKL}(\alpha_j) \qquad (2.15)$$

where α_j is the angle between (HKL) and the i^{th} member of the set of m symmetry-equivalent diffracting planes. In the absence of PO, the summation in equation (2.15) should reduce to m_{hkl} so the relation between observed intensity in the presence of PO, $[I_{2\theta}(obs)]$, and that of a uniform sample, $I_{2\theta}(random)$, can be expressed as :

$$I_{2\theta}(obs) = P_{hkl}\, I_{2\theta}(random) \qquad (2.16)$$

with

$$P_{hkl} = m_{hkl}^{-1} \sum_{j=1}^{m_{hkl}} P_{HKL}(\alpha_j) \qquad (2.17)$$

The summation in equations (2.15), (2.16) and (2.17) is known as the generalised multiplicity term (Dollase, 1986; Capkova, Peschar and Schenk; 1993).

2.1.4 Prior Studies of the March Model by Curtin Materials Research Group

The present study was preceded by investigations, conducted by the Curtin Materials Research Group, on the suitability of March model for PO corrections in powder diffraction analysis. It is relevant, in the context of the present study, to summarise these experiments.

Table (2.1) summarises Rietveld-March results for gibbsite, calcite and molybdite, molybdite diluted with 50% by weight silica gel, and kaolinite, respectively. These four materials all show pronounced PO. It is evident that Rietveld refinement improved the internal agreement between these scale factors for each material when the March model was employed (O'Connor, Li and Sitepu, 1991; Sitepu, 1991; O'Connor, Li and Sitepu, 1992; and Sitepu, O'Connor and Li, 1996) - see Table (2.1). The marginal gains in R_{WP} for kaolinite suggest that the March model is less appropriate for this material than gibbsite, molybdite and calcite. The quality of the Rietveld refinements involving random orientation and March PO models may also be gauged from the diffraction pattern plots. Figure 2.3(a), reproduced from O'Connor, Li and Sitepu (1991), shows the agreement between calculated and measured XRPD patterns for a highly-oriented gibbsite sample for

Table 2.1

Figures-of-Merit Single-Phase Rietveld Refinements [see Section (3.4)] with Gibbsite, Calcite, Molybdite and Kaolinite XRPD Data Using Random Orientation and March PO Models. (O'Connor, Li and Sitepu; 1991 and 1992)

The assumed PO directions for gibbsite, calcite, molybdite and kaolinite XRPD data were <001>, <104>, <010> and <001>, respectively.

Specimen	Random Orientation			March Model		
code[4]	R_{EXP}	R_{WP}	R_B	R_{WP}	R_B	r
Gibbsite						
SD	9.3	17.2	5.9	17.1	5.5	1.032
LP	10.0	25.7	12.2	18.4	4.7	0.758
BR	7.4	32.4	14.4	20.3	5.2	0.609
Calcite						
SD	10.4	20.4	9.8	18.4	4.4	0.949
LP	10.4	21.3	10.3	19.6	5.3	0.904
BR	10.7	32.1	22.2	25.5	10.8	0.793
Molybdite						
SD	7.7	33.8	22.8	23.4	11.9	0.755
LP	6.2	65.3	58.9	25.4	8.9	0.463
BR	7.2	72.6	64.2	28.6	10.8	0.550
Kaolinite						
SD	7.8	21.9	8.5	21.7	7.3	0.882
LP	7.5	24.0	8.7	23.8	8.6	0.681
BR	8.3	23.5	8.1	20.7	5.8	0.669

[4] SD = samples mounted by side-drifting.
LP = samples mounted by lightly front-pressing with a glass slide.
BR = samples mounted by back-pressing into briquettes at a pressure of 6 bar for 7 seconds with a Hertzog HDIF machine.

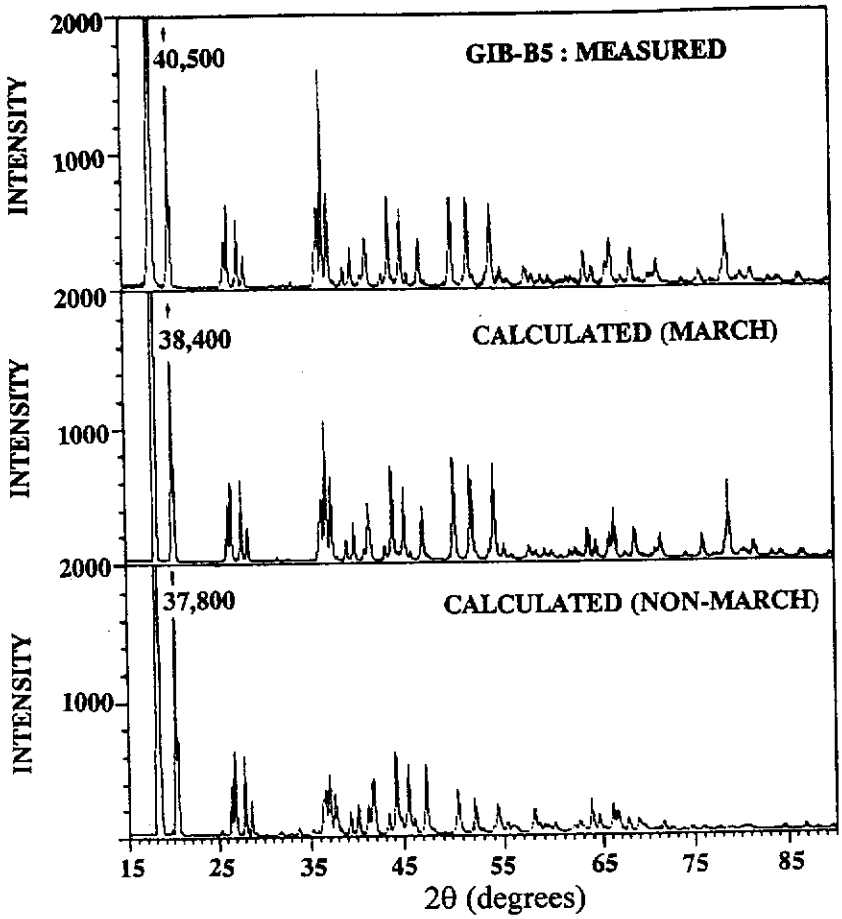

Figure 2.3(a). Measured XRPD pattern for a highly-oriented gibbsite (March parameter r = 0.61) and corresponding calculated patterns following Rietveld refinement. After O'Connor, Li and Sitepu (1991).

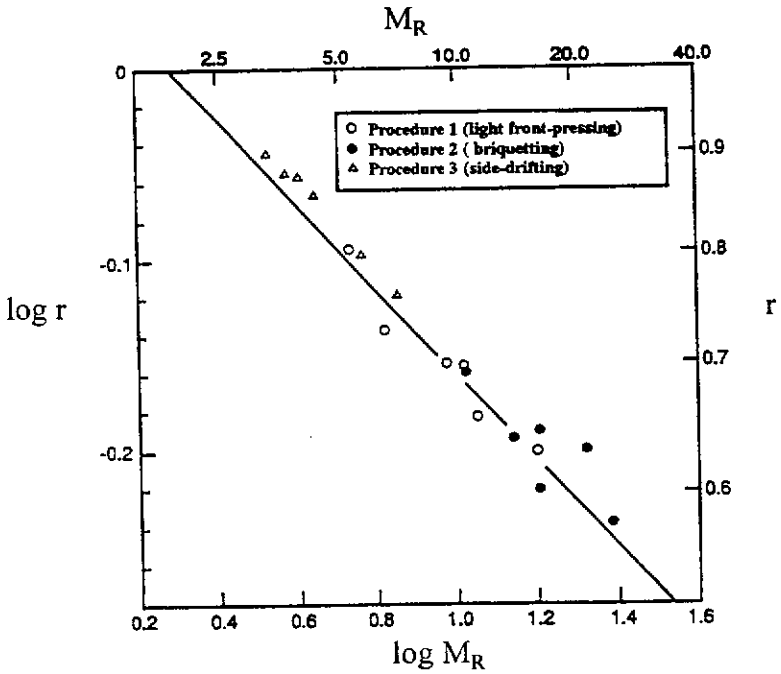

Figure 2.3(b). Logarithmic plot of March r-parameter from Rietveld refinements, versus measured line ratio, M_R for gibbsite specimens. The unbroken line is the theoretical r-M_R relation [see equation (2.18)]. After O'Connor, Li and Sitepu (1991).

which the Rietveld-March r-parameter was 0.61. The agreement was clearly superior when the March model was applied.

In assessing the effectiveness of the March model, O'Connor, Li and Sitepu (1991) proposed an alternative method for PO corrections in which the r-parameter was derived analytically from the intensity ratio of a pair of lines with different orientation angles, α_j. Such intensity ratios were designed *morphological ratios,* M_R, by O'Connor, Li and Sitepu (1991).

The validity of the March model for gibbsite XRPD data was tested by O'Connor, Li and Sitepu (1991) with M_R values for the (002) line for which $\alpha = 0°$ and the line doublet (110/200) for which $\alpha \approx 90°$. The theoretical relationship between M_R and the March r-parameter was given by :

$$r = 1.15 \cdot M_R^{-2/9} \tag{2.18}$$

Figure 2.3(b), from O'Connor, Li and Sitepu (1991), shows the excellent fit of log(r)-versus-log(M_R) for a suite of gibbsite samples with differing degrees of PO. The figure shows a linear relation between log(M_R) and log(r) which confirms with the theoretical expression. It is evident from the plot that the March model is an excellent descriptor of PO in gibbsite.

Additional r-M_R analysis performed with XRPD data for molybdite, calcite and kaolinite, did not show close agreement between the measured and theoretical plots which had been observed for gibbsite [O'Connor, Li and Sitepu (1992)]. The line pair selected for molybdite was (020) [$\alpha = 0°$] and (110) [$\alpha = 74°$]. The relationship between M_R and the March r-parameter for the line pair was given by :

$$M_R = 0.411(0.0756 + 0.9244r^{-3})^{3/2} \tag{2.19}$$

Selection of line (104) for calcite was obvious [$\alpha = 0°$]. However it was not possible to select a second line with α close to 90°. Line (110) [$\alpha = 52.6°$] was chosen on the basis as it is well-resolved, albeit relatively weak. The relationship for this line pair was,

$$M_R = 6.67(0.3688 + 0.6312r^{-3})^{3/2} \tag{2.20}$$

The line pair selected for kaolinite was (001) [$\alpha = 0°$] and (060) [$\alpha = 90°$] for which,

$$M_R = 10(0.0010 + 0.9989r^{-3})^{3/2} \tag{2.21}$$

Figure (2.4) reproduced from O'Connor, Li and Sitepu (1992), shows plots of r-versus-M_R for molybdite, calcite and kaolinite XRPD data. The plots trend in the general manner expected for r-versus-M_R, but do not agree closely with the theoretical plots. The linear regressions fit for the molybdite, calcite and kaolinite measured data were given by

$$M_R = 0.76r^{-1.95} \tag{2.22}$$

$$M_R = 8.67r^{-3.61} \tag{2.23}$$

$$M_R = 3.88r^{-3.12} \tag{2.24}$$

The r-values from Rietveld refinements exceed the values from line rationing analysis for all molybdite and kaolinite samples whereas the trend was reversed for the calcite results. These inconsistencies between the experimental and theoretical indicate shortcomings in the March model for these materials.

2.2 Texture Analysis with Eulerian Cradle Powder Diffraction Data

2.2.1 ODF Principles

Figure (2.5) shows there are three different reference frames that must be considered, *viz.* (i) the coordinate system K_m attached into the measuring instrument, (ii) the coordinate system K_s bound to the sample and (iii) the crystal coordinate system K_c fixed to every crystallite in the specimen. The ODF of a crystallite is defined as the rotation **g** that makes the coordinate systems K_c and K_s coincide. Bunge (1982) described that this rotation can be executed in many different ways for the use of the rotation **g** [equation (1.1b)]. In Figure (2.5a) the rotation is represented with the three angles ϑ, φ and ψ [in the Bunge (1982) notation : $\vartheta=\varphi_1$, $\varphi=\phi$ and $\psi=\varphi_2$ see equation (1.1c)]; where ϑ and φ are the direction angles of the axis **P** and ψ represents the rotation of Q axis (as well as also R axis) around the **P** axis.

The ODF f(**g**), is a function of φ_1, ϕ and φ_2 [see equation (1.1c)]. The crystal system K_c can be chosen in various ways, according to the space group symmetry of the material. The ODF must be invariant to the symmetry operations of the crystal. For this reason the symmetrised harmonic functions [equation (1.12)] are excellent for modelling the orientation distribution of crystallites. On this basis Bunge (1982) created a useful and reliable approach for texture analysis - see following summary.

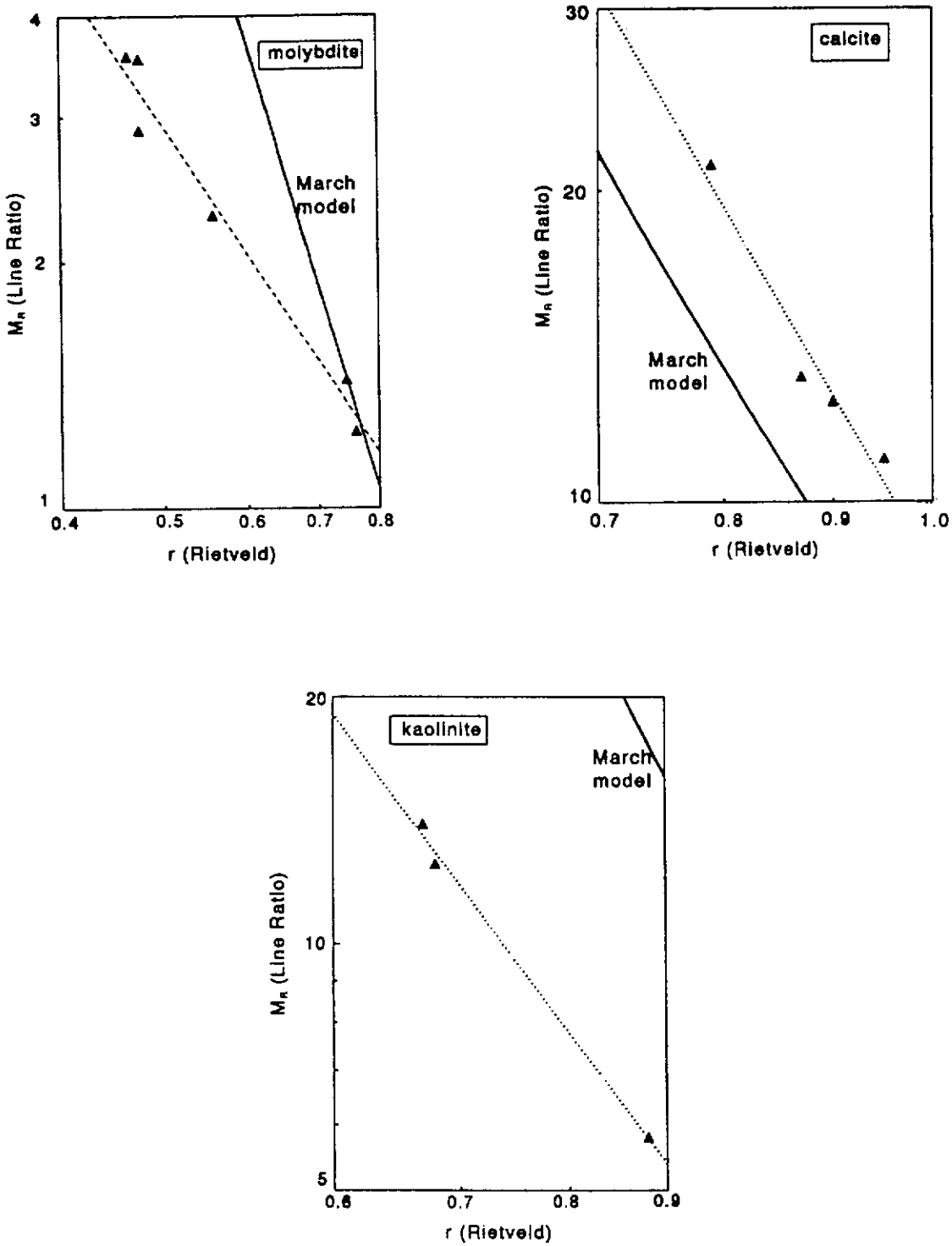

Figure 2.4. Plots of log(r)- versus- log(M_R) for molybdite, calcite and kaolinite XRPD data. The heavy lines indicate the relationship derived with the March formula. The broken line is the regression line for the measured data. After O'Connor, Li and Sitepu (1992).

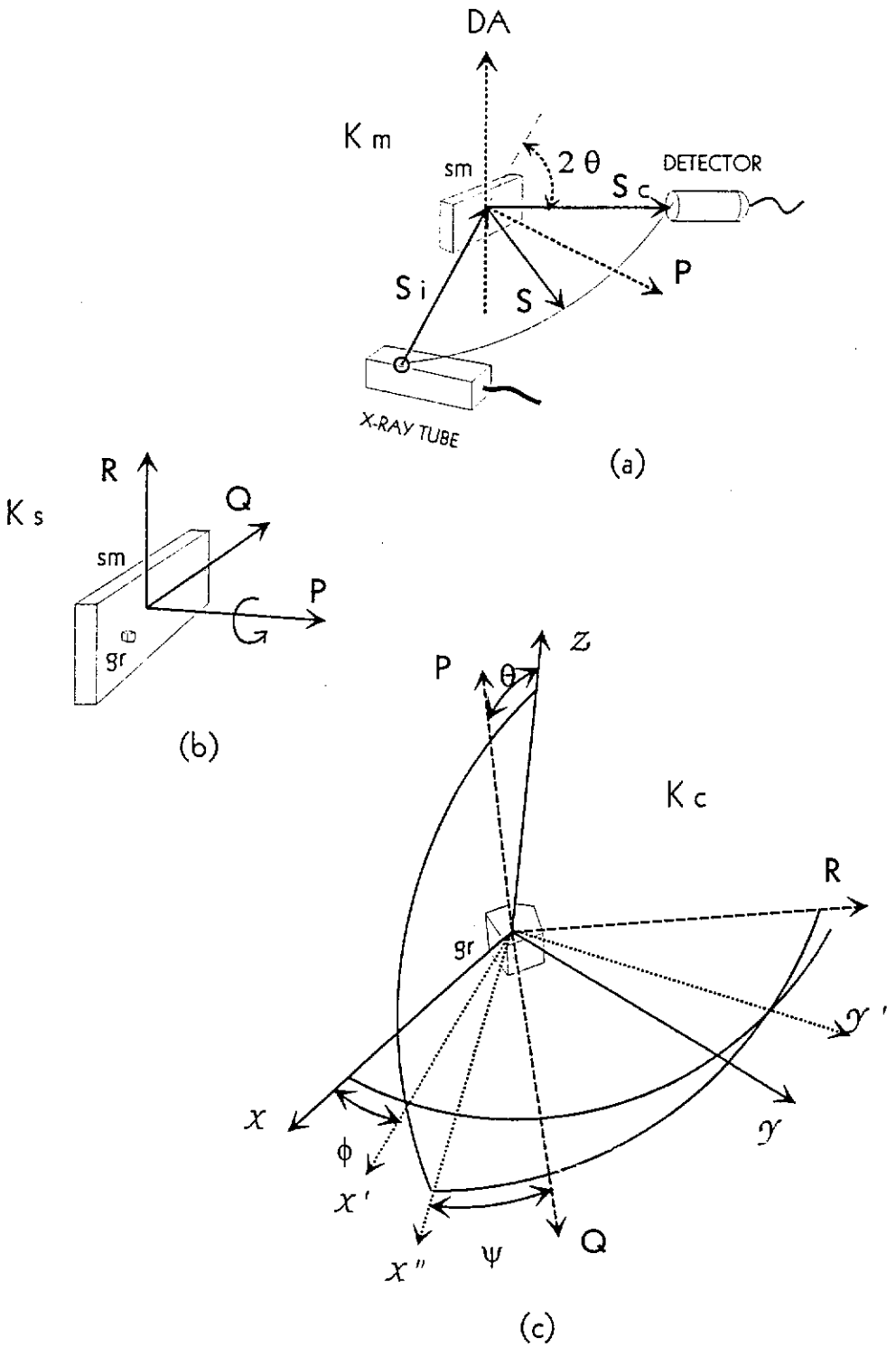

Figure (2.5). Coordinate system fixed (a) to the measuring instrument, (b) to the sample and (c) to a crystallite. After Jarvinen (1993).

Specification of the Crystal Orientation

The sample direction **y** is defined with respect to the sample coordinate system K_A either by cartesian coordinates or by spherical polar coordinates (Bunge, 1982)

$$\mathbf{y} = \{y_1, y_2, y_3\} = \{\alpha, \beta\} \tag{2.25}$$

The crystal coordinate system K_B consists of the same crystal directions in each crystallite, but it has a different orientation with reference to the sample coordinate system. The crystal direction **h** is specified in the crystal coordinate system K_B either by cartesian coordinates or by spherical polar coordinates (Bunge, 1982)

$$\mathbf{h} = \{h_1, h_2, h_3\} = \{\Theta, \gamma\} \tag{2.26}$$

Figure (2.6a) shows the crystal coordinate system parallel to the sample coordinate system. It is then rotated successively about the

$$z' \text{ axis} = [001] \text{ through the angle } \varphi_1 \tag{2.27a}$$

$$x' \text{ axis} = [010] \text{ through the angle } \Phi \tag{2.27b}$$

$$z' \text{ axis} = [001] \text{ through the angle } \varphi_2 \tag{2.27c}$$

The angles φ_1, ϕ, φ_2 described the final orientation of the crystal coordinate system K_B with respect to the sample coordinate system K_A [see equation (1.1c)]. All possible orientations can be obtained within the range :

$$0 \le \varphi_1 \le 2\pi, \quad 0 \le \phi \le \pi, \quad 0 \le \varphi_2 \le 2\pi \tag{2.28}$$

The three rotations in equation (2.27) may be expressed in matrix form :

$$\mathbf{g}^{z'}_{\varphi_1} = \begin{bmatrix} \cos\varphi_1 & \sin\varphi_1 & 0 \\ -\sin\varphi_1 & \cos\varphi_1 & 0 \\ 0 & 0 & 1 \end{bmatrix} \quad \mathbf{g}^{x'}_{\phi} = \begin{bmatrix} 1 & 0 & 0 \\ 0 & \cos\phi & \sin\phi \\ 0 & -\sin\phi & \cos\phi \end{bmatrix} \quad \mathbf{g}^{z'}_{\varphi_2} = \begin{bmatrix} \cos\varphi_2 & \sin\varphi_2 & 0 \\ -\sin\varphi_2 & \cos\varphi_2 & 0 \\ 0 & 0 & 1 \end{bmatrix} \tag{2.29}$$

The g is expressed by

$$\mathbf{g} = \{\varphi_1, \phi, \varphi_2\} = \mathbf{g}^{z'}_{\varphi_2} \cdot \mathbf{g}^{x'}_{\phi} \cdot \mathbf{g}^{z'}_{\varphi_1} \tag{2.30}$$

$$= \begin{bmatrix} \cos\varphi_1\cos\varphi_2 - \sin\varphi_1\sin\varphi_2\cos\phi & \sin\varphi_1\cos\varphi_2 + \cos\varphi_1\sin\varphi_2\cos\phi & \sin\varphi_2\sin\phi \\ -\cos\varphi_1\cos\varphi_2 - \sin\varphi_1\sin\varphi_2\cos\phi & -\sin\varphi_1\cos\varphi_2 + \cos\varphi_1\sin\varphi_2\cos\phi & \cos\varphi_2\sin\phi \\ \sin\varphi_1\sin\phi & -\cos\varphi_1\sin\phi & \cos\phi \end{bmatrix}$$

The three rotations in equation (2.27) can be carried out graphically using the 2D stereographic projection. If the x-y plane of the sample coordinate system is chosen as the projection plane, then the points representing the crystal x', y', z' axes are obtained by the orientation [see Figure (1.1b)]. By using this procedure, it is possible to represent an orientation given in Euler angles by poles in the pole-figure.

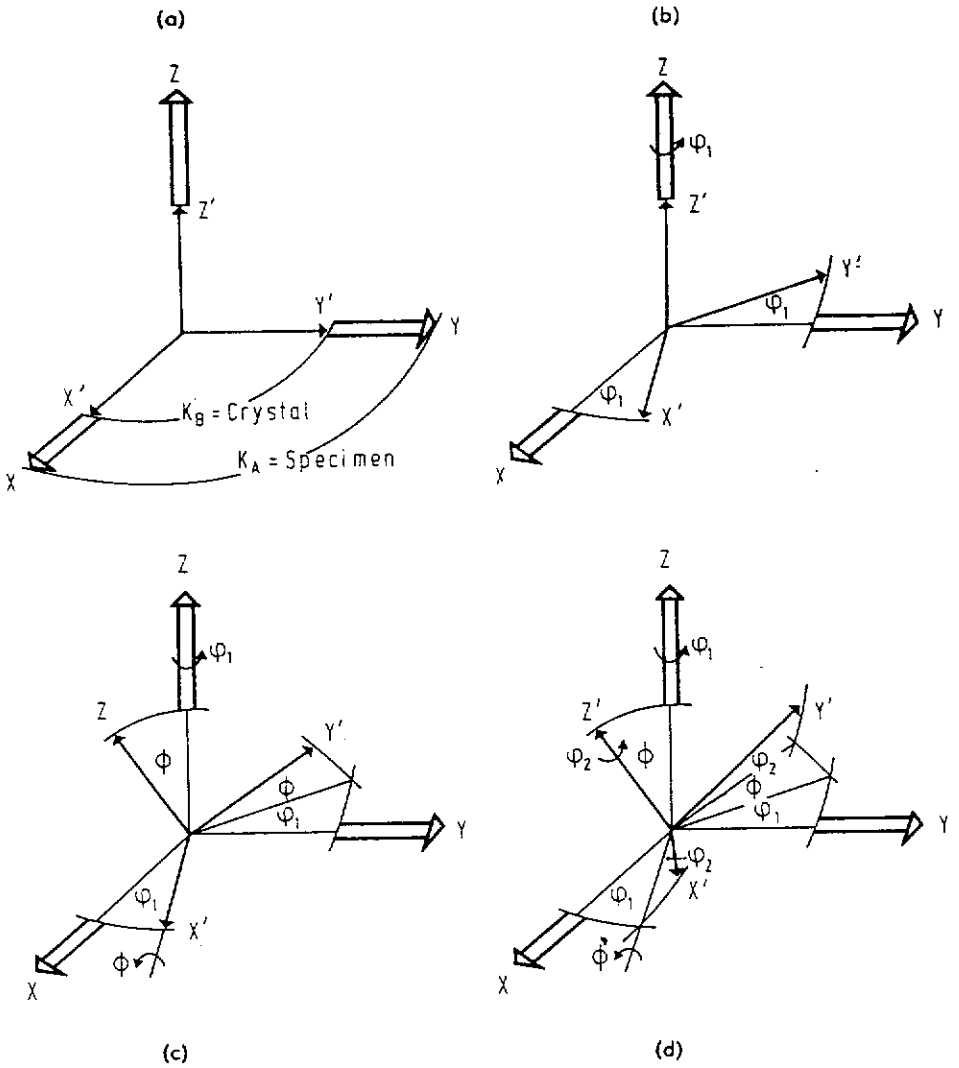

Figure 2.6. On the definition of the Euler angles $\{\varphi_1, \phi, \varphi_2\}$. After Bunge (1982).

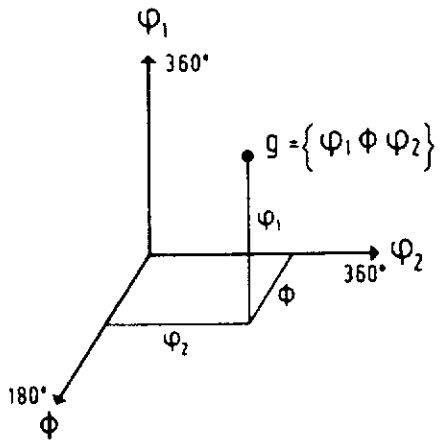

Figure 2.7. The Euler space corresponding to the definitions of the Euler angles $(\varphi_1 \phi \varphi_2)$. After Bunge (1982).

If the Euler angles are chosen as φ_1, ϕ and φ_2 [see equation (2.28)] and are represented in cartesian coordinates one specific orientation space which may be called the Euler space is obtained - see Figure (2.7). Each crystal orientation is represented by a point in the Euler space, and each point in the Euler space represents a crystal orientation. The Euler space is thus the space in which f(**g**) [equation (1.1a)] is to be represented.

Bunge (1982) showed that the ODF [equation (1.1)] must be invariant with respect to all crystal symmetry rotations $\mathbf{g}^c$. Sometimes the orientation arrangement of the crystals in the sample may have symmetries $\mathbf{g}^s$. These statistical symmetries are called *sample symmetries*. The ODF must then be invariant with respect to these symmetries

$$f(\mathbf{g}^c \cdot \mathbf{g} \cdot \mathbf{g}^s) = f(\mathbf{g}) \tag{2.31}$$

From the definition of the Euler angles [equation (1.1c)] it follows that they are periodic with period 2π. Thus the Euler space can be continued periodically to infinity outside the range given in equation (2.28). The ODF is then a 3D periodic function that has internal symmetries according to equation (2.31). The symmetries in the Euler space can thus be described by a space group determined by the crystal and sample symmetry which reduces the level of calculations to determine the ODF.

In Section (1.1) the relation between pole-figures and the ODF f(**g**) :

$$P_{\mathbf{h}}(\mathbf{y}) = \frac{1}{2\pi} \cdot \int_{\mathbf{h}\|\mathbf{y}} f(\mathbf{g}) d\chi \qquad \mathbf{y} = \{\alpha, \beta\} \qquad g = \{\varphi_1, \phi, \varphi_2\} \tag{2.32}$$

This equation is expressed in terms of the crystal direction **h** defined in the crystal coordinate system K_B [equation (2.26)] with respect to the crystal axes.

Texture analysis consists in solving the integral [equation (2.32)]. The unknown function f(**g**) is to be found using the known PDDF $P_{\mathbf{h}}(\mathbf{y})$ which is deduced from the pole-figures. Unfortunately, this is not a unique problem. There exist several corresponding ODFs for a given set of pole-figures. This ambiguity is linked with the existence of an inversion centre in the crystal symmetry and in the diffraction experiment (Friedel's Law). Then the ODF f(**g**) can be split into two parts (Bunge, 1982, 1985, 1986 and 1992) :

$$f(\mathbf{g}) = \tilde{f}(\mathbf{g}) + \overset{\approx}{f}(\mathbf{g}) \tag{2.33a}$$

with $$\int_{\mathbf{h}\|\mathbf{y}} \tilde{f}(\mathbf{g})d\mathbf{g} = P_{\mathbf{h}}(\mathbf{y}) \qquad (2.33b)$$

and with $$\int_{\mathbf{h}\|\mathbf{y}} \tilde{\tilde{f}}(\mathbf{g})d\mathbf{g} = 0 \qquad (2.33c)$$

where $\tilde{\tilde{f}}(\mathbf{g})$ is called the non directly-determinable part of the ODF (*or* odd-part of the ODF) which does not contribute to the PDDF. $\tilde{f}(\mathbf{g})$ is called the directly-determinable part of the ODF (*or* even-part of the ODF) which is directly related with the PDDFs obtained from diffraction experiments.

In the harmonic method (Bunge, 1982) the ODF is calculated in two stages (i) the directly-determinable part $\tilde{f}(\mathbf{g})$ is calculated using pole-figures data, and (ii) the not directly-determinable part is calculated using a positivity criterion. The harmonic method is outlined in further detail below.

2.2.2 The Mathematical Fundamentals of the Series Expansion Method for Analysing Pole-Figures Data

Most practical texture determinations are carried out with the series expansion method due to several valuable advances of this method compared with other methods described in Section (1.1). Dahms and Bunge (1989); Bunge (1982, 1985, 1986 and 1992); Bunge and Park (1996) highlighted the series expansion advantages:

- The representation of an arbitrary function by a system of orthogonal functions provides a most economic way to approximate this function rapidly with a small number of approximation steps.
- The coefficients of the series are the most comprehensive and sometimes the most concise representation of a texture function. They are very well suited to express several kinds of related functions such as pole figures, inverse pole figures, anisotropies of physical properties *etc.*
- The low-order terms of the series have a physical meaning of their own. Hence, these quantities have to be calculated anyway, even if other inversion methods are used to calculate the ODF.

Bunge (1982) showed that an analytical solution to equation (2.32) is the harmonic function $K_l^n(\mathbf{y})$ and $T_l^{mn}(\mathbf{g})$ which is given by

$$\frac{1}{2\pi}\cdot\int_{\mathbf{h}\|\mathbf{y}} T_l^{mn}(\mathbf{g})\cdot d\chi = \frac{2}{2l+1}\cdot K_l^{*m}(\mathbf{h})\cdot K_l^{n}(\mathbf{y}) \qquad (2.34)$$

There is one such function $T_l^{mn}(\mathbf{g})$ for every possible combination of the indices l, m, and n. The functions with low values of l being long-wave functions, those with high l values being short-wave functions, which means long or short angular distances between neighbouring maxima and minima of the functions.

In can be shown that any function f(**g**) can be composed by adding functions $T_l^{mn}(\mathbf{g})$ in appropriate amounts [equation (1.9)]. This equation is the general principle of series expansion, which is well-known in the form of Fourier analysis. The harmonic functions $T_l^{mn}(\mathbf{g})$ are functions of three variables, and their form is more complicated than the Fourier analysis, but the principle is the same. Similarly, the function $P_{\mathbf{h}}(\mathbf{y})$ can be composed of functions $K_l^{n}(\mathbf{y})$ [equation (1.10)]. Substituting equations (1.9) and (1.10) into equation (2.32) and take equation (2.34) into account, then the relation between the coefficients C_l^{mn} and $F_l^{n}(\mathbf{h})$ is given by :

$$F_l^{n}(\mathbf{h}) = \frac{4\pi}{2l+1}\cdot\sum_{m=-l}^{+l} C_l^{mn} K_l^{*m}(\mathbf{h}) \qquad (2.35)$$

where $K_l^{*m}(\mathbf{h})$ is the complex-conjugate quantity.

If the coefficients C_l^{mn} and $F_l^{n}(\mathbf{h})$ fulfil equation (2.35) then the functions f(**g**) and $P_{\mathbf{h}}(\mathbf{y})$ fulfil the fundamental relation of texture analysis [equation (2.32)]. Thus, the solution of equation (2.35) provides the solution of equation (2.32). Equation (2.35) is a system of linear equations with C_l^{mn} as unknowns. There is one such system for every combination of the indices l and n. It contains $(2l+1)$ unknowns, corresponding to the values of the index m with $(-l \le m \le +l)$. The number of equations in this system is given by the number of different pole-figure $P_{\mathbf{h}}(\mathbf{y})$. Thus, the coefficients C_l^{mn} can be determined uniquely up to $l = L$ if the coefficients $F_l^{n}(\mathbf{h})$ are known for $(2l+1)$ different pole-figures.

In equation (2.35) the functions $T_l^{mn}(\mathbf{g})$ with different values of m correspond to different crystal symmetries. If the function f(**g**) corresponds to triclinic crystal symmetry, then all values of m are needed in series expansion. If the crystal symmetry is higher, then only a selection of m values is required. Figure (2.8) shows

that symmetry reduces the number of unknowns in equation (2.35) and the number of pole-figures needed to solve equation (2.35).

The coefficients $F_l^n(\mathbf{h})$ of the series expansion of the pole-figure $P_{\mathbf{h}}(\mathbf{y})$ must be known in order to solve equation (2.35). They can be obtained if equation (1.10) is multiplied by $K_l^{*n'}(\mathbf{y})$ and integrated over $\mathbf{y}$:

$$\int P_{\mathbf{h}}(\mathbf{y}) \cdot K_l^{*n'}(\mathbf{y}) d\mathbf{y} = \sum_{l=0}^{\infty} \sum_{n=-l}^{+l} F_l^n(\mathbf{h}) \int K_l^n(\mathbf{y}) \cdot K_l^{*n'}(\mathbf{y}) d\mathbf{y} \tag{2.36}$$

and if the orthogonality relation of the harmonic functions is applied

$$\int K_l^m(\alpha,\beta) \cdot K_{l'}^{*m'}(\alpha,\beta) \sin\alpha d\alpha d\beta = \delta_{ll'} \cdot \delta_{mm'} \tag{2.37}$$

then $F_l^n(\mathbf{h})$ becomes :

$$F_l^n(\mathbf{h}) = \int P_{\mathbf{h}}(\mathbf{y}) \cdot K_l^{*n}(\mathbf{y}) d\mathbf{y} \tag{2.38}$$

The solution of equation (2.32) by the harmonic method is thus contained in equations (2.38), (2.35) and (1.9). It can be seen from equation (2.38) that the measured pole-figure $P_{\mathbf{h}}(\mathbf{y})$ is developed into a series with the coefficients $F_l^n(\mathbf{h})$ which is analogous to the Fourier analysis and will be called *texture analysis*. Then equation (2.35) is solved for unknowns C_l^{mn} which is called *coefficients transformation*. Therefore, the function f(**g**) can be finally synthesised for any desired value of **g**, which is called *texture synthesis* in analogy to Fourier synthesis.

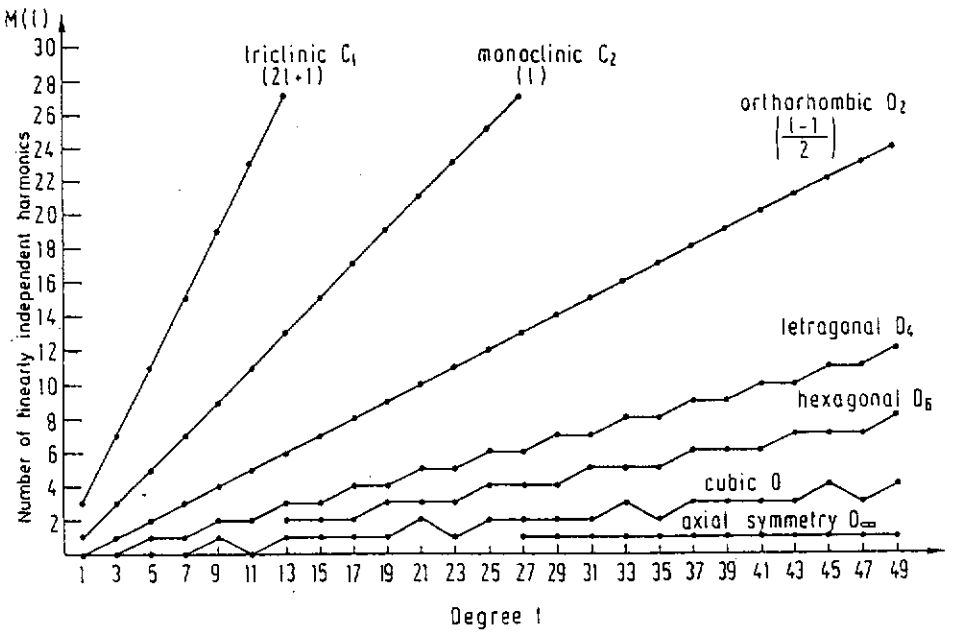

Figure 2.8. The number of independent harmonic functions of degree l for various symmetries. After Bunge (1982).

CHAPTER 3

EXPERIMENTAL PROGRAM

3.1 Experimental Design

Experiments were designed to meet the study objectives stated in Section (1.6) and according to the broad research plan presented in Section (1.7). The principal aspects of experimental design were : -

(i) selection of the materials,

(ii) strategies for powder diffraction data measurement and

(iii) diffraction data analysis.

Materials Selection

The principal criteria for materials selection were : -

1. Availability of information on the general form of *pole-density distributions* (PDDs) for prospective materials, including knowledge that the PDDs for the selected materials would be unipolar.
2. Substantial sensitivity of the PDDs to pressure in cylindrical compacted specimens.
3. Suitability of the materials for both XRPD and NPD experiments in relation to influences which might degrade the data - principally sources of systematic error other than PO, such as microabsorption and extinction.
4. Conformity of the common crystallite shapes in the selected materials with the rod- or disk-shaped crystallites modelled in the March (1932) theory.
5. Chemical purity as impurities might alter the texture and also introduce spurious data into the diffraction patterns.

Further details on the rationale for selecting specimens for the study are given in Section (3.2).

Powder Diffraction Experiments

The strategic issues considered in planning the XRPD and NPD experiments, were:

- Measurement of diffraction data for near-surface characterisation of texture by XRPD and also of bulk texture by NPD so that texture would be fully characterised.
- Direct determination of PDDFs by texture diffractometry for appraisal of March-model PDDFs determined by Rietveld pattern-fitting.
- Collection of diffraction patterns using uniaxially-pressed cylindrical compacts for which the pressure would be varied systematically.
- Range of PO values to be studied for each material would be extended by analysing additional powders containing 50% silica gel (Calvert *et al.*, 1983).

Sitepu (1991), O'Connor, Li and Sitepu (1991, 1992) and Sitepu, O'Connor and Li (1996) employed various sample milling/mounting combinations to produce a wide range of PO effects with gibbsite, molybdite, calcite and kaolinite specimens. On the basis of these studies, molybdite and calcite powders were selected for the thesis project - see Table (3.1).

Table 3.1

March r-parameters from Molybdite and Calcite XRPD Data (Sitepu, 1991)

Sample	PO r-parameter calculated from Rietveld[5] refinements with the March model	
	Molybdite[6]	*Calcite*
Side-drifted	0.679(2) [0.774(4)]	0.957(4)
Light-front-pressing	0.498(2) [0.679(3)]	0.879(8)
Briquetted at 6 bar for 7 s	0.475(2) [0.664(3)]	0.814(3)

[5]Rietveld analysis with March model did not involve summing of equivalent reflections [see Section (3.4)]. The assumed PO directions for molybdite and calcite were <010> (Kihlborg, 1963) and <104> (Dollase, 1986), respectively.

[6]Values for molybdite (100% by weight) and mixed with 50% by weight silica gel are given in the first line and in square brackets, respectively. The uncertainties are in parentheses.

XRPD data were to be collected for each material using two sample mounting procedures designed to extend the range of PO conditions :

- side-drifting,
- uniaxial-pressing with systematically-varied pressures.

Diffraction Data Analysis

Each diffractometry data set was to be analysed by Rietveld analysis with particular reference to PDD character, and PDDs were to be measured independently using x-ray and neutron pole-figures with a view to using these data to assess the validity of PDDs from Rietveld modelling.

3.2 Materials Selection and Pelletising

The specimens selected for the study were chosen to satisfy the objectives stated in Section (3.1) - specifically to provide a wide range of PO conditions in the selected materials,

- molybdite [MoO_3]
- calcite [$CaCO_3$].

The molybdite and calcite materials were obtained from BDH Chemicals Limited, Poole, England and AJAX Chemical Pty. Limited, Auburn, Australia, respectively, as ANALAR analytical reagents.

The particle size distributions (PSDs) for the molybdite and calcite as-received powders, measured with a Malvern Master Sizer laser instrument, are shown in Figures 3.1(a) and (b). Table (3.2) gives an analysis of the PSDs in terms of XRPD intensity reproducibility according to Klug and Alexander (1974). The results indicate that intensity reproducibility for both molybdite and calcite discrete Bragg peaks should be approximately of 8% and 5%, respectively. It was evident from the results that the PSDs for molybdite and calcite as-received were adequate, based on the criteria given in Table (3.2).

Table 3.2
Target Particle Sizes from Klug and Alexander (1974) and PSDs for the As-received Molybdite and Calcite Powders (Sitepu, 1991)

Sample	LAC[7] (cm^{-1})	Intensity Reproducibility (Klug and Alexander, 1974)			Measured D[v,0.5][8] in μm [Figures 3.1(a) and (b)]
		5μm	10μm	15μm	As-received
Molybdite	501	2.5%	6.8%	12.5%	10.8
Calcite	190	1.6%	3.8%	6.9%	13.4

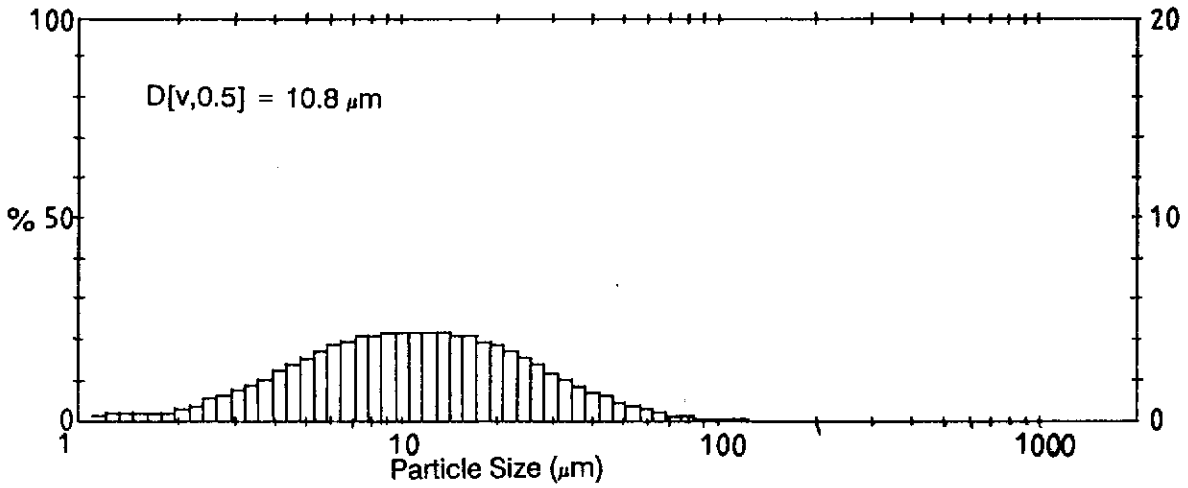

Figure 3.1(a). PSDs for molybdite as-received samples. Median volumetric D[v,0.5] is 10.8μm.

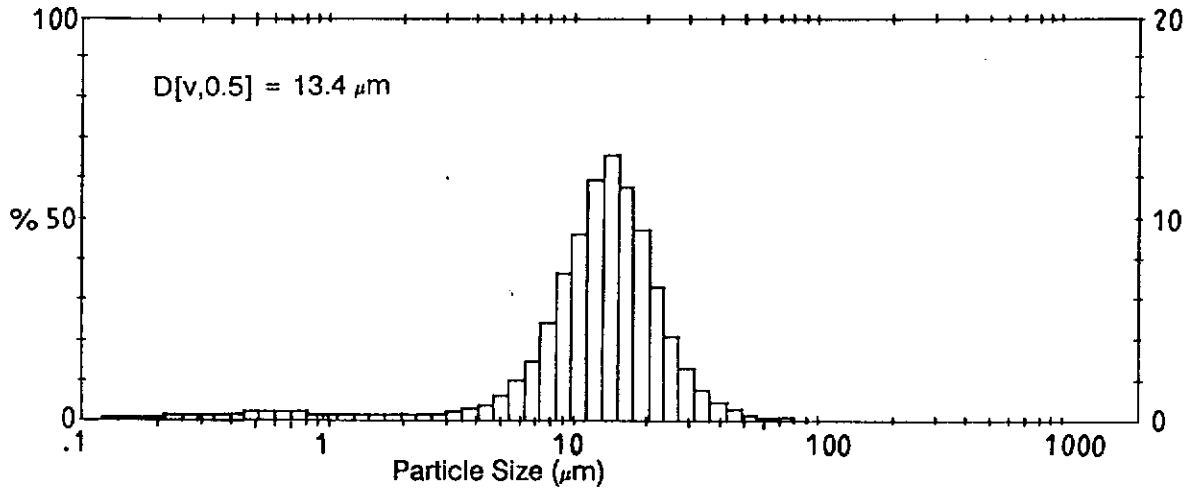

Figure 3.1(b). PSDs for calcite as-received samples. Median volumetric D[v,0.5] is 13.4μm.

[7] linear attenuation coefficients, CuKα radiation (1.54184Å).
[8] volumetric median value for PSD.

Molybdite Powders

PO is generally substantial in molybdite powders due to the blade-like needle shape. Calvert *et al.* (1983) demonstrated the considerable sensitivity of molybdite diffraction patterns to sample preparation and mounting by examining data for samples prepared by spray-drying, side-drifting and pressing.

In view of the substantial variation in the March r-parameter which can be obtained with molybdite [see Table (3.1)] the material was regarded as an excellent choice for the study. Further attractions were :

(i) consistency of the platy crystallite shapes with the theoretical requirement for the March model that crystallites should be either disk- or rod-like, and

(ii) availability of a detailed description of the crystal structure in the literature (Kihlborg, 1963).

Additional molybdite powders, to which 50% silica gel had been added, were examined in the XRPD diffraction experiments to extend the range of March r-values obtained in the study.

Calcite Powders

Calcite was selected in view of the results reported by Dollase (1986) which indicated that PO was moderate for the samples examined in that study, *ca.* r = 0.89(5). The material was thought to merit inclusion in the present study as a means of testing the reliability of the correction procedures for values of March PO r-parameter close to 1.0 - see Table (3.1). Further attractions were :

(i) consistency of the flat-plate particle shape commonly observed in calcite appears to satisfy the disk-shaped crystallite form - one of the 2 crystallite types modelled by the March function, and

(ii) the crystal structure of calcite is well known (Megaw, 1970 and 1973).

As for molybdite, the set of textures examined was extended by preparing additional calcite powders mixed with silica gel.

Sample Pelletising Procedures for Diffraction Experiments

Side-drifted mounting was employed to produce XRPD mounts with minimal PO for each of the materials investigated. The side-drifting was performed by fixing

a glass slide to the front surface of the x-ray sample holder and then loading the material through the gap between the slide and holder by tapping with a spatula. The glass slide was then carefully removed leaving the sample securely packed in the holder when the holder had sufficient material in place.

Samples with a range of textures were prepared by uniaxial-pressing at different pressures. For XRPD, approximately 3.5g of powder was compacted in a cylindrical steel die 19mm in diameter [see Table (3.3)]. The set of discs examined by XRPD diffractometry was also used in the XRPD texture work. A separate set of discs (approximately 15g of powder) was pressed for the NPD experiments as the relatively weak beam intensities required use of more volumuous specimens. The heights of the XRPD and NPD discs were approximately 0.5cm and 3cm, respectively.

Table 3.3

Sample Pelletising Procedures

Pelletising Conditions	Pressure (MPa)	Molybdite Specimen Codes[9]		Calcite Specimen Codes[9]	
		XRPD	NPD	XRPD	NPD
Not pressed	0	M0X	M0N	C0X	C0N
		M0X(S)	M0N(S)	C0X(S)	-
Uniaxial-pressing	44	M2X	M2N	C2X	C2N
		M2X(S)	M2N(S)	C2X(S)	-
	66	M3X	M3N	-	-
		M3X(S)	M3N(S)	-	-
	88	M4X	M4N	C4X	C4N
		M4X(S)	-	C4X(S)	-
	110	M5X	M5N	-	-
		M5X(S)	M5N(S)	-	-
	132	-	-	C6X	C6N
		-	-	C6X(S)	-
	176	-	-	C8X	C8N
		-	-	C8X(S)	-

[9] Specimens Codes:

First letter: M and C for molybdite and calcite, respectively.

Second letter: Digit represents pressure in ×1000lbs units (conversion factor, 1000lbs units to MPa =22).

Third letter: X for XRPD, N for NPD.

Fourth letter (parentheses): (S) signifies that 50% by weight silica gel has been added.

3.3 Powder Diffractometry Measurements

X-ray Diffraction Pattern Measurements

Step-scanned patterns were measured at Curtin University of Technology with a Siemens D500 Bragg-Brentano x-ray powder diffractometer fitted with a graphite diffracted-beam monochromator [see Figure (3.2)]. The Bragg-Brentano parafocussing geometry uses a diverging beam from a line source which is directed to the sample through an incident beam aperture, designated the divergence slit system [I and II in Figure (3.2)]. The conical diffracted radiation beam for each reciprocal lattice vector is sampled by the detector aperture (IV). Slit III, situated in the diffracted beam, is an antiscattter slit. Off-plane divergence is reduced by a söller slit placed between the specimen and detector.

Data collection details are given in Table (3.4). The basis on which various conditions/settings were selected follows.

- the divergence slit provided specimen coverage ranging from ~40.2mm to 3.9mm over the 2θ data collection range so that the sample fully collected the incident beam over the range;
- the depth of powder in the sample cup exceeded the calculated infinite depth range for the powders employed: 4μm to 42μm for MoO_3 and 11μm to 110μm for $CaCO_3$ for the 2θ range;
- the receiving slit was selected to approximately match the effective focal spot width of the tube;
- data were not recorded below 10° in 2θ because Bragg peaks do not occur below this angle for the materials considered, and data were collected to 2θ = 130° because the Bragg intensities were barely observable beyond this angle;
- counting time of 1s/step ensured reasonable intensity counting statistics;
- a detector step size of 0.04° was employed to provide adequate sampling of the peaks (FWHM ≈ 0.1 - 0.3°) which is consistent with the guidelines described by Hill and Madsen (1984, 1986) and Hill (1993) who showed that increasing counting times beyond one 1s/step, and reducing the step size below 0.04° 2θ made negligible improvement to Rietveld parameter estimated standard deviations and R-factors;

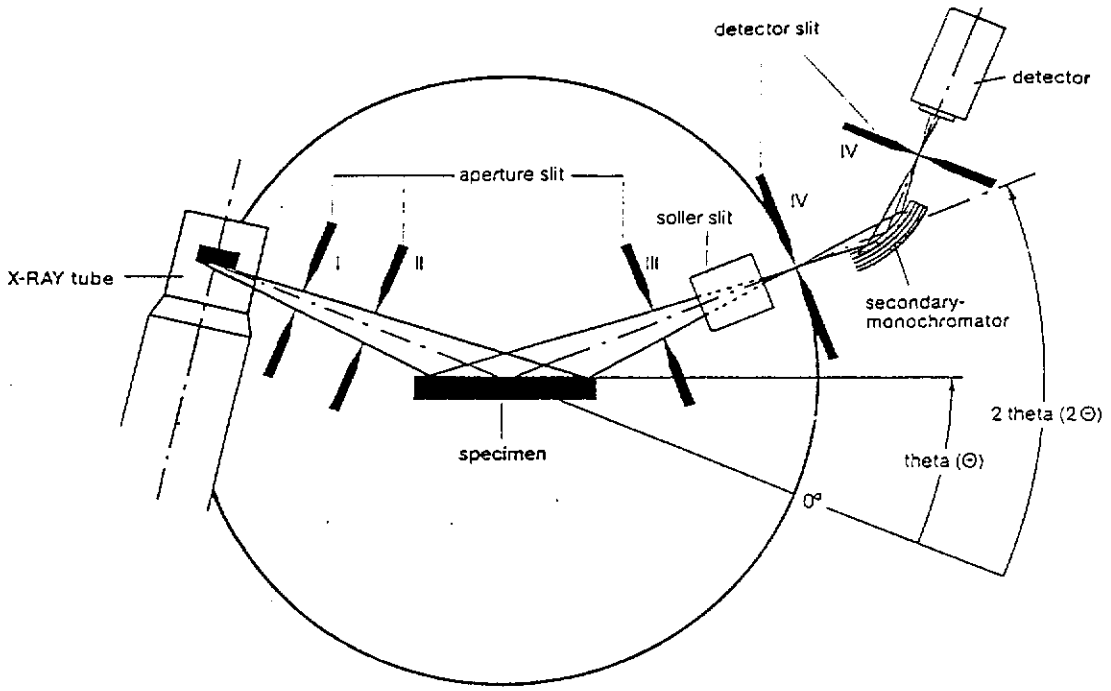

Figure 3.2. Schematic diagram of Bragg-Brentano x-ray powder diffractometer used for pattern measurements (taken from Siemens, 1986; p2/2).

Table 3.4
XRPD Pattern Measurement Conditions

Instrument:	Siemens D500
Radiation :	Cu-anode tube, type FF Cu 4KE 60kV 1.5kW, operated at 40kV and 30mA Effective focal spot size, $0.04\times8mm^2$ Unfiltered Wavelength: CuKα = 1.5418Å, $K\alpha_1$= 1.54060Å $K\alpha_2$ = 1.54439Å
Optics :	Bragg-Brentano, measuring circle diameter = 401mm Incident beam divergence = 1°, receiving slit = 0.05° Scatter slits divergence = 1° Soller slit divergence = 1°
Specimen :	Holder - circular format, diameter = 23 mm Rotation 'on' for all measurements
Detection :	Graphite diffracted beam monochromator set for CuKα NaI scintillator with pulse height analysis
Acquisition:	Angular range in 2θ, 10° - 130° Step size, 0.04° Counting time, 1 s/step

- the full-width at half-maximum (FWHM) resolution curve, for the diffractometer obtained with a NIST LaB_6 sample, is provided in Figure (3.3) which shows the values for U, V, W and γ (pseudo-Voigt function) are 0.0069, -0.0078, 0.0193 and 0.213, respectively. For comparison, the FWHM resolution function of the HRPD neutron diffractometer for an α-Al_2O_3 sample is also plotted in Figure (3.3) with the U, V and W values are being 0.058, -0.114 and 0.122, respectively (Howard, Ball, Davis and Elcombe; 1983).

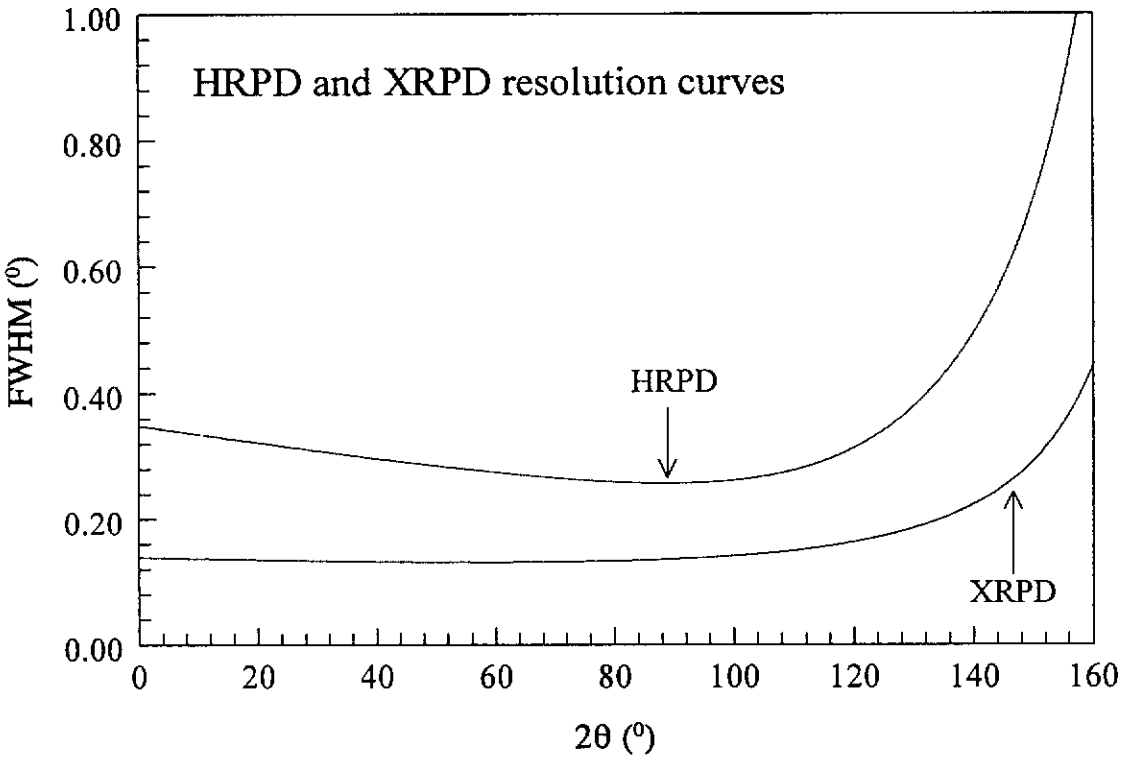

Figure 3.3. FWHM curve for (a) Siemens D500 x-ray diffractometer (Bragg-Brentano optics) using LaB_6 sample and (b) HRPD Debye-Scherrer instrument for α-Al_2O_3 sample.

Texture X-ray Diffractometry

Pole-figure measurements were performed at Curtin University of Technology with a Siemens D5000 diffractometer fitted with a Siemens open-circle Eulerian cradle. Figure (3.4) shows a schematic diagram of the four-circle diffractometer instrument. Angles χ and φ correspond to the pole-figure angles α and β for the pole-figure measurements described in Section (2.3). The instrument design details and data acquisition conditions are given in Table (3.5).

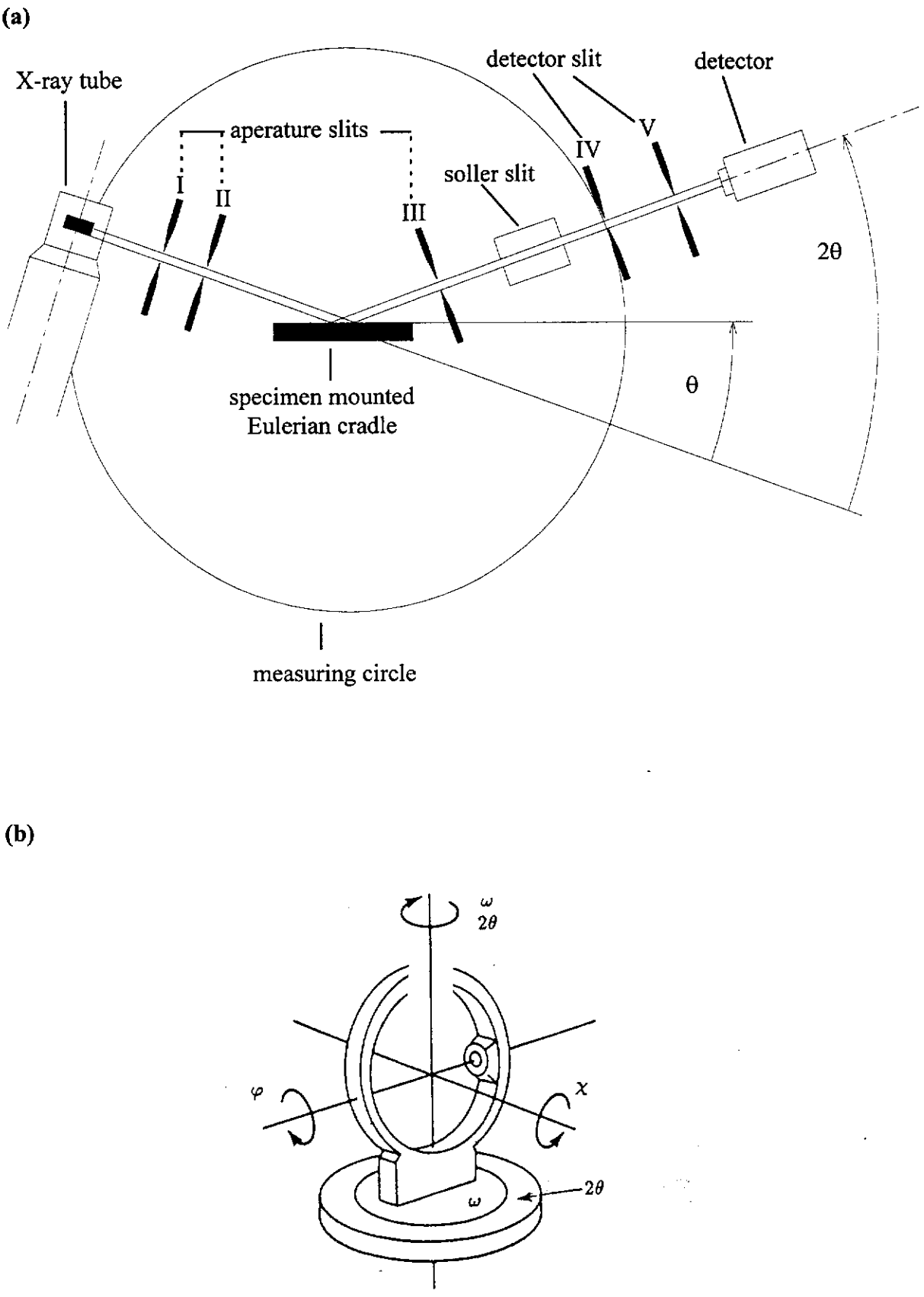

Figure 3.4. Schematic diagram of x-ray texture diffractometer incorporating an open Eulerian cradle. (a) Vertical plane defined by incident and diffracted beams and (b) Eulerian cradle.

Table 3.5
XRPD Texture Diffractometry Measurement Conditions

Instrument:	Siemens D5000
Radiation :	Cu-anode tube, type FL Cu 4KE FE 801013 60kV 2.2kW, operated at 40kv and 30mA Effective focal spot size, $0.04\times12mm^2$ (long fine focus, short anode) Ni filter used for pattern measurements, unfiltered for pole-figure measurements Wavelengths: CuKα = 1.5418Å, Kα_1= 1.54060Å Kα_2 = 1.54439Å Specimen coverage : 5mm×20mm
Optics :	Parallel-beam, measuring circle diameter = 500mm Eulerian cradle - diameter 37mm Divergence - incident beam = 1°, diffracted beam = 0.05° Scatter slits divergence = 1° Soller slit divergence = 1°
Detection :	NaI scintillator with pulse height analysis
Acquisition:	Ranges for pole-figures - 0-60° for χ, 0-360° for ϕ Step sizes, $\Delta\chi = \Delta\varphi = 5°$ Counting time, 14 s/step.

Data were measured using quasi-parallel beam optics. The incident beam was directed to the specimen through aperture slits. The diffracted radiation passed through a third aperture (receiving slit) and pre-detector slit.

The bases on which various conditions/settings were selected are as follows :

- The pole-figure data collection process was managed with the Siemens TEXD5 software package.
- During pole-figure measurement, the counter was fixed to record the Bragg peak and the specimen was rocked using the χ and φ axes.
- In x-ray texture studies conducted by Wenk *et al.* (1984) and neutron texture round-robin studies coordinated by Wenk (1991), the precision of the pole-figure data was excellent when $\Delta\chi = \Delta\varphi = 5°$. As a result, the same increment was employed in this study.

- Out-of-plane divergence was controlled by soller collimators placed between focus and specimen, and between specimen and scatter slit.
- The diffractometer did not permit spinning of the sample to ensure rotational symmetry.

Prior to pole-figure measurement, a set of suitable Bragg-reflections was selected, and the 2θ-values for the local background measurements were determined.

The texture intensity measurements were converted to PDDs by a two-step procedure involving (i) correction for defocussing and (ii) normalisation.

Defocussing corrections (Chernock and Beck, 1952; Chernock *et al.*, 1953; Huijser-Gerits and Rieck, 1974) were applied using a texture diffractometry data set collected with a side-drifted α-Al_2O_3 powder which was assumed to be randomly-oriented. The 26 background-corrected intensity values, recorded at intervals of 5° in ϕ for each χ setting, were averaged to provide the mean intensity I_χ^r. The intensity correction factor for each χ was taken to be the ratio,

$$C(\chi) = \frac{I_\chi^r}{I_0^r} \tag{3.1}$$

where I_0^r is the intensity at $\chi = 0$.

The measured PDDs for the textured specimens were then derived from the defocussing-corrected intensities according to the following description in which I_χ^t represents the intensity of the textured specimen after averaging over the 72 ϕ settings. A plot of I_χ^t-versus-χ was fitted with a polynomial :

$$I_\chi^t = a_0 + a_1\chi + a_2\chi^2 + a_3\chi^3 \tag{3.2a}$$

Normalisation was then performed with the expression :

$$PDD = \frac{\int_0^{60^\circ} I_\chi^t \cdot d\chi}{\int_0^{60^\circ} d\chi} \tag{3.2b}$$

Results for the defocussing and normalisation measurements are reported in Section (5.2).

Neutron Diffraction Pattern Measurements

NPD data were collected at room temperature with the high-resolution, fixed-wavelength, multi-detector powder diffractometer (HRPD) at the Australian Nuclear Science and Technology Organisation (ANSTO) High Flux Australian Reactor (HIFAR) at the Lucas Heights research Laboratories, near Sydney, NSW. The HRPD instrument has been described by Howard, Ball, Davis and Elcombe (1983); Howard and Kennedy (1994); Kennedy (1995); and Knott (1998). A schematic diagram of the instrument is shown in Figure (3.5), and the instrument settings used for data collection are given in Table (3.6). Figure (3.3) shows the resolution function for the instrument.

The effective angular range of the 24-detector HRPD instrument was 0° to 154°. The step size chosen was 0.05° so that sufficient steps were taken through each peak. The resolution is approximately 0.25° at best, and therefore approximately 10 steps were taken over each peak.

Counting times for HRPD to obtain reasonable counting statistics are sample dependent, typically ranging from 20s to more than 100s. The times chosen for measurement of all molybdite and calcite samples varied between 40 and 50 s/step to ensure reasonable counting statistics. A wavelength of 1.49Å was chosen because of its comparability with the XRPD CuKα wavelength, 1.5418Å.

Data were recorded for the compacted specimens described in Table (3.3). For each specimen, patterns were acquired for two mounts, (i) with the specimen cylinder axis coincident with the HRPD rotation axis and (ii) normal to the axis. The patterns recorded by each detector were merged during data reduction to allow for counter offsets and relative detection efficiency.

Neutron Texture Diffractometry

Pole-figure measurements were performed at room temperature with the fixed-wavelength four-circle, single crystal diffractometer (2TANA) at the ANSTO HIFAR facility. The maximum 2θ is approximately 118°, and over this range, the reflection FWHMs are typically 0.4° at 2θ = 5°, increasing to approximately 0.75° at 2θ = 105°. A schematic diagram of the instrument is shown in Figure (3.6), and the settings employed for pole-figure measurements are given in Table (3.7).

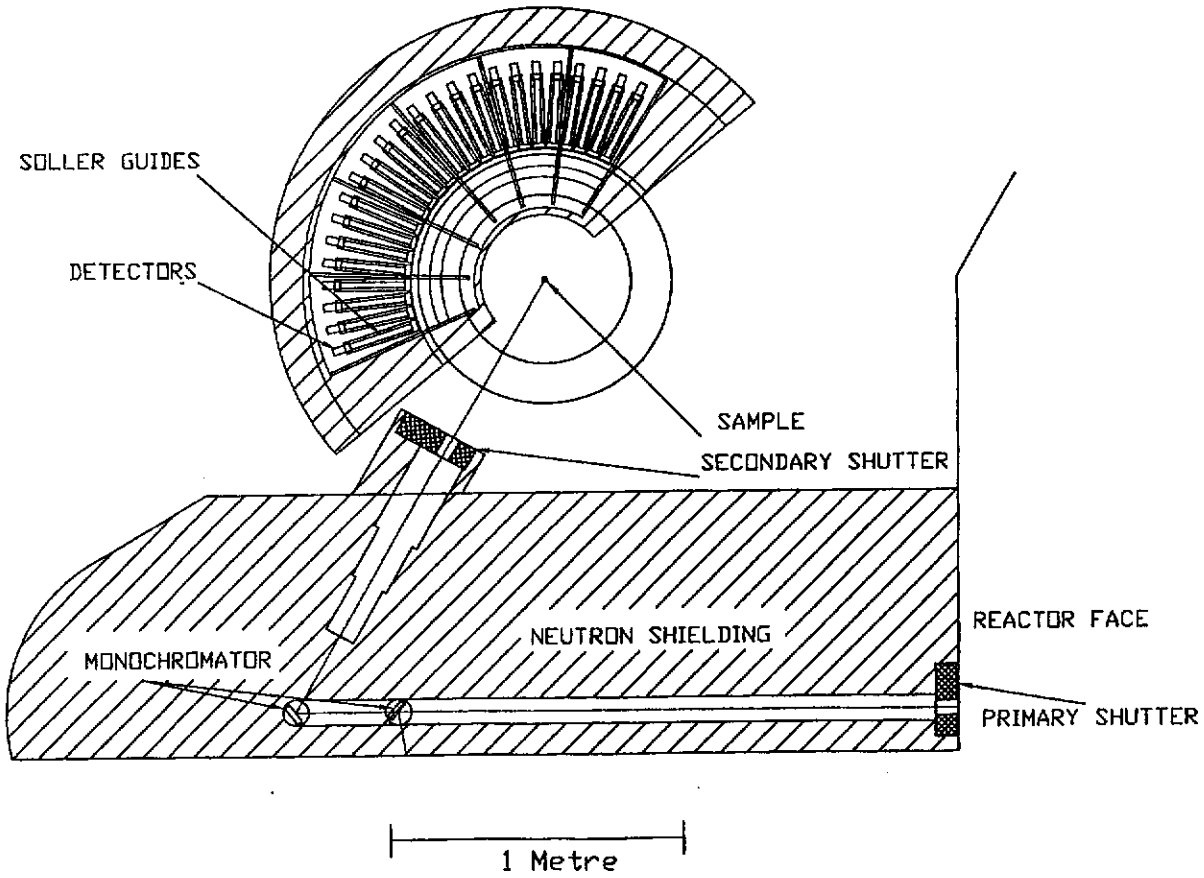

Figure 3.5. Schematic diagram of the HRPD neutron diffractometer used for pattern measurements (Howard, Ball, Davis and Elcombe, 1983).

Table 3.6
NPD Pattern Measurement Conditions

Instrument:	HRPD
Radiation:	Ge single crystal monochromator, take-off angle = 120° Wavelength = 1.493 Å
Optics:	Debye-Scherrer
Specimens:	• Vanadium can (16mm diameter, 5cm height) for non-pressed materials • Uniaxially-pressed cylinders (19mm diameter, 3cm height) • Rotation 'on' for all measurements
Detection:	24 ^{3}He detectors, separated by 5° in 2θ
Acquisition:	Angular range in 2θ, 10 - 154° Step size, 0.05° Counting time, approx. 40-50 s/step (controlled by beam monitor)

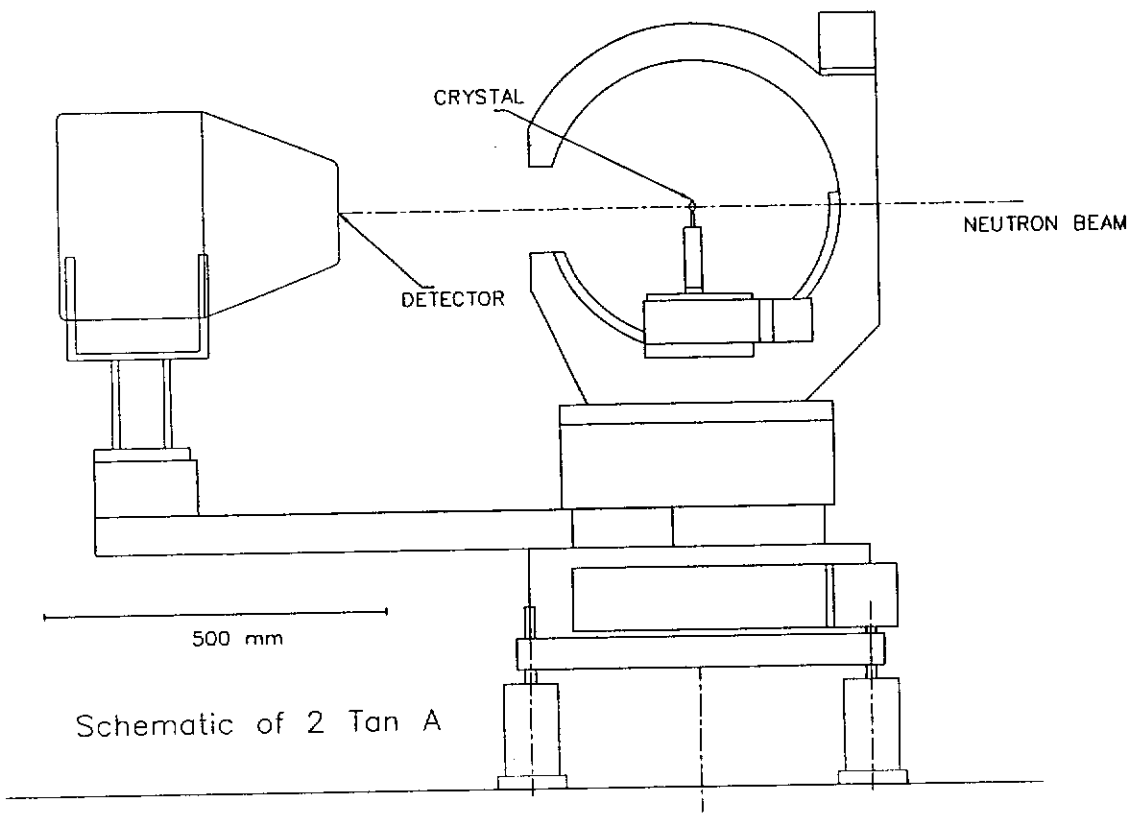

Figure 3.6. Schematic diagram of single crystal diffractometer (2TANA) used for neutron texture measurements.

Table 3.7
Neutron Texture Diffractometry Measurement Conditions

Instrument:	2TANA
Radiation:	Cu single-crystal monochromator, take-off angle = 58° Wavelength = 1.237Å
Optics:	Single-crystal
Detection:	1 ^{3}He detector
Acquisition:	Ranges for pole-figures: 0 - 90° for χ, 0 - 270° for φ Step size, $\Delta\chi = \Delta\varphi = 30°$ Counting time, approx. 6-7 s/step (controlled by monitor)

Settings for texture analysis were chosen as follows. The incident beam slit was removed and the detector slit was completely open, with the entire cross section of the detector (10mm in diameter) being active. While use of uncollimated optics reduced data collection times to realistic levels, this resulted in the Bragg lines being broader than in the powder pattern measurements with HRPD.

The instrument was used to measure pole-figures for

(i) one calcite powder, *i.e.* using a 16mm vanadium can sample holder and

(ii) two compacted calcite powders, which had been uniaxial-pressed for 88 and 176 MPa, respectively, along the cylindrical axis (see Table 3.3). Six Bragg-peaks (012), (104), (006), (113) and (018) were chosen according to the JCPDS pattern number 5-586.

Based on preliminary scans, peak positions were selected at 2θ values of 18.62°, 23.59°, 25.18°, 31.52° and 37.82°. Corresponding positions for measuring the background were at 2θ = 17.5°, 22.5°, 26.5°, 32.5° and 38.5°. A monitor count was chosen to provide approximate counting statistics of 10%. On this basis, the time required to measure the 5 peaks and background was approximately 8 minutes.

3.4 Rietveld Analysis of Diffraction Data

(i) Rietveld Method Principles

Rietveld (1967, 1969) described a structure refinement method involving the use of whole-pattern powder diffraction data. Initially, the technique was restricted to the determination of structural parameters, *viz.* atom positions, temperature factors, site occupancy values and lattice parameters. Subsequently, the Rietveld method has been developed to characterise macroscopic descriptors (Young, 1993) - notably phase composition, texture, crystallite size, crystallite strain and extinction. The method may be used with XRPD and NPD data.

The basis of the Rietveld procedure is to minimise the residual:

$$R = \sum_{i=1}^{N} w_i \left| Y_i - Y_{ci} \right|^2 \qquad (3.3)$$

over the N measurements comprising the diffraction pattern, using iterative least squares. Here, Y_i is the observed intensity at the ith point in the pattern, Y_{ci} is the

corresponding calculated intensity and w_i is a weighting factor. The values of w_i are normally set according to Poisson counting statistics :

$$w_i = \frac{1}{Y_{ci}} \tag{3.4}$$

The expression for Y_{ci} employed in this study [see (iv) following for program details] is that for a flat, infinitely-thick specimen, with the summations being taken over neighbouring Bragg reflections and component phases according to :

$$Y_{ci} = s\sum_j L_j \left|F_j\right|^2 \phi(2\theta_i - 2\theta_j) P_j + Y_{bi} \tag{3.5}$$

where $2\theta_i$ and $2\theta_j$ are the detector angles corresponding to point i and Bragg peak j, respectively.

Term s is the phase scale factor which in effect scales the calculated pattern for the phase to the measured pattern. The refined, or best, value for s will result in the approximation :

$$\sum_i Y_i \approx s\sum_i Y_{ci} \tag{3.6}$$

Term L_j is the product of the three factors -

$$L_j = Lr_j \cdot p_j \cdot m_j \tag{3.7a}$$

where :

Lr_j is the Lorentz factor :

$$Lr_j = \frac{1}{(2\sin^2\theta_j \cdot \cos\theta_j)} \tag{3.7b}$$

p_j is the polarisation factor. For unpolarised x-ray radiation, p_j has the value :

$$p_j = \frac{(1 + K\cos^2 2\theta)}{1 + K} \tag{3.7c}$$

where K is $\cos^2 2\theta_M$ when a diffracted beam monochromator is used (θ_M being the monochromator Bragg angle), and K = 1 when a monochromator is not employed. For the graphite monochromator used in this study, $2\theta_M = 26.6°$ (JCPDS pattern 25-0284) and K = 0.8.

m_j is the multiplicity corresponding to the number of equivalent reflections for a given Bragg peak - specification of the space group with Rietveld programs yields the multiplicities.

Factor $|F_j|$ is the modulus of structure factor $F_j(hkl)$ for Bragg peak j, produced by summing over the k atoms in the unit cell:

$$F_j(hkl) = \sum_k f_k \cdot o_k \cdot \exp[2\pi i\{hx_k + ky_k + lz_k\}] \cdot T_k \qquad (3.8)$$

where f_k is the scattering factor of atom k (x-ray and neutron scattering factors, International Tables for X-ray Crystallography, 1995 Volume C, pp. 476 - 486 and pp. 384 - 391, respectively); o_k is the site occupancy factor; h, k and l are the Miller indices; x_k, y_k and z_k are the atom fractional position co-ordinates and T_k are the Debye-Waller factors :

$$T_k = \exp(-B_k \sin^2\theta / \lambda^2) \qquad (3.9)$$

for temperature factor B_k assuming isotropic motion.

Various mathematical forms are available in Rietveld software to represent the *peak profile function, $\phi(2\theta_i - 2\theta_j)$.* The pseudo-Voigt function, comprising a sum of Lorenztian and Gaussian components, was used for all refinements in the study, for both XRPD and NPD data. The function is given by :

$$\phi(2\theta_i - 2\theta_j) = \gamma \cdot \frac{C_o^{1/2}}{\pi \cdot H_k} \cdot \left[1 + C_o \cdot \frac{(2\theta_i - 2\theta_j)^2}{H_j^2}\right]^{-1}$$

$$+(1-\gamma) \cdot \frac{C_1^{1/2}}{\pi^{1/2} \cdot H_k} \cdot \exp\left[-C_1 \cdot \frac{(2\theta_i - 2\theta_j)^2}{H_j^2}\right] \qquad (3.10)$$

where $C_o = 4$, $C_1 = 4 \ln 2$, H_j is the FWHM of the jth Bragg reflection and γ is the Lorentzian-Gaussian mixing parameter.

H_j has the form derived by Caglioti, Paoletti and Ricci (1958) for crystal-monochromated neutron diffractometry,

$$H_j^2 = U \tan^2 \theta_j + V \tan \theta_j + W \qquad (3.11)$$

where U, V and W are refinable parameters.

Peak asymmetry was modelled using the function

$$A_{ik} = 1 - AS[\text{sign}(2\theta_i - 2\theta_k)] (2\theta_i - 2\theta_k)^2 \cot(\theta_k) \qquad (3.12)$$

involving asymmetry parameter AS (Rietveld, 1969; Howard, 1982).

Term Y_{bi}, the background component of the pattern, was modelled in the present study with the polynomial expression :

$$Y_{bi} = \sum_{m=-1}^{4} B_m (2\theta_i)^m \tag{3.13}$$

where the B_m are refinable parameters.

Term P_j, the PO factor, was modelled in this study with the March function described in Chapter 1 equation (1.18).

(ii) Estimates of Precision for the Refinement Parameters

The estimated standard deviations (esds) for the Rietveld parameters were derived with the expression for parameter j :

$$\sigma_j = \left[M_{jj}^{-1} \cdot \frac{\sum_{i=1}^{N} w_i \cdot (Y_{io} - Y_{ic})^2}{N - P} \right] \tag{3.14}$$

where N is the number of observations, P is the number of parameters being refined and M_{jj}^{-1} is the diagonal element obtained by inversion of the normal matrix with elements M_{jk} given by :

$$M_{jk} = -\sum_i 2 w_i \cdot \left[(Y_i - Y_{ci}) \cdot \frac{\partial^2 Y_{ci}}{\partial x_i \cdot \partial x_k} \right] - \left[\frac{\partial Y_{ci}}{\partial x_j} \right] \cdot \left[\frac{\partial Y_{ci}}{\partial x_k} \right] \tag{3.15}$$

where x_j and x_k are adjustable parameters.

The reliability of the esds has been discussed by Sakata and Cooper (1979), Pawley (1980), Prince (1981, 1985, 1993), Cooper (1982), Baharie and Pawley (1983), Hill and Madsen (1986) and Hill and Cranswick (1994). The esds are correct only if there are no systematic errors in the measured data or deficiencies in the model. Otherwise the values will be underestimated.

(iii) Refinement Quality Measures

Refinement quality is assessed using *figures-of-merit* and *difference plots*, the former comprising two types of profile R-factors, a goodness-of-fit index (GOFI) and phase Bragg R-factors (R_B). The *profile R-factor* is given by :

$$R_P = \frac{\sum_i |Y_i - Y_{ci}|^2}{\sum_i Y_i} \tag{3.16}$$

and the corresponding weighted form is,

$$R_{WP} = \left[\frac{\sum_{i=1}^{n} w_i |Y_i - Y_{ci}|^2}{\sum_{i=1}^{n} w_i \cdot Y_i^2} \right]^{1/2} \tag{3.17}$$

Ideally R_{WP} has value,

$$R_{EXP} = \left[\frac{N - P}{\sum_{i=1}^{n} w_i \cdot Y_i^2} \right]^{1/2} \tag{3.18}$$

The GOFI is given by :

$$GOFI = [\frac{R_{WP}}{R_{EXP}}]^2 \tag{3.19}$$

A fully-refined model with 'perfect' data would give GOFI = 1.0 (Prince, 1993).

The Bragg R-factor is defined by :

$$R_B = \frac{\sum_{i=1}^{n} |I_{jo} - I_{jc}|}{\sum_{i=1}^{n} I_{jo}} \tag{3.20}$$

were I_{jo} and I_{jc} are the observed and calculated Bragg intensities for reflection j, the observed intensities being determined assuming they are in the same proportion as their calculated counterparts. Factor I_{jo} is calculated, as described by Rietveld (1969), with the expression,

$$I_{jo} = \sum_{i=1}^{n} w_i F_j^2 \frac{Y_i}{Y_{ci}} \tag{3.21}$$

where the summation is taken over all observed profile intensities, Y_i which can theoretically contribute to the observed integrated intensities I_{jo}.

Factor R_B is a measure of agreement between the observed and calculated Bragg intensities, based on crystal structure parameters. Hill and Madsen (1987)

emphasised that R_B relies more heavily on crystal structure parameters than other agreement indices.

Of the three R-factors, R_{WP} is the most valuable as the numerator is the quantity minimised by least-squares in the Rietveld refinement process. In addition to the R factors, difference plots were used to compare the agreement between calculated and observed patterns. For example, Figure (3.7) shows the agreement between measured and calculated XRPD pattern-fitting improved dramatically when the March formula (equation 1.18) was used for the molybdite M4X sample - briquetted for 88MPa.

(iv) Rietveld Software

The Rietveld program used in the present study was a PC version of the LHPM program (Hill and Howard, 1986) developed by Howard and Hunter (1996). A notable aspect of the doctoral study concerned recognition of the need to allow for symmetry-equivalent reflections, as proposed by Dollase (1986). It was discovered during the PhD study that the LHPM Rietveld program, used initially by the author, did not allow for contributions from symmetry-equivalent reflections.

General strategies for performing Rietveld refinements have been described by Kisi (1994). The following details pertain to the XRPD and NPD calculations performed in this study :

- structural parameters for the molybdite and calcite phases are given in Tables (3.8) and (3.9), respectively - all positional parameters were fixed at the published values, and the thermal parameters and cell parameters were refined;
- the background component of the XRPD and NPD patterns, Y_{bi}, was modelled with a 4-parameter polynomial as defined in equation (3.13);
- zero point $2\theta_o$ (off-set in the 2θ scale of the goniometer);
- phase scale factor;
- March parameter r_i for the phase according to a specified direction of PO.

The directions of PO used for the XRPD refinements were <010> for MoO_3 and <104> for $CaCO_3$ as recommended by Kihlborg (1963) and Dollase (1986), respectively. For NPD, the PO directions for MoO_3 was <010> and for $CaCO_3$ was <001> (Peschar *et al.*, 1995) as the <001> gave NPD pattern fits superior to those obtained with the <104> direction (see Section 4.4.2).

(a) Random Orientation Assumed

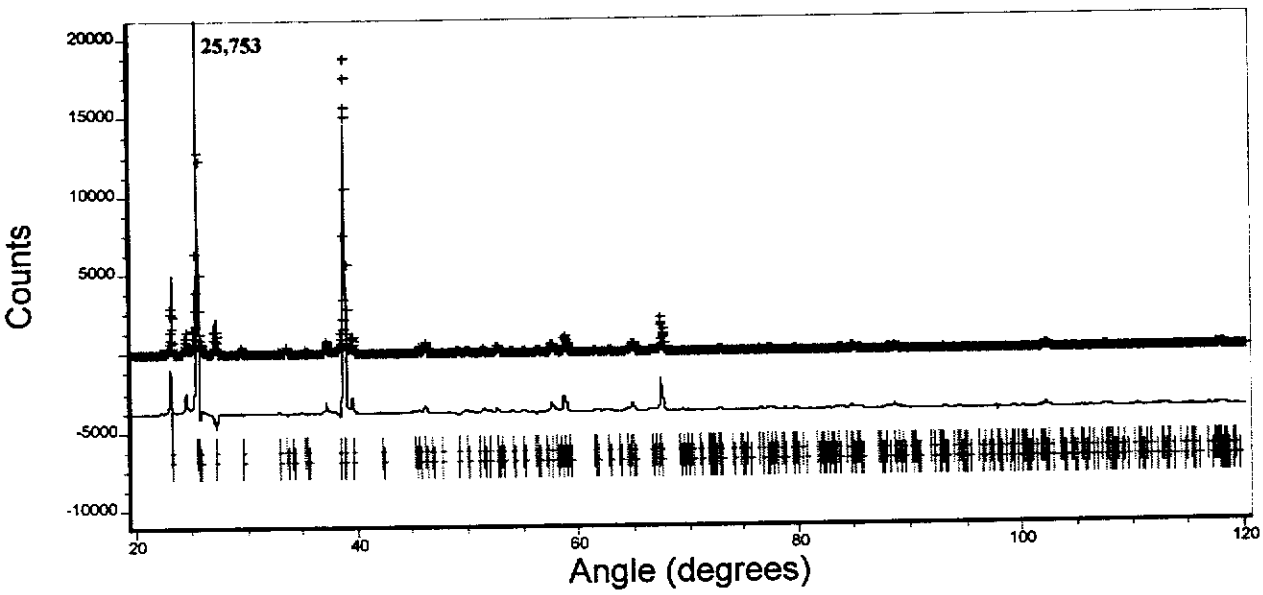

(b) March Model

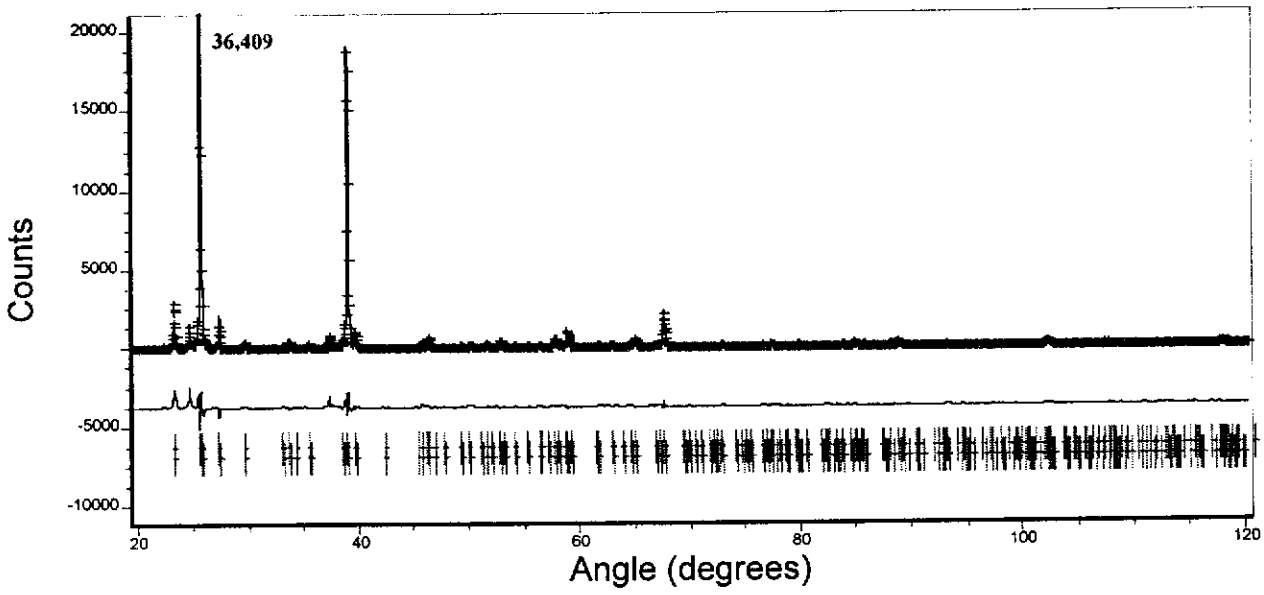

Figure 3.7. Agreement between calculated and measured XRPD patterns for molybdite powder specimen (M4X - briquetted for 88MPa) following Rietveld refinement with the March model. The observed data are indicated by plus sign and the calculated profile is the continuous line in the same field. The set of vertical lines below the profiles represent the positions of all possible Bragg reflections. The lower plot is the difference between the measured and calculated patterns on the same scale as the measured and calculated patterns.

Refinements were carried out until all parameter shifts were less than 0.1 of the corresponding esd and results were also monitored by observing the *figures-of-merit* and *difference plots*.

Table 3.8

Crystal Structure Model for Molybdite, MoO_3 (Kihlborg, 1963)

Atom Position	Wyckoff Code[10]	x	y	z	B $(Å)^2$
Mo	4(c)	0.087	0.102	0.250	0.230
O(1)	4(c)	0.500	0.435	0.250	0.561
O(2)	4(c)	0.521	0.087	0.250	0.628
O(3)	4(c)	0.037	0.221	0.250	0.951

- Space group : Pbnm (No. 62).
- Unit cell parameters: a = 3.9628 Å, b = 13.855 Å, c = 3.6964 Å and $\alpha = \beta = \gamma = 90°$.

Table 3.9

Crystal Structure Model for Calcite, $CaCO_3$ Megaw (1970 and 1973)

Atom Position	Wyckoff Code[11]	x	y	z	B $(Å)^2$
Ca	6(b)	0.000	0.000	0.000	0.183
C	6(a)	0.000	0.000	0.250	0.183
O	18(e)	0.257	0.000	0.250	0.244

- Space group : $R\bar{3}c$ (No. 167)
- Unit cell parameters : a = 4.990 Å, b = 4.990 Å, c = 17.002 Å, $\alpha = \beta = 90°$ and $\gamma = 120°$.

[10] Co-ordinates, 4(c) = x,y,1/4; 1/2-x,1/2+y,1/4; 1/2+x,1/2-y,3/4; x,y,3/4.

[11] Co-ordinates 6(b) = 0,0,0; 0,0,1/2.
6(a) = 0,0,1/4; 0,0,3/4.
18(e) = x,0,1/4; 0,x,1/4; -x,-x,1/4; -x,0,3/4; 0,-x,3/4; x,x,3/4.

3.5 Physical Modelling of March Parameter-Versus-Pressure for Uniaxially-Pressed Cylinders

The NPD data were collected for two configurations, (i) 'normal mount' with the specimen cylindrical axis coincident with the instrument rotation axis, and (ii) 'transverse mount' with the cylindrical axis normal to the instrument axis - see Figure (3.8).

Expressions were developed by the author in the course of the study (see following derivation) which link the March r-parameter to the compaction pressure via the bulk modulus of the powder. The expressions provide a novel method for the determination of bulk modulus from diffraction data. Section (4.5) describes use of the formulae in evaluating the March model.

The relationship between the compaction pressure and March r-parameter has been developed from the definition of bulk modulus :

$$B \equiv \frac{volume\ stress}{volume\ strain} = -\frac{\Delta P}{\Delta V / V} \tag{3.22}$$

where ΔP is the compaction pressure and $\Delta V/V$ is the fractional volume change. It may be assumed that the radius remains constant as the powder is pressed in a rigid die. Then, denoting the radius as R, initial height as d_o and the change in d_o as Δd,

$$V = \pi\ R^2 d_0 \tag{3.23a}$$

and

$$\Delta V = \pi\ R^2 \Delta d \tag{3.23b}$$

Substituting equations 3.23(a) and (b) into equation (3.22) yields :

$$\frac{d}{d_o} = 1 - \frac{\Delta P}{B} \tag{3.24}$$

The March r-parameter is now introduced using the relationships,

$$r = \frac{d}{d_o} \quad \text{for platy crystallites, and} \tag{3.25a}$$

$$r = \frac{d_o}{d} \quad \text{for acicular crystallites (Dollase, 1986).} \tag{3.25b}$$

The r-ΔP relationship should therefore have the forms,

$$r = 1 - \frac{\Delta P}{B} \quad \text{for platy crystallites, and} \tag{3.26a}$$

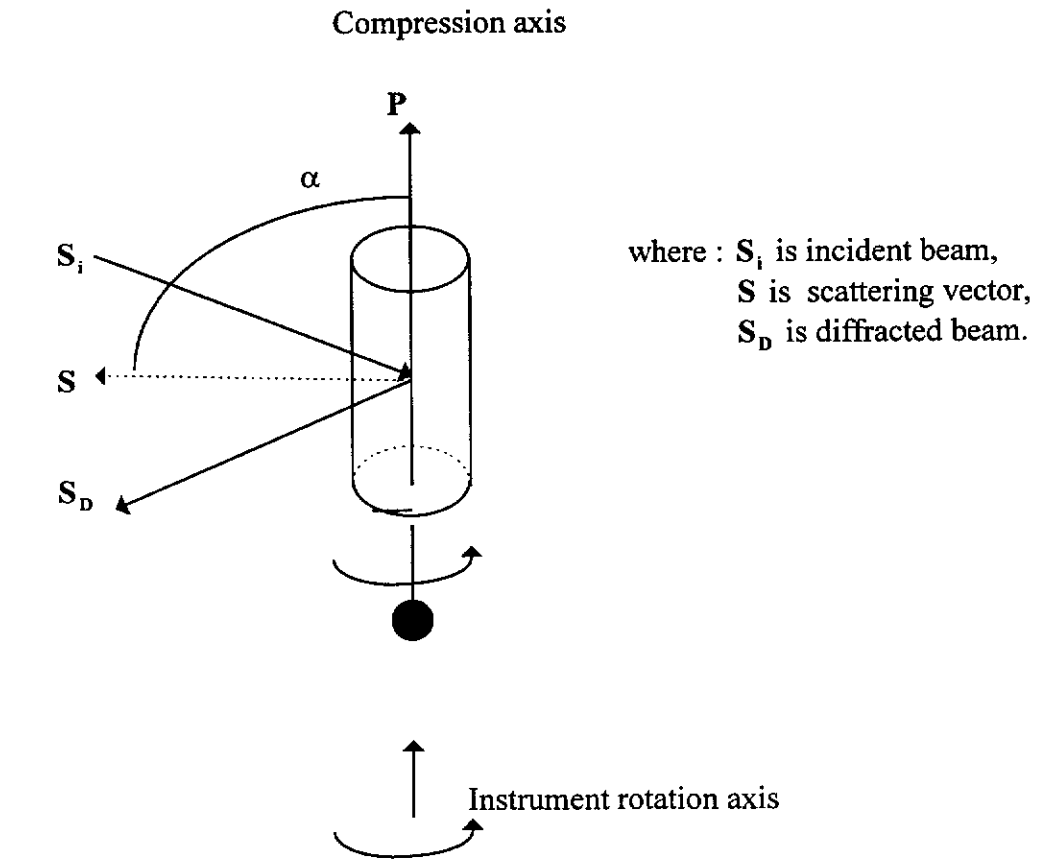

(a) Normal mount - instrument rotation and specimen compression axes coincident.

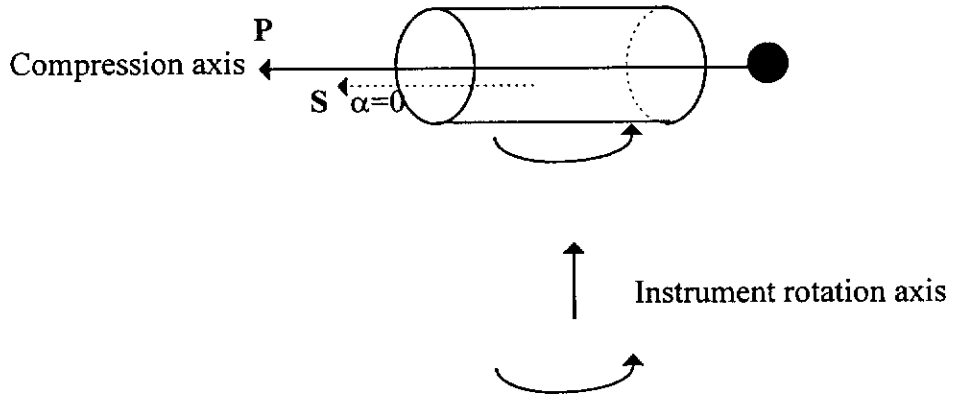

(b) Transverse mount - instrument rotation and specimen compression axes perpendicular.

Figure 3.8. Orientation for the compressed molybdite and calcite powders for the NPD measurements. In (a) the compression axis is normal to the plane defined by the incident and diffracted beams; whereas (b) depicts the compression axis in the plane of the incident and diffracted beams.

$$r = [1 - \frac{\Delta P}{B}]^{-1} \text{ for acicular crystallites.} \qquad (3.26b)$$

For platy crystallites, a plot of r-versus-ΔP should be linear, and would yield the bulk modulus, whereas a plot of 1/r-versus-ΔP would be required for acicular crystallites.

Expressions are now relating March parameters r_H (for the normal mount) and r_V (for transverse mount).

$$P_k = \left[r^{-1} \sin^2 \alpha + r^2 \cos^2 \alpha\right]^{-3/2} \qquad (3.27)$$

Then,

$$P_k(\alpha = \frac{\pi}{2}) = r_V^{3/2}, \textit{for vertical mounting}$$
$$P_k(\alpha = 0) = r_H^{-3}, \textit{for horizontal mounting} \qquad (3.28)$$

Taking the March-Dollase PO correction factor for the transformation to be constant because it is symmetric across $\alpha = 0$ and $\alpha = \pi/2$ [see Sections (1.4) and (1.5)], equation (3.27) yields the relationship :

$$r_H = r_V^{-1/2} \qquad (3.29)$$

It follows that :

$$r_H = (1 - \frac{\Delta P}{B})^{-1/2} \qquad \text{for platy crystallites} \qquad (3.30)$$

$$r_H = (1 - \frac{\Delta P}{B})^{1/2} \qquad \text{for acicular crystallites} \qquad (3.31)$$

3.6 Bulk Modulus Measurements

In view of the relationship linking March parameter r and the compaction pressure ΔP via the powder bulk modulus B [equation (3.26)], B measurements were conducted to permit comparison with Rietveld-derived bulk modulus. Measurements were made with four powders - molybdite, molybdite diluted with 50% by weight silica gel, calcite and calcite diluted with 50% by weight silica gel. Bulk modulus measurements were made with powder samples using the die which had been employed to prepare samples for NPD.

Approximately 15g of powder was placed in a cylindrical steel die assembly of diameter 19mm - see Figure (3.9). The plunger was then inserted into the die and allowed to stablise. The distance between the compressor and the top of die (L_0), corresponding to the initial (unstressed) height of the cylindrical powder volume, was measured using a vernier calliper to an accuracy of 0.02mm. The die was

positioned under the uniaxial press and the designated pressure was applied. The reduced length (L) was then measured. For molybdite, this procedure was performed for pressures of 44MPa, 66MPa, 88MPa and 110MPa and for calcite samples using pressures of 44MPa, 88MPa, 132MPa and 176MPa. These pressure selections were the same as those employed for both XRPD and NPD. The same procedure was applied to diluted material with 50% by weight silica gel.

Values of B were extracted from plots from plots of l-versus-P [Section (4.5)].

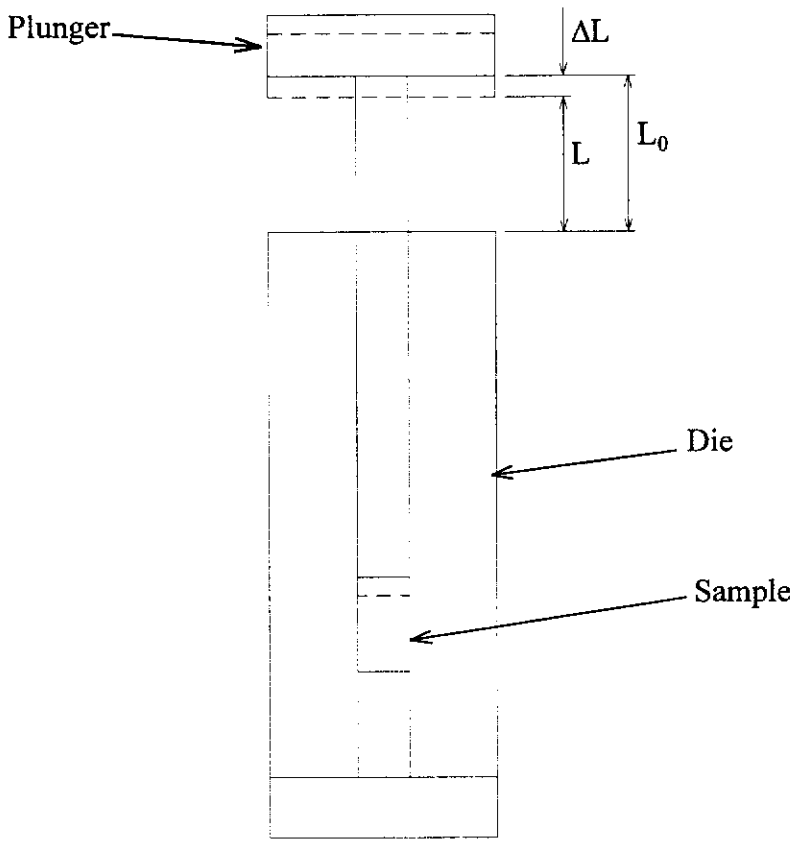

Figure 3.9. The cylindrical steel die assembly used for direct measurement of bulk modulus.

3.7 Texture Computations from Pole-Figure Measurements Using Series Expansion

The calculation of PDDs from pole-figure measurements was carried out in three steps - see Section (2.2) for details.

In the first step, called *texture analysis,* the coefficients $F_l^n(\mathbf{h})$ are calculated according to equation (1.10). This step requires multiplication of the experimental

pole-figures by the spherical harmonics of all required orders l and n and integration over the whole sphere. It is assumed here that the pole-figure is known all over the sphere.

In the second step, called *coefficients transformation,* systems of linear equations are to be solved (one for each combination of l and n) for the unknown C_l^{mn}, the coefficients of the ODF according to equation (2.35).

In the third step, termed *texture synthesis,* the orientation density $f(\varphi_1\phi\varphi_2)$ is calculated for every required orientation $\varphi_1\phi\varphi_2$ according to equation (1.9). Usually, function $f(\varphi_1\phi\varphi_2)$ is required for the complete range of orientation parameters, and the calculation is carried out in equiangular steps $\Delta\varphi_1$ $\Delta\phi$ $\Delta\varphi_2$. This operation requires calculation of a very large number of orientation points. If the range [see equation (2.28)] used in the experimental work was 6°, then there are $60 \times 30 \times 60 =$ 108,000 points that are printed out by the computer in 2D sections. A more elegant way is to contour each 2D section by interpolation between grid points and plotting of lines corresponding to equal density.

Texture Analysis Software

Texture analysis was conducted with the texture diffractometry data using the ODF-AT software system developed by LM2P[12] and SOCABIM[13]. Normalised PDDs were assembled using a two stage process (i) *Procedure 1* - construction of PDDs from *single* Bragg-peak data following normalisation by series expansion (SE) analysis, and (ii) *Procedure 2* - re-construction of PDDs following SE analysis of the *full set* of Bragg-peak data.

Procedure 1 is confined to the determination of normalisation factors for the PDD measurements and to the subsequent construction of pole-figures using the single Bragg-peak data. Procedure 2, which requires the procedure 1 analysis as a preliminary step, is a more sophisticated method which provides re-constructed PDDs using the entire set of diffraction data.

The schematic in Figure (3.9) summarises the procedure for computing PDDs once the pole-figure has been measured.

[12] University of Metz, LM2P, Ile du Saulcy, 57045 METZ Cedex, France.
[13] SOCABIM, 9 bis villa du Bel-Air.

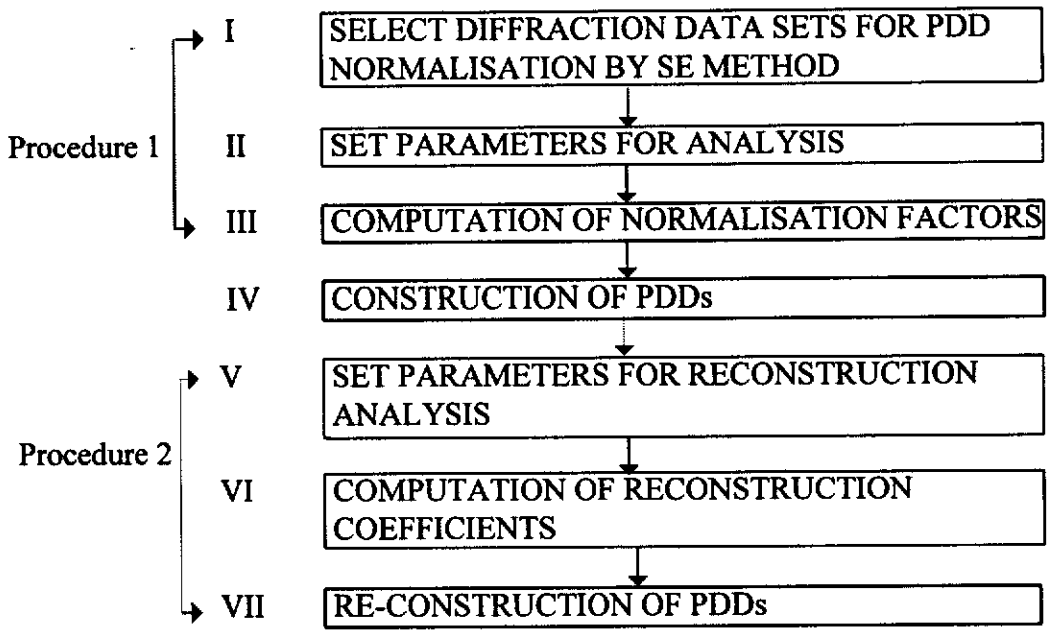

Figure 3.10. Procedure for assembling pole-figures from PDD measurements (see footnotes 12 and 13).

Procedure 1

The crystal symmetry must be specified plus the rank for pole-figure harmonic expansion l in equation (1.10) and Table (3.10). Orthorhombic symmetry was nominated for molybdite and hexagonal symmetry for calcite. When selecting the value of l, the user must verify that sufficient pole-figures are available for the computation - see Figure (2.8). Once the C_l^{mn} coefficients of the series expansion of $\tilde{f}(\mathbf{g})$ are calculated it is possible to recalculate any pole-figure. Procedure 1 generates a partial set of C_l^{mn} coefficients (for l = even) which are used with equation (1.10) to calculate normalisation factors.

Procedure 2

Once the even C_l^{mn} coefficients had been calculated during the texture analysis it is possible to start the texture synthesis. The texture synthesis consists in calculating the values of f(**g**) [the directly-determinable part or even part of the ODF] or the values of the complete ODF f(**g**) on a regular grid in the Euler space [equation (2.33a)].

The maximum rank of even coefficients for molybdite and calcite specimens are ≤ 30 and ≤ 22, respectively, which they must be equal to (or less than) the l used for texture analysis. *The maximum rank of odd coefficients* for molybdite and calcite powders were employed ≤ 21 and ≤ 17, respectively (Bunge, 1982). When the positivity technique was used for the calculation of a complete ODF, the convergence was obtained in 10 cycles. The steps in φ_1, ϕ and φ_2 in the Euler space were fixed as well as the maximum value for φ_1 [$15° \leq \varphi_1 \leq 360°$; $6° \leq \phi \leq 90°$; $6° \leq \varphi_2 \leq 9°$] - see Bunge (1982).

Table 3.10

Typical values for final l (Bunge, 1982)

The necessary minimal number of pole-figures (experimental + supplementary) for analysis is indicated in parentheses.

Crystal symmetry → / Texture type ↓	Cubic	Hexagonal	Tetragonal	Trigonal	Orthorhombic
sharp texture	34(≥3)	28(≥5)	22(≥6)	22(≥8)	22(≥12)
weak texture	22(≥2)	16(≥3)	16(≥5)	16(≥6)	12(≥7)

CHAPTER 4

RIETVELD TEXTURE ANALYSIS EXPERIMENTS

4.1 Pre-amble

PDDF modelling with x-ray data was conducted with molybdite and calcite specimens with a view to using these data to examine the validity of the March model. Parallel modelling with neutron data was carried out in order to compare the bulk, or global, texture information with the near-surface characterisations performed with x-ray data.

A valuable result from the study is the distinct difference observed for calcite between the direction of near-surface texture, as measured by XRPD, and bulk texture characterised by NPD.

The chapter provides appraisals of the March model in terms of the deterioration in the quality of Rietveld fits as the powder compression pressure increases. The appraisal includes a detailed examination of the relationship between March parameter r and uniaxial pressure developed in the study [see Section (3.5)].

4.2 Rietveld Computations

The parameters refined in all Rietveld computations were the instrument zero-point; polynomial background parameters; phase scale factor; profile parameters for the pseudo-Voight function [U, V, W, As and γ - see Section (3.4)]; lattice parameters; atom positional parameters; atom isotropic thermal parameters; and phase March r-parameter.

Table (4.1) shows the XRPD refinement trials with calcite samples in which <104> was assumed to be the direction of PO. It is evident that the summing of symmetry equivalents gave significantly improved figures-of-merit. Also, the r-parameters determined with summing of equivalents were substantially higher for all data sets. Thus, neglect of symmetry equivalents summing biases the parameter

Table 4.1.

Influence of Equivalent Reflection Summing on March r-parameter and Figures-of-Merit - Calcite Powders (100%) - XRPD Data

- PO direction assumed to be <104>. Results for summing and non-summing of equivalent reflections are given in the first and second lines, respectively.
- Inclusion of equivalent reflection summing did not influence results for (i) molybdite with PO direction <010> or (ii) for calcite with PO direction <001>. Results not included.

Pressure (MPa)	Sample Code[14]	Figures-of-Merit					
		R_{EXP}	R_P	R_{WP}	R_B	GOFI	March Parameter r
0	C0X	13.93	15.67	23.61	4.30	2.87	0.965(8)
			15.63	23.61	4.34	2.87	0.989(6)
44	C2X	12.91	16.42	23.32	5.50	3.26	0.682(4)
			17.53	24.35	8.26	3.56	0.825(5)
88	C4X	11.13	15.88	28.10	6.71	6.37	0.460(3)
			17.70	30.44	8.01	7.47	0.556(4)
132	C6X	9.20	15.19	26.51	8.21	8.31	0.437(3)
			16.92	28.78	8.87	9.79	0.522(4)
176	C8X	8.60	15.28	26.00	7.97	9.13	0.424(3)
			16.71	28.24	8.42	10.77	0.507(4)

[14] See Table (3.3); Sample Pelletising Procedures.
Symbol: C = calcite
X = x-ray
Digit represents pressure in ×1000lbs units (conversion factor, 1000lbs units to MPa =22).

values. The summing of equivalent reflections did not influence results for (i) molybdite XRPD and NPD data with PO direction <010> or (ii) calcite NPD data with PO direction <001>.

4.3 X-ray Diffraction Experiments

4.3.1 Molybdite X-ray Experiments

Molybdite (100% by weight)

Figure (4.1) compares the measured XRPD data for the 100% molybdite non-pressed sample and one of the pressed powders - that prepared with a pressure of 110MPa. The comparison shows the influence of pressing on the intensities. For example, the intensities for the three most intense lines (020) at $2\theta = 12.77°$, (040) at $2\theta = 25.70°$ and (060) at $2\theta = 39.66°$ increase from 9,050, 11,750 and 6,050 by factors of 4.4, 5.2 and 5.1, respectively, whereas the intensity of the line (110) at $2\theta = 23.33°$ reduces from 3,880 by a factor of 0.9. These dramatic changes contrast with the subtle intensity shifts found in the corresponding sets of NPD data for molybdite - [see Section (4.4) Figure (4.8)]. It is evident that the XRPD PO bias, deriving from the near-surface texture, differs radically from the bulk texture influencing the NPD intensities.

Table (4.2) compares the Rietveld refinement results for parallel calculations involving PO and random orientation. The values for the figures-of-merit - R_P, R_{WP}, R_B - all decreased substantially when the March model was applied. It is noted, though, that the weighted R-factors R_{WP} still substantially exceeded the 'expected' values R_{EXP} when the March model was applied.

The R_{WP} and R_B factors for the molybdite samples, all of which show substantial PO, ranged between 49.9 - 87.0% and 37.9 - 79.6%, respectively, before the March model was employed; whereas the corresponding values with the March model, 24.3 - 25.5% and 5.6 - 10.1%, were substantially lower. It is noted in drawing these comparisons, that the R_{WP} value should be close to R_{EXP} if the model is basically correct, *i.e.* GOFI = 1.00, ideally. The GOFI for the refinements with the March model ranged from 8.1 for the 'random' powder (M0X) to 17.4 for the most heavily pressed (M5X). These results show that the March model does not fit the

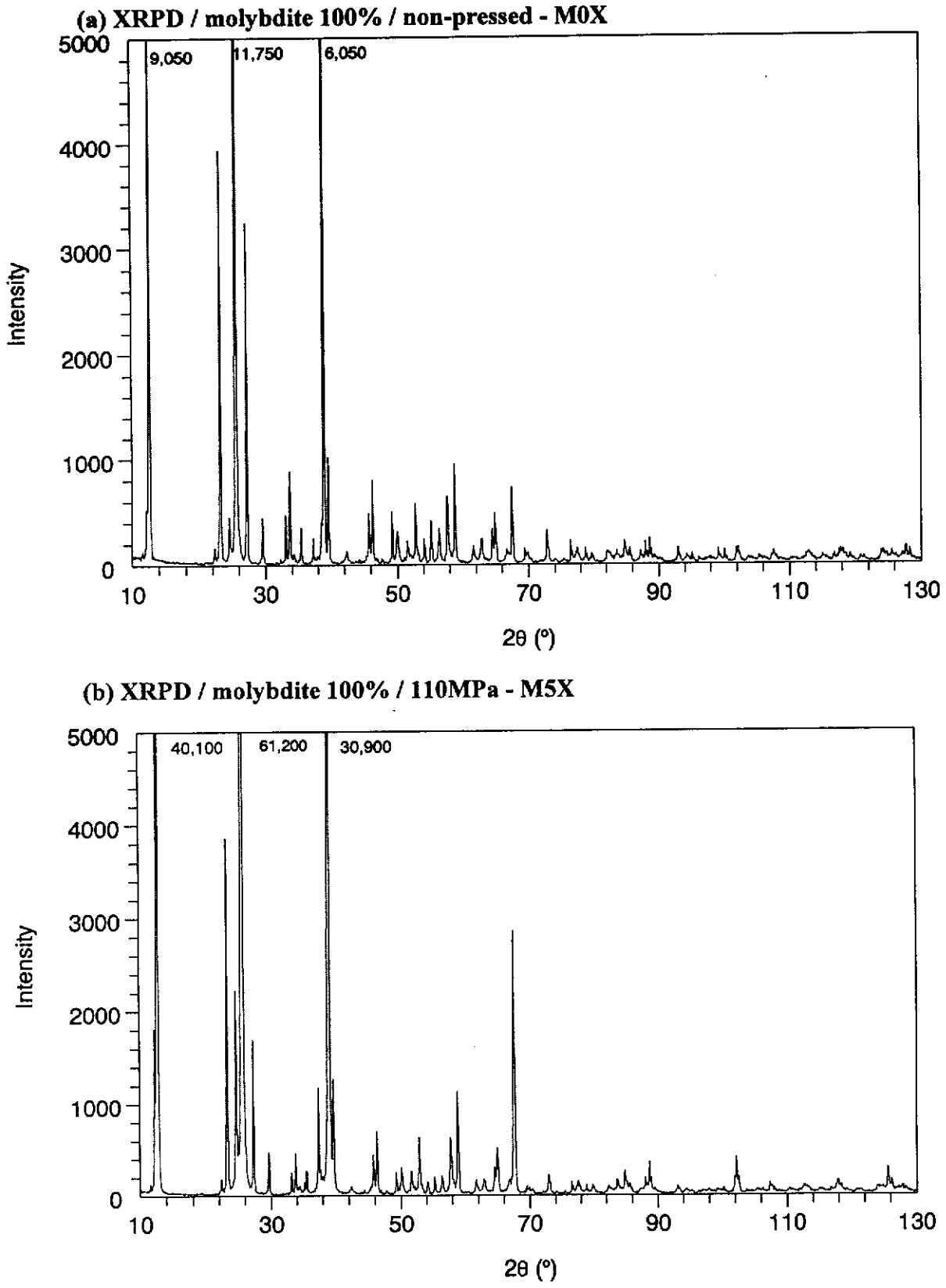

Figure 4.1. Comparison of molybdite XRPD patterns for (a) non-pressed mount and (b) powder pressed at 110MPa.

Table 4.2.
XRPD Rietveld Refinement Results for Molybdite Powders

- Assumed direction of PO, <010> (Kihlborg, 1963).
- Values for random orientation (r = 1.000) model given in parentheses.
- Data for undiluted specimens are given in the first two lines of results for each pressure, and results for specimens diluted with silica gel (50% by weight) given in third and fourth lines.

Pressure (MPa)	Sample Code[15]	Figures-of-Merit					
		R_{EXP}	R_P	R_{WP}	R_B	GOFI	March r-Parameter
0	M0X	8.95	19.06 (40.81)	25.50 (49.90)	10.11 (37.95)	8.13 (31.10)	0.611(2)
	M0X(S)	8.35	16.06 (23.25)	20.44 (29.06)	9.00 (20.74)	6.00 (12.12)	0.742(3)
44	M2X	7.89	16.86 (59.47)	24.73 (68.43)	9.15 (57.77)	9.81 (75.09)	0.459(2)
	M2X(S)	8.67	16.52 (28.42)	21.34 (36.10)	9.37 (29.51)	6.06 (17.32)	0.665(3)
66	M3X	8.31	14.70 (70.60)	24.51 (76.75)	8.45 (72.30)	9.42 (133.4)	0.455(2)
	M3X(S)	9.09	16.14 (34.44)	20.61 (42.65)	10.27 (36.63)	5.14 (22.00)	0.618(2)
88	M4X	7.20	14.75 (72.07)	24.34 (80.55)	6.04 (74.74)	11.43 (125.2)	0.402(2)
	M4X(S)	9.26	16.32 (37.09)	21.55 (46.62)	9.76 (40.83)	5.41 (25.33)	0.588(2)
110	M5X	6.00	14.25 (78.03)	25.07 (86.98)	5.63 (79.57)	17.42 (21.01)	0.373(2)
	M5X(S)	7.71	14.41 (52.49)	18.62 (63.17)	5.83 (67.05)	9.12 (26.67)	0.586(2)

[15] See Table (3.3); Sample Pelletising Procedures.
Symbol: M = molybdite
X = x-ray
S = silica gel addition
Digit represents pressure in ×1000lbs units (conversion factor, 1000lbs units to MPa =22).

well as it might. Note also that the disagreement between R_{WP} and R_{EXP} for gibbsite refinements by O'Connor, Li and Sitepu (1991) with the March model was also substantial.

The variation of the March PO parameter with uniaxial pressure is shown in Figure (4.2a). The results show that the r-parameters trend in the manner expected from equation (3.26a), *viz.* a linear reduction in r as briquetting pressure increases. The r-pressure results are considered further in Section (4.4).

Side-drifting failed to produce an r-value close to 1.0 thus indicating that the technique produced samples with substantial residual PO. This observation was also made in the molybdite XRPD study of O'Connor, Li and Sitepu (1992). While the preparation of spray-dried molybdite powders reported by Calvert *et al.* (1983) did produce randomised powders, it is evident that side-drifting is inadequate for this purpose.

The difference plots shown in Figure (4.3) show residual features which probably indicate inadequacies in the March model for representing texture in the material. While the plots show that the March model was effective in substantially improving agreement between calculated and measured data, it appears on this basis that the model is not ideal for molybdite.

Molybdite diluted with silica gel (50% by weight)

Figure (4.4) demonstrates the influence of dilution on the diffraction pattern for the molybdite powder with a compression of 88MPa, M4X. Inspection of the two patterns shows a substantial reduction in the Bragg intensities when the powder is diluted. The reduction factor is not linear across the patterns as dilution reduces the level of PO.

The March PO parameters and refinement indices for the diluted molybdite samples are given in Table (4.2). When the March model was not employed in the Rietveld refinements, the R_{WP} and R_B values ranged between 29.1 - 63.2% and 20.7 - 67.1%, respectively. The corresponding factors with the March model, 18.6 - 21.6%, and 5.8 - 10.3%, were substantially lower as was also observed for the undiluted samples. Again, as for the 100% molybdite powders, the GOFI values substantially exceeded 1.00, ranging from 5.1 to 9.1.

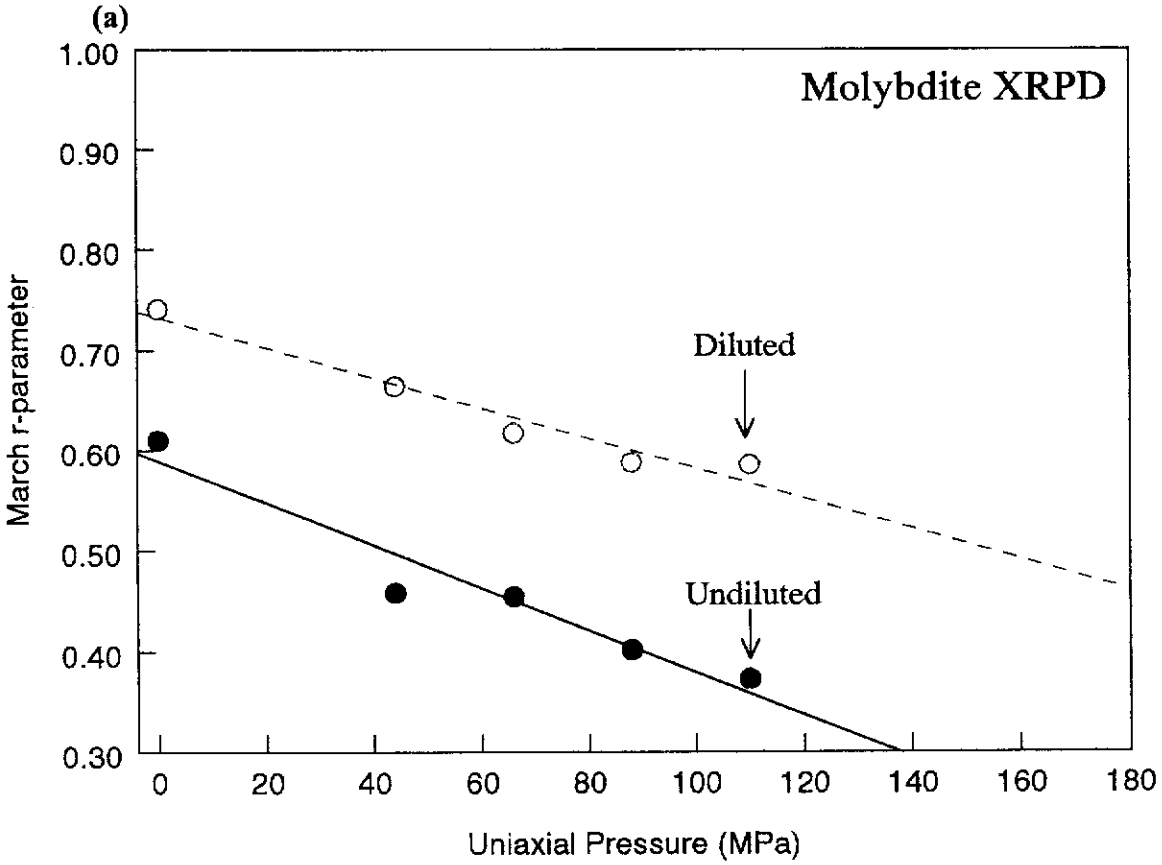

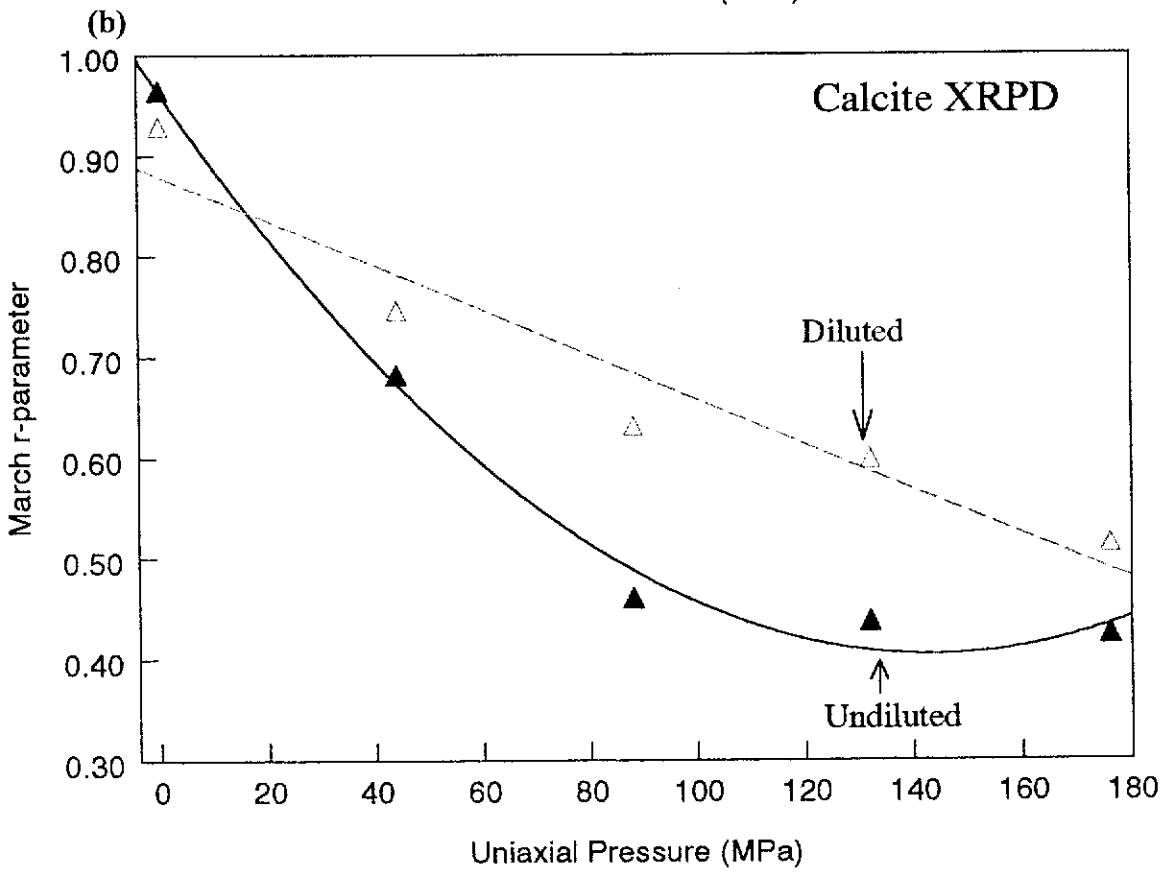

Figure 4.2. Variation in March PO parameter with uniaxial pressure for XRPD (a) molybdite and (b) calcite. Linear regressions shown for both suites of molybdite, and for 50% diluted calcite. Second order polynomial fit shown for the pure calcite specimens.

(a) Molybdite non-pressed sample - M0X (XRPD)

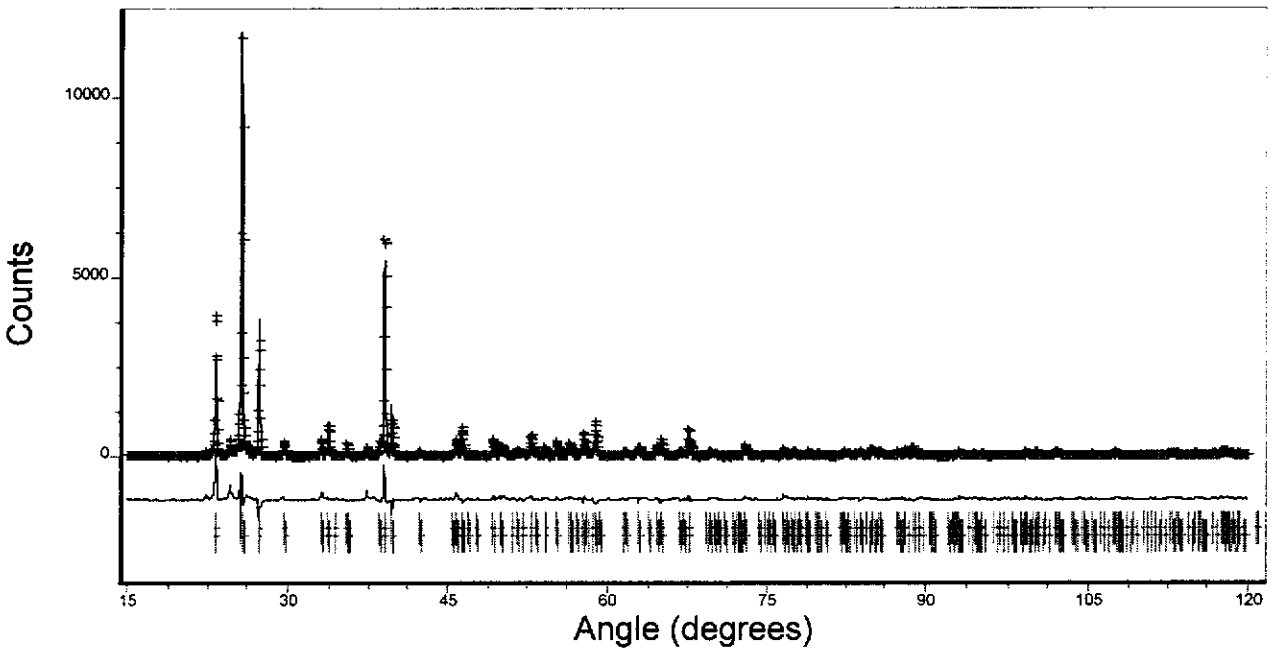

(b) Molybdite sample pressed at 110MPa - M5X (XRPD)

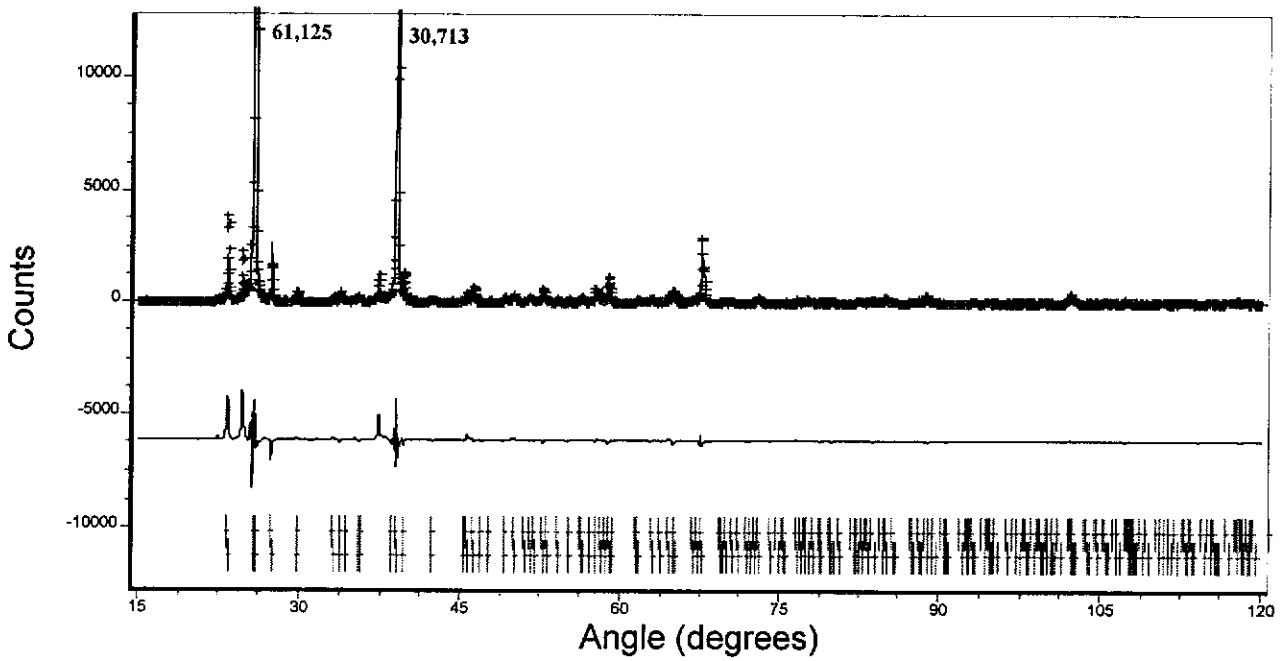

Figure 4.3. Agreement between calculated and measured XRPD patterns for selected molybdite powder specimens following Rietveld refinement with the March model. The observed data are indicated by plus signs and the calculated profile is the continuous line in the same field. The set of vertical lines below the profiles represent the positions of all possible Bragg reflections. The lower plot is the difference between the measured and calculated patterns on the same scale as the measured and calculated patterns.

(a) XRPD / molybdite + 50% silica gel / 88MPa - M4X(S)

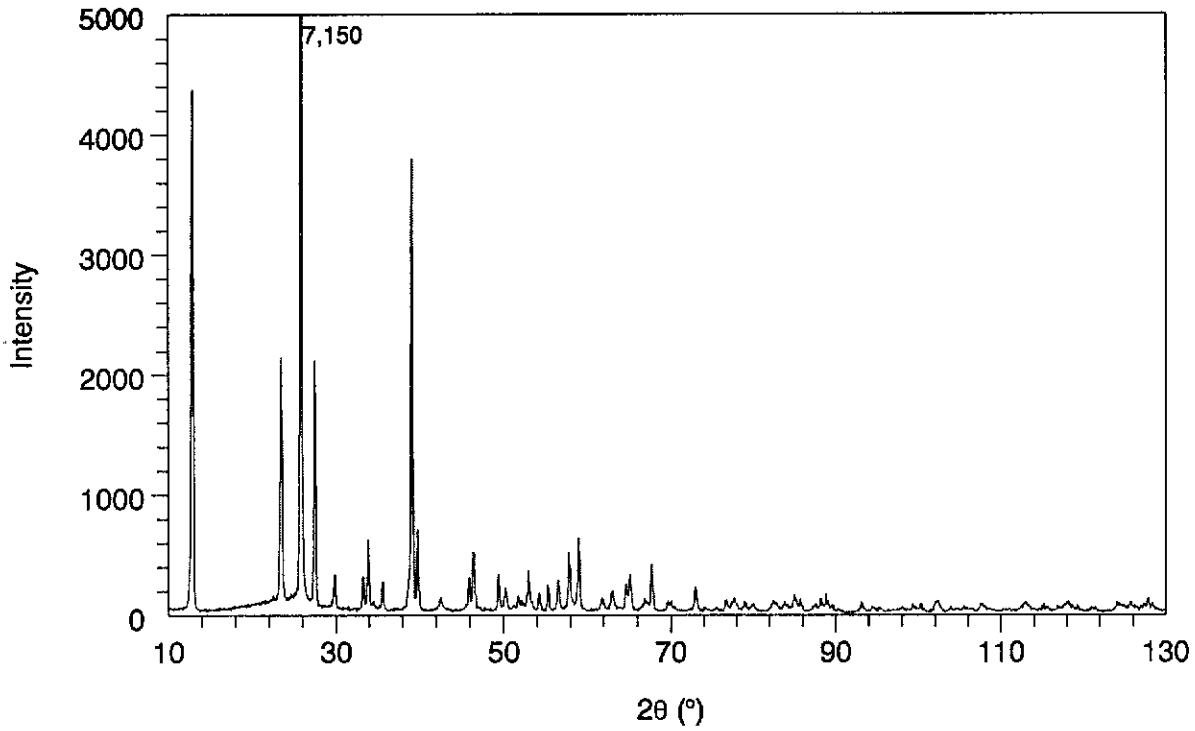

(b) XRPD / molybdite 100% / 88MPa - M4X

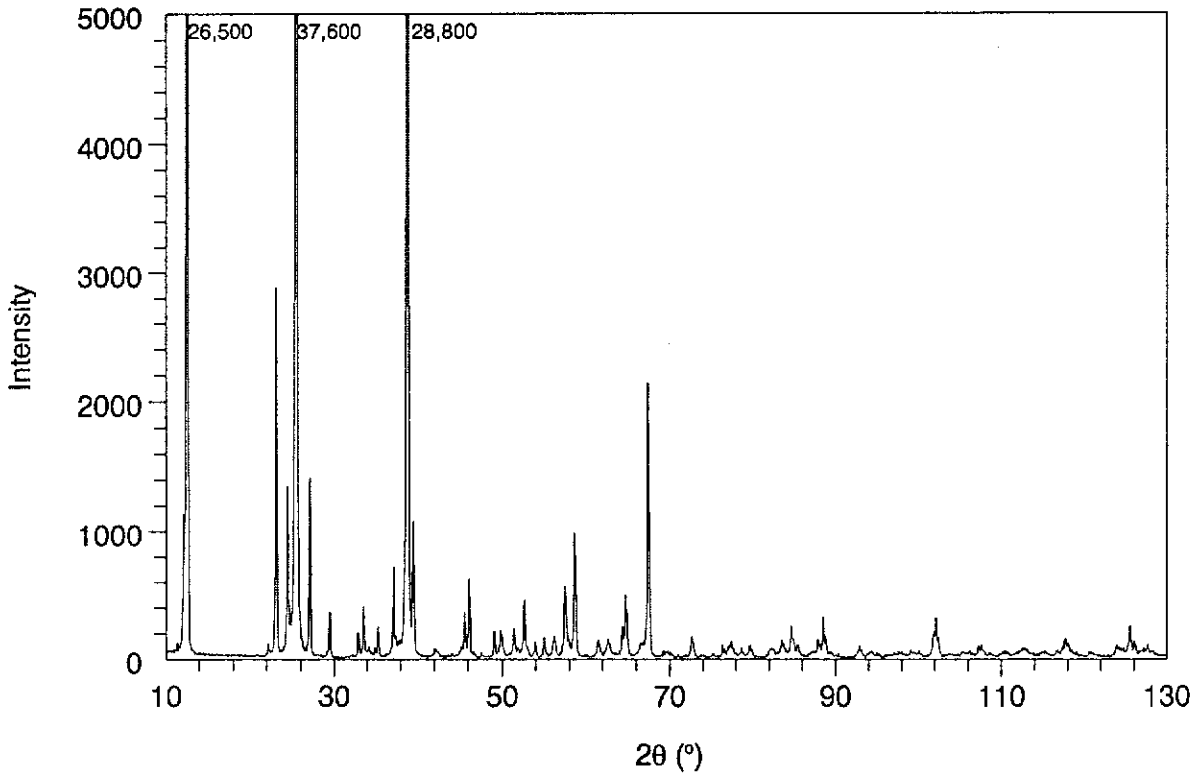

Figure 4.4. Influence of 50% silica gel addition on the molybdite XRPD data - specimen M4X(S) pressed at 88MPa.

All r-values show a substantial increase following dilution. As for the undiluted molybdite powders, the r-pressure plot [see Figure (4.2)], is linear as expected - see further discussion in Section (4.5). The r-intercept for the r-pressure plot for zero pressure 0.59 is closer to zero then the value for the undiluted set 0.73 thus showing that dilution did reduce PO. The results show that side-drifting failed to produce a randomised powder, even with dilution.

4.3.2 Calcite X-ray Experiments

Calcite (100% by Weight)

Figure (4.5) shows the differences between the XRPD patterns for the side-drifted powder (C0X) and the most heavily pressed powder (C8X). The patterns shows the well-known response of the (104) line to pressure, the initial intensity 5,805 increasing by a factor of 8.4. Also, it is instructive to note that numerous other lines respond readily to pressure, some increasing and others reducing.

The refinement indices and r-parameters are given in Table (4.3). The r-value for the randomised sample (C0X) is 0.96(1), indicating that the value differs only marginally from the ideal (1.00) which contrasts with the much smaller values for molybdite side-drifted powders. Also, the GOFI value (2.9, both for random model and when using the March model) again shows that assuming random orientation is basically correct.

As the pressure is applied, the fit indices for the random orientation model become progressively inferior to the refinements with PO. While the March model substantially improves the agreement between measured and calculated patterns [see also difference plots in Figure (4.6)], the GOFI increases as the applied pressure increases - from 3.3 (COX) to 9.1 (C8X). Therefore, as with the 2 sets of molybdite results, the capacity of the March model to provide satisfactory agreement steadily diminishes as PO becomes more substantial.

The variation in r-parameter with applied pressure, as shown in Figure (4.2b), is not linear whereas the corresponding relationships for both molybdite powder suites were both linear. There is a linear decrease in parameter to 88MPa beyond which the r-value reaches a plateau which is not completely unexpected as the r-

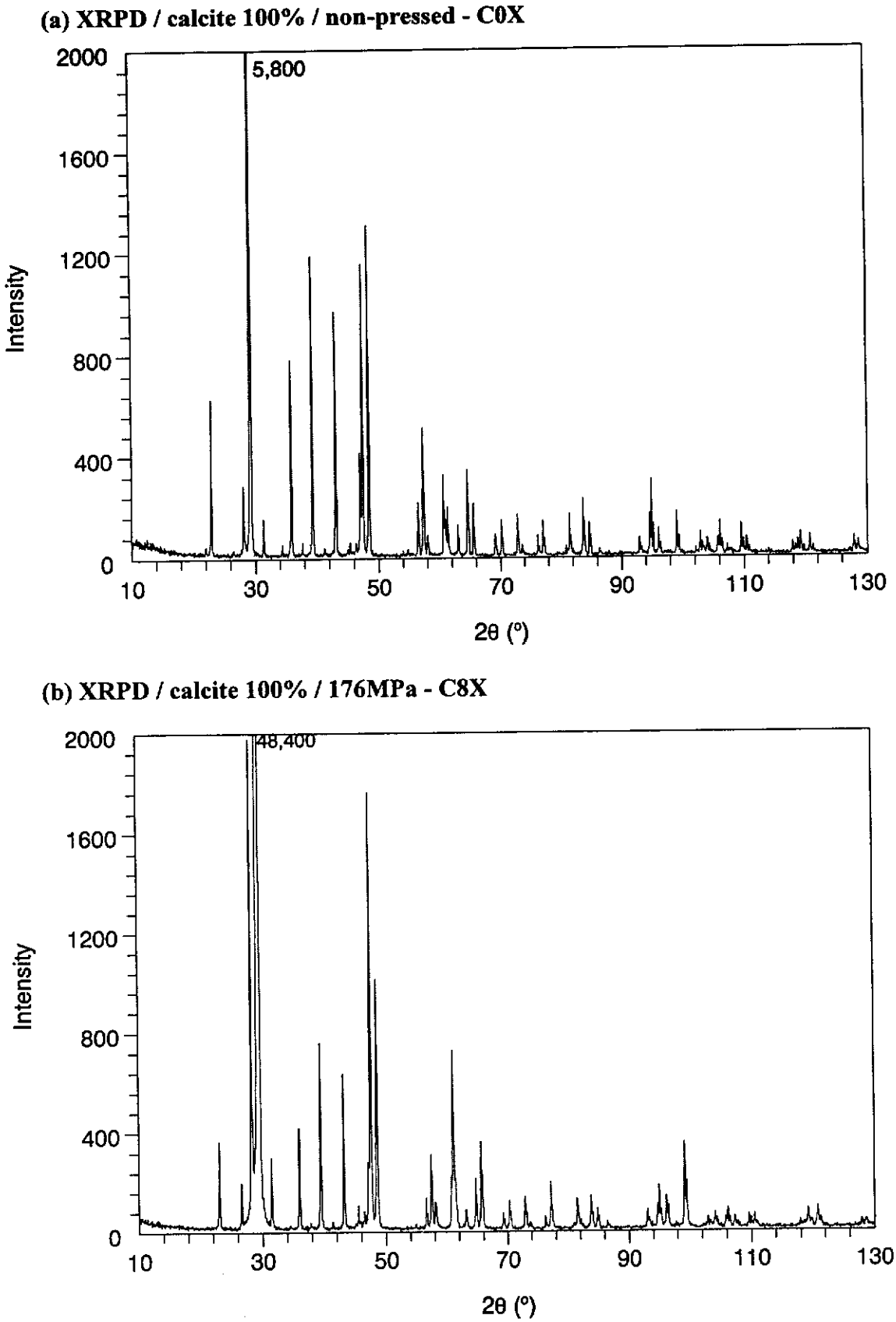

Figure 4.5. Comparison of calcite XRPD patterns for (a) non-pressed mount and (b) powder pressed at 176MPa.

Table 4.3.
XRPD Rietveld Refinement Results for Calcite Powders

- Assumed direction of PO was <104> Dollase (1986).
- Values for random orientation (r = 1.000) model given in parentheses.
- Data for undiluted specimens are given in the first two lines of results for each pressure, and results for specimens diluted with 50% by weight silica gel given in third and fourth lines.

Pressure (MPa)	Sample Code[16]	Figures-of-Merit					
		R_{EXP}	R_P	R_{WP}	R_B	GOFI	March r-Parameter
0	C0X	13.93	15.67 (15.71)	23.61 (23.62)	4.30 (4.45)	2.87 (2.87)	0.965(8)
	C0X(S)	10.42	15.91 (15.99)	20.28 (20.31)	4.37 (4.34)	3.79 (3.80)	0.930(5)
44	C2X	12.91	16.42 (22.39)	23.32 (29.10)	5.50 (17.35)	3.26 (5.08)	0.682(4)
	C2X(S)	13.12	19.24 (24.20)	24.96 (30.67)	6.42 (12.24)	3.62 (5.40)	0.746(1)
88	C4X	11.13	15.88 (52.02)	28.10 (60.27)	6.71 (51.72)	6.37 (29.29)	0.460(3)
	C4X(S)	10.71	18.07 (26.71)	23.87 (33.46)	6.69 (19.37)	4.96 (9.66)	0.631(6)
132	C6X	9.20	15.19 (55.21)	26.51 (63.23)	8.21 (56.58)	8.31 (47.25)	0.437(3)
	C6X(S)	11.95	19.55 (28.07)	25.44 (34.61)	8.44 (25.07)	4.54 (8.29)	0.599(5)
176	C8X	8.60	15.28 (57.03)	26.00 (65.07)	7.97 (58.77)	9.13 (57.16)	0.424(3)
	C8X(S)	13.29	17.77 (27.22)	24.30 (37.01)	7.13 (14.98)	3.34 (7.59)	0.514(4)

[16] See Table (3.3); Sample Pelletising Procedures.
Symbol: C = calcite
X = x-ray
S = silica gel addition
Digit represents pressure in ×1000lbs units (conversion factor, 1000lbs units to MPa =22).

(a) Calcite non-pressed sample - C0X (XRPD)

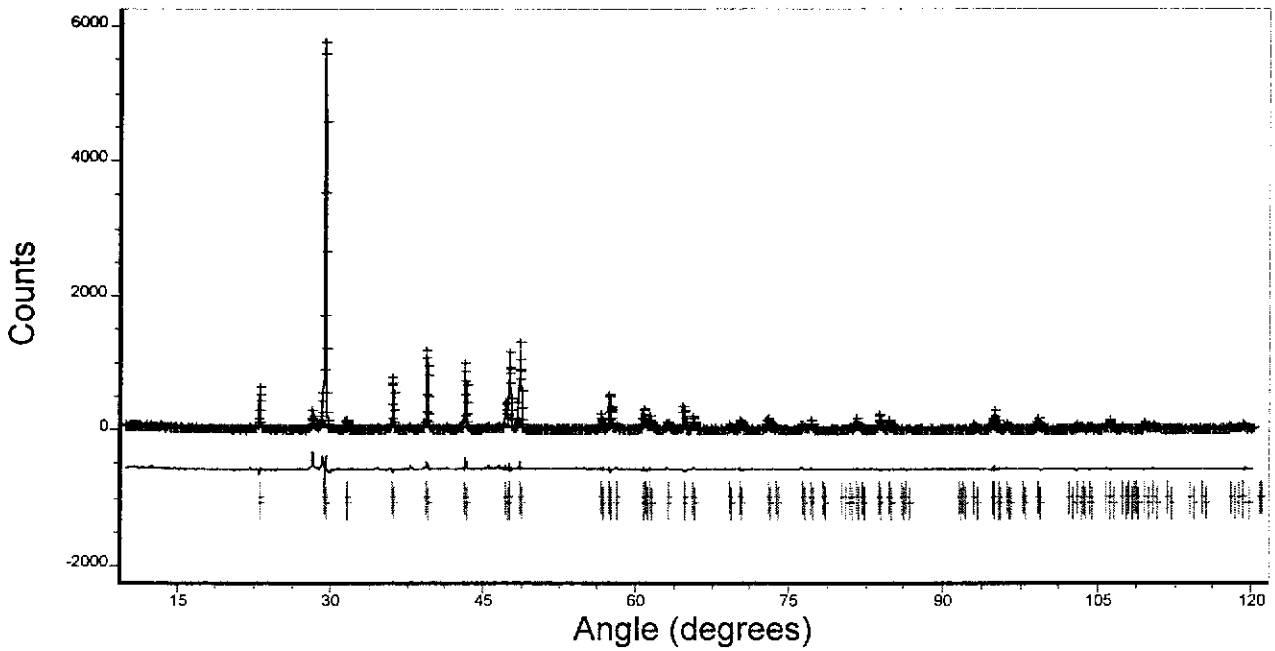

(b) Calcite sample pressed at 176MPa - C8X (XRPD)

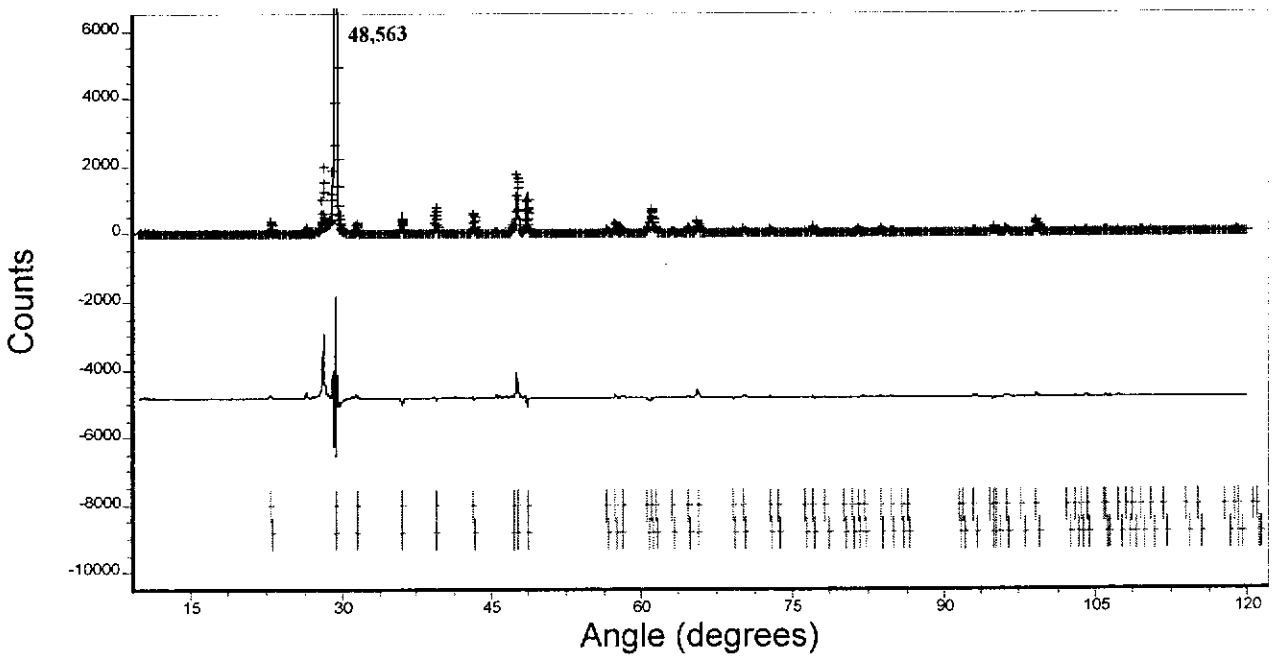

Figure 4.6. Agreement between calculated and measured XRPD patterns for selected calcite powder specimens following Rietveld refinement with the March model. The observed data are indicated by plus signs and the calculated profile is the continuous line in the same field. The set of vertical lines below the profiles represent the positions of all possible Bragg reflections. The lower plot is the difference between the measured and calculated patterns on the same scale as the measured and calculated patterns.

parameter cannot increase indefinitely with pressure. This behavior is discussed later in the chapter [Section (4.5)].

Calcite diluted with silica gel (50% by weight)

Figure (4.7) shows the influence of the silica gel addition on the appearance of the pattern for calcite specimens with the compression of 144MPa, C6X(S). A substantial reduction in the Bragg intensities is shown in the diluted diffraction pattern compared with undiluted. As for the diluted molybdite pattern, the reduction factor is not linear across the pattern as dilution reduces the PO level.

Figure (4.2b) shows that the r-pressure plot is linear and similar in gradient to the plots for molybdite and the diluted powders. Thus, the apparent saturation of the relationship observed for the 100% calcite powder was not found for the diluted suite of calcites. As the pressure increases, the refinements for the diluted materials all provide superior fits compared with those assuming random orientation. Also, the GOFI values are much closer to 1.00 than the corresponding values for the molybdite powders, the largest GOFI for a diluted calcite being 5.0 for C4X(S) and the lowest being 3.6 for C2X(S).

4.4 Neutron Diffraction Experiments

The NPD results should be considered in light of the fundamentally different nature of the information provided, *viz.* that the PO influence comes from the bulk of the specimen, whereas the XRPD results presented in Section (4.3) involve near-surface information. The NPD results for "normal" mounts, for which the cylinder axis is coincident with the rotation axis of the Debye-Scherrer instrument used for data collection.

4.4.1 Molybdite Neutron Experiments

Figure (4.8) shows the differences between the NPD patterns for the side-drifted powder (M0N) and the most heavily compressed powder (M5N). In contrast to the XRPD data [see Figure (4.1)], the differences between the two NPD patterns are more subtle.

(a) XRPD / calcite + 50% silica gel / 144MPa - C6X(S)

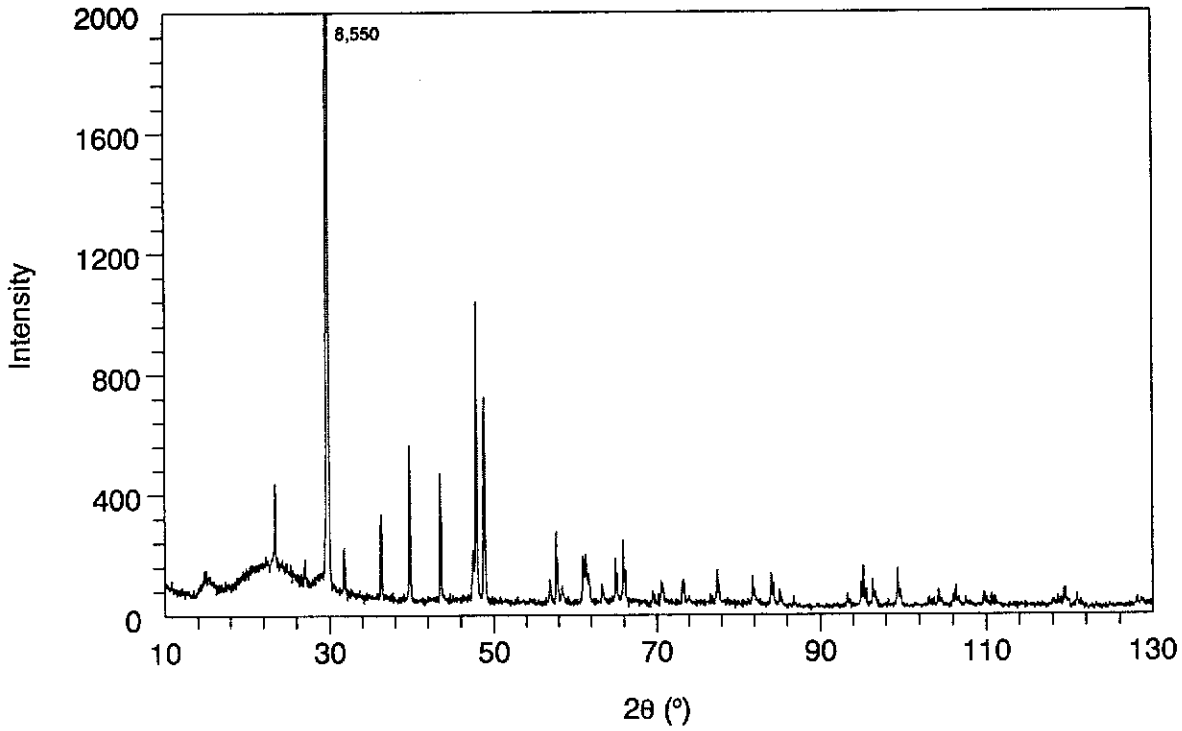

(b) XRPD / calcite 100% / 144MPa - C6X

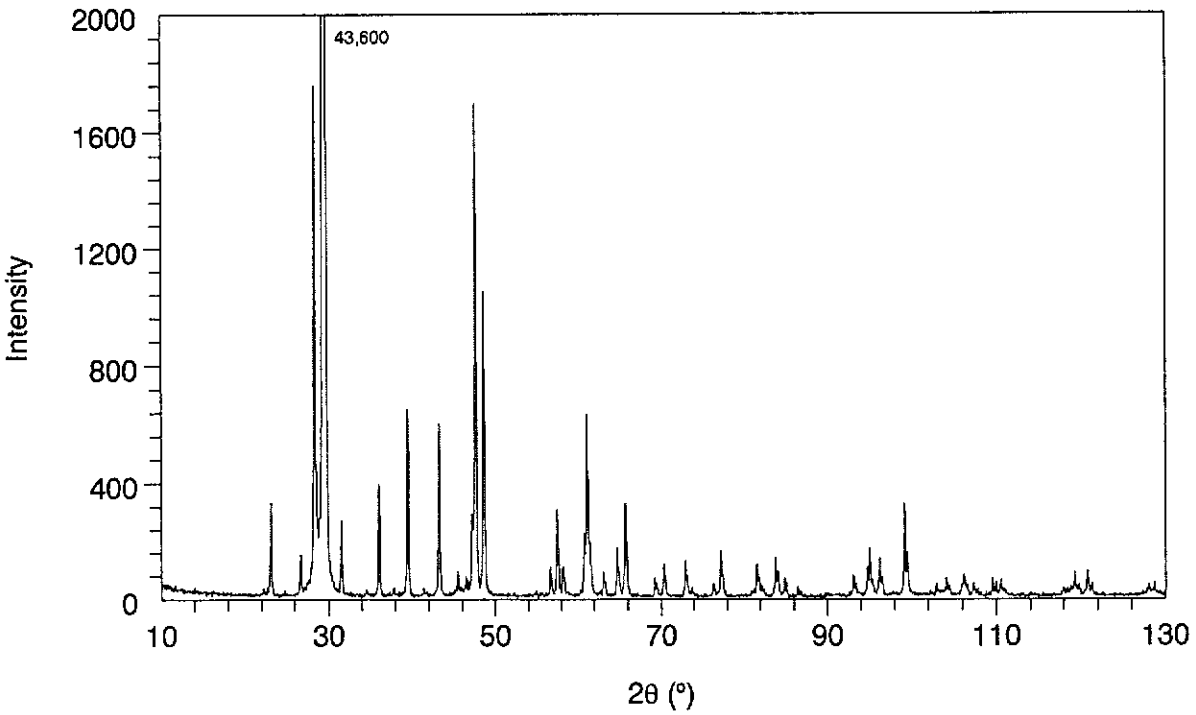

Figure 4.7. Influence of 50% silica gel addition on the calcite XRPD data - specimen C6X(S) pressed at 144MPa.

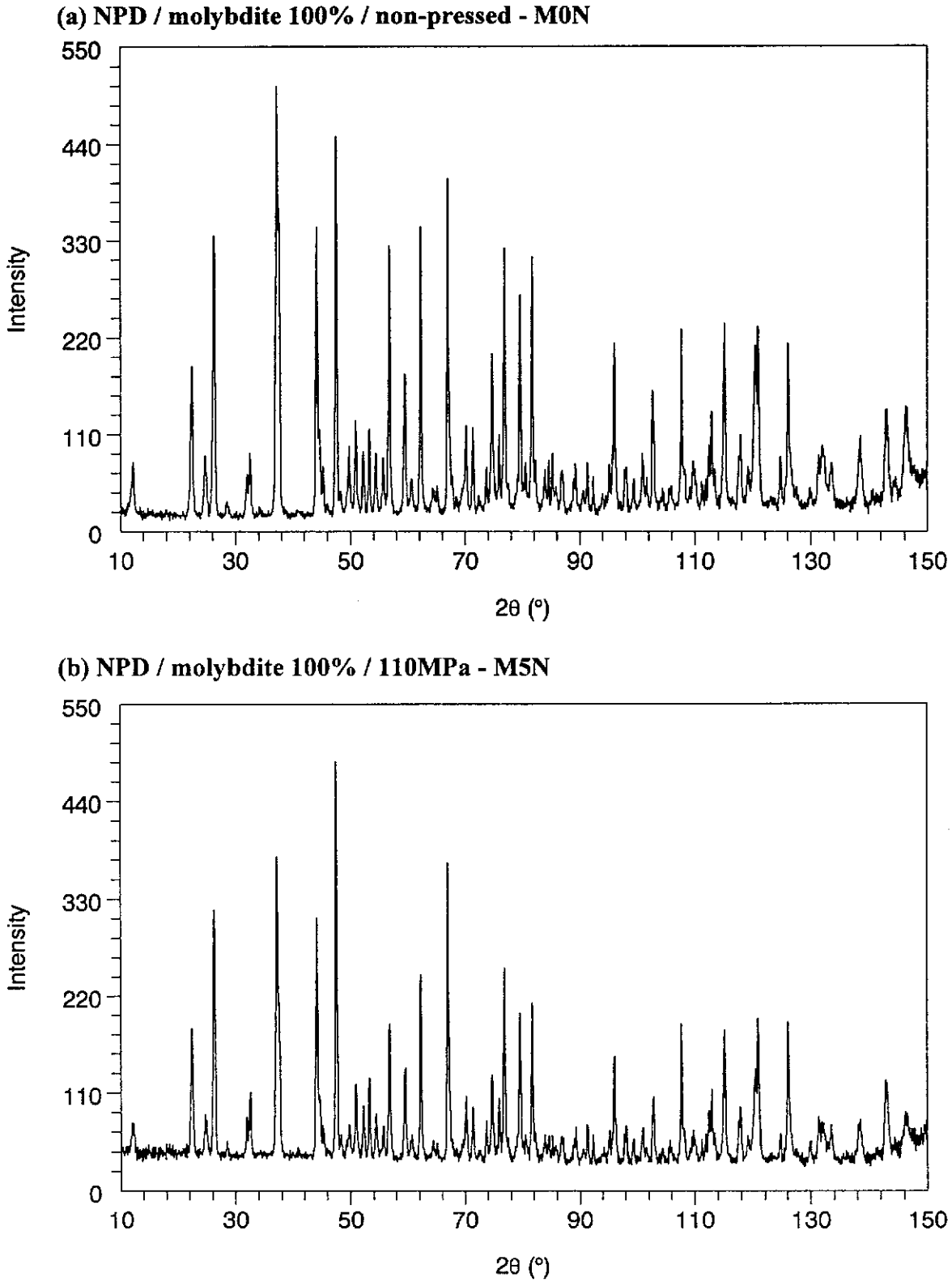

Figure 4.8. Comparison of molybdite NPD patterns for (a) non-pressed powder and (b) powder pressed at 110MPa - normal mounts.

Table 4.4
NPD Rietveld Refinement Results for Molybdite Powders - Cylindrical Specimens Mounted *Parallel* to Instrument Rotation Axis
(Normal Mounts)

- Assumed direction of PO, <010> (Kihlborg, 1963).
- Values for random orientation (r = 1.000) model given in parentheses.
- Data for undiluted specimens are given in the first two lines of results for each pressure, and results for specimens diluted with silica gel (50% by weight) given in third and fourth lines.

Pressure (MPa)	Sample Code[17]	Figures-of-Merit					
		R_{EXP}	R_P	R_{WP}	R_B	GOFI	March r-Parameter
0	M0N	5.48	10.26 (10.41)	12.61 (12.79)	5.47 (5.50)	5.30 (5.45)	1.031(3)
	M0N(S)	3.28	4.97 (5.08)	5.91 (6.06)	3.42 (3.97)	3.25 (3.41)	1.092(8)
44	M2N	5.31	8.32 (10.48)	9.99 (13.23)	5.53 (9.37)	3.54 (6.22)	1.178(2)
	M2N(S)	2.86	3.79 (3.95)	4.56 (4.78)	2.54 (3.28)	2.54 (2.79)	1.129(8)
66	M3N	9.26	10.94 (12.92)	13.32 (15.86)	5.30 (9.41)	2.07 (2.93)	1.183(6)
	M3N(S)	2.37	3.23 (3.38)	3.90 (4.16)	2.14 (2.89)	2.71 (3.07)	1.145(8)
88	M4N	5.39	8.15 (10.80)	9.82 (13.89)	5.48 (10.25)	3.32 (6.63)	1.203(4)
	M4N(S)	Not Measured					
110	M5N	5.32	8.40 (11.18)	10.06 (14.42)	5.78 (10.77)	3.58 (7.35)	1.212(4)
	M5N(S)	3.07	5.05 (5.23)	7.07 (7.26)	4.57 (5.71)	5.31 (5.60)	1.187(7)

[17] See Table (3.3); Sample Pelletising Procedures.
Symbol: M = molybdite
N = neutron
S = silica gel addition
Digit represents pressure in ×1000lbs units (conversion factor, 1000lbs units to MPa =22).

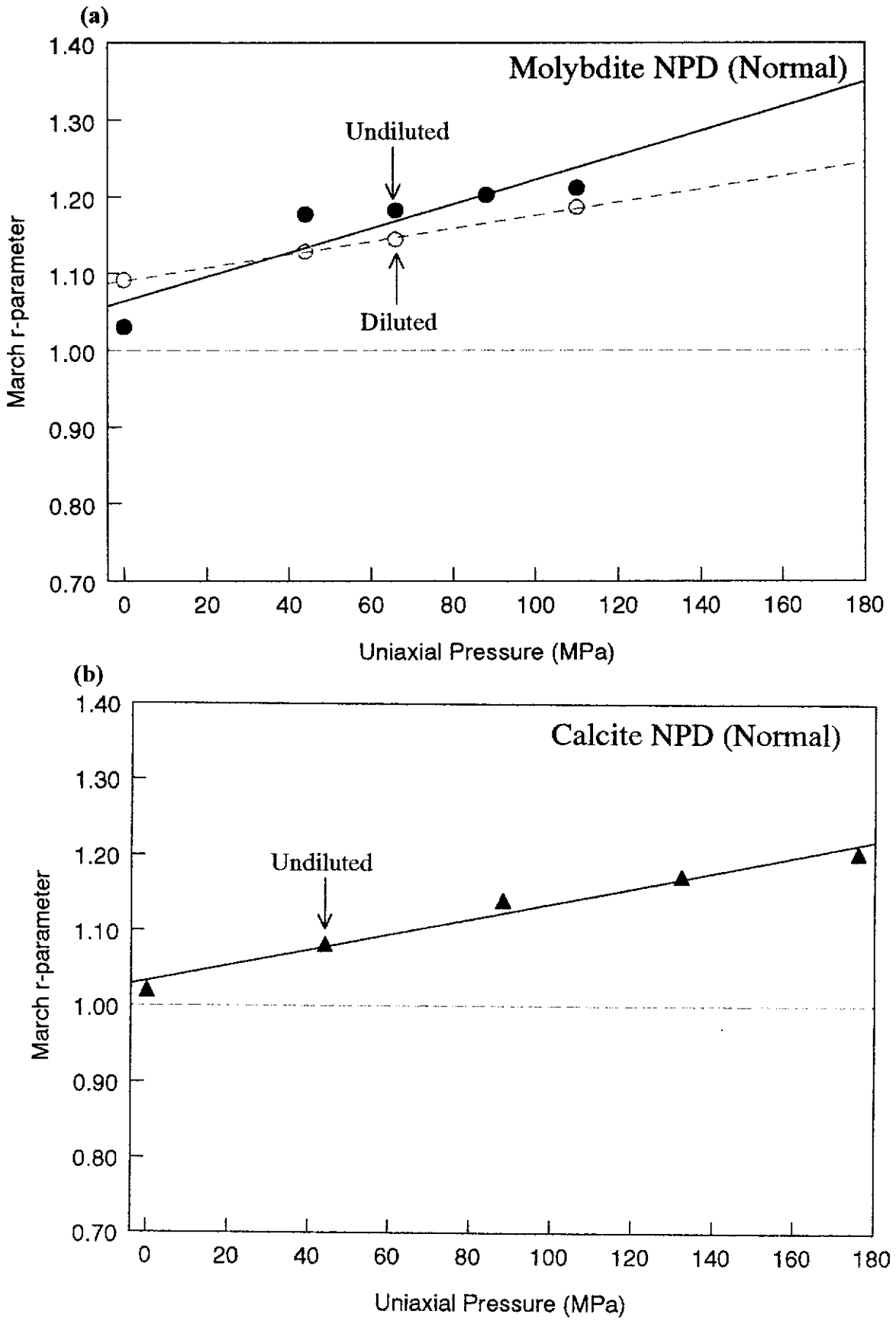

Figure 4.9. Variation in March PO parameter with uniaxial pressure for NPD (a) molybdite and (b) calcite. Linear regressions shown for the three suites of samples.

The refinement results for the "normal" mounts are given in Table (4.4) and the plot of r-versus-pressure is given in Figure (4.9). It is seen from the table that the values for R_{WP} and R_B for the pressed materials all decreased substantially when PO was included in the model. However, the GOFI figures-of-merit still substantially exceeded the 'expected' value 1.00 when the March model was applied to the data for the pressed samples. In contrast with the results for the molybdite XRPD data, the GOFI does not increase markedly as the pressure increases. Therefore it might be concluded that the March model provides better PO modelling for the XRPD data.

It is interesting to note that the unpressed sample gave results consistent with the material being randomly oriented which contrasts with the strong PO indicated by the XRPD data for side-drifting.

Figure (4.10) shows the difference plots for randomly-oriented specimen (MON) and the most heavily pressed powder (M5N) for the normal mount data. The agreement between measured and calculated patterns improved substantially when the March model was employed. Moreover, the GOFI ranges from 2.1 to 5.3 which are approximately 0.23 and 0.31 times the corresponding XRPD GOFI.

The expected linear form of the r-versus-pressure plot has been tested [see Figure (4.9)] against a linear regression fit. It is not clear from the scatter of points in the plot that the relation is linear. The gradient of the regression plot [see Figure (4.9)] is close to that for the XRPD analysis but reversed in sign [see Figure (4.2)].

Table (4.5) shows the PO refinement results for the transverse mounts, *i.e.* with the sample rotation axis parallel to the Debye-Scherrer instrument rotation axis. The r values show a clear linear decrease with pressure as expected [see Figure (4.11)] which compares the r-pressure relationships for the normal and transverse mounts). As for the normal mount results, the GOFI values indicate that the quality of the March model refinements did not deteriorate with the application of pressure. Interpretation of the results, in terms of the reversal in gradient of the r-pressure plot according to mounting mode, is addressed in Section (4.6).

As for the molybdite XRPD data, results are also presented for a suite of specimens diluted with 50% by weight silica gel [see Table (4.4), Figure (4.9) and Figure (4.12)]. The results show that dilution had a small, but discernible, influence

(a) Molybdite non-pressed sample - M0N (NPD)

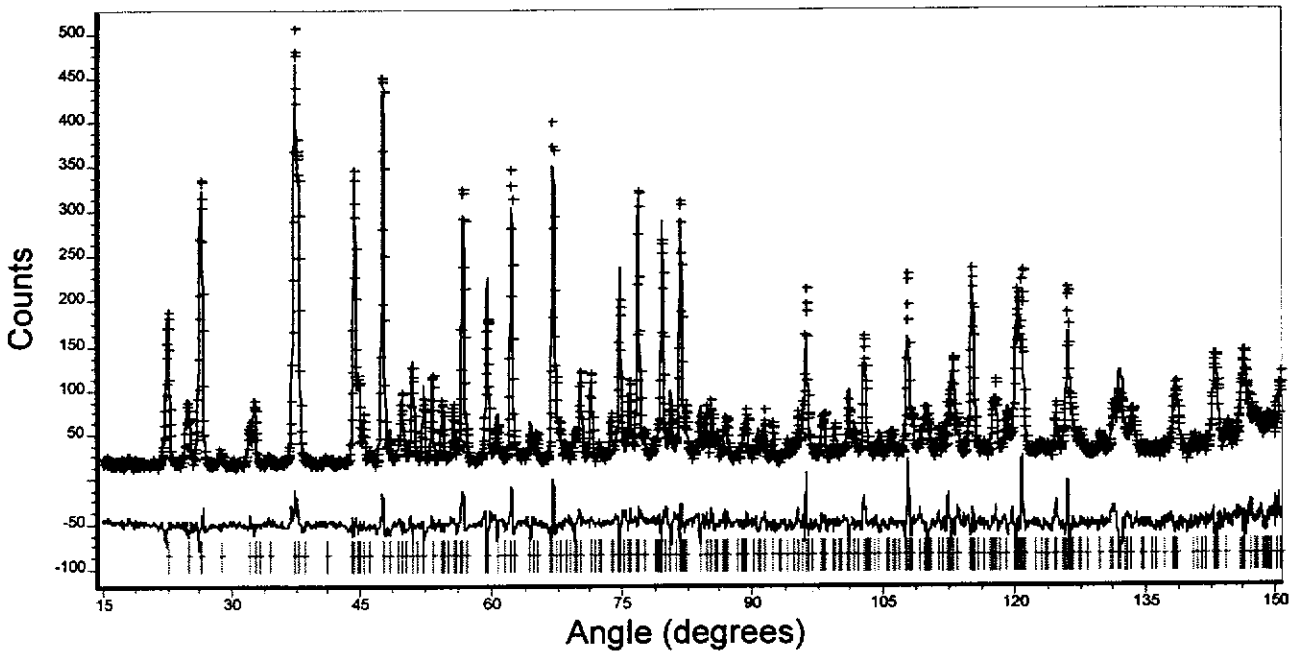

(b) Molybdite sample pressed at 110MPa - M5N (NPD)

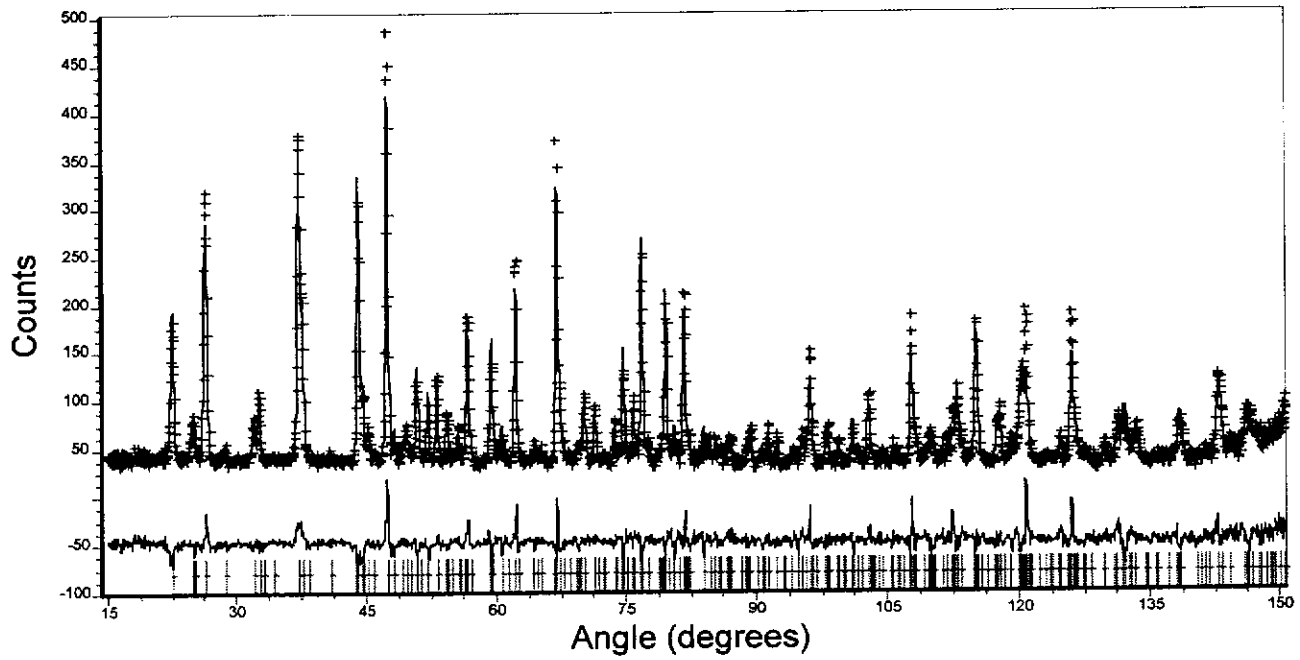

Figure 4.10. Agreement between calculated and measured NPD patterns for selected molybdite powder specimens following Rietveld refinement with the March model - normal mounts. The observed data are indicated by plus signs and the calculated profile is the continuous line in the same field. The set of vertical lines below the profiles represent the positions of all possible Bragg reflections. The lower plot is the difference between the measured and calculated patterns on the same scale as the measured and calculated patterns.

Table 4.5

NPD Rietveld Refinement Results for Molybdite Powders - Cylindrical Specimens Mounted *normal* to Instrument Rotation Axis

(Transverse Mounts)

- Assumed direction of PO, <010> (Kihlborg, 1963).
- Values for random orientation (r = 1.000) model given in parentheses.

Pressure (MPa)	Sample Code[18]	Figures-of-Merit					
		R_{EXP}	R_P	R_{WP}	R_B	GOFI	March r-Parameter
44	M2N	5.27	7.19 (7.40)	8.86 (9.12)	3.77 (4.49)	2.83 (3.00)	0.959(5)
66	M3N	5.92	8.30 (8.65)	9.95 (10.34)	4.29 (5.15)	2.83 (3.06)	0.951(3)
88	M4N	5.45	7.70 (8.06)	9.32 (9.71)	3.98 (4.84)	2.92 (3.17)	0.950(3)
110	M5N	5.39	7.37 (7.80)	8.98 (9.51)	3.91 (4.97)	2.78 (3.12)	0.944(2)

[18] See Table (3.3); Sample Pelletising Procedures.
Symbol: M = molybdite
N = neutron
Digit represents pressure in ×1000lbs units (conversion factor, 1000lbs units to MPa =22).

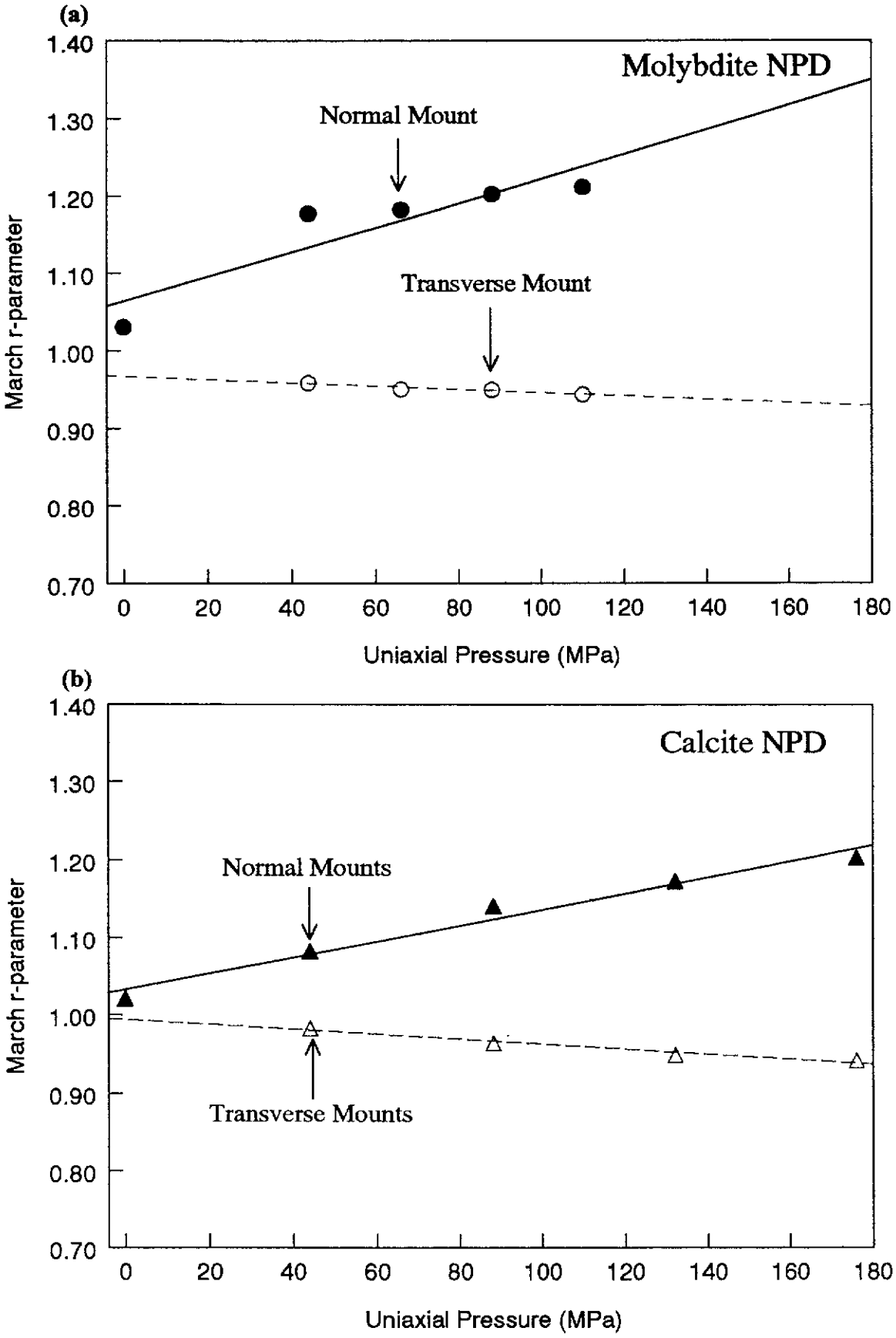

Figure 4.11. Comparison of March PO parameters versus uniaxial pressure for NPD data (a) molybdite and (b) calcite - normal transverse mounts.

(a) NPD / molybdite + 50% silica gel / 66MPa - M3N(S)

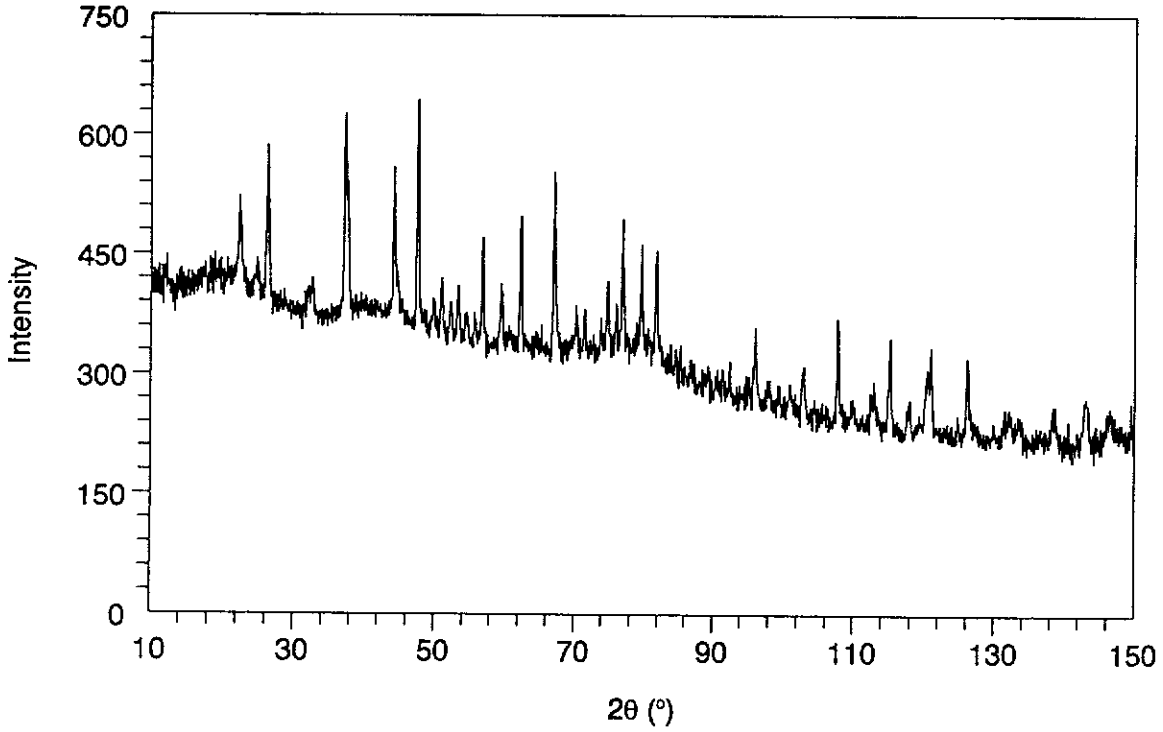

(b) NPD / molybdite 100% / 66MPa - M3N

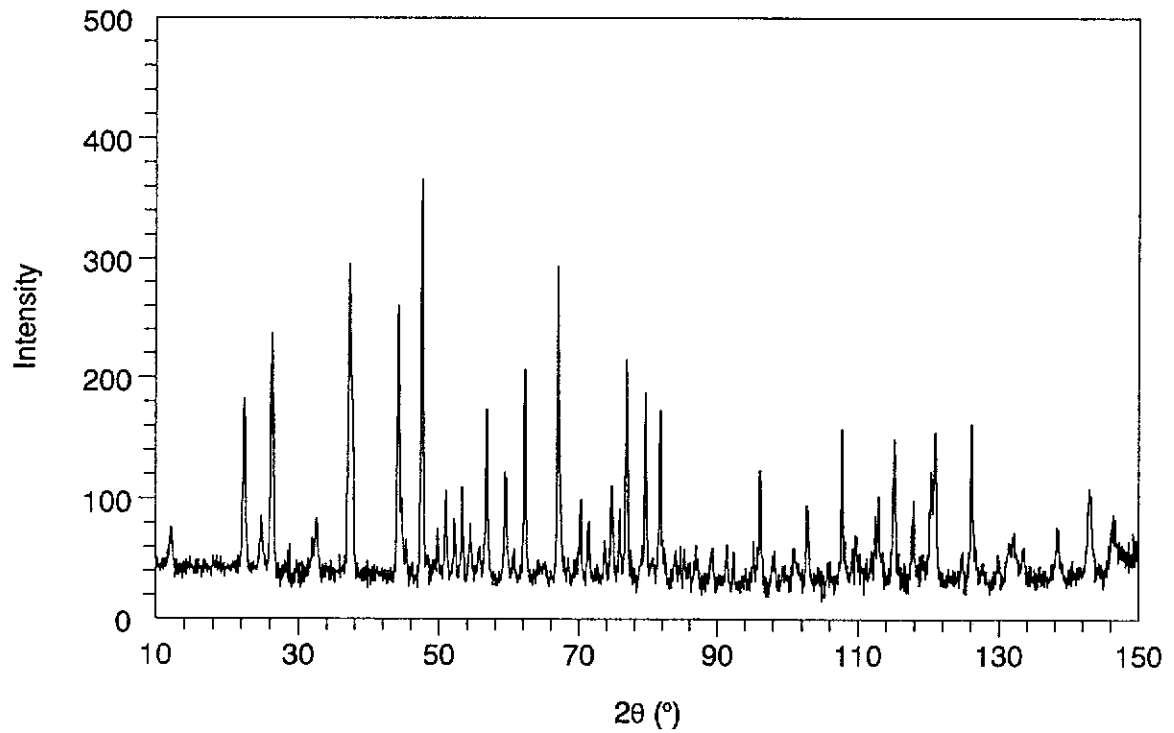

Figure 4.12. Influence of 50% silica gel addition on the molybdite NPD and data - samples M3N(S) non-pressed and M3N pressed at 66MPa.

on the PO for NPD data. It appears that the bulk texture is influenced by dilution, but considerably less than the effect seen with the XRPD data were the interaction between the mineral grains and the walls of the press (i) markedly influences the observed texture, and also (ii) because of the interaction is reduced more readily by dilution with silica gel which diminishes the grain-press interaction.

4.4.2 Calcite Neutron Experiments

The calcite experiments were confined to undiluted powders mainly due to the limited access to the NPD facilities for the project.

Figure (4.13) compares the normal-mount NPD pattern for the unpressed material (C0N) with that for the most heavily-pressed powder (C8N). The differences are evident, but not dramatic, which contrasts starkly with the sensitivity of the XRPD pattern to pressure. As for the molybdite NPD data, the influence of pressing on the bulk texture is less evident for the calcite NPD data than found for the XRPD data.

The results for the unpressed calcite powder in Table (4.6) and Figure (4.9b) show that this powder is essentially random, and that the application of pressure increases the r-parameter linearly from 1.0 as expected from equation (3.26).

Figure (4.14) shows that the agreement between the calculated and measured NPD patterns improved when the March model was used. The GOFI for all samples ranged from (i) 2.2 to 3.3 for the normal mount when <001> was taken to be the direction of PO - see Table (4.6) and (ii) 2.2 to 2.4 for the transverse mount - see Table (4.7).

For the normal mount, the GOFI for the NPD data were 0.7 and 0.4 lower than both for the lowest and highest GOFI of the XRPD data when the PO direction of the latter was taken to be <104>. It is interesting to note here that the PO direction of the near-surface derived from the XRPD data is different from that for the bulk sample obtained from NPD data. This observation is possibly an additional reason why the plots of r-versus-pressure are (i) linear and positive in slope for the NPD data and (ii) non-linear and negative of slope for XRPD data.

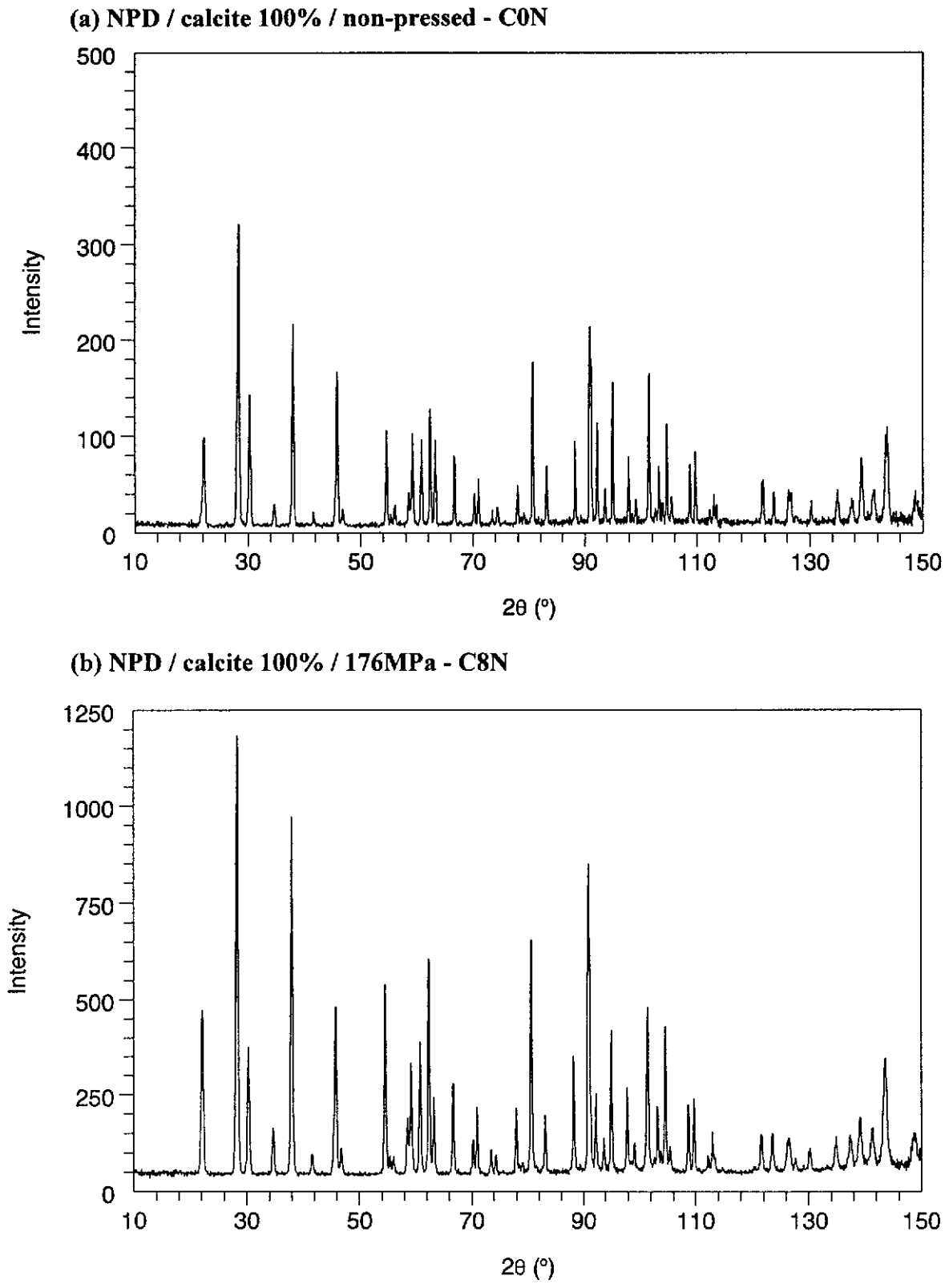

Figure 4.13. Comparison of calcite NPD patterns for (a) non-pressed powder and (b) powder pressed at 176MPa - normal mounts.

Table 4.6

NPD Rietveld Refinement Results for Calcite Powders - Cylindrical Specimens Mounted *parallel* to Instrument Rotation Axis (Normal Mounts).

- Data for specimens given in first and second lines for each pressure obtained when assumed directions of PO were <001> and <104>, respectively.
- Values for random orientation model (r = 1.000) given in the second line.

Pressure (MPa)	Sample Code[19]	PO direction	Figures-of-Merit					
			R_{EXP}	R_P	R_{WP}	R_B	GOFI	March Parameter r
0	C0N	<001>	9.28	11.10	13.59	4.02	2.15	1.021(3)
		<104>		11.10	13.61	4.12	2.15	1.070(1)
				(11.24)	(13.72)	(4.49)	(2.19)	
44	C2N	<001>	4.47	6.74	8.09	4.01	3.28	1.082(2)
		<104>		7.51	8.94	5.93	4.01	1.189(7)
				(8.60)	(10.38)	(8.04)	(5.39)	
88	C4N	<001>	4.47	6.11	7.22	3.50	2.61	1.141(2)
		<104>		7.80	9.35	7.78	4.38	1.276(8)
				(9.19)	(11.68)	(10.81)	(6.83)	
132	C6N	<001>	5.77	7.55	9.00	3.37	2.43	1.173(3)
		<104>		10.16	11.97	9.40	4.31	1.320(9)
				(12.03)	(14.95)	(13.11)	(6.71)	
176	C8N	<001>	4.35	6.58	7.91	3.19	3.30	1.203(2)
		<104>		10.11	12.25	10.72	7.92	1.357(9)
				(12.29)	(15.96)	(14.50)	(13.45)	

[19] See Table (3.3); Sample Pelletising Procedures.
Symbol: C = calcite
N = neutron
Digit represents pressure in ×1000lbs units (conversion factor, 1000lbs units to MPa =22).

(a) Calcite non-pressed sample - C0N (NPD)

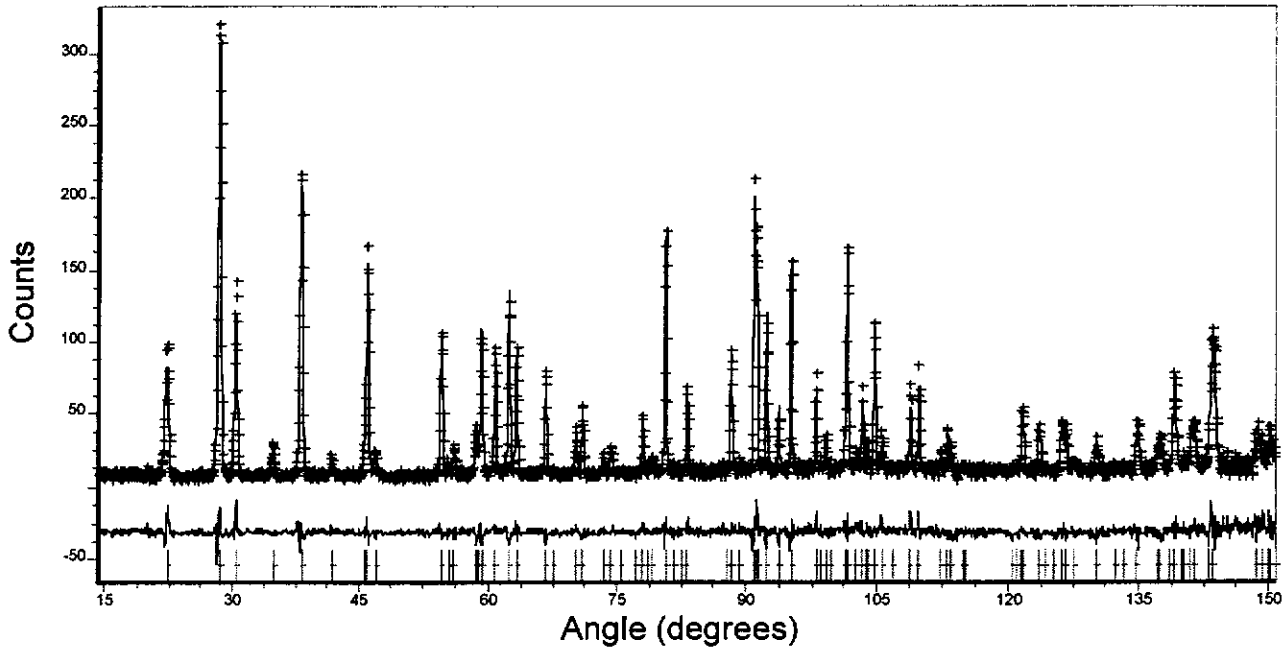

(b) Calcite sample pressed at 176MPa - C8N (NPD)

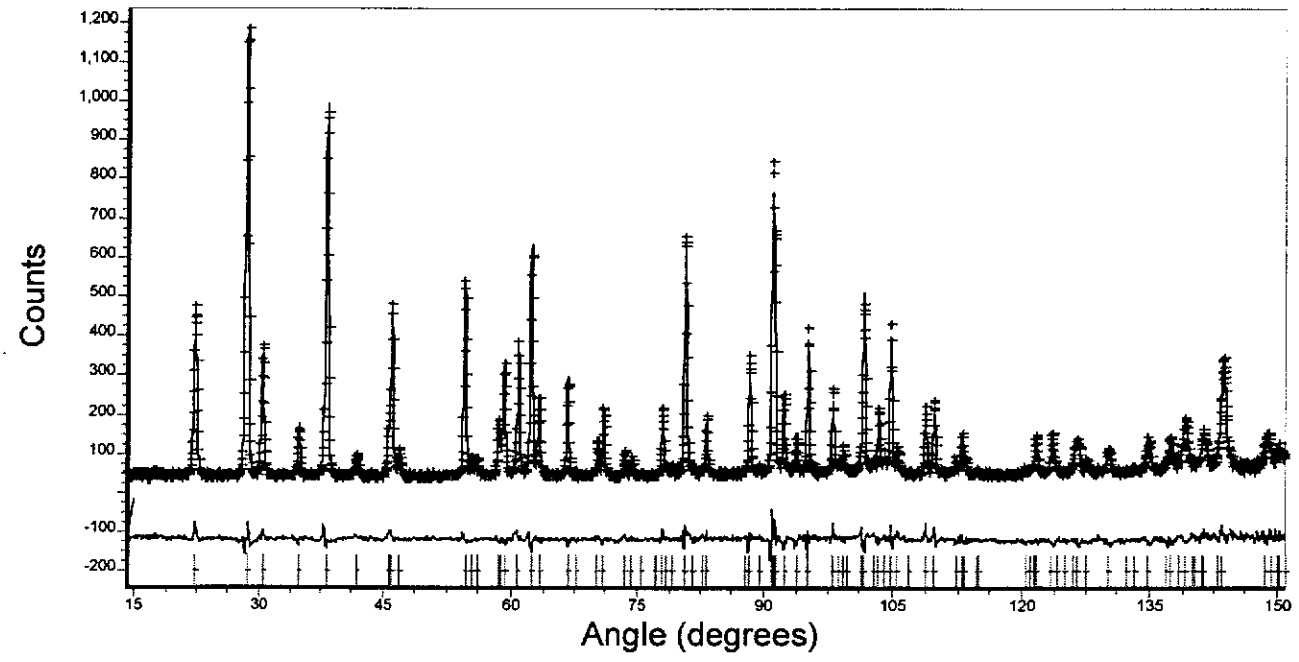

Figure 4.14. Agreement between calculated and measured NPD patterns for selected calcite powder specimens following Rietveld refinement with the March model - normal mount. The observed data are indicated by plus signs and the calculated profile is the continuous line in the same field. The set of vertical lines below the profiles represent the positions of all possible Bragg reflections. The lower plot is the difference between the measured and calculated patterns on the same scale as the measured and calculated patterns.

Table 4.7

NPD Rietveld Refinement Results for Calcite Powders - Cylindrical Specimens Mounted *normal* to Instrument Rotation Axis (Transverse Mount).

- Data for specimens given in first and second lines for each pressure obtained when assumed directions of PO were <001> and <104>, respectively.
- Values for random orientation model (r = 1.000) given in the second line.

Pressure (MPa)	Sample Code[20]	PO direction	Figures-of-Merit					
			R_{EXP}	R_P	R_{WP}	R_B	GOFI	March Parameter r
44	C2N	<001>	5.75	7.45	8.93	4.32	2.41	0.983(2)
		<104>		7.46	8.95	4.40	2.42	0.948(8)
				(7.53)	(9.04)	(4.40)	(2.47)	
88	C4N	<001>	5.34	6.72	7.93	3.92	2.21	0.964(2)
		<104>		6.83	8.06	4.13	2.28	0.913(7)
				(7.04)	(8.32)	(4.59)	(2.43)	
132	C6N	<001>	6.22	7.89	9.66	3.47	2.41	0.949(2)
		<104>		8.29	9.99	4.42	2.58	0.883(7)
				(8.72)	(10.57)	(5.36)	(2.89)	
176	C8N	<001>	5.43	6.85	8.25	3.37	2.31	0.942(2)
		<104>		7.23	8.68	4.31	2.55	0.874(6)
				(7.76)	(9.33)	(5.40)	(2.95)	

[20] See Table (3.3); Sample Pelletising Procedures.
Symbol: C = calcite
N = neutron
Digit represents pressure in ×1000lbs units (conversion factor, 1000lbs units to MPa =22).

It is evident from Tables (4.2), (4.3), (4.4), (4.5), (4.6) and (4.7) that the GOFI figures-of-merit for all NPD data of molybdite and calcite powders are closer to the ideal value 1.0 for a correct model than the figures-of-merit for XRPD data. The agreement indices for calcite indicate that the March model was more effective for the NPD data. The inferior agreement between the calculated and measured XRPD data sets for calcite is discussed in Section (4.6).

4.5 Bulk Modulus Measurements

The procedure used to measure bulk modulus is described in Section (3.6). These measurements were performed to assess the quality of the bulk moduli derived from Rietveld analysis.

Figures 4.15(a) and (b) show plots of powder cylinder length L versus uniaxial pressure for molybdite and calcite powders. Equation (3.22) was used to estimate the bulk modulus for each powders - see Table (4.8) for results.

Interpretation of the results in Table (4.8) requires some preliminary comment on the assumption underpinning the methods used to determine bulk moduli, (i) directly from compression measurements and (ii) from plots of Rietveld *r* parameter versus uniaxial pressure. For both methods it was assumed that the pressure-volume relationship is linear for the samples examined, whereas the powder volume is expected to plateau as the pressure increases, signifying that the porosity has become minimal.

It must be also emphasised that the bulk moduli values estimated in this study apply to powders, whereas bulk moduli values in the literature mainly refer to single crystals or densified polycrystalline solids such as sintered ceramics and metals - for example Chang and Ahmad (1982) quote a value of 7.3×10^4 MPa for calcite, measured for single crystal material, which is two orders of magnitude greater than the results reported here for powders. The true bulk moduli for such solids relate to the resistance of the unit cell to compression, whereas powder values reported relate to the extent to which powders with substantial porosity may be densified.

(a)

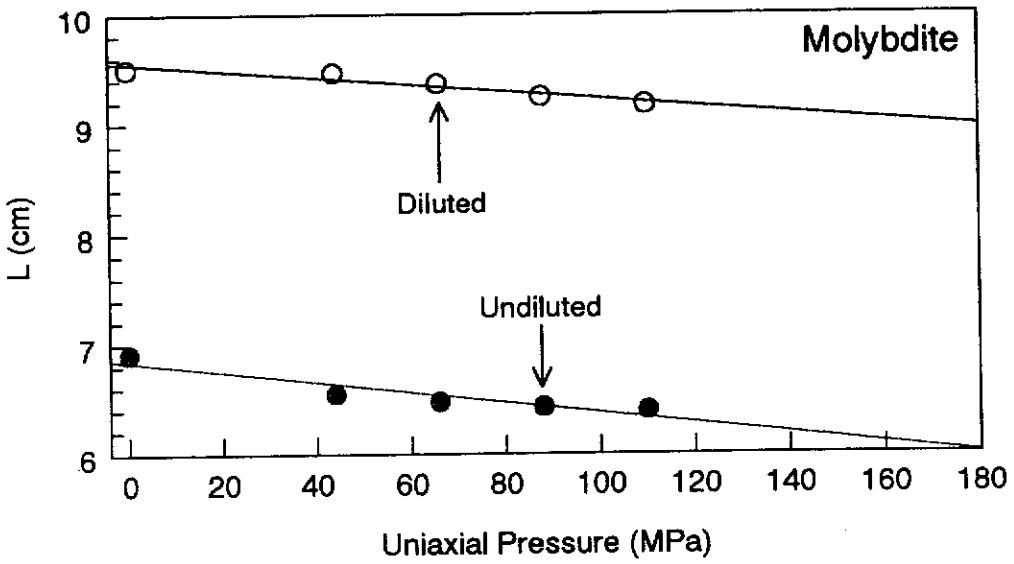

(b)

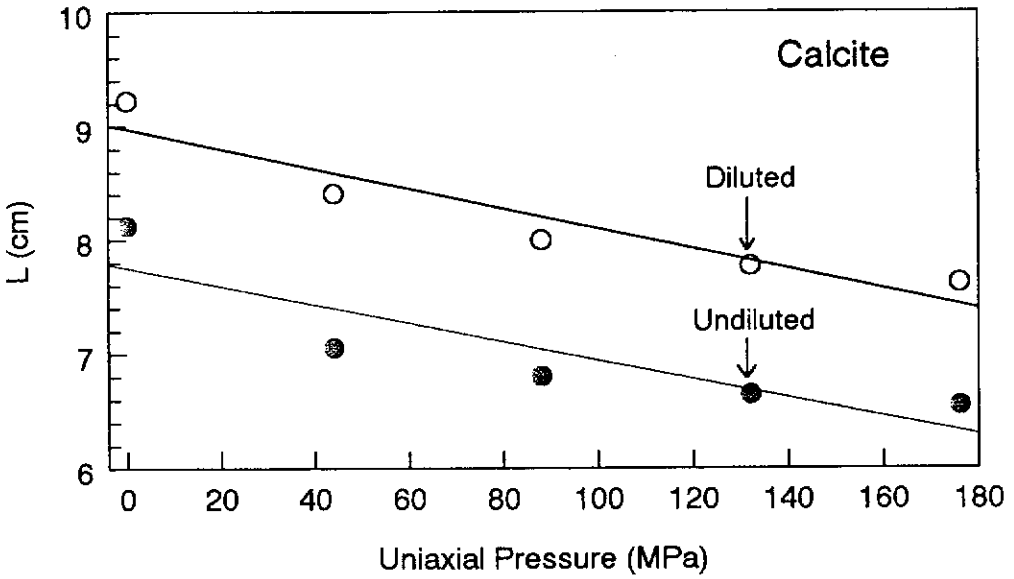

Figure 4.15 Variation in L with uniaxial pressure for (a) molybdite and (b) calcite powders. Linear regressions shown for each molybdite and calcite suite.

Table 4.8

Comparison Between Bulk Modulus (B) Values Obtained From Direct Measurement and Derived From Rietveld Analysis with the March Model

Material	Pressure values, MPa	Bulk modulus, (measured), MPa	Bulk modulus (Rietveld), MPa	
			NPD	XRPD
Molybdite				
Undiluted	All values	1500 ± 50	630 ± 21	480 ± 14
	44→110	3040 ± 50	1801 ± 141	552 ± 40
Diluted	All values	3000 ± 200	1160 ± 8	660 ± 42
Calcite				
Undiluted	All values	1000 ± 100	970 ± 10	130 ± 27
	0,44	330	721	289
	44→176	2100 ± 50	1136 ± 45	707 ± 60
Diluted	All values	1050 ± 50	not measured	450 ± 26
	0,44	500		571
	44→176	1550 ± 50		824 ± 11

The clear difference between bulk and near-surface texture, observed from the NPD and XRPD Rietveld results for calcite, suggest that the direct measurement results might be expected to conform more closely with the NPD bulk modulus values than with those from XRPD.

The plots in Figure (4.15) and the estimated bulk moduli in Table (4.8) indicate the following :

- The plots for diluted molybdite in Figures (4.2) and (4.15) are close to linear, and the bulk modulus measured directly is ×3 that for the Rietveld NPD analysis.
- The two plots for undiluted molybdite are also near-linear, and the bulk modulus measured directly again exceeds the Rietveld NPD results.
- The plots for calcite in Figure (4.15) show clear indications of 'plateauing' as the pressure increases, *i.e.* non-linearity in the pressure-volume relationship. A similar plateauing effect is seen for the undiluted calcite Rietveld plots in Figure (4.2), although the plateauing is less evident for the diluted calcite Rietveld results.

- The molybdite bulk moduli from the NPD Rietveld plots, while comparable with the 'directly measured' values, are both approximately 60% of the corresponding measured value, indicating some possible deficiency in the March formalism.
- The XRPD bulk modulus estimates are systematically less than the NPD values, perhaps indicating that the near-surface nature of the assessment for XRPD provides a texture fundamentally different from that of the bulk.
- By contrast, the calcite NPD results for undiluted powder agree closely with the directly measured value.

4.6 Discussion

Adequacy of the March Model for PO Analysis

Figure (4.16) shows the variation in GOFI figure-of-merit with pressure. When the March model was employed in the Rietveld refinements, the GOFI for the undiluted molybdite (100%) XRPD data and that diluted with 50% silica gel ranged from 8.1→17.4 and, 5.1→9.1, respectively. The corresponding factors for the molybdite NPD data, 2.1→5.3 and 2.5→5.3, were substantially lower than those for the XRPD data. It is evident from these results that the quality of the Rietveld 'fit' diminishes progressively as the level of PO increases [see March r-parameter values in Tables (4.2), (4.3), (4.5) and (4.7)]. The lower values obtained for the NPD refinements may be attributed to the generally lower PO levels observed for the bulk material. These comments are supported by the plots of GOFI-versus-r in Figure (4.17). As for molybdite, the plots of GOFI-versus-pressure and GOFI-versus-r [Figures (4.16) and (4.17)] results in the same conclusions.

The results in Figure (4.17) clearly show the increasing inadequacy of the March model as the PO becomes more pronounced.

Pressure-PO Relationships

The results in Section (4.5) [Figure (4.15) and Table (4.8)] have shown that the March model provides bulk material results which point to inadequacies in the Rietveld model.

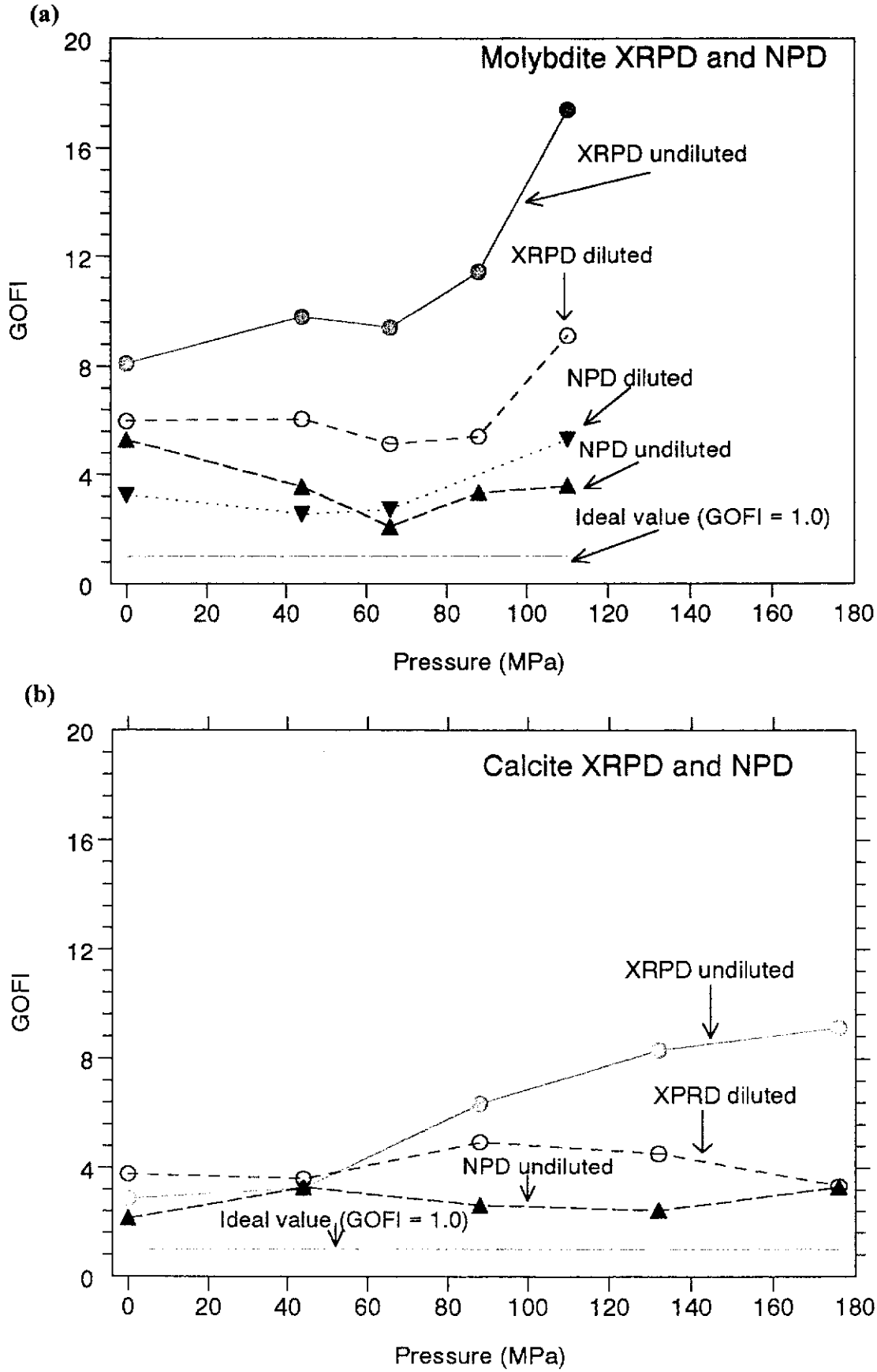

Figure 4.16. Variation in GOFI figures-of-merit with uniaxial pressure for XRPD and NPD data of (a) molybdite and (b) calcite.

(a)

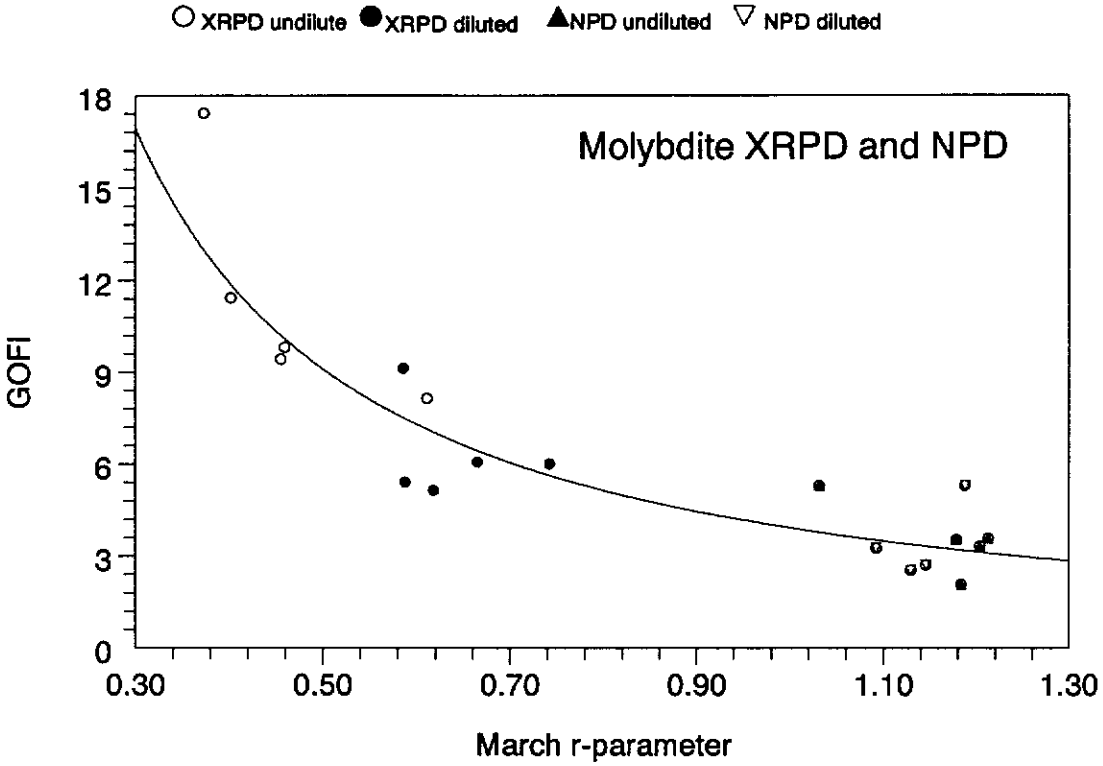

(b)

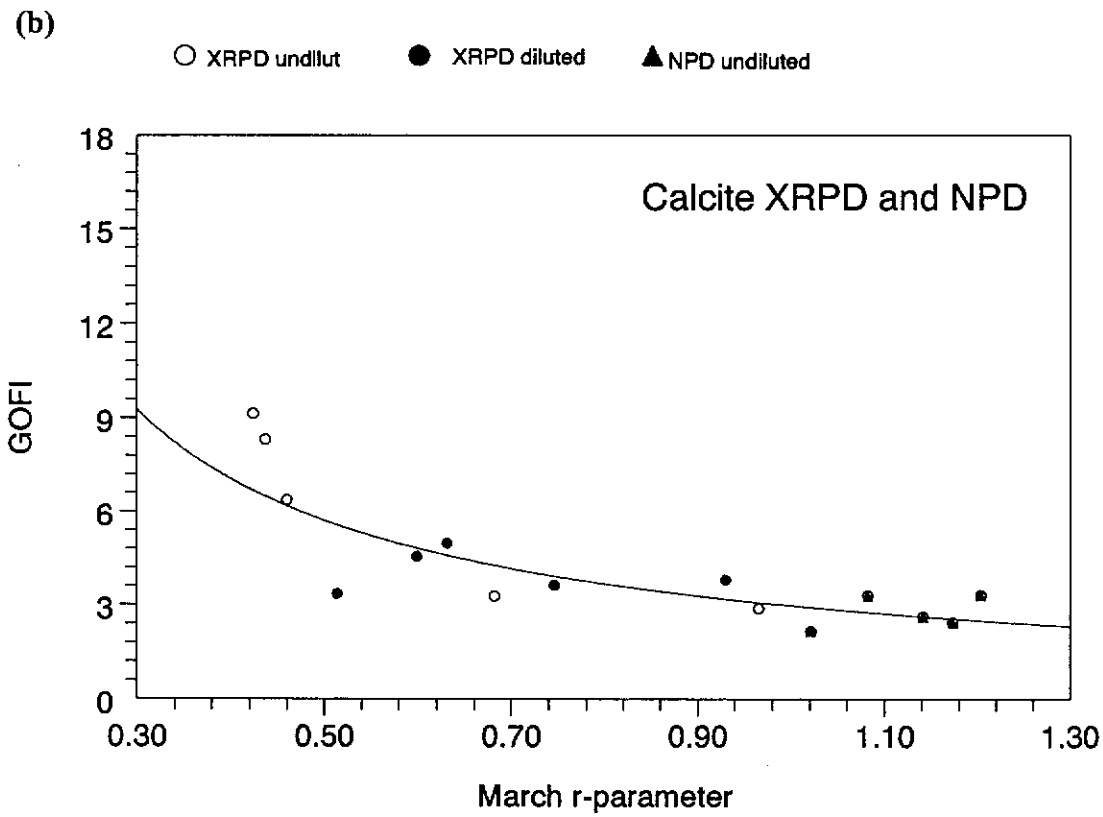

Figure 4.17. Variation in GOFI figures-of-merit with March r-parameter for XRPD and NPD data of (a) molybdite and (b) calcite.

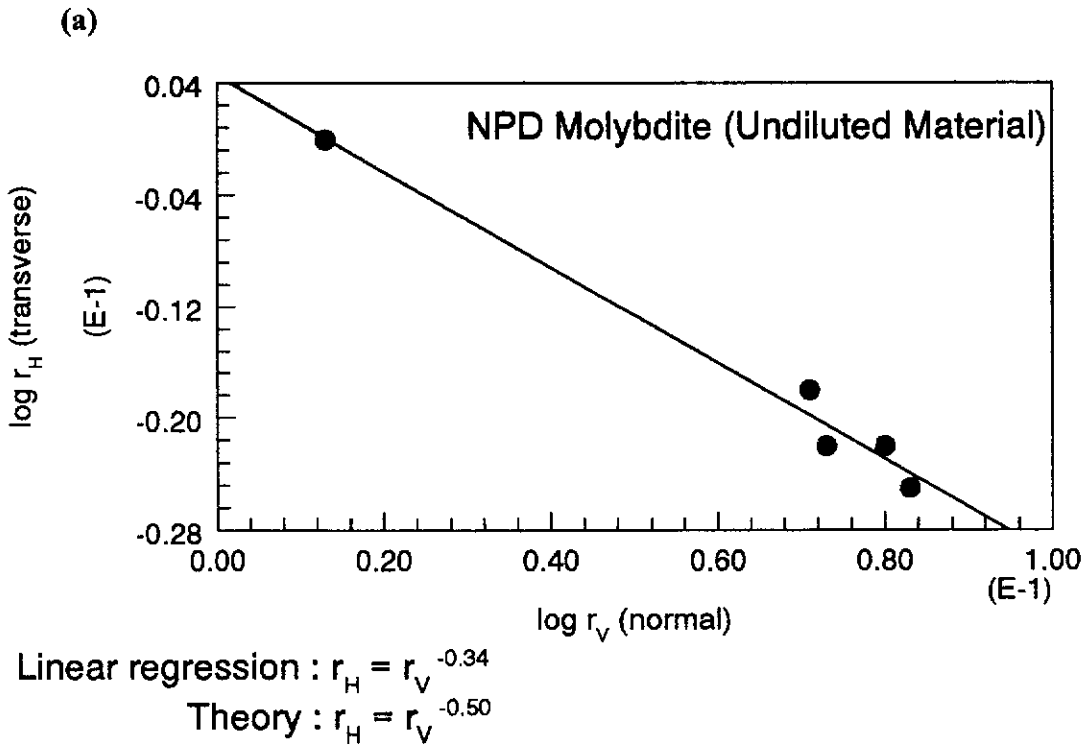

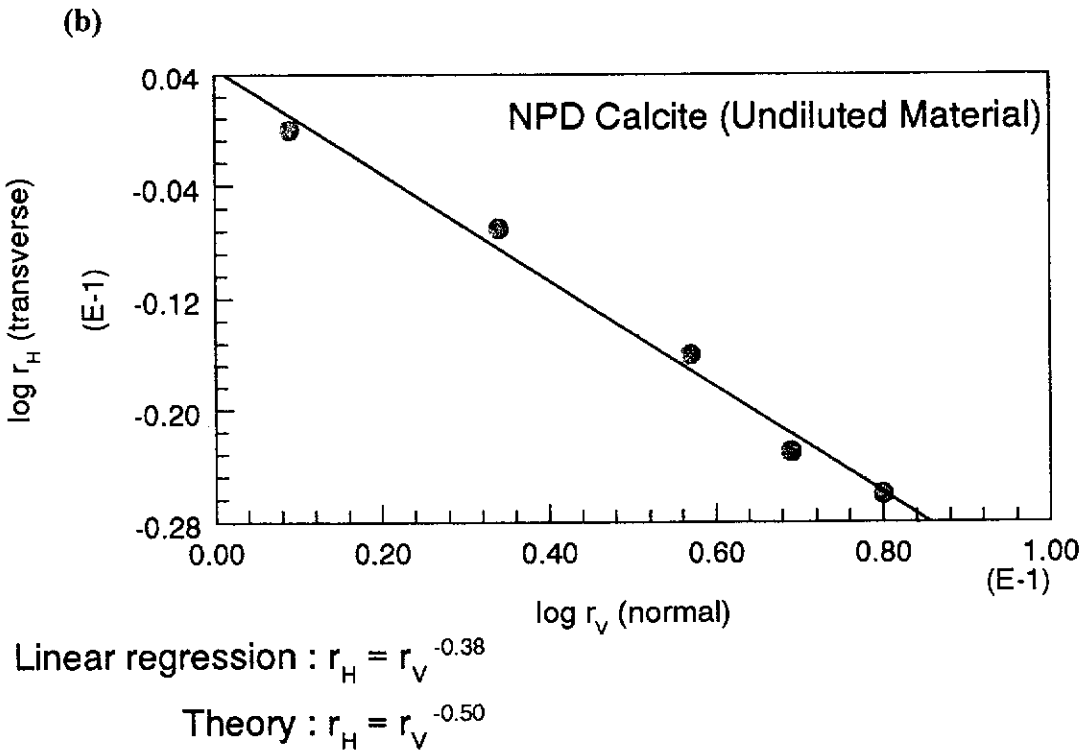

Figure 4.18. March plots of log r_H(transverse)-versus-r_V(normal) derived from Rietveld analyses for (a) molybdite and (b) calcite. The linear regression lines are shown.

Figure (4.18) gives additional evaluations of the NPD March model results in Tables (4.4), (4.5), (4.6) and (4.7). The log-log plots test the actual form of the r_H-r_V relationship which was proposed in Section (3.5) [equation (3.29)] to be of the form,

$$r_H = r_V^{-1/2}$$

according to the March model. Both log-log plots show excellent linearity. However, the actual exponent values are 0.34 and 0.36, rather than 0.50, which may indicate a relationship,

$$r_H \approx r_V^{-1/3}$$

Again, this finding points to a deficiency in the model.

Texture Differences for the Bulk and Near-Surface Material

When <104> was taken to be the PO direction for the highly-oriented calcite specimens, the GOFI for the XRPD data gave better results than <001> which appeared to be most appropriate direction for the NPD.

CHAPTER 5

TEXTURE ANALYSIS FROM POLE-FIGURE MEASUREMENTS

5.1 Introduction

The application of Rietveld texture modelling with Bragg-Brentano data, with molybdite and calcite powders, was presented in Chapter 4. This chapter presents the results of directly-measured texture distributions using diffractometers fitted with Eulerian cradle attachments whereby the specimen may be tilted relative to the plane defined by the incident beams. The purpose of these texture diffractometer assessments was to examine the texture distributions in more detail than is possible by Rietveld analysis, with particular reference to assessing the extent of agreement between the two approaches for texture characterisation.

Figure (5.1) depicts, in diffractometer space, the linkages between the PDD as sampled with Bragg-Brentano and texture diffractometry geometries. The following equivalences are noted for the cylindrically-symmetric distributions considered in this study -

(i) The Bragg-Brentano PO intensity correction function, $P_H(\alpha)$, for Bragg plane **h** tilted at angle α to the plane of PO **H**, assuming cylindrical symmetry, should be the same as the PDD for **H**, $P_H(\chi)$, which is measured directly by texture diffractometry [see also Figures (1.2a), (3.4), (3.7) and equations (1.9), (1.10), (3.2)]. Therefore, $P_H(\alpha)$ derived using Rietveld analysis of Bragg-Brentano data, should agree with the PDD for **H** measured by texture diffractometry.

(ii) The PDDs from texture diffractometry for Bragg plane **H**, inclined at any general angle α to **H**, should agree with the March-model value of $P_H(\alpha)$ at tilt angle $\chi=0°$ if there are no deficiencies in the latter.

Before presenting the results for molybdite and calcite, details are given of some experimental information too detailed for inclusion in Chapter 3.

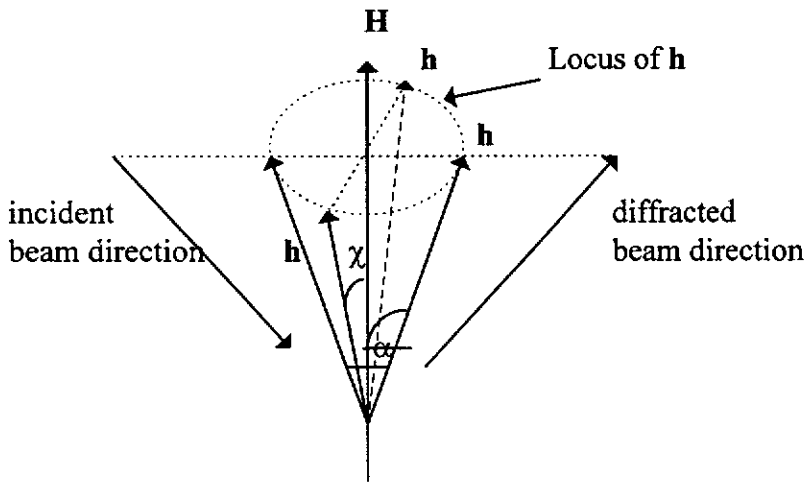

Figure 5.1. Diagram showing the equivalence between (i) angle α between vector **h** (general Bragg plane) and the PO direction **H** in Bragg-Brentano diffractometry and (ii) the **H**-plane tilt angle χ in texture diffractometry.

5.2 X-ray Pole-Figure Measurements

5.2.1 X-ray Data Processing

Background corrections

Figure (5.2) shows the method used to correct the Bragg peak intensities for background intensity. The mean background at the Bragg peak position is given by

$$I_B = 0.5\ [I\{2\theta_{hkl} + \Delta(2\theta)\} + I\{2\theta_{hkl} - \Delta(2\theta)\}] \qquad (5.1)$$

the background being measured on either side of the Bragg peak for off-set angle $\Delta(2\theta)$. For each peak, a suitable off-set was determined by scanning the peak prior to the pole-figure measurements.

Defocussing corrections and normalisation

The procedures employed to apply defocussing corrections to the measured pole-figures were outlined in Section (3.3). Further details are described here and typical results are provided.

An α-Al_2O_3 powder was used to provide pole-figure for instrument defocussing corrections. The corundum was Linde-type 1.0C powder of nominal particle size 1.0μm, marketed by Union Carbide. The specimen was mounted by side-drifting with the aim of obtaining a randomly-oriented specimen. Prior to pole-figure data collection, the mounted powder was analysed by Bragg-Brentano

diffractometry to check the degree of randomisation according to the March r-parameter which would be 1.000 for a randomly oriented powder. Rietveld analysis of the data provided a value r = 0.997(4), indicating a highly random powder.

The α-Al_2O_3 <104> reflection was selected to measure pole-figure data for defocussing corrections, this reflection being chosen as it has the strongest intensity - JCPDS pattern 5-586. The pole-figure is shown in Figure (5.3), and Table (5.1) presents the mean values of background and peak intensities, averaged over ϕ for each χ setting, which were used to construct the defocussing correction function - see Section (3.3) for details of the procedure. A program written by the author, was used to produce the data in Table (5.1). Figure (5.4) shows the defocussing correction function derived in this way.

The ϕ-averaged intensities were normalised over the measured range of χ, according to Section (3.3). As the measurements did not extend beyond $\chi = 60°$, this procedure is described as 'quasi-normalisation'.

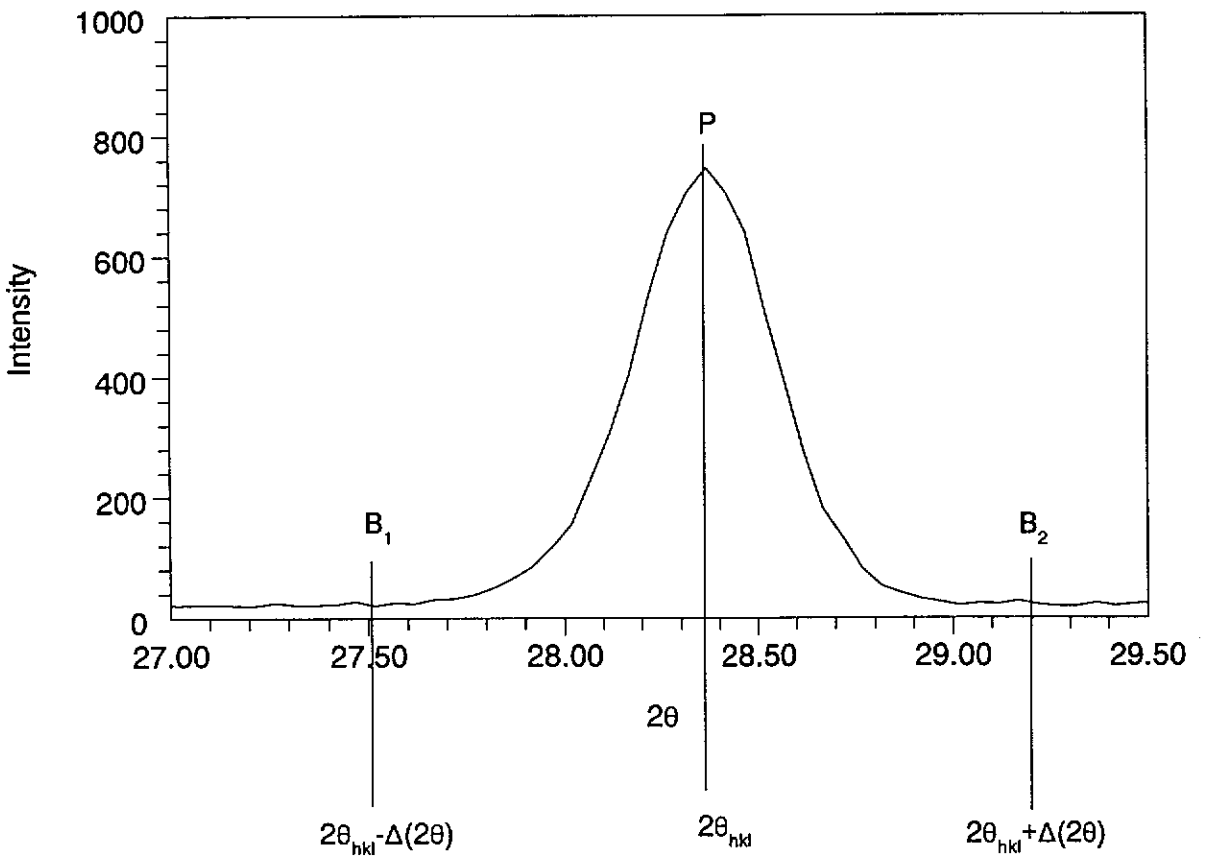

Figure 5.2. Estimation of the background diffraction intensity.

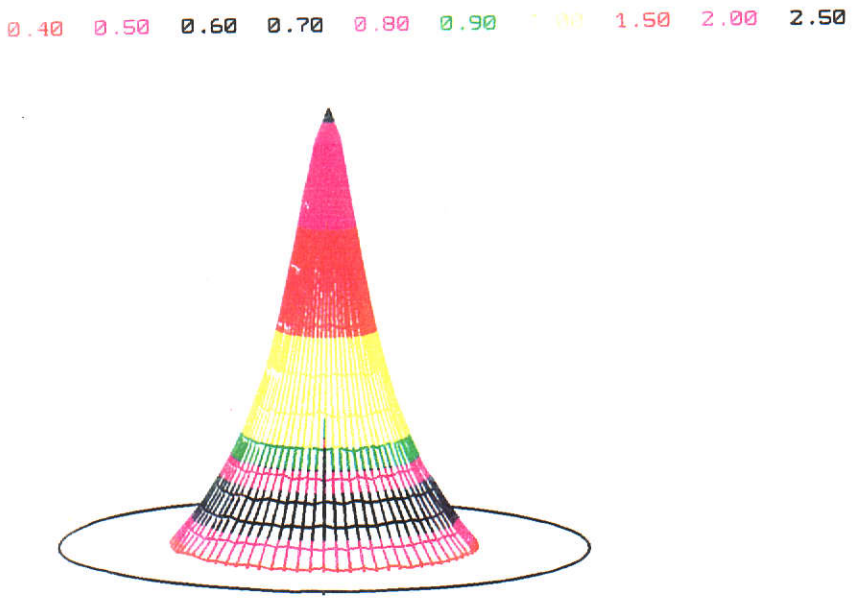

Figure 5.3. Measured α-Al_2O_3 powder <104> XRPD pole-figure, uncorrected for defocussing. The contour levels are in random density units.

Table 5.1
Measurements for X-ray Pole-Figure Defocussing Corrections with α-Al_2O_3 Powder

Measurements made with <104> line. Values for I_χ and B_χ taken over the range $\phi = 0 - 360°$, with step $\Delta\chi = \Delta\phi = 5°$.

χ[21](°)	B_χ[22] ($\times 10^{-3}$) (counts)	I_χ[23] $\times (10^{-3})$ (counts)
0	5.2	59.6
5	5.9	56.1
10	7.0	49.4
15	8.5	42.6
20	10.3	36.1
25	12.2	30.9
30	13.4	26.7
35	13.5	23.3
40	13.0	20.2
45	11.8	17.7
50	10.5	15.3
55	9.1	13.1
60	7.7	11.0

[21] χ = tilt angle
[22] B_χ = mean background intensity
[23] I_χ = mean intensity uncorrected for background

Figure (5.5) shows the 'quasi-normalisation' results for the <110>, <113> and <024> pole-figure data for the same material after normalisation and then correcting for defocussing with Figure (5.4). The results appear to show that the method successfully removed defocussing bias.

The series expansion (SE) analysis procedure described in Section (3.6) was employed to provide an additional assessment of the validity of the α-Al_2O_3 defocussing correction procedure. The measured pole-figures for the <104>, <110>, <113> and <024> lines, after correction for defocussing according to the plot in Figure (5.4), were normalised by SE analysis. Figures (5.6) and (5.7) show the pole-figure results for <104> and <204> by the quasi-normalisation method and after SE analysis.

The pole-density values for the <104> data ranged from 0.996→1.001 for quasi-normalisation (χ=0 to 90°) and, 1.54→0.51 for SE analysis. The corresponding spreads in pole-densities, following SE analysis, were [Figure (5.7)]

- quasi-normalisation χ=0 to 60°

(i) 2.28 → 0.93 for <110>,

(ii) 1.32 → 0.79 for <113> and

(iii) 1.31 → 0.65 for <024>.

- recalculated from (χ=0 to 90°)

(i) 0.23 → 1.61 for <110>,

(ii) 0.81 → 1.73 for <113> and

(iii) 0.76 → 1.29 for <024>.

The figure shows the quality of normalisation and defocussing following SE analysis which is inferior in quality to that shown in Figure (5.5).

5.2.2 Molybdite X-ray Pole-Figures

Figure (5.8) shows 2D and 3D colour representations of the <020> XRPD pole-figures for 2 of the 5 molybdite samples, M0X (side-drifted) and M5X (most heavily pressed), after (i) correction for defocussing with the <104> Al_2O_3 pole-figure data and (ii) normalisation. The complete set of 2D and 3D representations for the directions <020>, <110>, <021>, <111> and <150>, for all samples, are shown

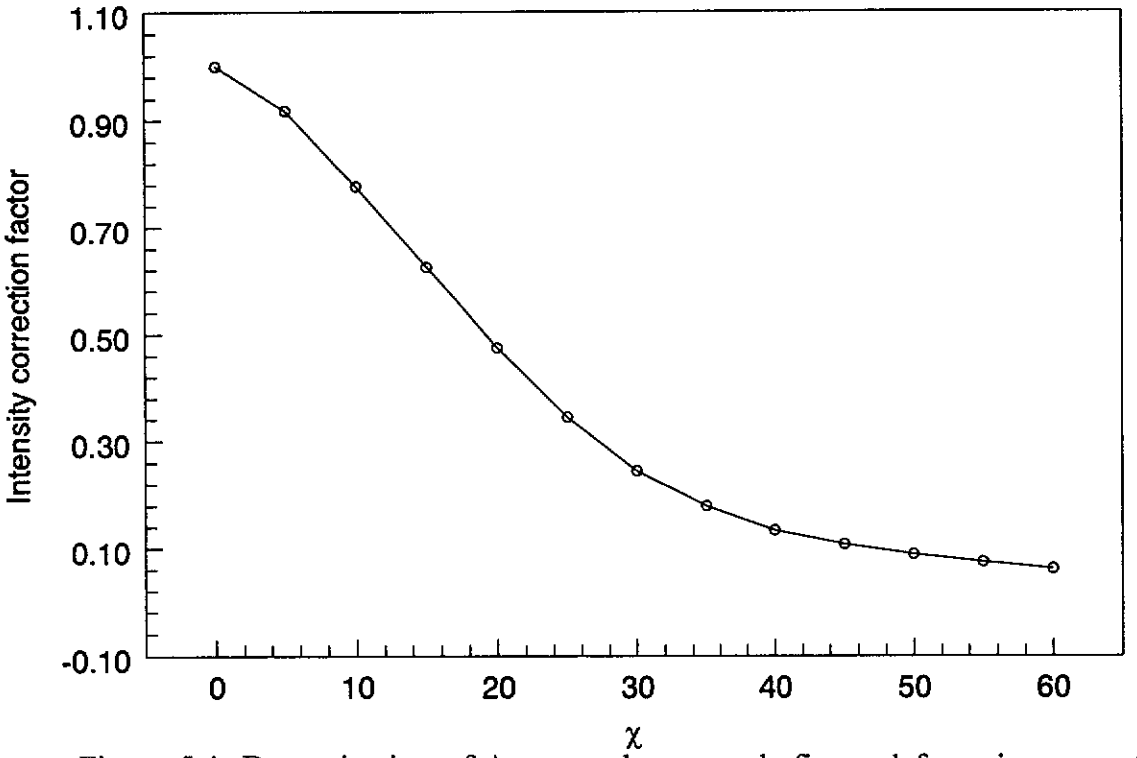

Figure 5.4. Determination of ϕ-averaged x-ray pole-figure defocussing correction function using a side-drifted α-Al_2O_3 powder. Constructed with <104> pole-figure data in Table (5.1).

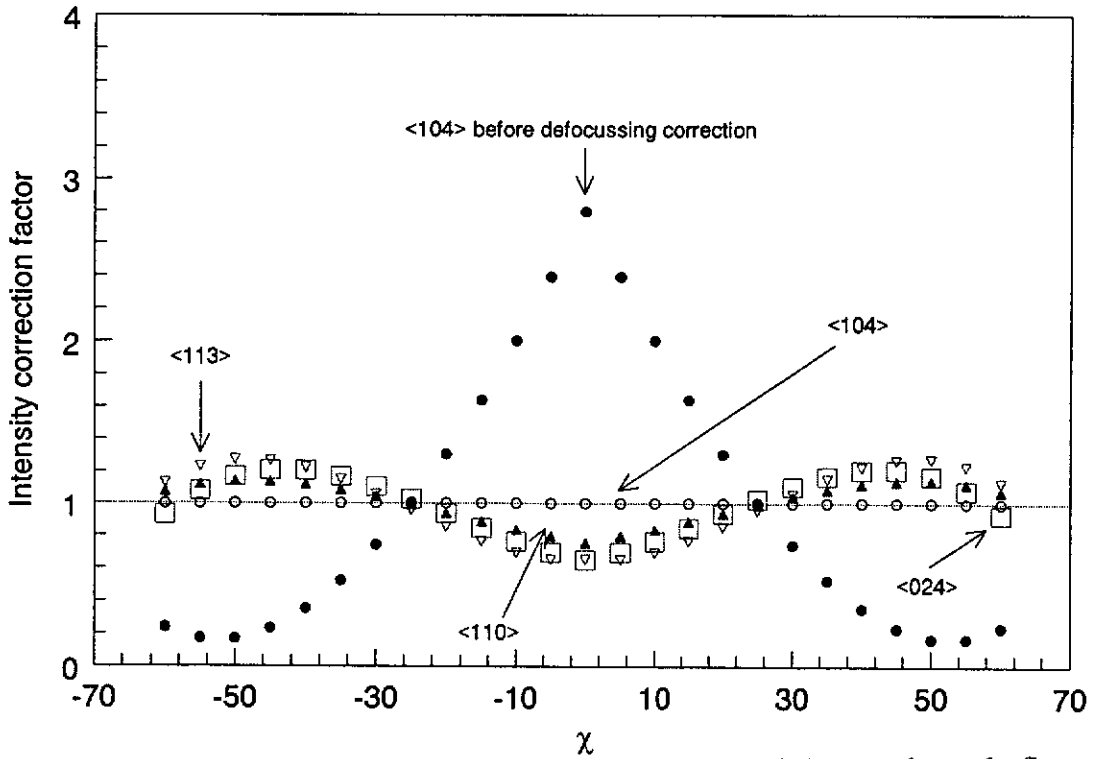

Figure 5.5. Quasi-normalised PDDs for the <104> α-Al_2O_3 powder pole-figure in Figure (5.3) and for the <110>, <113> and <024> pole-figures after correction for defocussing using the function in Figure (5.4).

<104> Pole-figure after correction for defocussing and quasi-normalisation

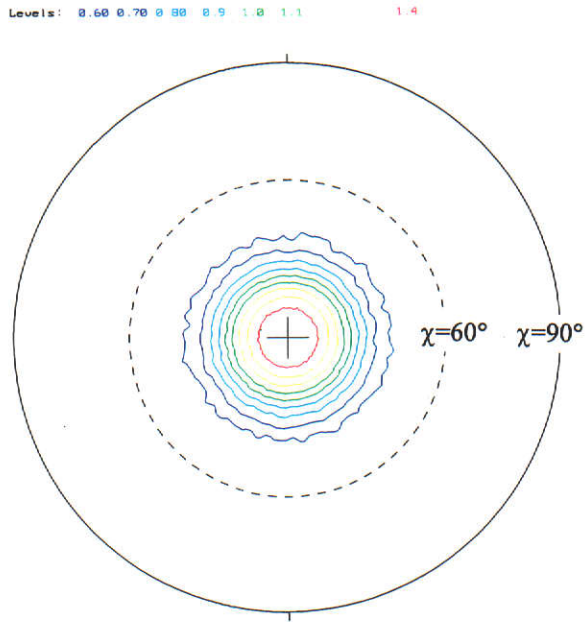

<104> Pole-figure recalculated following SE analysis with data for <104>, <110>, <113> and <024> lines

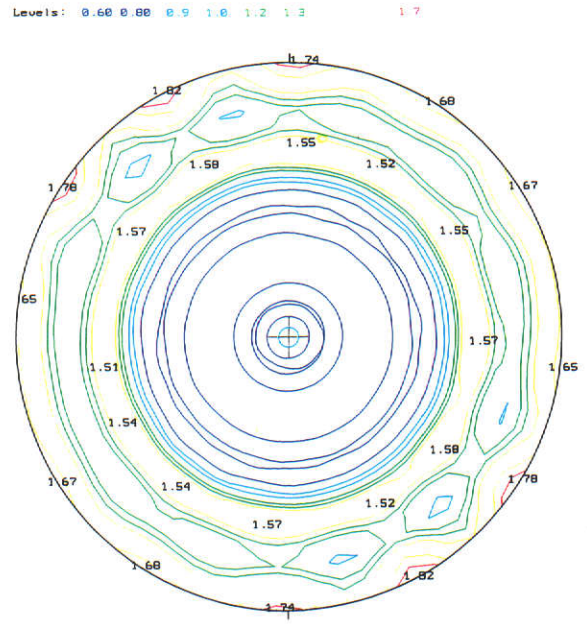

Figure 5.6(a). <104> pole-figure for α-Al_2O_3 side-drifted sample. Above:- pole-figure after defocussing corrections and quasi-normalisation (χ = 0 to 60°). Below:- pole-figure recalculated (χ = 0 to 90°) after SE analysis. The contour levels are in random density (mrd) units.

<024> Pole-figure after correction for defocussing and quasi-normalisation

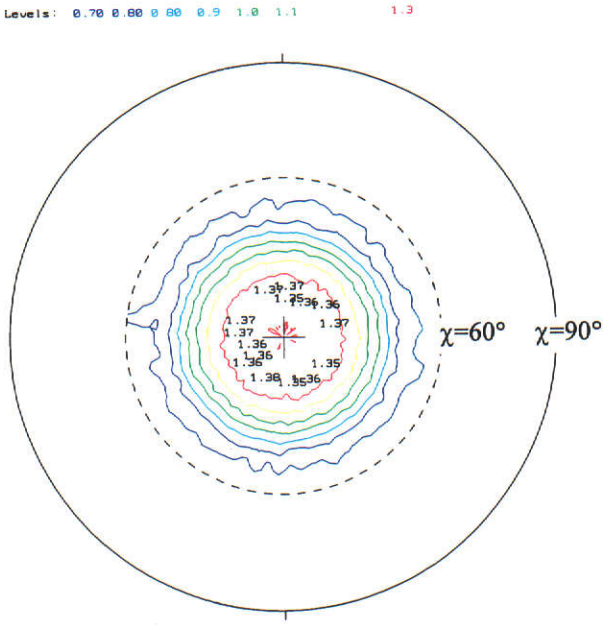

<024> Pole-figure recalculated following SE analysis with data for <104>, <110>, <113> and <024> lines

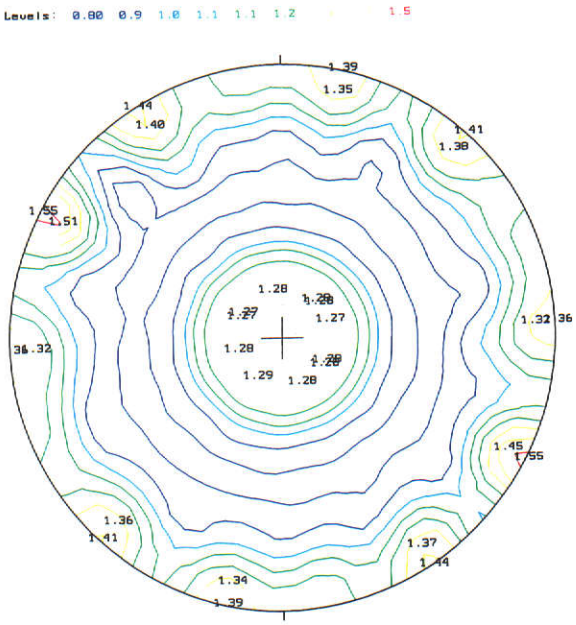

Figure 5.6(b). <024> pole-figure for α-Al_2O_3 side-drifted sample. Above:- pole-figure after defocussing corrections and quasi-normalisation (χ=0 to 60°). Below:- pole-figure recalculated (χ=0 to 90°) after SE analysis. The contour levels are in random density units.

Normalised pole-figures following SE analysis with data for <104>, <110>, <113> and <024> lines

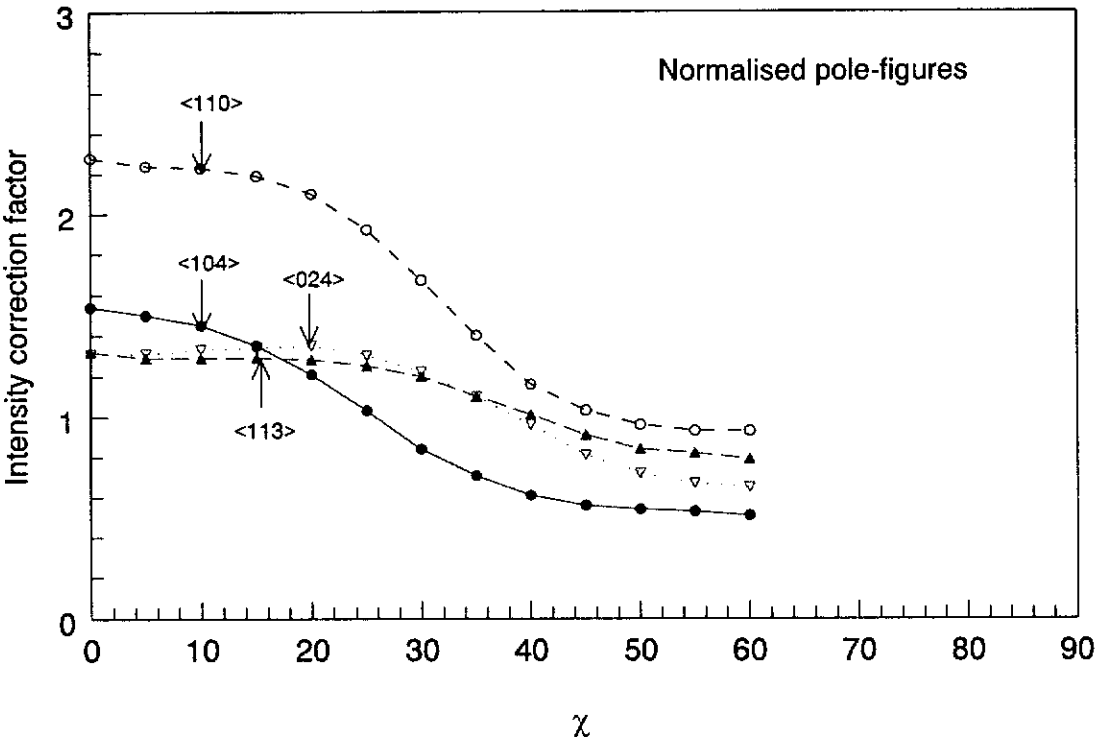

Recalculated pole-figures following SE analysis with data for <104>, <110>, <113> and <024> lines

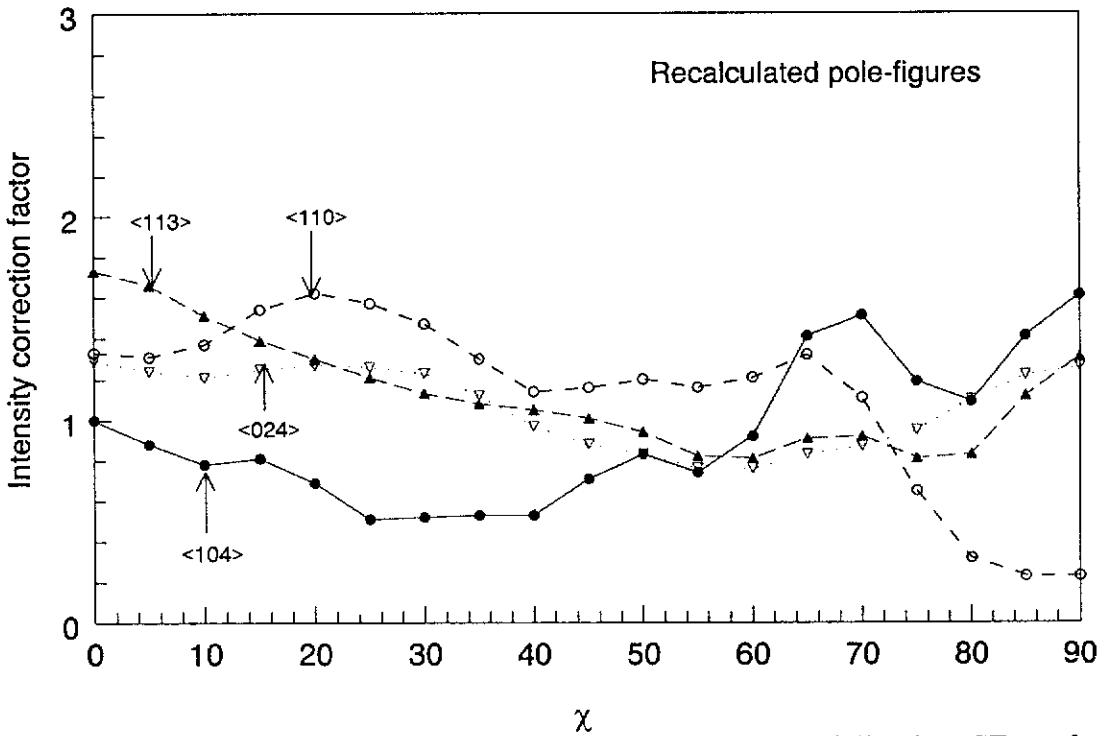

Figure 5.7. Pole-figures for α-Al_2O_3 side-drifted sample following SE analysis. Above:- pole-figure after defocussing corrections and quasi-normalisation (χ = 0 to 60°). Below:- pole-figure recalculated after SE analysis (χ = 0 to 90°).

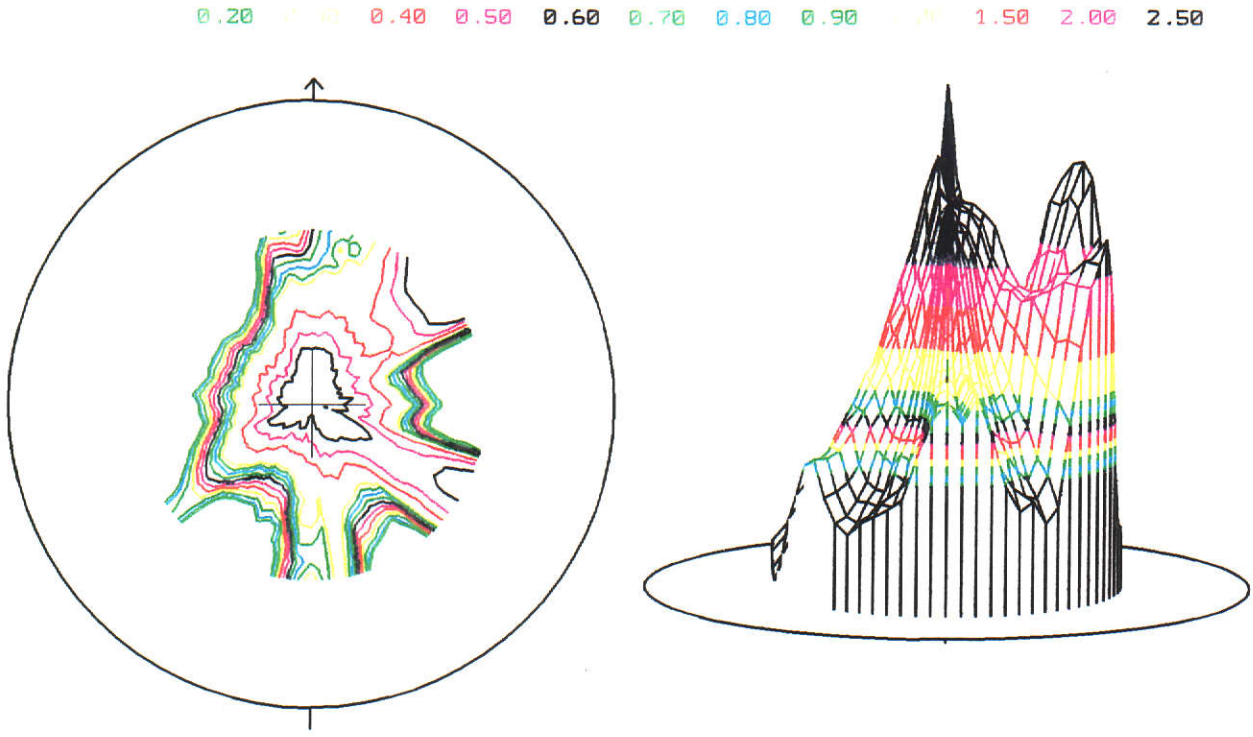

(a)

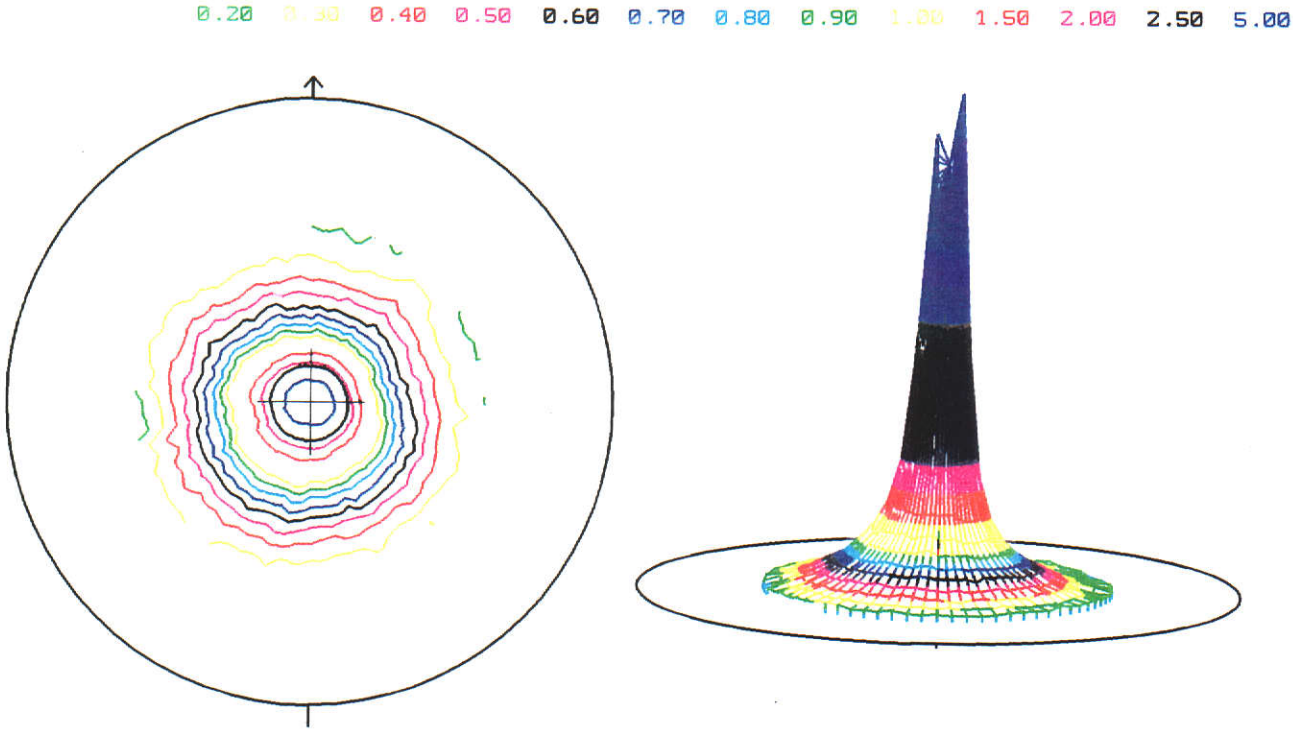

(b)

Figure 5.8. 2D and 3D representations of the molybdite <020> XRPD pole-figures: (a) side drifted - M0X, (b) briquetted for 110MPa - M5X. The contour levels are in random density units.

in Appendix (2). The plots in Appendix (2) are not given in their original colour form with colour-coded contour levels as the cost of colour-copying these diagrams was prohibitively expensive. The original diagrams have been archived. It is evident from Figure (5.8a) that the side-drifted material has substantial texture, as indicated also by the Rietveld modelling results in Chapter 4. This observation underlines the value of using pole-figure measurements to test randomness in powders which have been prepared for XRPD analysis.

The quasi-normalisation method described in Sections (3.3) and (5.2.1) was used to generate the PO correction factors for the pole-figure data - see Figures (5.9) - (5.13). The set of pole-figures for the side-drifted powder, M0X, are self-consistent in that they show in detail the texture character in each material. The <020> set [Figure (5.9)] show that the initial texture increases substantially with the application of 44MPa pressure, and then more slowly for 66, 88 and 110MPa. The other pole-figures are generally consistent with this behaviour with the exception of the M5X plot for <150> (110MPa) which is unexplained.

Figure (5.14) shows the <020> pole-figures for the molybdite samples M0X and M5X derived by SE analysis, and Table (5.2) gives the results of an analysis of the entire set of the <020>, <110>, <021>, <111> and <150> pole-figures for all 5 samples. The PDD values obtained by quasi-normalisation and those extracted from Rietveld analysis with the March model are included for comparison. The results show that there are distinct differences between the PDDs obtained by quasi-normalisation and by SE. On this basis, SE analysis should be preferred in future studies.

Section (5.4) provides further comments on the pole-figure and March results.

5.2.3 Calcite X-ray Pole-Figures

Figure (5.15) shows 2D and 3D colour views of the <104> XRPD pole-figures for 2 of the 5 calcite samples, C0X (side-drifted) and C8X (most heavily pressed), after (i) correction for defocussing with the <104> Al_2O_3 pole-figure data and (ii) normalisation. The complete set of 2D and 3D representations for the directions <104>, <021>, <006>, <110>, <113> and <202>, for all samples, are shown in

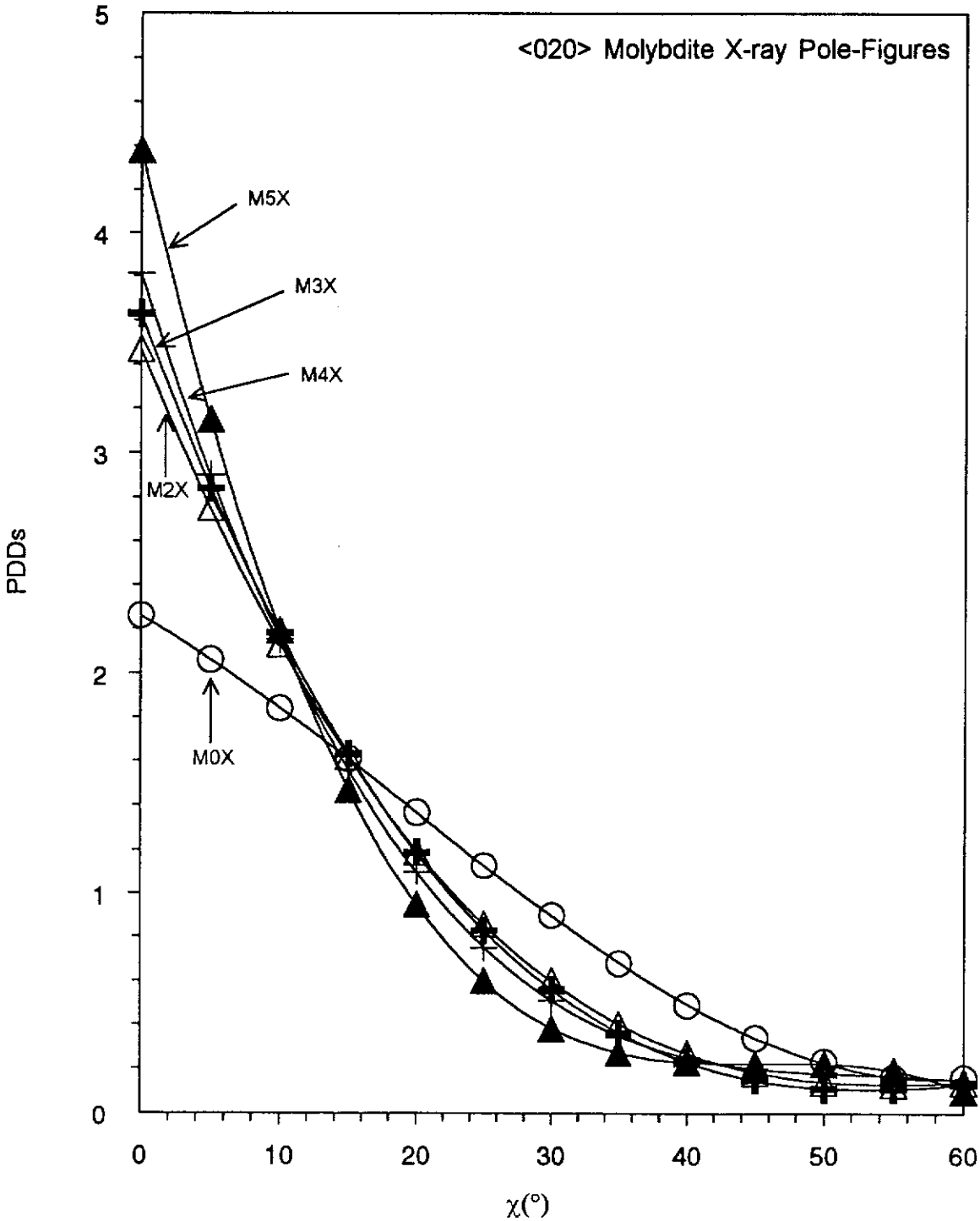

Figure 5.9. 'Quasi-normalised' PDDs for the molybdite <020> XRPD pole-figures: side-drifted - M0X; briquetted for 44MPa - M2X; briquetted for 66MPa - M3X; briquetted for 88MPa - M4X; and briquetted for 110MPa - M5X.

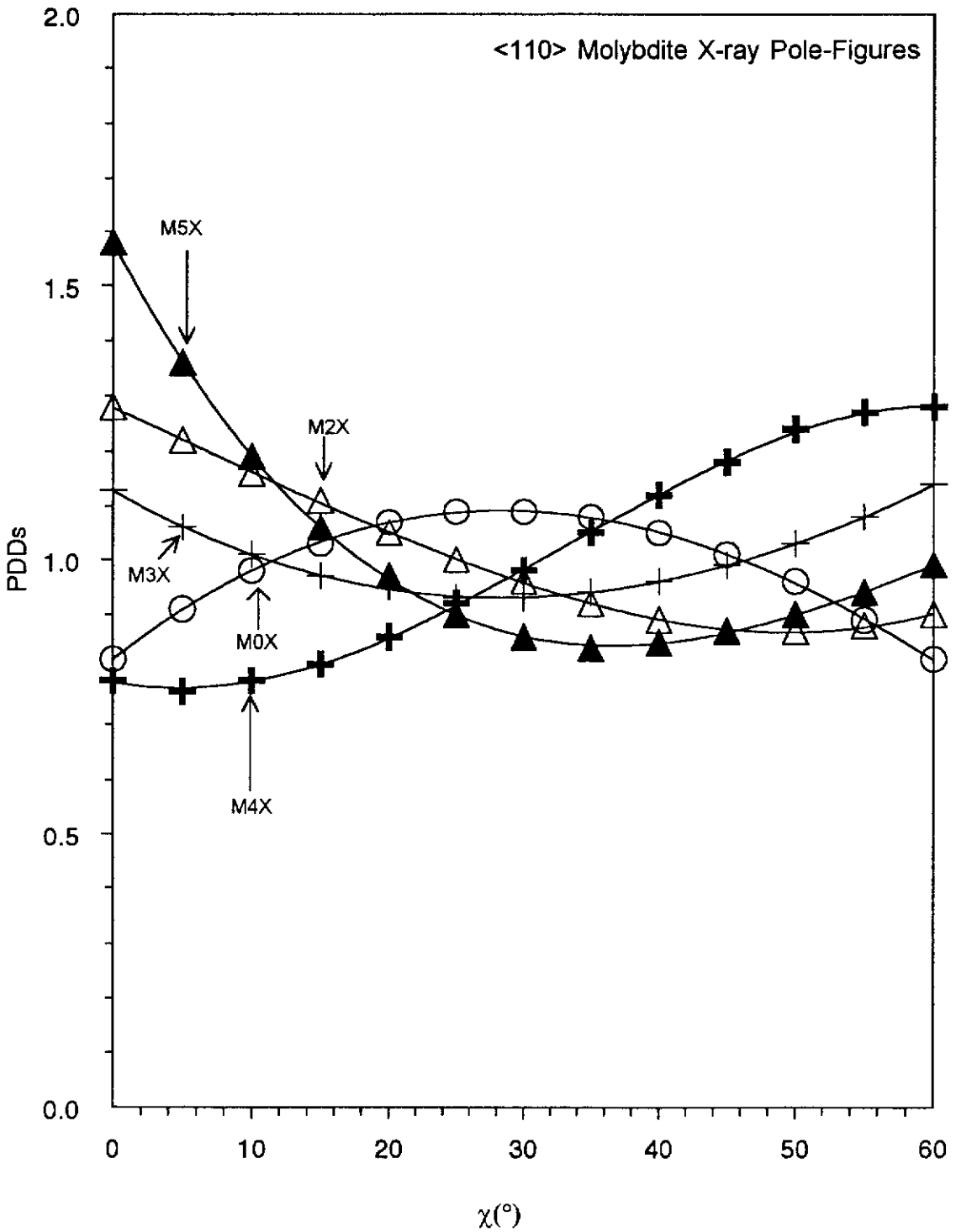

Figure 5.10. 'Quasi-normalised' PDDs for the molybdite <110> XRPD pole-figures: side-drifted - M0X; briquetted for 44MPa - M2X; briquetted for 66MPa - M3X; briquetted for 88MPa - M4X; and briquetted for 110MPa - M5X.

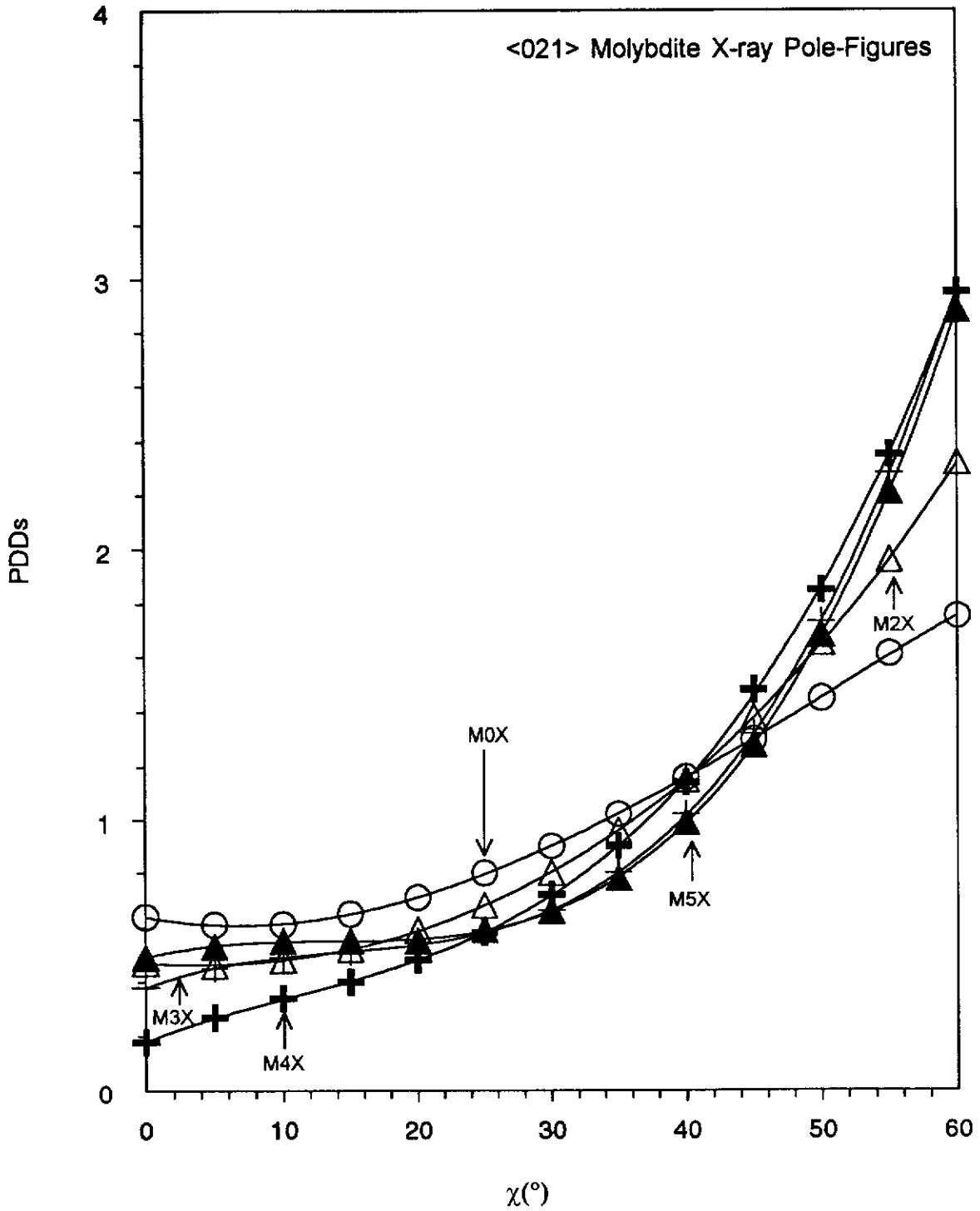

Figure 5.11. 'Quasi-normalised' PDDs for the molybdite <021> XRPD pole-figures: side-drifted - M0X; briquetted for 44MPa - M2X; briquetted for 66MPa - M3X; briquetted for 88MPa - M4X; and briquetted for 110MPa - M5X.

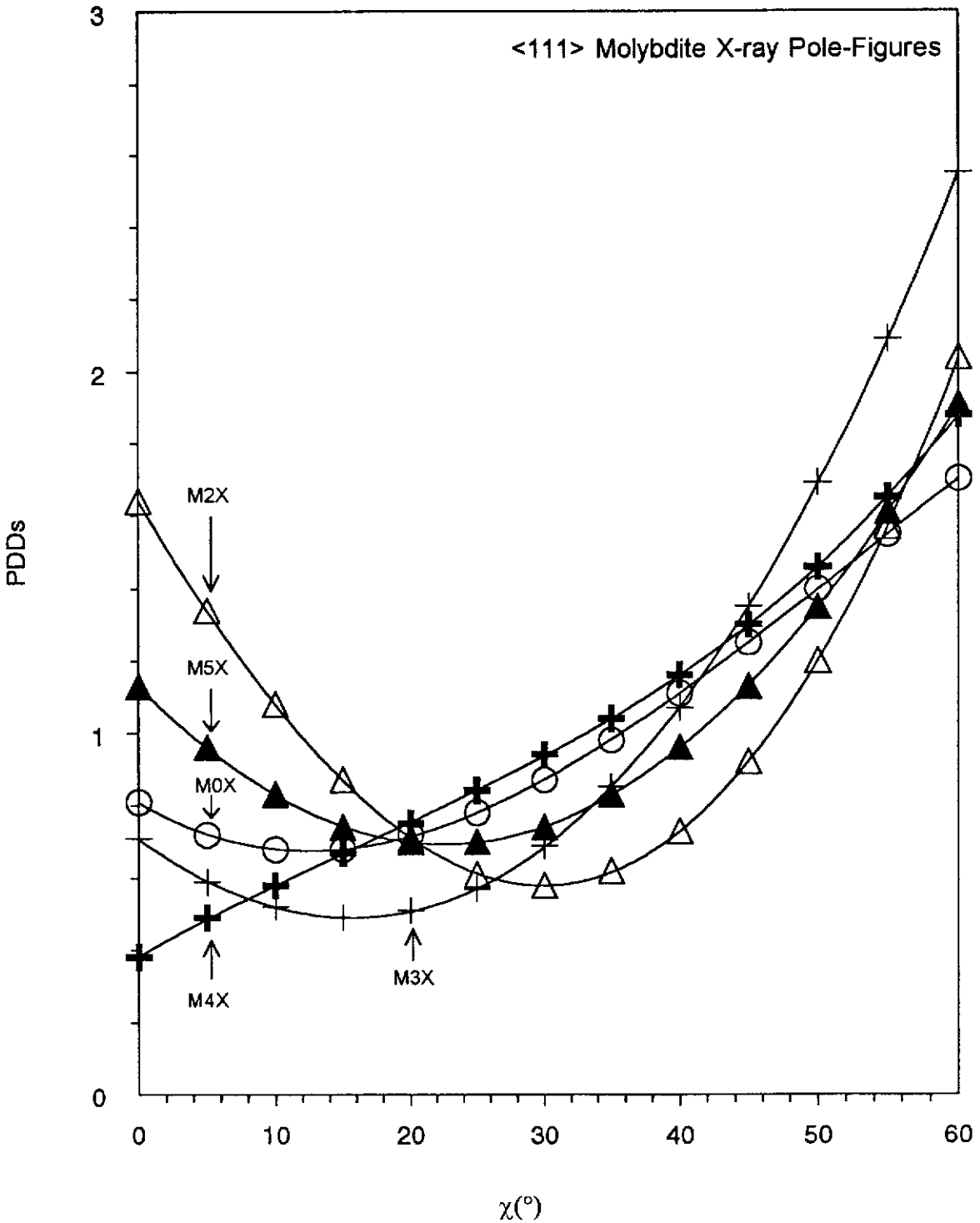

Figure 5.12. 'Quasi-normalised' PDDs for the molybdite <111> XRPD pole-figures: side-drifted - M0X; briquetted for 44MPa - M2X; briquetted for 66MPa - M3X; briquetted for 88MPa - M4X; and briquetted for 110MPa - M5X.

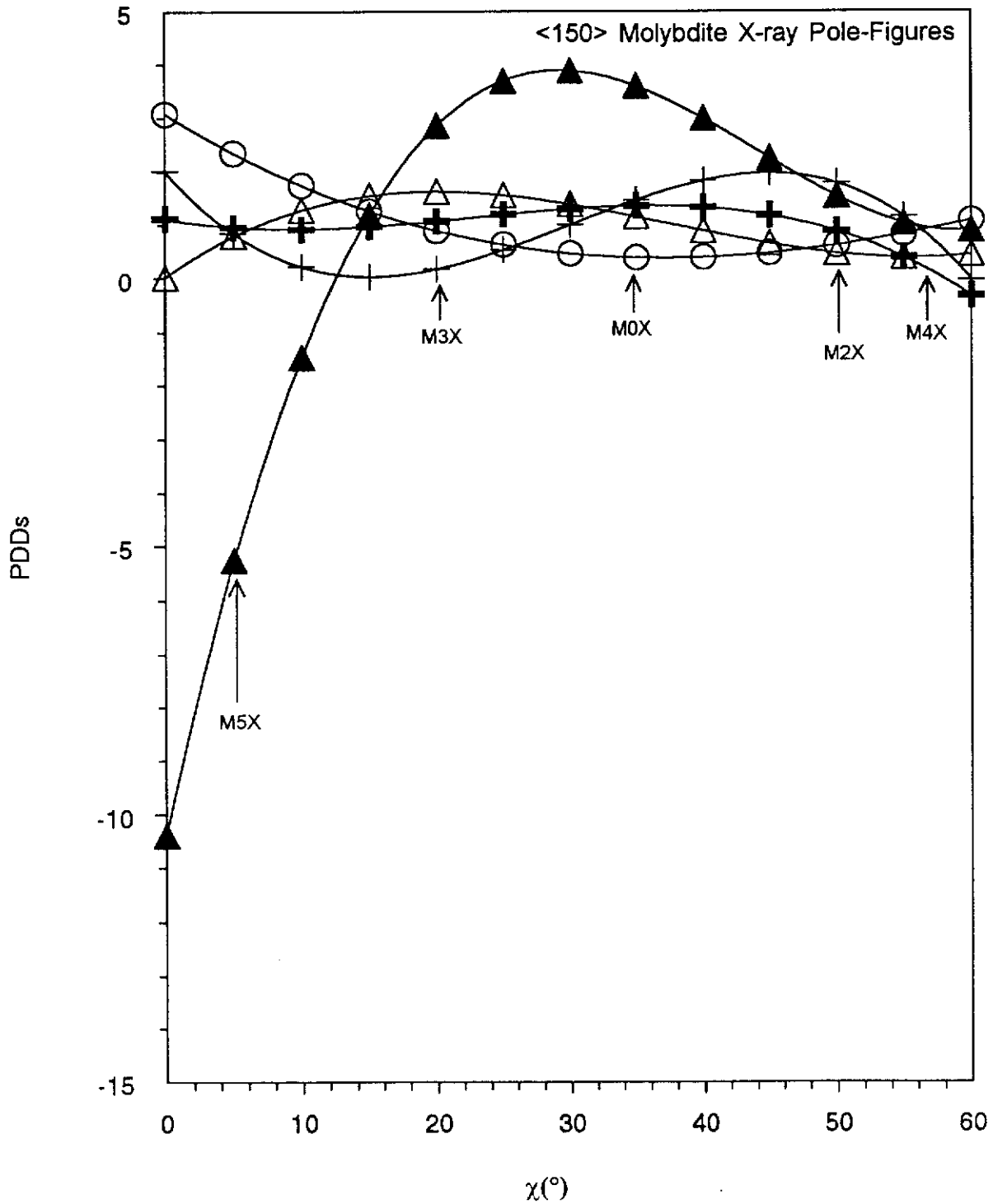

Figure 5.13. 'Quasi-normalised' PDDs for the molybdite <150> XRPD pole-figures: side-drifted - M0X; briquetted for 44MPa - M2X; briquetted for 66MPa - M3X; briquetted for 88MPa - M4X; and briquetted for 110MPa - M5X.

(a) SE analysis - normalised

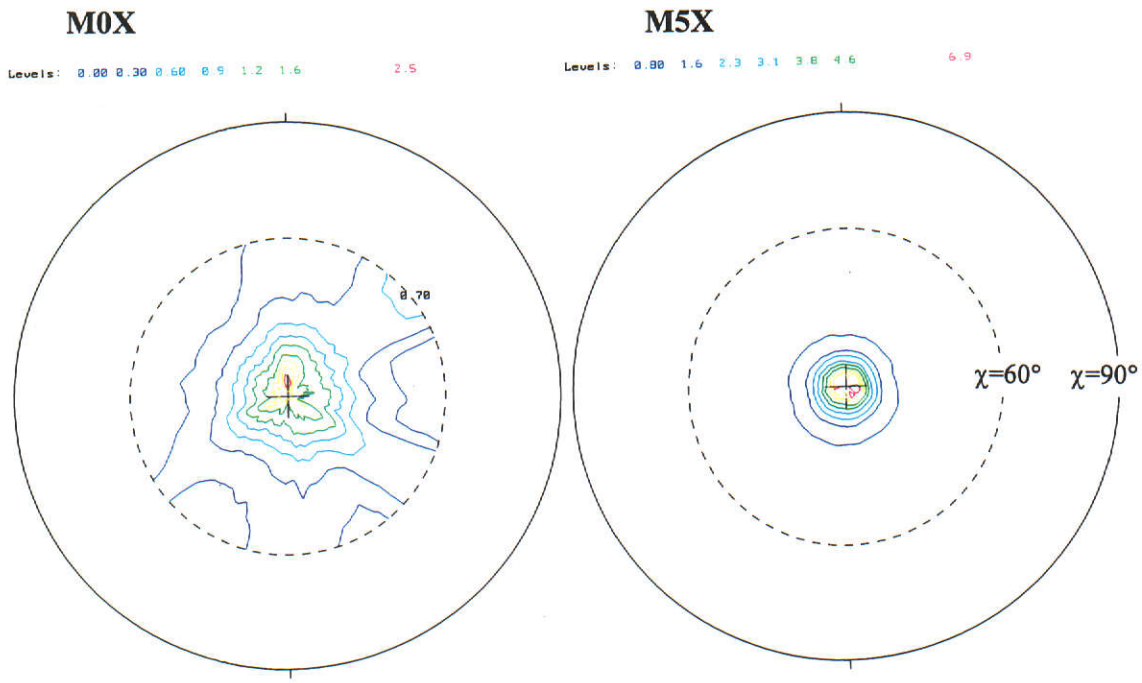

(b) SE analysis - recalculated

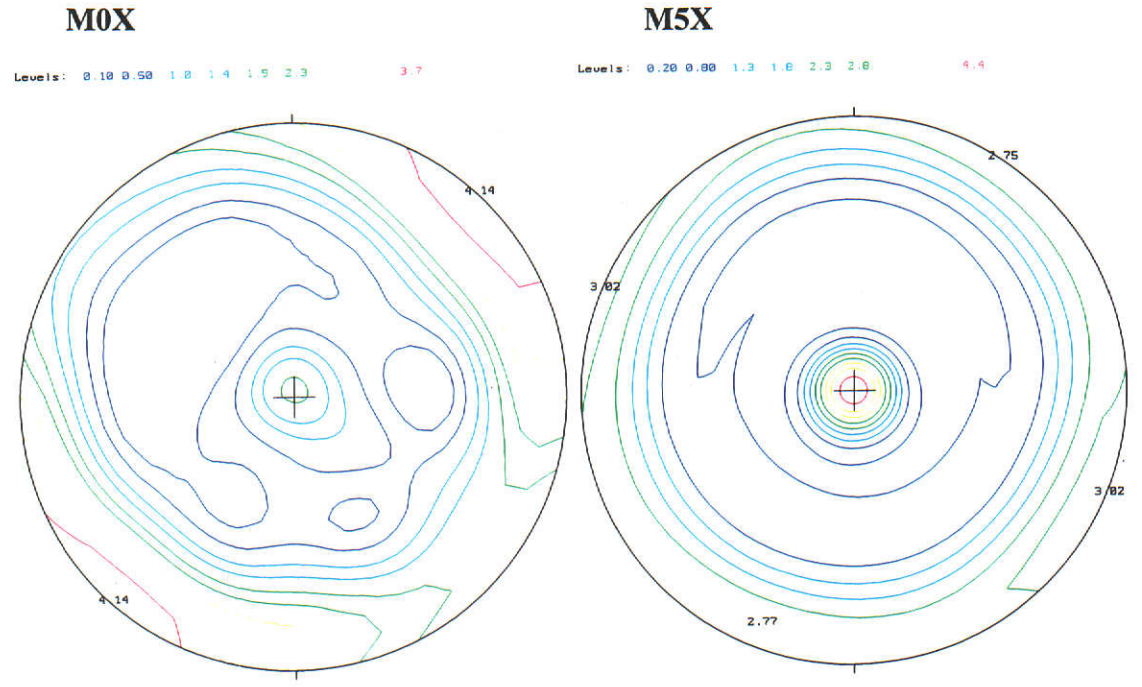

Figure 5.14. The molybdite <020> XRPD normalised (above) and recalculated (below) pole-figures from SE analysis. The contour levels are in random density units.

Table 5.2

Molybdite Minimum and Maximum XRPD PDD Values from SE analysis

Code	hkl	SE Analysis				Quasi-Normalisation χ=0°	March model
		Normalised Pole-Figure		Recalculated Pole-Figure			
		Minimum	Maximum	Minimum	Maximum		
M0X	020	-0.3	2.8	-0.4	4.1	2.3	4.4
M2X		-0.2	6.2	-0.8	5.3	3.5	10.3
M3X		-0.1	12.7	-0.3	7.1	3.8	10.6
M4X		-0.1	11.6	-0.2	8.1	3.6	15.4
M5X		0.0	7.7	-0.3	4.9	4.4	19.3
M0X	110	0.1	2.4	0.2	1.9	0.8	0.5
M2X		-1.1	4.1	-0.6	2.9	1.3	0.4
M3X		0.5	2.9	0.1	2.3	1.1	0.3
M4X		0.7	1.8	0.5	1.8	0.8	0.3
M5X		0.7	4.4	0.5	3.5	1.6	0.3
M0X	021	-0.6	2.2	0.0	1.8	0.6	0.6
M2X		-2.0	2.9	-0.8	2.8	0.5	0.4
M3X		0.5	2.2	0.2	1.8	0.4	0.4
M4X		0.3	2.0	-0.2	1.8	0.2	0.4
M5X		0.4	2.0	0.1	1.7	0.5	0.3
M0X	111	-0.3	2.4	-0.3	2.0	0.8	0.5
M2X		-15.9	6.8	-6.9	4.4	1.6	0.3
M3X		0.4	2.3	-0.1	1.9	0.7	0.3
M4X		0.1	2.0	0.3	1.9	0.4	0.3
M5X		-0.2	2.8	-0.1	2.2	1.1	0.2
M0X	150	-1.3	5.0	-0.4	4.2	3.1	1.4
M2X		-2.8	3.7	-0.7	5.3	0.0	1.3
M3X		-1.4	4.7	-0.9	3.4	2.0	1.3
M4X		-6.2	2.5	-0.5	3.1	1.1	1.1
M5X		-0.2	2.5	-0.1	2.2	-10.4	1.0

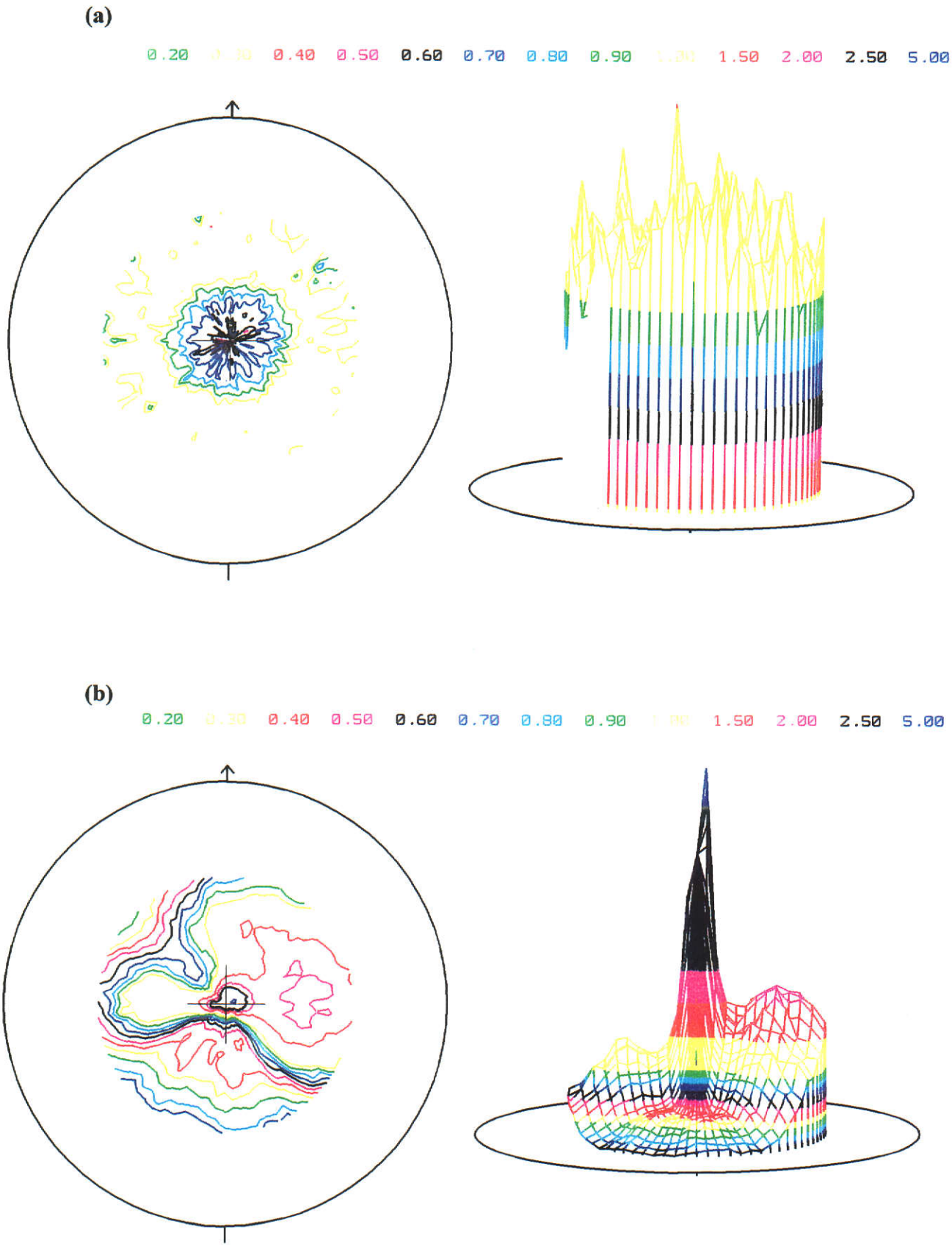

Figure 5.15. 2D and 3D representations of the calcite <104> XRPD pole-figures: (a) side drifted - C0X and (b) briquetted for 176MPa - C8X. The contour levels are in random density units.

Appendix (2). As for the corresponding molybdite plots, the calcite diagrams in Appendix (2) are not given in their original colour form with colour-coded contour levels as the cost of colour-copying these diagrams was prohibitively expensive.

It is interesting to examine the <104> pole-figures in light of this direction clearly being the PO direction for the calcite XRPD data from the results in Chapter 4. In contrast with the corresponding molybdite plots [Figure (5.8)], the C0X pole-figure is reasonably consistent with the expectation that side-drifting produced a randomly-oriented powder, and that the application of uniaxial pressure will have caused substantial orientation along <104>. As for the molybdite plots, pole-figure assessment is clearly of value for the assessment of randomness in powders for XRPD powder pattern analysis.

The quasi-normalisation method described in Sections (3.4) and (5.2.1) was used to generate the PO correction factors for the pole-figure data - see Figures (5.16) - (5.21). The set of pole-figures for the side-drifted powder, M0X, are self-consistent in that they show in detail the texture character in each material. The <104> set [Figure (5.16)] show that the substantial texture develops along this direction with the application of 44MPa pressure, but the values for $\chi = 0°$ do not show a further increase as the pressure increases to 66, 88 and 110MPa. This behaviour is qualitatively consistent with the plots of March r-parameter versus pressure shown in Chapter 4, *i.e.* the texture along <104> plateaus as the pressure increases.

The pole-figures for the other directions [Figures (5.17) - (5.21)] indicate the complex manner in which the PDD changes with the application of pressure. These show that the assumption that the texture has a unipolar distribution about <104> is only a crude approximation when substantial pressure is applied.

Figure (5.22) shows the <104> pole-figures for the molybdite samples M0X and M5X derived by SE analysis, and Table (5.3) gives the results of an analysis of the entire set of the <104>, <021>, <006>, <110>, <113> and <202> pole-figures for all 5 samples. The PDD values obtained by direct measurement and those extracted from Rietveld analysis with the March model are included for comparison. The comments made in Section (5.2.2) for molybdite [Table (5.2)] also apply here.

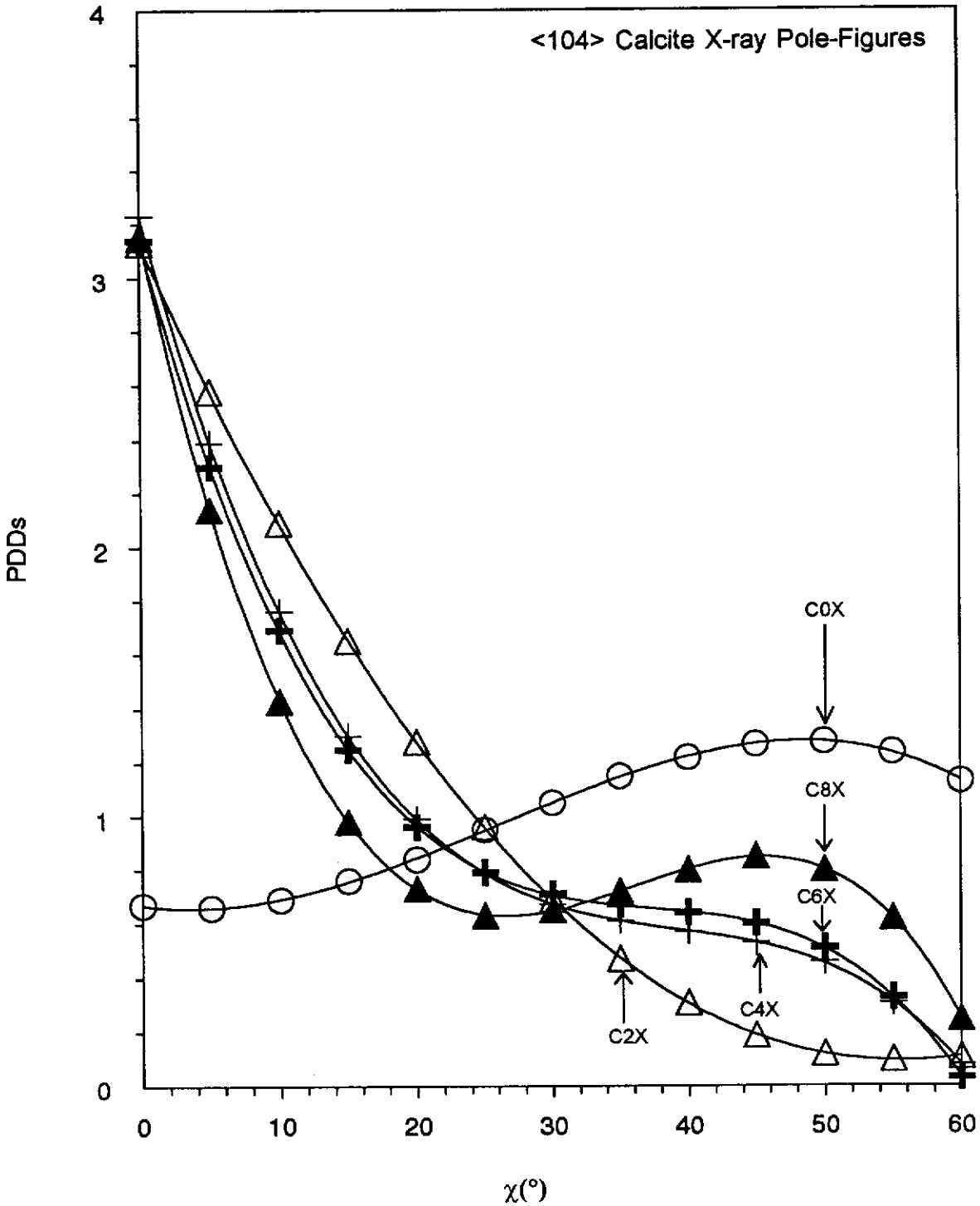

Figure 5.16. 'Quasi-normalised' PDDs for the calcite <104> XRPD pole-figures: side-drifted - C0X; briquetted for 44MPa - C2X; briquetted for 88MPa - C4X; briquetted for 132MPa - C6X; and briquetted for 176MPa - C8X.

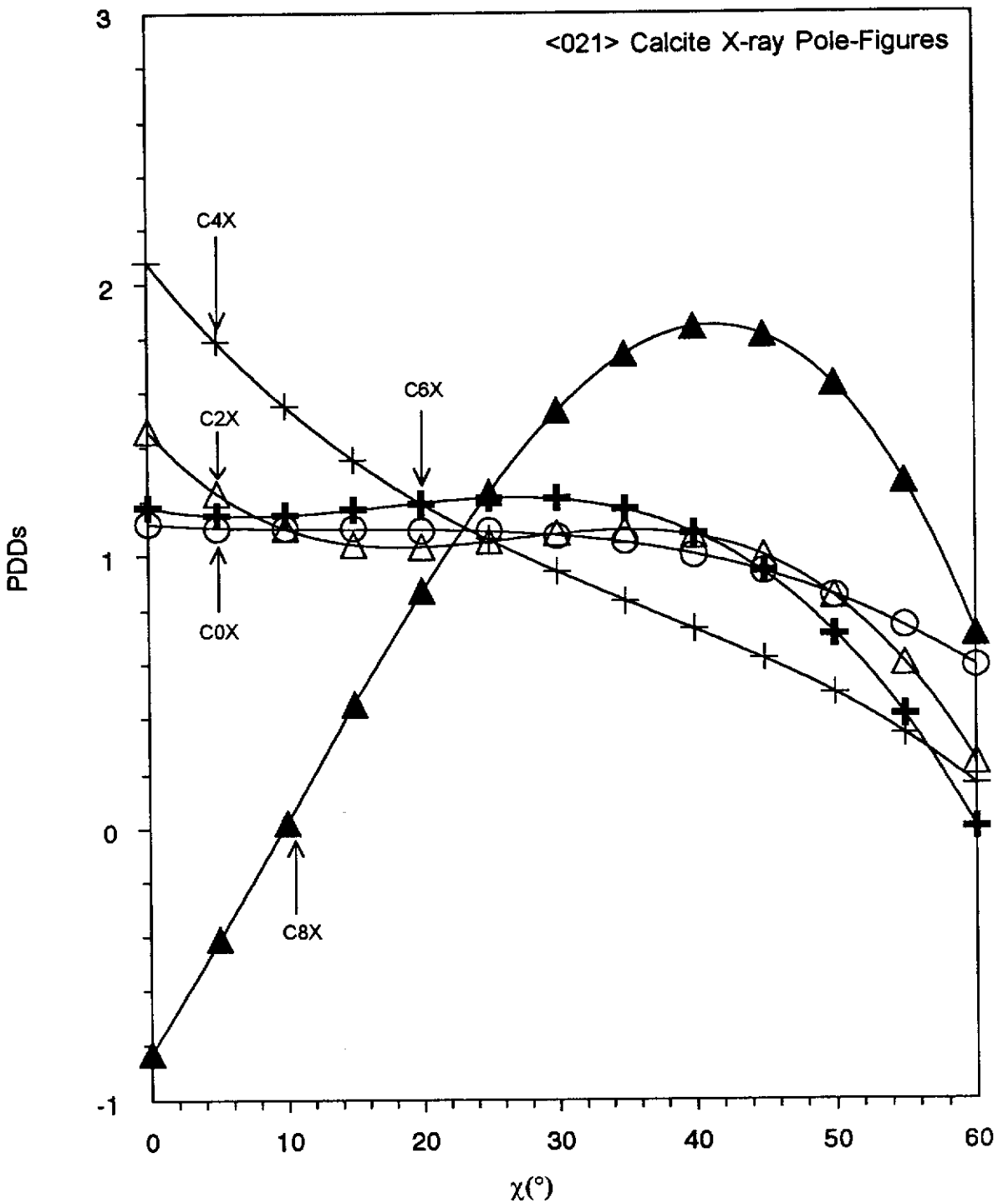

Figure 5.17. 'Quasi-normalised' PDDs for the calcite <021> XRPD pole-figures: side-drifted - C0X; briquetted for 44MPa - C2X; briquetted for 88MPa - C4X; briquetted for 132MPa - C6X; and briquetted for 176MPa - C8X.

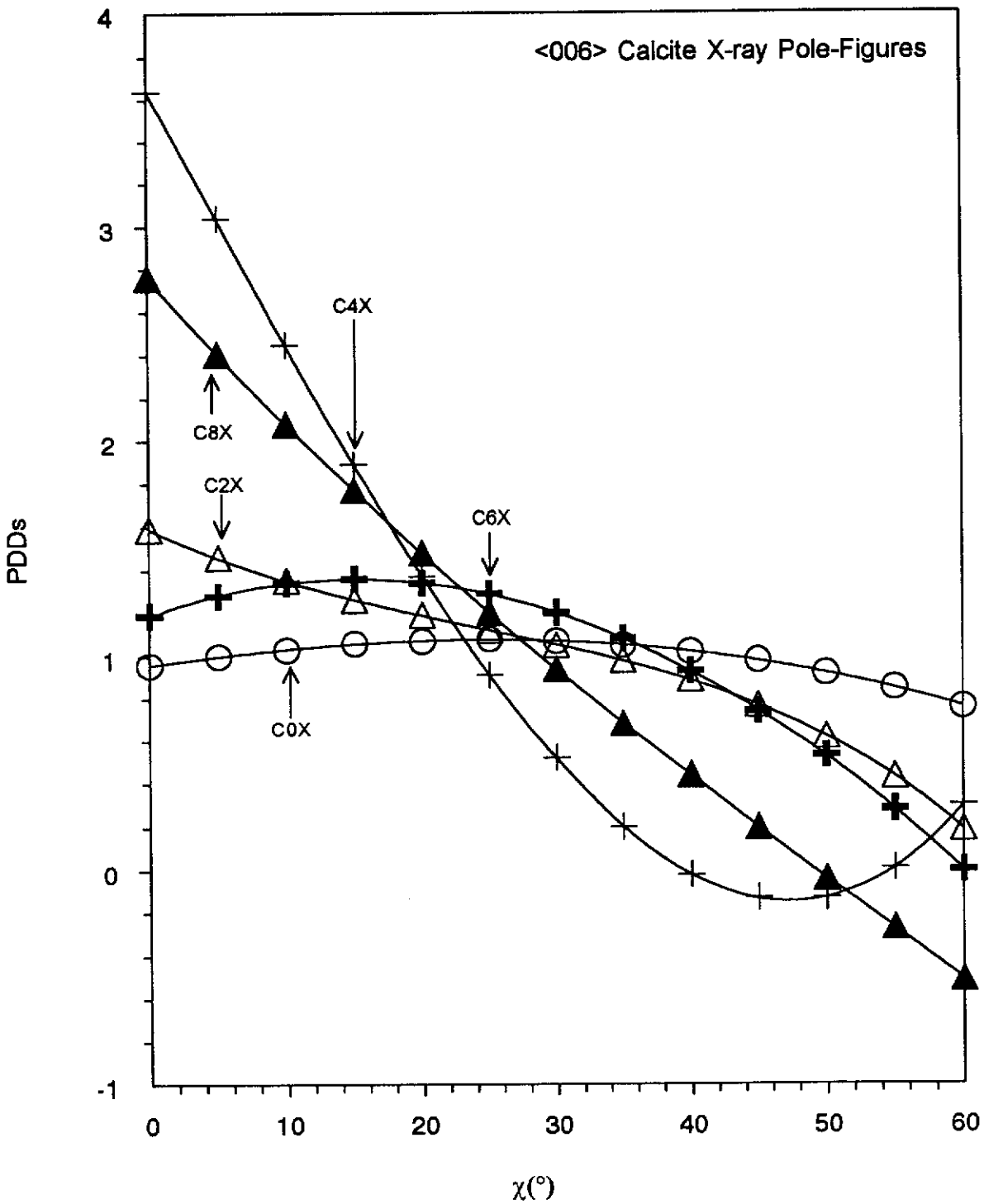

Figure 5.18. 'Quasi-normalised' PDDs for the calcite <006> XRPD pole-figures: side-drifted - C0X; briquetted for 44MPa - C2X; briquetted for 88MPa - C4X; briquetted for 132MPa - C6X; and briquetted for 176MPa - C8X.

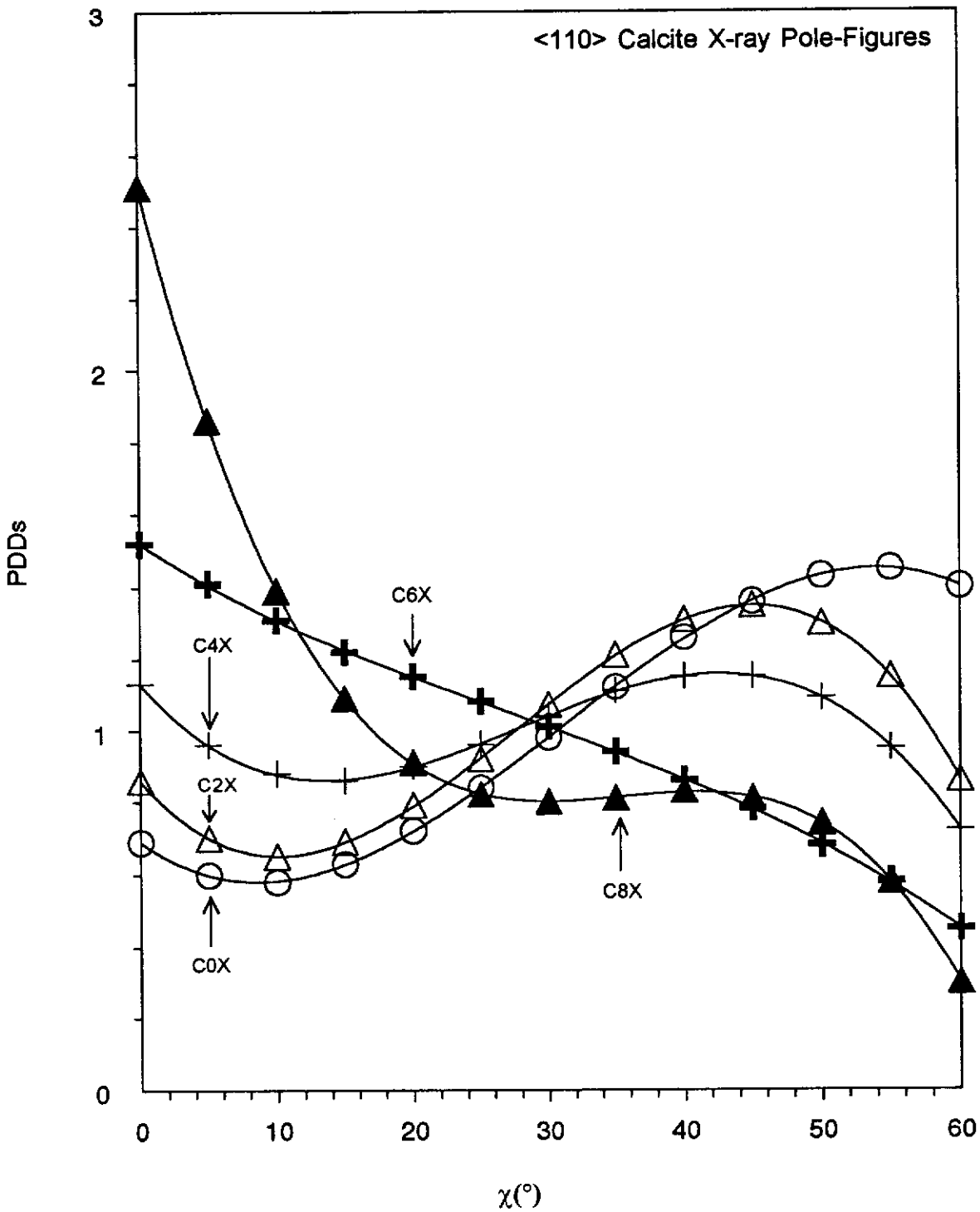

Figure 5.19. 'Quasi-normalised' PDDs for the calcite <110> XRPD pole-figures: side-drifted - C0X; briquetted for 44MPa - C2X; briquetted for 88MPa - C4X; briquetted for 132MPa - C6X; and briquetted for 176MPa - C8X.

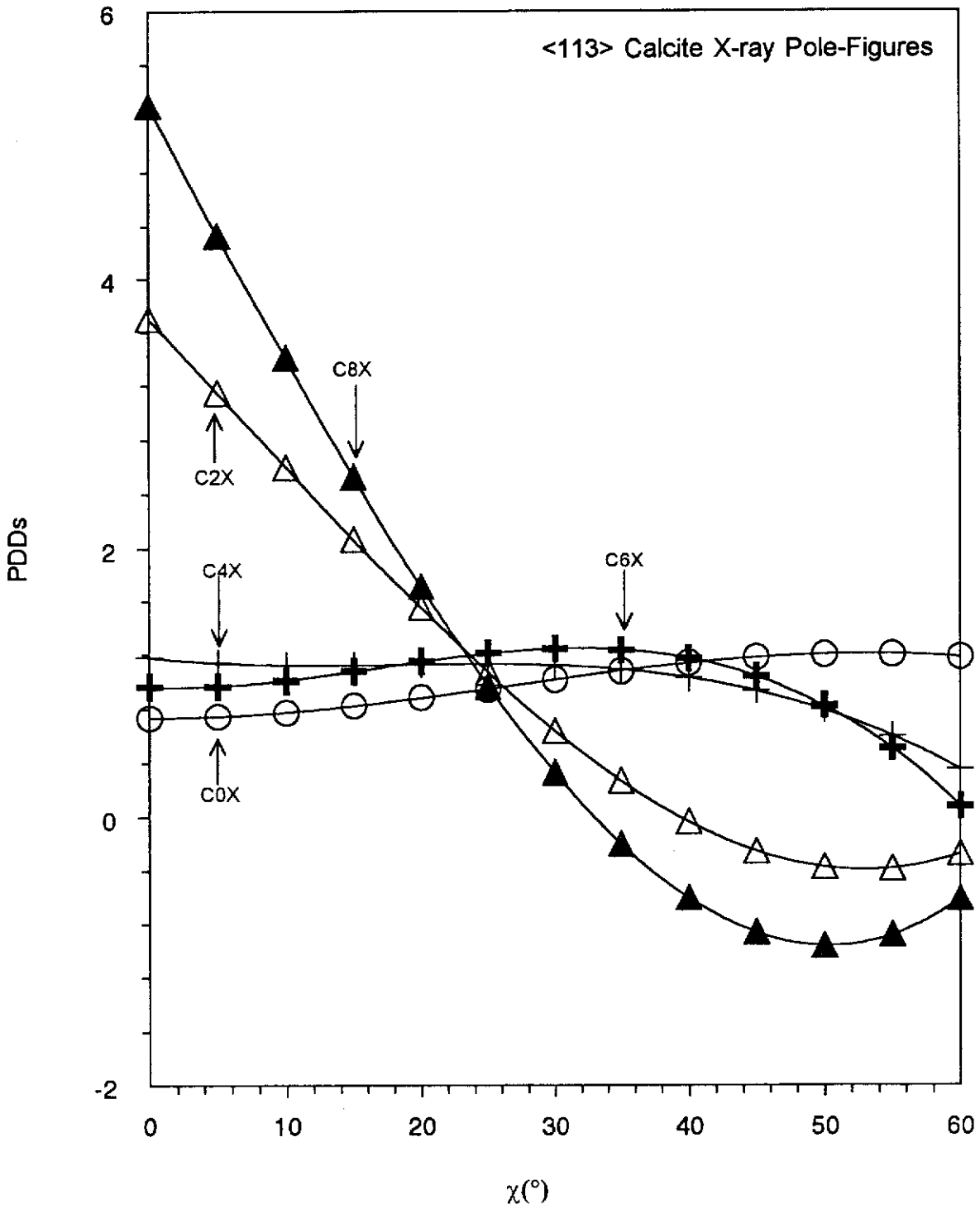

Figure 5.20. 'Quasi-normalised' PDDs for the calcite <113> XRPD pole-figures: side-drifted - C0X; briquetted for 44MPa - C2X; briquetted for 88MPa - C4X; briquetted for 132MPa - C6X; and briquetted for 176MPa - C8X.

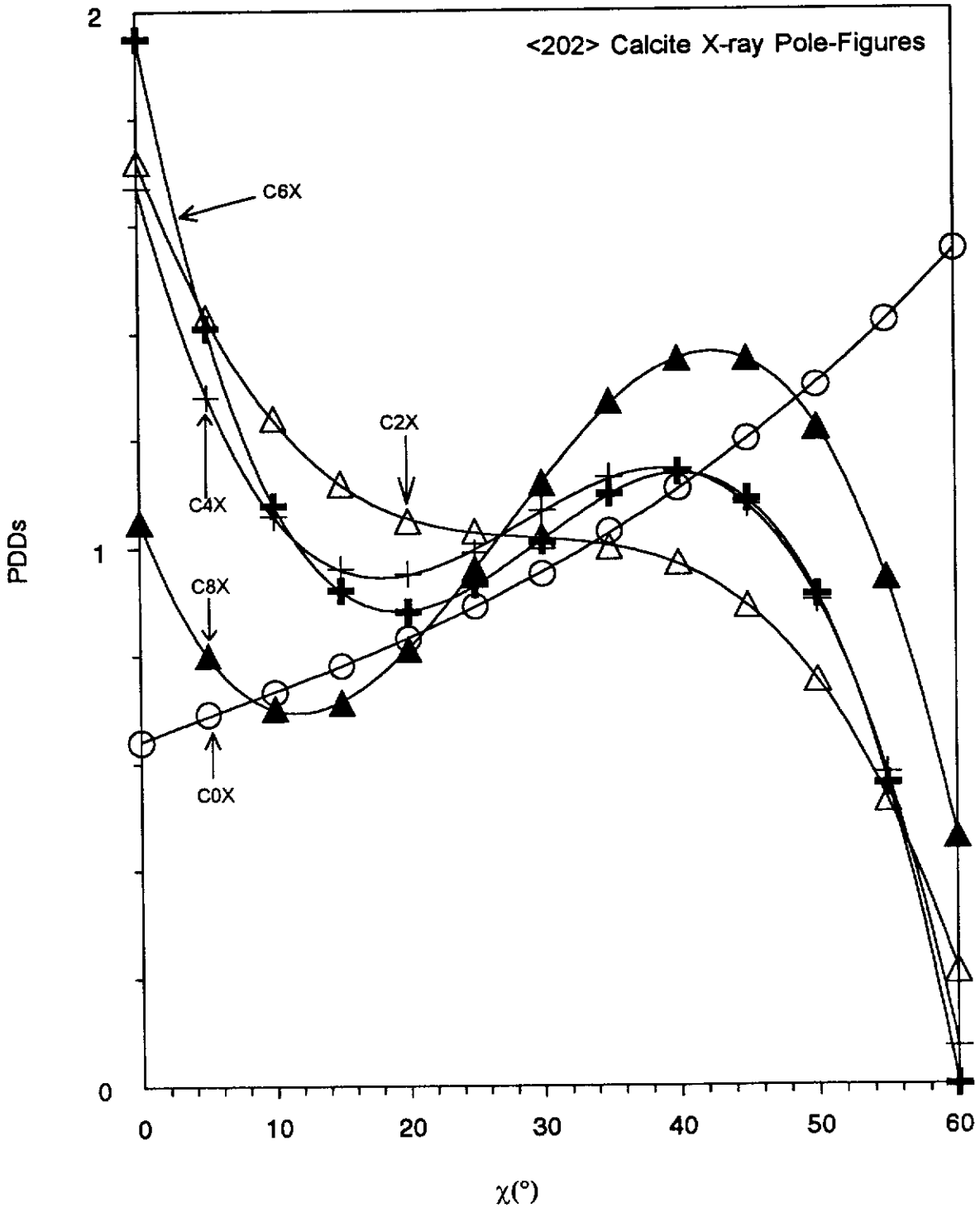

Figure 5.21. 'Quasi-normalised' PDDs for the calcite <202> XRPD pole-figures: side-drifted - C0X; briquetted for 44MPa - C2X; briquetted for 88MPa - C4X; briquetted for 132MPa - C6X; and briquetted for 176MPa - C8X.

(a) SE analysis - normalised

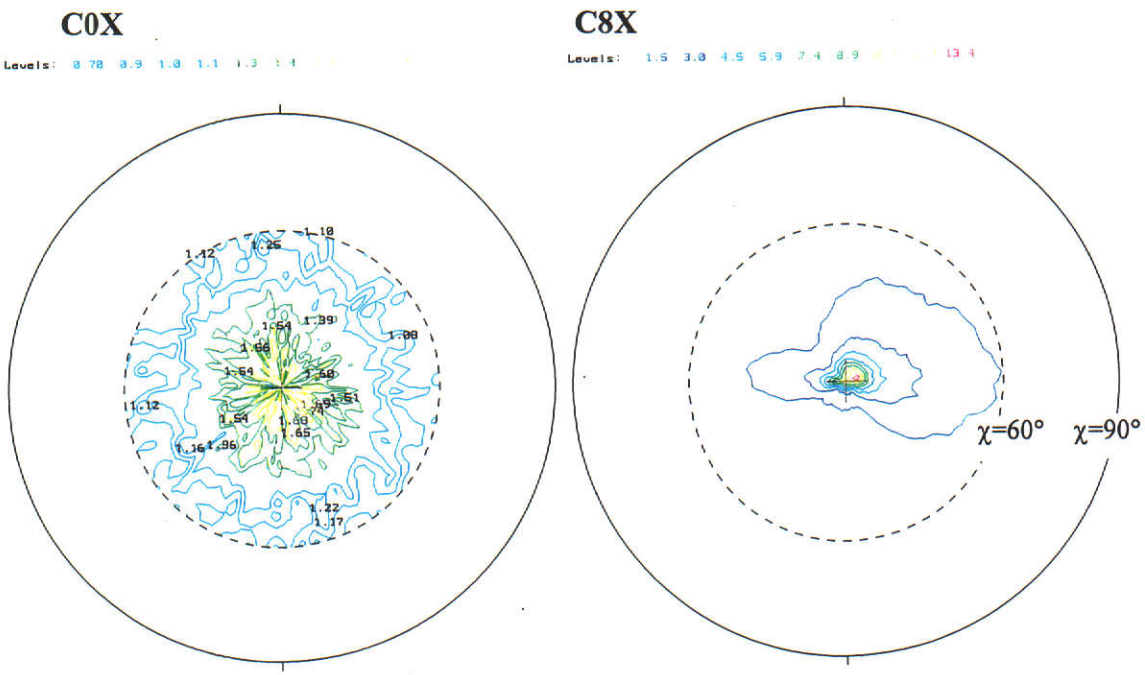

(b) SE analysis - recalculated

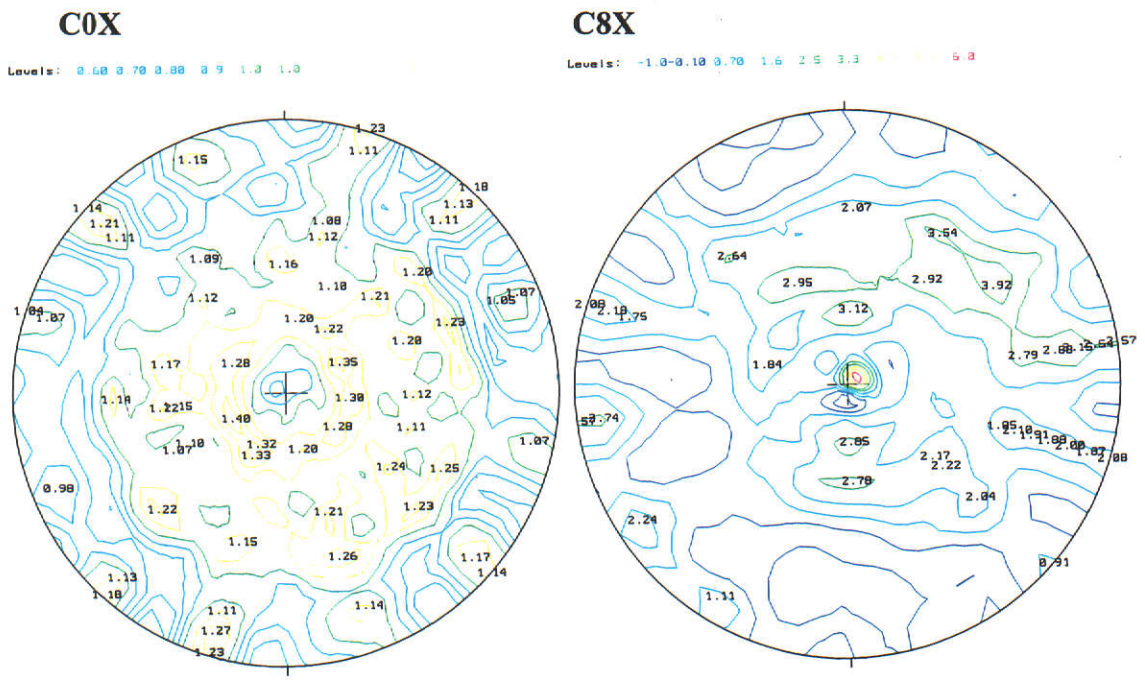

Figure 5.22. The calcite <104> XRPD normalised (above) and recalculated (below) pole-figures from SE analysis. The contour levels are in random density units.

Table 5.3

Calcite Minimum and Maximum XRPD PDD Values from SE analysis

Code	khl	SE Analysis				Quasi-Normalisation χ=0°	March model
		Normalised Pole-Figure		Recalculated Pole-Figure			
		Minimum	Maximum	Minimum	Maximum		
C0X	104	0.6	1.9	0.5	1.4	0.7	1.1
C2X		-0.6	6.2	-0.6	3.4	3.1	3.2
C4X		-0.1	1.4	-3.6	6.0	3.2	10.3
C6X		-2.6	0.0	-2.7	3.4	3.1	12.0
C8X		0.0	14.9	-1.9	6.8	3.2	13.1
C0X	021	-2.7	2.8	-0.4	1.9	1.1	1.0
C2X		-2.8	5.3	-0.7	3.4	1.5	0.9
C4X		-7.2	13.0	-2.2	7.4	2.1	0.6
C6X		-3.2	7.6	-1.9	4.1	1.2	0.6
C8X		-1.5	2.8	-1.8	5.2	-0.8	0.6
C0X	006	-0.5	3.9	0.0	2.5	1.0	1.0
C2X		-1.4	5.4	-0.8	5.0	1.6	1.1
C4X		-33.2	15.3	-23.3	13.1	3.6	0.8
C6X		-11.7	2.7	-10.7	16.2	1.2	0.7
C8X		-9.0	19.6	-6.2	15.7	2.8	0.7
C0X	110	0.5	1.2	0.5	2.0	0.7	1.0
C2X		0.1	2.1	-0.4	3.4	0.9	0.9
C4X		-3.3	9.8	-5.4	10.4	1.1	0.6
C6X		-3.6	13.8	-5.4	8.6	1.5	0.5
C8X		-1.0	1.9	-1.8	6.9	2.5	0.5
C0X	113	0.4	1.9	0.6	1.4	0.7	1.1
C2X		-0.4	1.7	-0.8	3.5	3.7	1.5
C4X		-1.6	7.0	-1.9	7.8	1.2	1.5
C6X		-0.3	5.3	-1.0	4.8	1.0	1.4
C8X		-3.6	1.4	-2.8	5.5	5.3	1.4
C0X	202	0.4	1.9	0.7	1.4	0.6	1.1
C2X		-2.3	9.8	-1.3	5.4	1.7	1.6
C4X		-4.0	10.2	-4.0	7.6	1.7	1.6
C6X		-2.0	4.6	-2.0	3.5	1.9	1.5
C8X		-0.8	4.7	-0.3	3.7	1.1	1.5

Section (5.4) provides further comments comparing the pole-figure and March results.

5.3 Neutron Pole-Figure Measurements

5.3.1 Neutron Data Processing

The procedures used to obtain the PDD for each of the selected Bragg reflections were essentially the same as that followed for the XRPD texture data processing described in Section (5.2.1). Defocussing corrections were not employed in generating the neutron-pole figures as these are not required for the transmission geometry employed to acquire the NPD data.

5.3.2 Calcite Neutron Pole-Figures

Figure (5.23) shows 2D and 3D views of the calcite <006> NPD pole-figures for 2 of the 3 calcite samples, C0N (not pressed) and C8N (most heavily pressed). The complete set of 2D and 3D representations for the directions <104>, <021>, <006>, <113> and <018>, for all samples, is given in Appendix (2). The plots in the Appendix are not shown in their original colour format with colour-coded contour levels as the cost of colour-copying these diagrams was prohibitively expensive. The original diagrams have been archived.

The discussion on the calcite NPD Rietveld modelling results in Chapter 4 concludes that the direction of PO for bulk calcite material, as measured by NPD, is <001> whereas <104> is the most appropriate PO direction for the XRPD data. The plots in Figure (5.23) for specimen C0N are consistent with the Rietveld analysis of this powder which indicated an essentially random powder (r = 1.000). The subtle differences between the C0N and C8N pole-figures are consistent with the Rietveld r-parameter for C8N being slightly less than unity.

As for the XRPD pole-figures, quasi-normalisation was used to generate PO correction factors from the pole-figure data - see Figures (5.24) - (5.28). The set of pole-figures for the side-drifted powder, C0N, are consistent with the XRPD results in that <006> shows less variation with χ than that observed for the other directions,

(a)

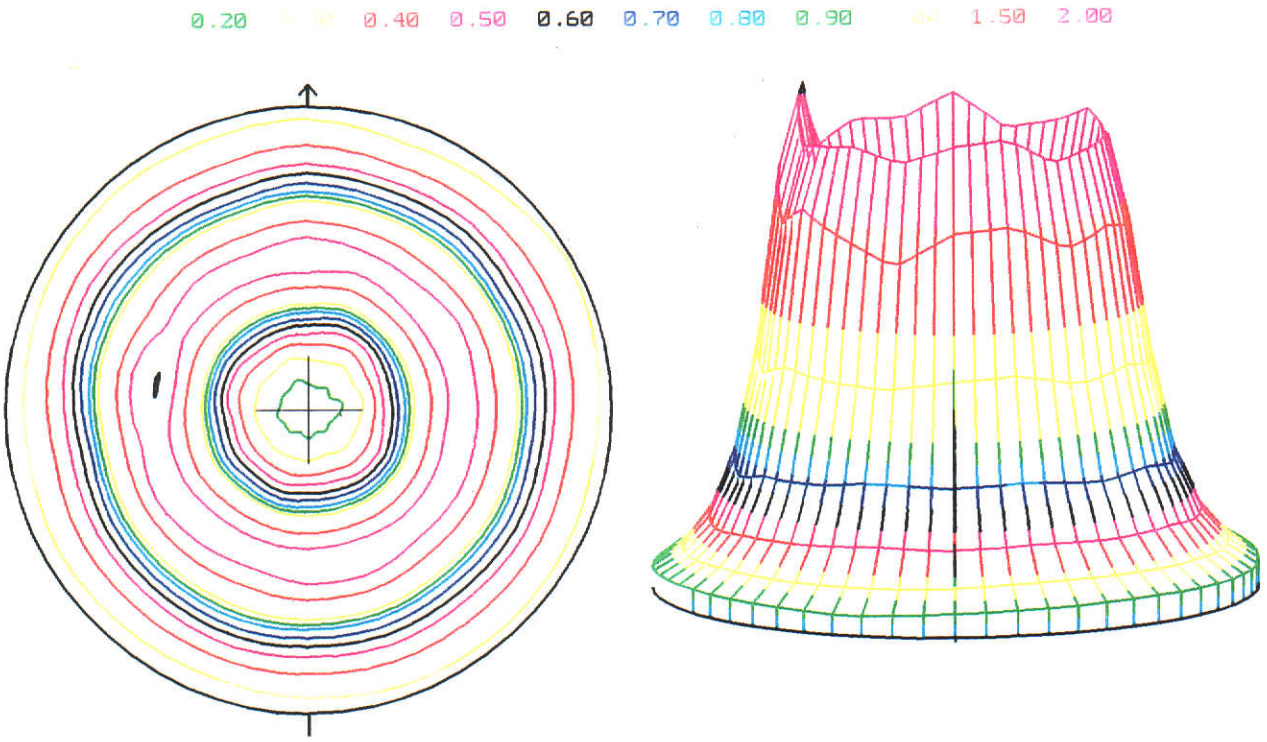

(b)

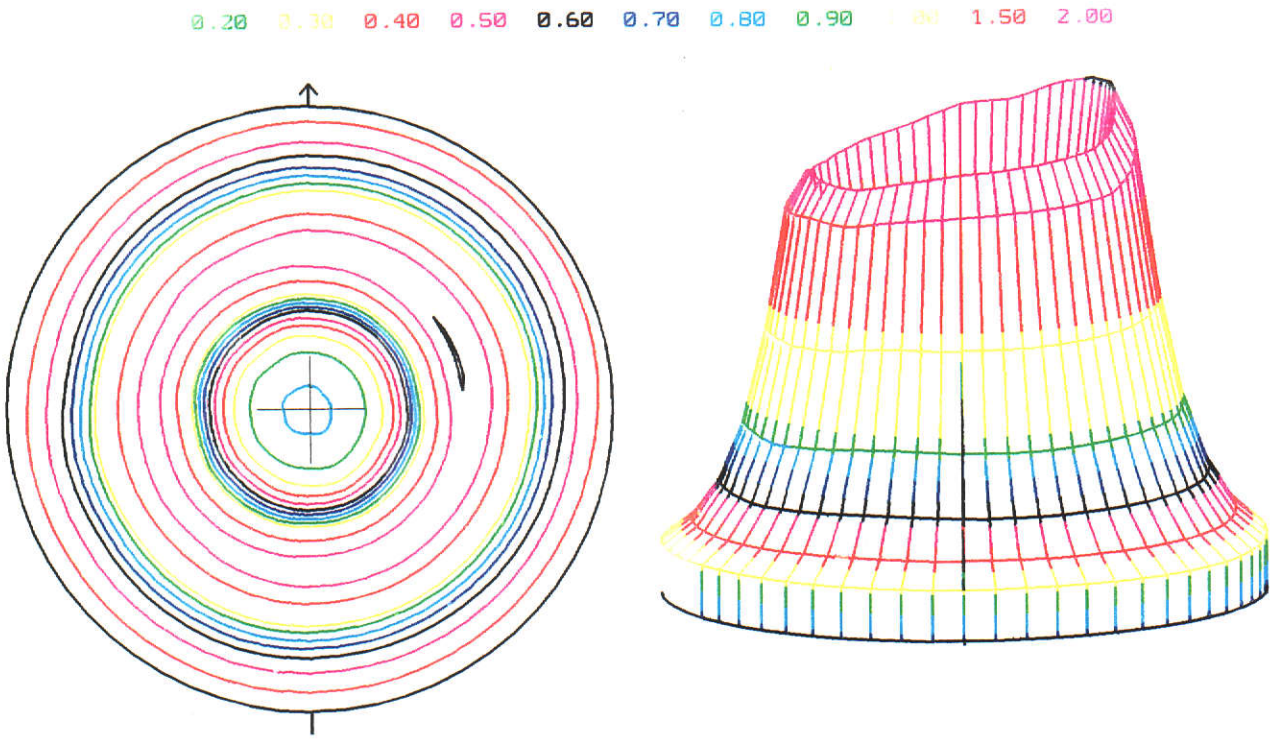

Figure 5.23. 2D and 3D representations of the calcite <006> neutron pole-figures: (a) non pressed - C0N, and (b) briquetted for 176MPa - C8N. The contour levels are in random density units.

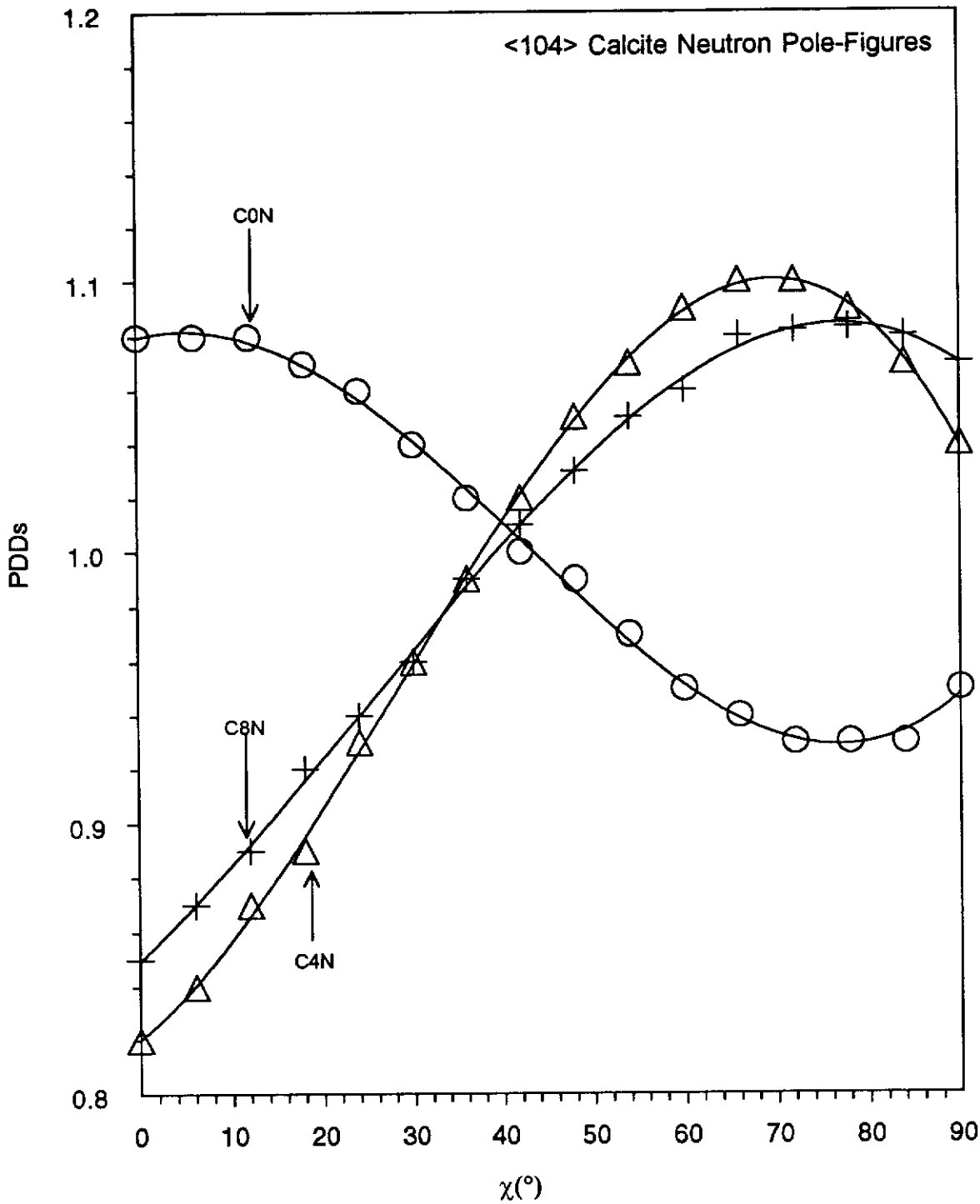

Figure 5.24. 'Quasi-normalised' PDDs for the calcite <104> neutron pole-figures: non pressed - C0N; briquetted for 88MPa - C4N; and briquetted for 176MPa - C8N.

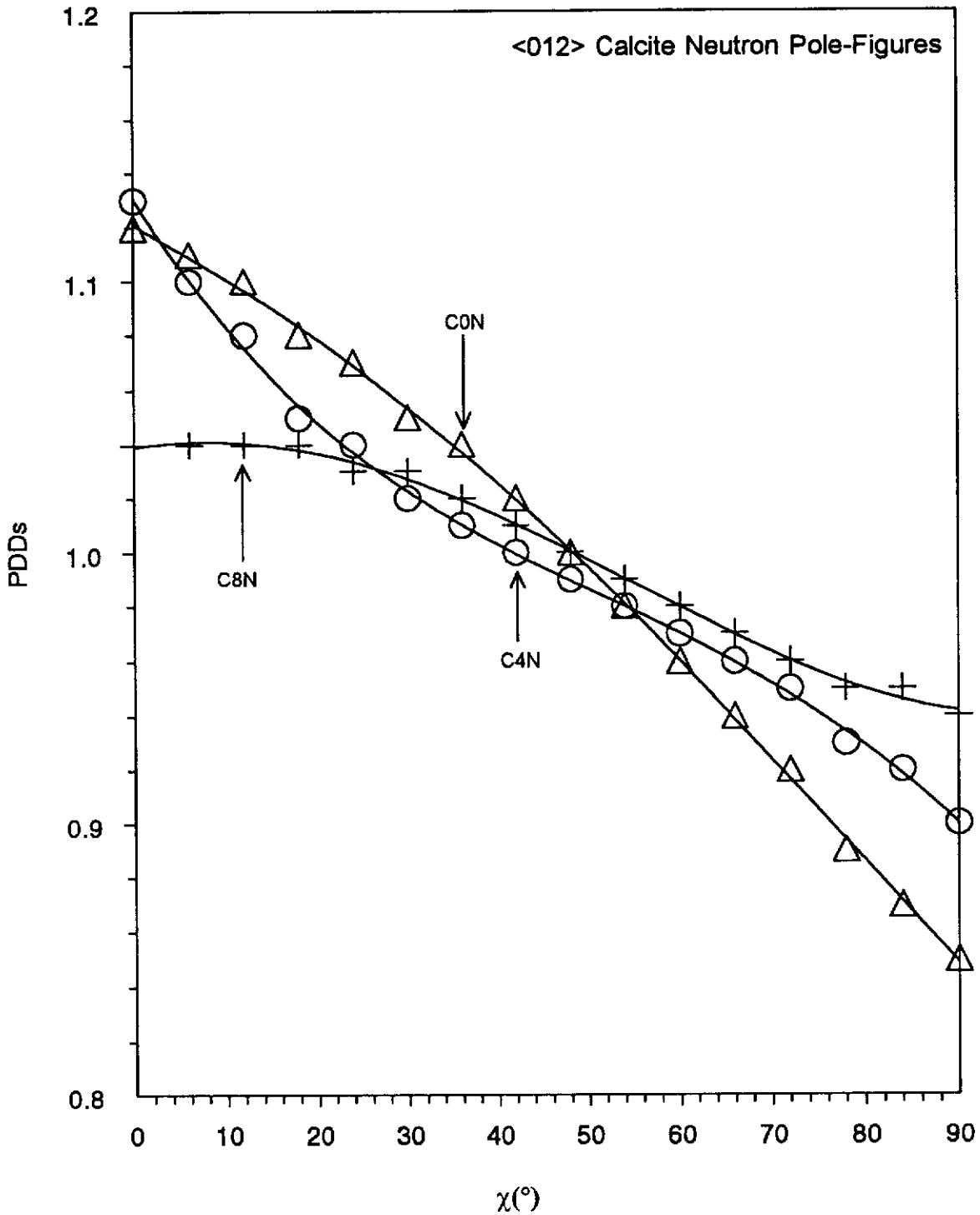

Figure 5.25. 'Quasi-normalised' PDDs for the calcite <012> neutron pole-figures: non pressed - C0N; briquetted for 88MPa - C4N; and briquetted for 176MPa - C8N.

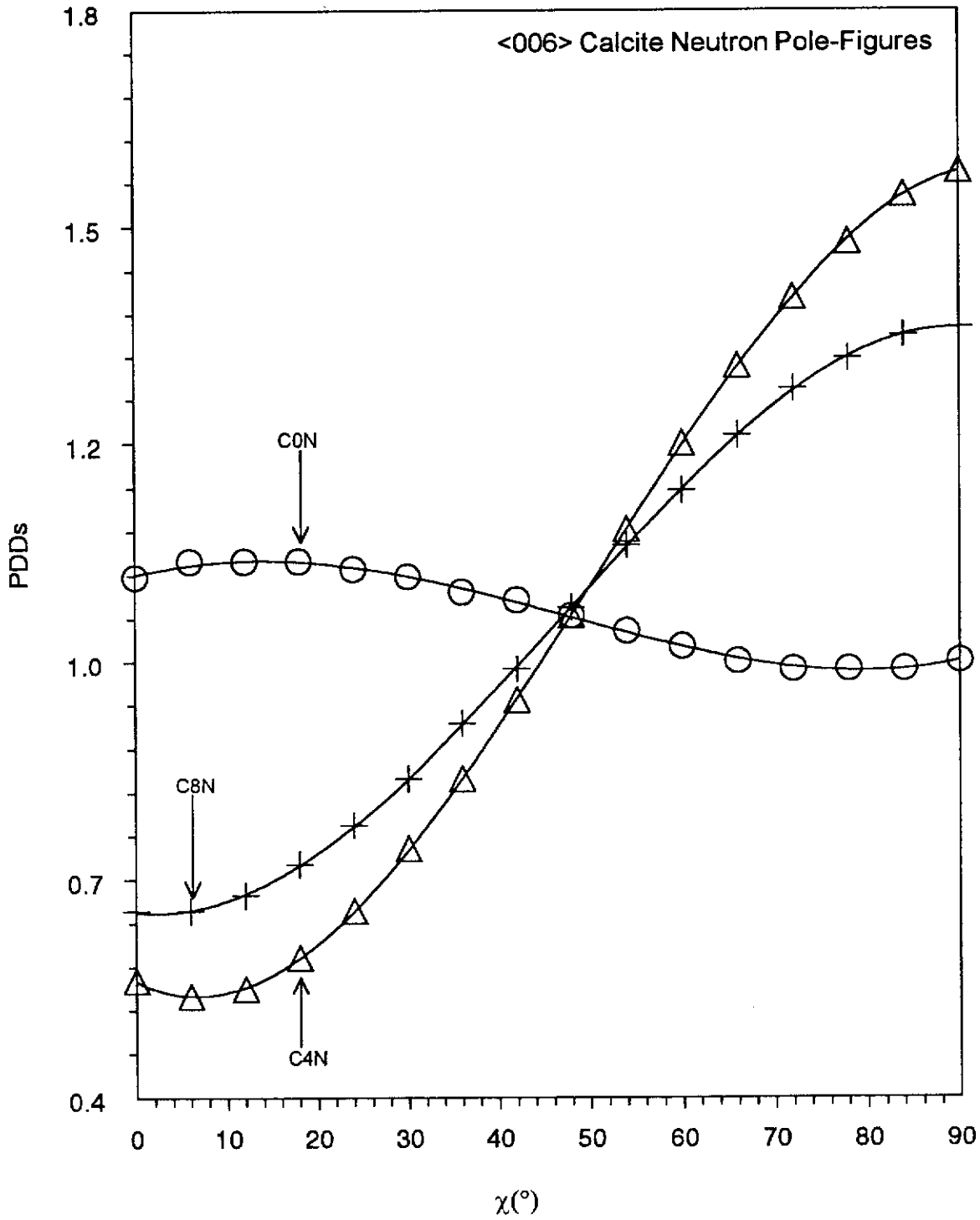

Figure 5.26. 'Quasi-normalised' PDDs for the calcite <006> neutron pole-figures: non pressed - C0N; briquetted for 88MPa - C4N; and briquetted for 176MPa - C8N.

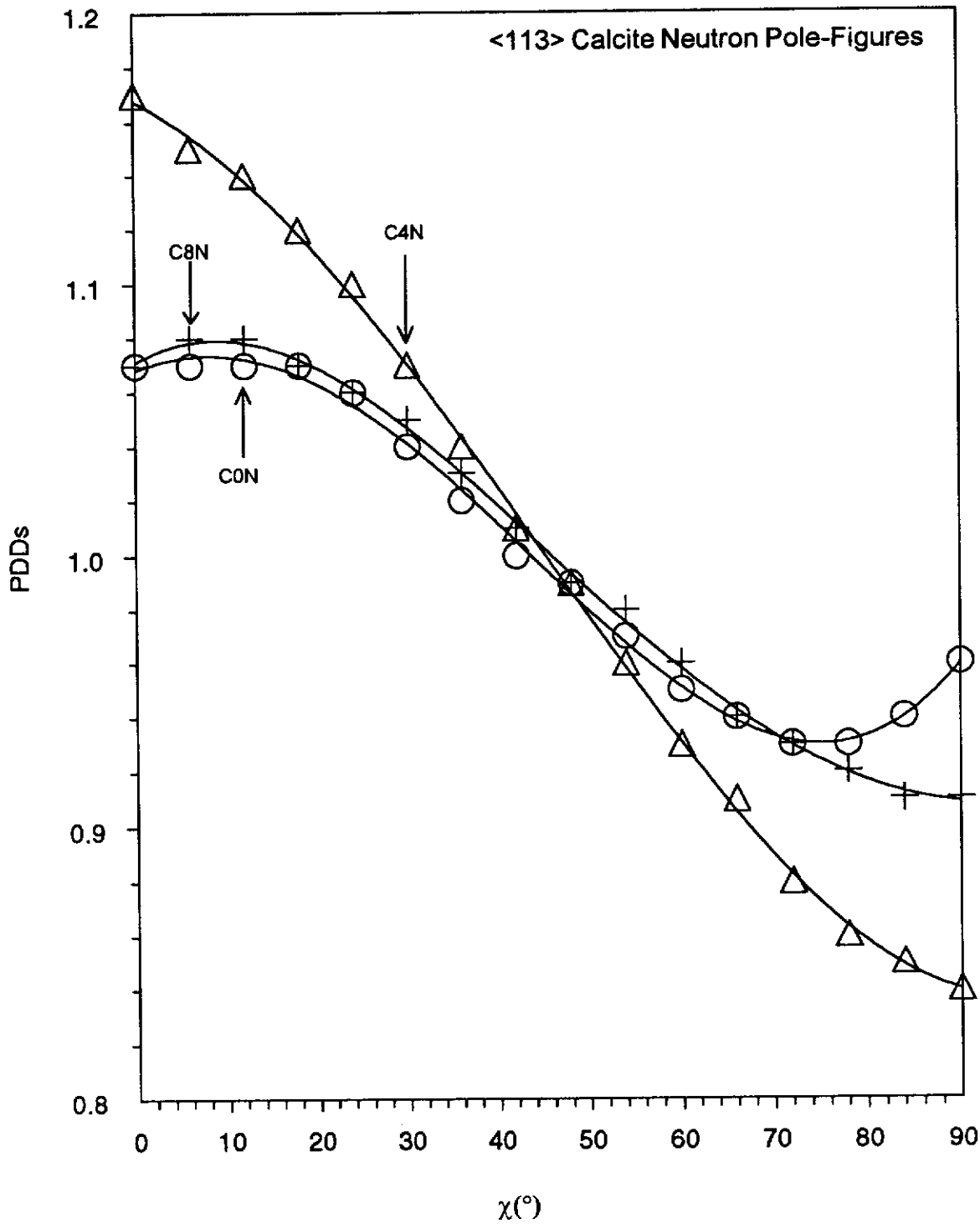

Figure 5.27. 'Quasi-normalised' PDDs for the calcite <113> neutron pole-figures: non pressed - C0N; briquetted for 88MPa - C4N; and briquetted for 176MPa - C8N.

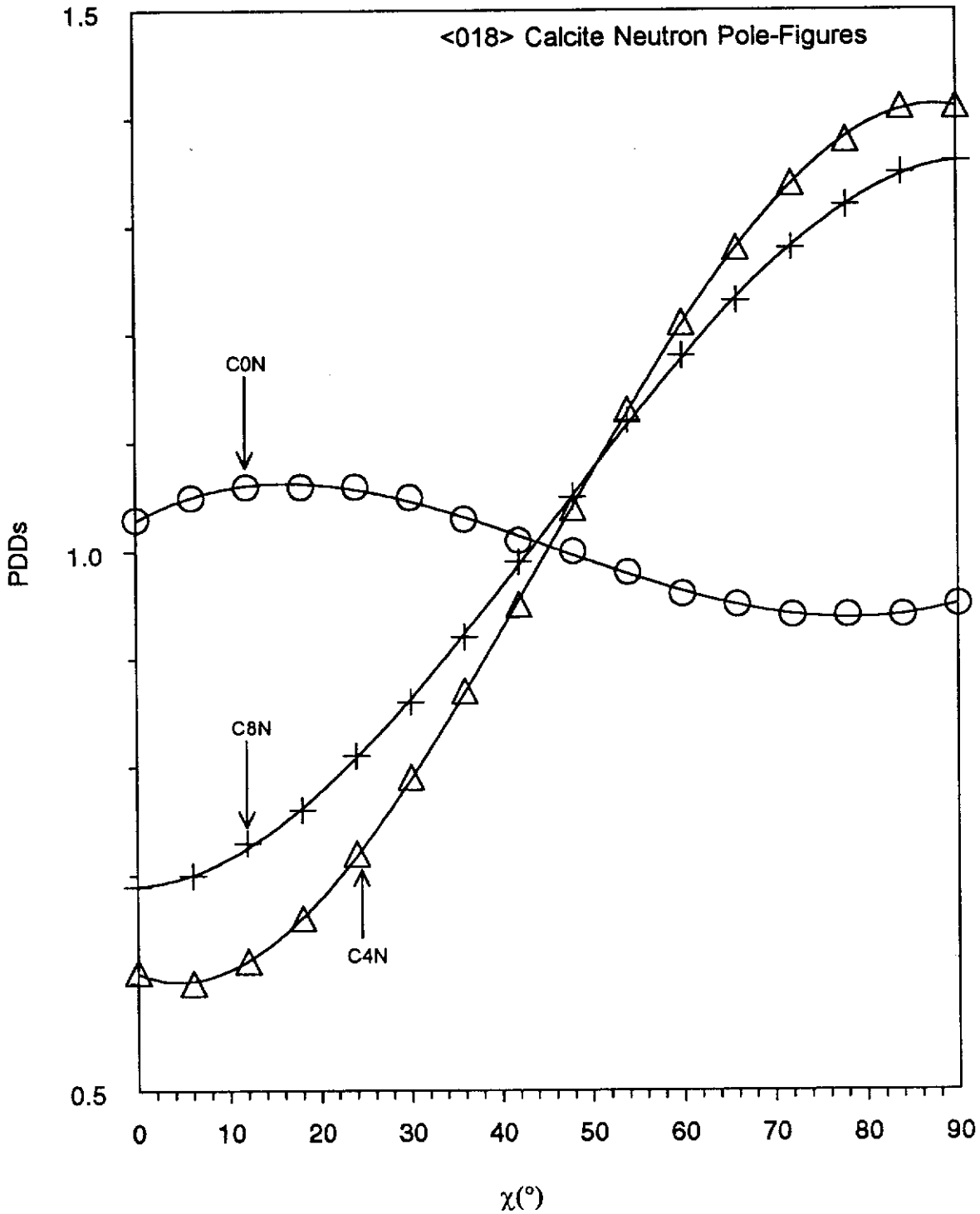

Figure 5.28. 'Quasi-normalised' PDDs for the calcite <018> neutron pole-figures: non pressed - C0N; briquetted for 88MPa - C4N; and briquetted for 176MPa - C8N.

(a) SE analysis - normalised

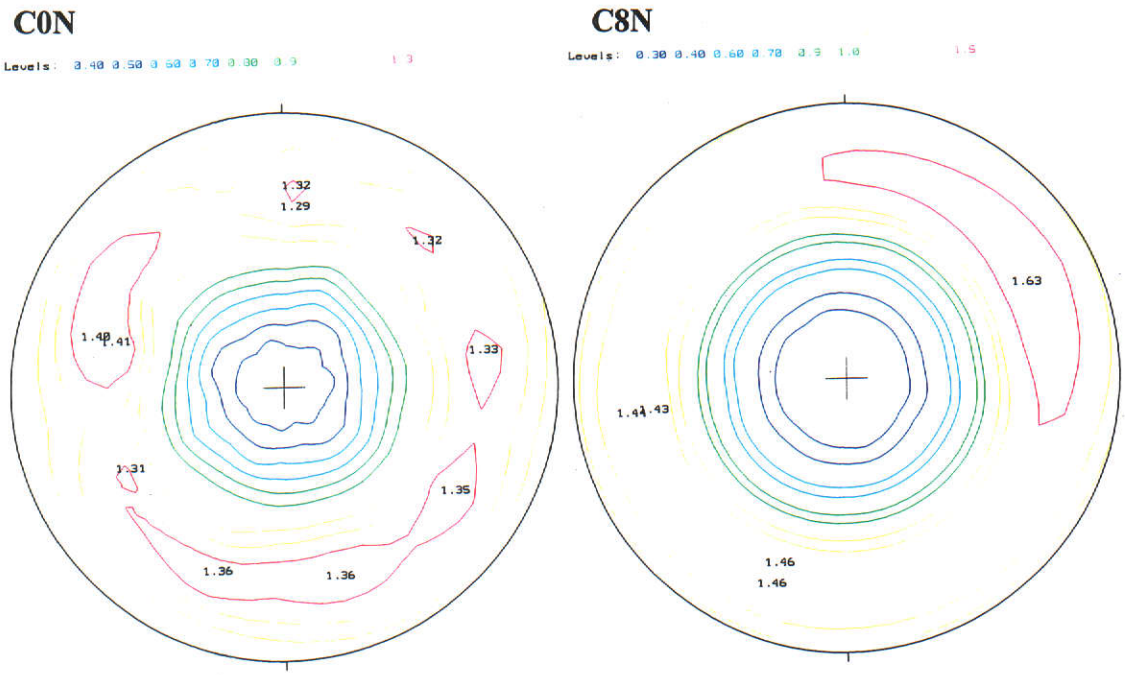

(b) SE analysis - recalculated

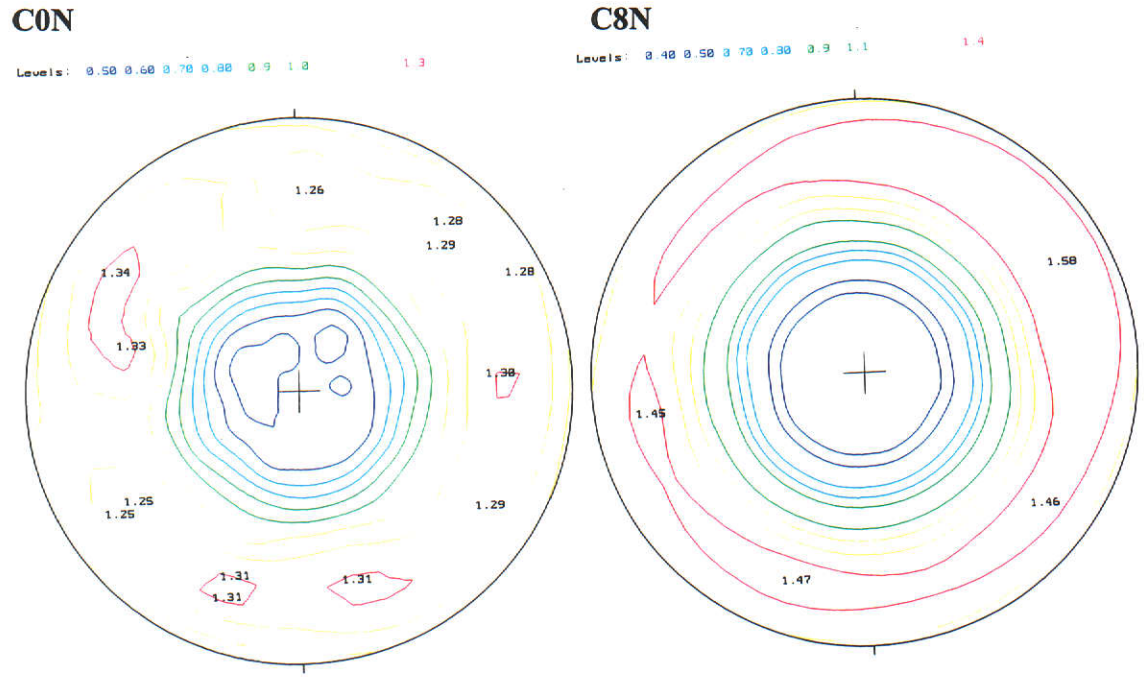

Figure 5.29. The calcite <006> neutron pole-figures normalised (above) and recalculated (below) after SE analysis. The contour levels are in random density units.

Table 5.4

Calcite Minimum and Maximum NPD PDD Values from SE analysis

Code	hkl	SE Analysis				Quasi-Normalisation	March model
		Normalised Pole-Figure		Recalculated Pole-Figure			
		Minimum	Maximum	Minimum	Maximum	χ=0°	
C0N	104	0.2	1.3	0.7	1.1	1.1	0.9
C4N		0.2	1.3	0.4	1.2	0.8	0.7
C8N		0.2	1.3	0.5	1.1	0.9	0.6
C0N	012	0.2	1.3	0.8	1.2	1.1	1.0
C4N		0.2	1.3	0.8	1.2	1.1	0.9
C8N		0.2	1.2	0.8	1.2	1.0	0.9
C0N	006	0.2	1.4	0.5	1.3	1.1	1.0
C4N		0.1	1.6	0.2	1.6	0.6	0.9
C8N		0.1	1.6	0.3	1.6	0.6	0.8
C0N	113	0.2	1.3	0.8	1.3	1.1	1.0
C4N		0.2	1.2	0.8	1.4	1.2	0.8
C8N		0.2	1.2	0.8	1.4	1.1	0.7
C0N	018	0.2	1.5	0.4	1.3	1.0	1.0
C4N		0.1	1.5	0.1	1.4	0.6	0.9
C8N		0.1	1.5	0.2	1.4	0.7	0.9

including <104>. The influence of pressure on the <006> pole-figure [Figure (5.26)] shows consistency with the XRPD diffractometry results [Section (4.4.2)] in that (i) the <006> PDD responds to pressure more readily than do the other directions examined here, and (ii) the reduction in PDD for $\chi = 0°$ to values well below unity agrees with there being Rietveld r-parameter values less than 1.00 for NPD data.

The texture-pressure responses for the set of directions examined is more complex than might be expected from the NPD Rietveld r-pressure plot [Figure (4.11b)] again indicating that the March model gives texture character descriptions which might be described as simplistic.

Figure (5.29) shows the <001> pole-figures for the calcite samples C0N and C8N derived by SE analysis, and Table (5.3) gives a numerical summary of the features of PDDs extracted using the <012>, <104>, <006>, <113> and <018> pole-figures. The PDD values obtained by direct measurement and those extracted from Rietveld analysis with the March model are included for comparison.

5.4 Discussion

The pole-figure measurements have confirmed the findings in Chapter 4 from Rietveld refinements that bulk material textures, as obtained by NRPD, are profoundly different from those derived by XRPD. The near-surface character of the XRPD measurements means that the x-ray texture results may be, at least in large part, attributed to effects induced by uniaxial pressing. Therefore, the XRPD-derived textures are unlikely to provide useful information on the 'true' texture of the powder, even for the near-surface, when pressing is employed. However, it seems likely that NPD does provide reasonable descriptions of bulk textures in uniaxially-pressed powders.

Figures (5.30) - (5.32) show comparisons of the PDDs from pole-figure analysis and the corresponding plots from the Rietveld analyses. The agreement is satisfactory for the limited NPD data available [see calcite results in Figure (5.32), and Tables (5.2) and (5.3)], but poor for the XRPD data [Figures (5.30) and (5.31)]. The apparent 'failure' of the Rietveld model is obvious from the much higher PDD

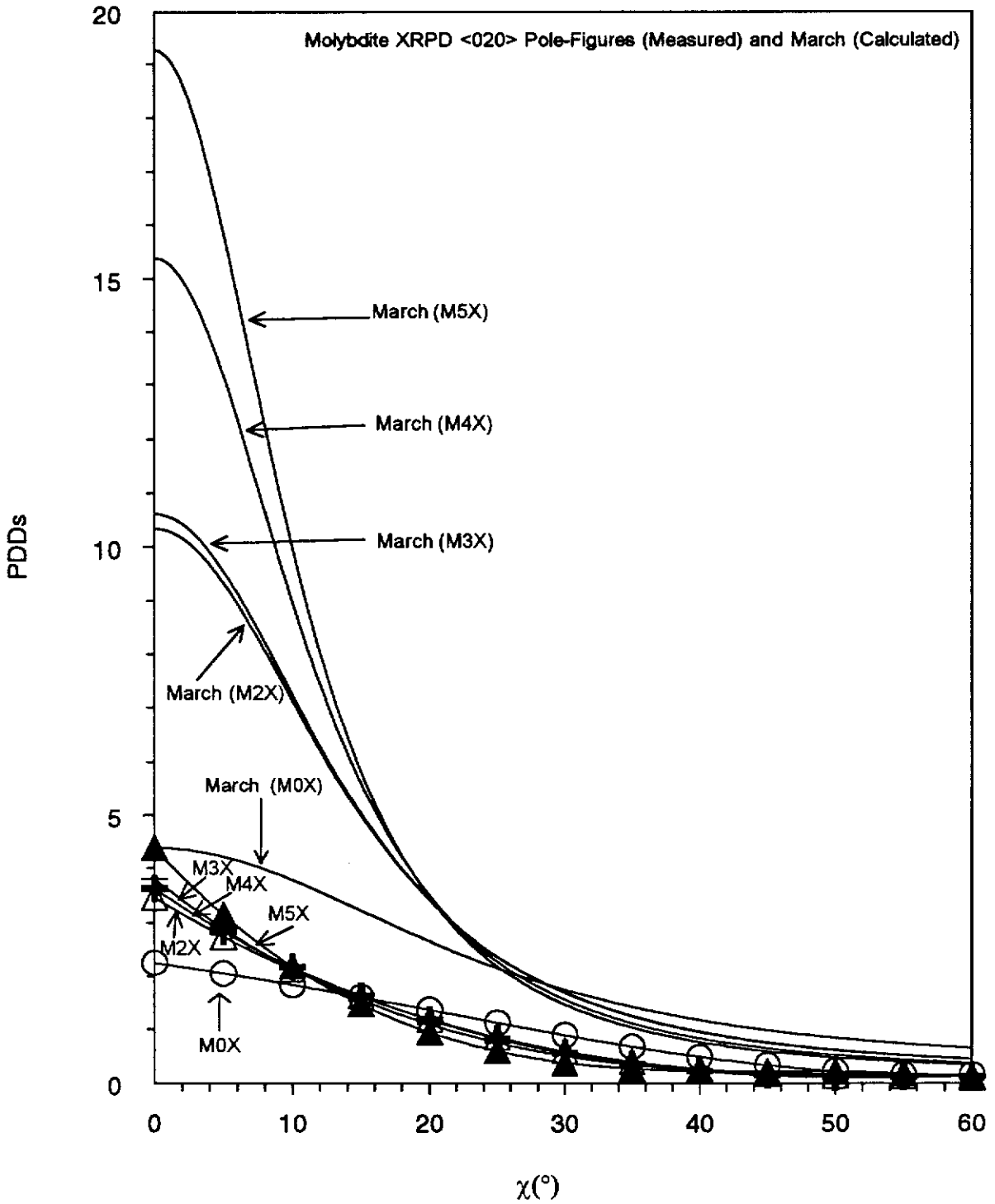

Figure 5.30. Plots of molybdite XRPD <020> PDDs derived from pole-figures and Rietveld r-parameters: non pressed - M0X; briquetted for 44MPa - M2X; briquetted for 66MPa - M3X; briquetted for 88MPa - M4X; and briquetted for 110MPa - M5X.

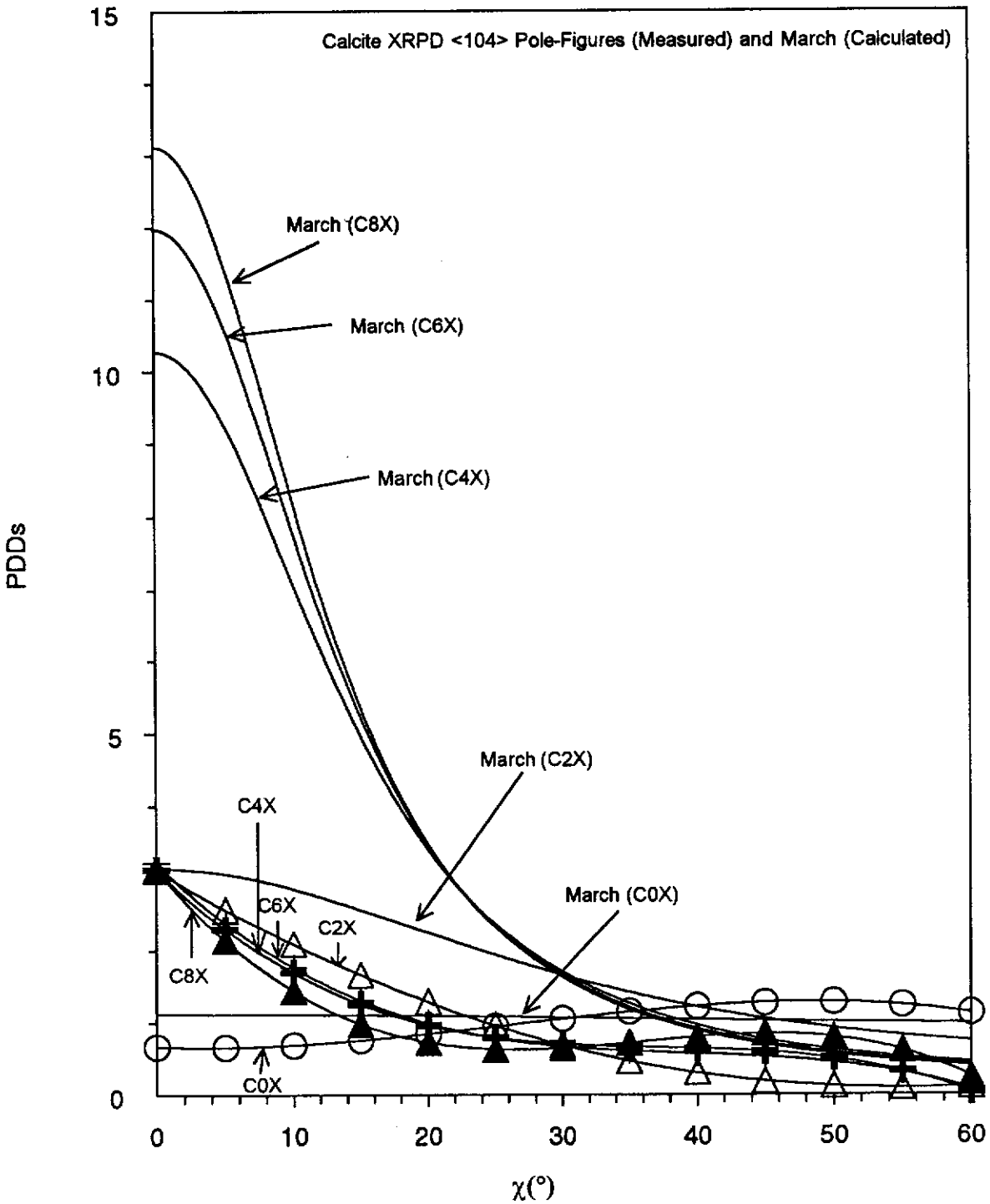

Figure 5.31. Plots of calcite XRPD <104> PDDs derived from pole-figures and Rietveld r-parameters: non pressed - C0X; briquetted for 44MPa - C2X; briquetted for 132MPa - C6X; briquetted for 88MPa - C4X; and briquetted for 176MPa - C8X.

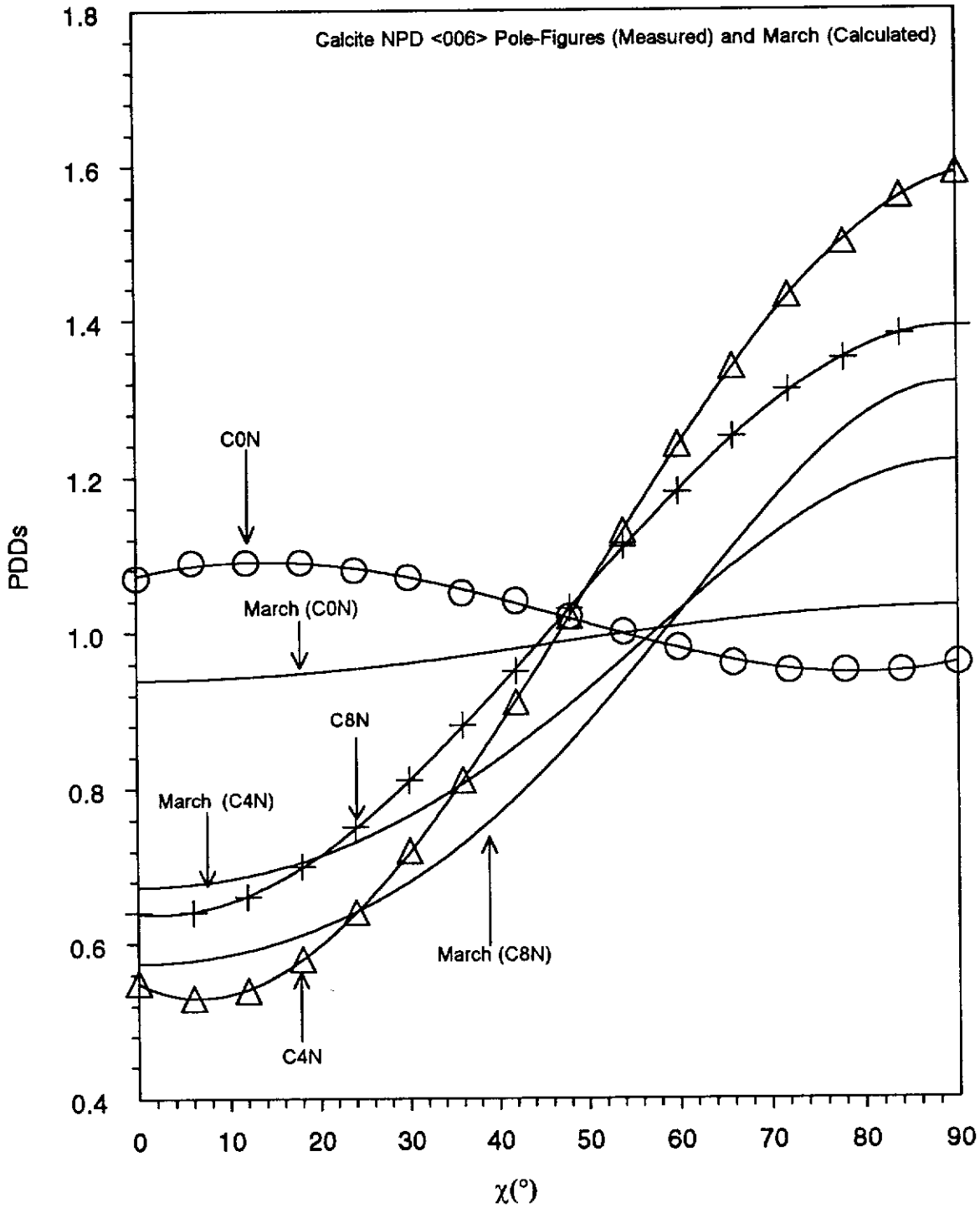

Figure 5.32. Plots of calcite NPD <006> PDDs derived from pole-figures and Rietveld r-parameters: non pressed - C0N; briquetted for 88MPa - C4N; and briquetted for 176MPa - C8N.

values obtained as χ approaches zero. The poor agreement obtained for the XRPD data may be attributed to the complexity of the near-surface pole figures obtained with x-rays, and to the inability of the Rietveld model to accommodate these complexities.

CHAPTER 6

CONCLUSIONS

6.1 Review of Study Objectives

The statement of objectives in Section (1.6) needs to be restated in summarising the results reported in Chapters 4 and 5:

> *to extend the work of Li et al. (1990); Sitepu (1991); O'Connor, Li and Sitepu (1991, 1992); and Sitepu, O'Connor and Li (1996) on the general applicability of the March (1932) model for modelling PO with both XRPD and NPD powder data, with reference to :*
>
> - *the reliability of the March model and*
> - *its use in correcting of powder diffraction intensities for PO bias.*

6.2 Conclusions

The conclusions reached in the study are the following:

- The March model appears to provide adequate PO representations for moderate levels of PO only. The method gave increasingly unsatisfactory GOFI values for r-parameters less than approximately 0.9. *It is therefore recommended that spherical harmonic modelling be employed for more substantial levels of PO in that spherical harmonic modelling does not suffer from the approximation made for the March model.*
- The XRPD results (pole-figure and Rietveld), which might be expected to provide details of the near-surface texture, appear to largely reflect the near-surface texture induced by uniaxial pressing.
- In contrast to the XRPD textures, the descriptions from NPD analysis are probably correct for the bulk material and not substantially influenced by the pressing procedure.

- A formalism developed in the study for converting the March r-parameter to a bulk modulus estimate (and, therefore, a measure of powder compressibility) has been largely validated by direct measurements of bulk modulus.
- The differences in textures obtained by XRPD and NPD is exemplified by the surprising result that the calcite PO direction is clearly different for the 2 data sets.
- The testing of powder randomness by directly measuring the pole-density is a valuable tool for x-ray powder diffractometry when random powders are required.
- A useful outcome of the NPD work has been the discovery that some Rietveld codes, including the LHPM software used extensively in Australia, have not correctly allowed for symmetry-equivalent reflections. Symmetry-equivalent reflection contributions must be taken into account by Rietveld programs in modelling texture.

REFERENCES

Ahtee, M., Nurmela, M., Suortti, P. and Jarvinen, M. (1989). *Correction of preferred orientation in Rietveld refinement.* Journal of Applied Crystallography, 22, 261-268.

Altomare, A., Cascarano, G., Giacovazzo, C. and Guagliardi, A. (1994). *Early finding of preferred orientation: a new method.* Journal of Applied Crystallography, 27, 1045-1050.

Altomare, A., Burla, M.C., Cascarano, G., Giacovazzo, C., Guagliardi, A., Moliterni, A.G.G. and Polidori, G. (1996). *Early finding of preferred orientation: applications to direct methods.* Journal of Applied Crystallography, 29, 341-345.

Baharie, E. and Pawley, G.S. (1983). *Counting statistics and powder diffraction scan refinements.* Journal of Applied Crystallography, 16, 404-406.

Berar, J.F. and Garnier, P. (1992). *A versatile program for Rietveld refinement.* In Accuracy in Powder Diffraction II: Proceedings of the International Conference, Gaithersburg, USA, May 26-28, 1992. Edited by E. Prince and J.K. Stalick. NIST Special Publication 846, page 212.

Bunge, H.J. (1965). *Zun Darstellung allgemeiner Texturen.* Zeitschr. Metallkunde, 56, 872-874.

Bunge, H.J. (1982). *Texture analysis in materials science.* Butterworth Publications, London.

Bunge, H.J. (1985). *Representation of preferred orientations.* In Preferred Orientation in Deformed Metals and Rocks, edited by H.-R. Wenk, pp. 73-108. Orlando: Academic Press.

Bunge, H.J. (1986). *Experimental techniques of texture analysis.* DGM Informations-gesellschaft: Verlag.

Bunge, H.J. (1992). *Preferred orientation analysis in textured materials.* Advances in X-ray Analysis, 35, 263-275.

Bunge, H.J. and Park, N.J. (1996). *A probability criterion for correct indexing of powder diffraction diagrams on the basis of preferred orientation.* Powder Diffraction, 11, 209-217.

Caglioti, G., Paoletti, A., and Ricci, F.P. (1958). *Choice of collimators for a crystal spectrometer for neutron diffraction.* Nuclear Instruments, 3, 223-228.

Calvert, L.D., Sirianni, A.F., Gainsford, G.J. and Hubbard, C.R. (1983). *A comparison of methods for reducing preferred orientation.* Advances in X-ray Analysis, 26, 105-110.

Capkova, P., Peschar, R. and Schenk, H. (1993). *Partial multiplicity factors for texture correction of cubic structures in the disc-shaped crystallite model.* Journal of Applied Crystallography, 26, 449-452.

Capkova, P. and Valvoda, V. (1974). *Preferred orientation in powder samples of magnesium and magnesium-cadmium alloys.* Czechoslovakia Journal of Physics, B24, 891-900.

Cerny, R., Valvoda, V. and Chladek, M. (1995). *Empirical texture corrections for asymmetric diffraction and inclined textures.* Journal of Applied Crystallography, 28, 247-253.

Chang, Y. and Ahmad, N. (1982). *Thermodynamics data on metal carbonates and oxides.* Warrendale, PA.

Chen, T. (1991). *Finite-strain analysis in a fault-bounded series of folds.* Doctor of Phylosophy Thesis. University of California, Los Angles.

Chernock, W. P. and Beck, P.A. (1952). *Analysis of certain errors in the x-ray reflection method for the quantitative determination of preferred orientation.* Journal of Applied Physics, 23, 341-345.

Chernock, W. P., Mueller, M.H., Fish, H.R. and Beck, P.A. (1953). *An automatic x-ray reflection specimen holder for the quantitative determination of preferred orientation.* Rev. Sci. Instrum., 24, 925-929.

Cooper, M.J. (1982). *The analysis of powder diffraction data.* Acta Crystallography, A38, 264-269.

Dahms, M. and Bunge, H.J. (1989). *The iterative series-expansion method for quantitative phase analysis. I. General outline.* Journal of Applied Crystallography, 22, 439-447.

Dollase, W.A. (1986). *Correction of intensities for preferred orientation in powder diffractometry: application of the March model.* Journal of Applied Crystallography, 19, 267-272.

Etheridge, M.A. and Oertel, G. (1979). *Strain measurements from phyllosilicate preferred orientation - a precautionary note.* Tectonophysics, 60, 107-120.

Ferrari, M. and Lutterotti, L. (1994). *Method for the simultaneous determination of anisotropic residual stresses and texture by x-ray diffraction.* Journal of Applied Physics, 76, 7246-7255.

Hill, R.J. (1993). *Data collection strategies: fitting the experiment to the need.* . In the Rietveld method, edited by R.A. Young, International Union of Crystallography, Oxford University Press, Great Britain, pp. 61-101.

Hill, R.J. and Cranswick, L.M.D. (1994). *Rietveld refinement round robin. II. Analysis of monoclinic ZrO_2.* Journal of Applied Crystallography, 27, 802-844.

Hill, R.J. and Howard, C.J. (1986). *A computer program for Rietveld analysis of fixed wavelength x-ray and neutron powder diffraction patterns.* Australian Atomic Energy Commission Research Establishment.

Hill, R.J. and Madsen, I.C. (1984). *The effect of profile step counting time on the determination of crystal structure parameters by x-ray Rietveld analysis.* Journal of Applied Crystallography, 17, 297-306.

Hill, R.J. and Madsen, I.C. (1986). *The effect of profile step width on the determination of crystal structure parameters and estimated standard deviations by x-ray Rietveld analysis.* Journal of Applied Crystallography, 19, 10-18.

Hill, R.J. and Madsen, I.C. (1987). *Data collection strategies for constant wavelength Rietveld analysis.* Powder Diffraction, 2, 146-162.

Howard, C.J. (1982). *The approximation of asymmetric neutron powder diffraction peaks by sums of gaussians.* Journal of Applied Crystallography, 15, 615-620.

Howard, C.J., Ball, C.J., Davies, R.L. and Elcombe, M.M. (1983). *The Australian high resolution neutron powder diffractometer.* Australian Journal of Physics, 36, 507-518.

Howard, C.J. and Hunter, B.A. (1996). *A computer program for Rietveld analysis of x-ray and neutron diffraction patterns.* Australian Nuclear Science and Technology Organisation (ANSTO), Lucas Heights Research Laboratories, NSW, Australia. Revised July 1996.

Howard, C.J. and Kennedy, S.J. (1994). *Neutron diffraction.* Materials Forum, 18, 155-176.

Huejser-Gerits, E.M.C. and Rieck, G.D. (1974). *Defocusing effects in the reflection technique for the determination of preferred orientation.* Journal of Applied Crystallography, 7, 286-290.

Imhof, J. (1977). *Die Bestimmung einer naherung fur die funktion der orientierungsverteilung aus einer polfigur.* Z. Metallkunde, 68, 38-43.

International Tables for X-ray Crystallography (1995), Volume C. Mathematical, Physical and Chemical Tables. Edited by A.J. Wilson. Kluwer Academic Publishers, Dordrecht, The Nederlands, pp. 384-391 and 476-486.

Iyengar, S. S. and Percec, S. (1994). *Rietveld analysis of high density polyethylene.* Powder Diffraction, 9, 217-220.

Jarvinen, M. (1993). *Application of symmetrised harmonics expansion to correction of the preferred orientation effect.* Journal of Applied Crystallography, 19, 267-272.

Jarvinen, M. (1995). *A surface-layer texture model for correction of the PO effect.* Journal of Applied Crystallography, 28, 400-407.

Jarvinen, M., Merisalo, M., Pesonen, A. and Inkinen, O. (1970). *Correction of integrated x-ray intensities for preferred orientation in cubic powders.* Journal of Applied Crystallography, 3, 313-318.

Judson, E.A., Hill, D.N., Young, R.A., Cagle, J.R., Lackey, W.J., Carter, W.B. and Barefield, E.K. (1994). *An analysis of preferred orientation in $YBa_2Cu_3O_{7-x}$ superconducting films deposited by CVD on single-rystal and polycrystalline substrates.* Powder Diffraction, 9, 250-259.

Kennedy, S.J. (1995). *Applications of neutron powder diffraction in materials research.* Advances in X-ray Analysis, 38, 35-46.

Kihlborg, L. (1963). *Least squares refinement of the crystal structure of molybdenum trioxide.* Arkiv for Kemi, 21, 357-364.

Kisi, E.H. (1994). *Rietveld analysis of powder diffraction patterns.* Materials Forum, 18, 135-153.

Klug, H.P. and Alexander, L.E. (1974). *X-ray diffraction procedures.* 2nd ed. New York: John Wiley and Sons.

Knott, R. (1998). *Neutron scattering in Australia.* Neutron News, 9, 23-32.

Larson, A.C. and Von Dreele, R.B. (1986). *GSAS: general structure analysis system.* Los Alamos National Laboratory Report LAUR, 86-748. Los Alamos, N.M., USA.

Lasocha, W. and Schenk, H. (1997). *A simplified, texture-based method for intensity determination of overlapping reflections in powder diffraction.* Journal of Applied Crystallography, 30, 561-564.

Li, D.Y., O'Connor, B.H., Roach, G.I.D. and Cornell, J.B. (1990). *Use of x-ray powder diffraction Rietveld pattern-fitting for characterising preferred orientation in gibbsites.* Powder Diffraction, 5, 79-85.

Lipshie, S.R. (1984). *Development of phyllosilicate preferred orientation in naturally and experimentally metamorphosed and deformed rocks.* Doctor of Philosophy Thesis. University of California, Los Angeles, USA.

March, A. (1932). *Mathematische theorie der regelung nach der korngestalt bei affiner deformation.* Zeitschr for Kristallographie, 81, 285-297.

Matthies, S. (1979). *On the reproducibilty of the orientation distribution function of texture samples from pole figures (ghost phenomena).* Phys. Status Solidi B, 92, 135-138.

Matthies, S., Lutterotti, L. and Wenk, H.R. (1997). *Advances in texture analysis from diffraction spectra.* Journal of Applied Crystallography, 30, 31-42.

Matthies, S. and Vinel, W.G. (1982). *On the reproducibility of the orientation distribution function of textured samples from reduced pole figures using the conception of a conditional ghost correction.* Phys. Statatus Solidi B, 112, 111-120.

Matthies, S. and Wenk, H.R. (1985). *ODF reproduction with conditional ghost correction.* In Preferred Orientation in Deformed Metals and Rocks, edited by H.-R. Wenk. Orlando: Academic Press.

Megaw, H.D. (1970). *Thermal vibrations and a lattice mode in calcite and sodium nitrate.* Acta Crystallography, A26, 235-244.

Megaw, H.D. (1973). *Crystal structure: a working approach.* W.B. Saunders Co., Philadelphia, pp. 241-247.

Muller, J., Esling, C., and Bunge, H.J. (1981). *An inversion formula expressing the texture function in terms of angular distribution functions.* Journal of Physics, 42, 161-165.

O'Connor, B.H., Li, D.Y. and Sitepu, H. (1991). *Strategies for preferred orientation corrections in x-ray powder diffraction using line intensity ratios.* Advances in X-ray Analysis, 34, 409-415.

O'Connor, B.H., Li, D.Y. and Sitepu, H. (1992). *Texture characterisation in x-ray powder diffraction using the March formula.* Advances in X-ray Analysis, 35, 277-283.

Oertel, G. (1985). *Re-orientation due to grain shape.* In Preferred Orientation in Deformed Metals and Rocks, edited by H.-R Wenk, pp. 259-265. Orlando: Academic Press Inc.

Owens, W.H. (1973). *Srain modification of angular density distributions.* Tectonophysics, 16, 249-261.

Parrish, W. and Huang, T.C. (1983). *Accuracy and precision of intensities in x-ray polycrystalline diffraction.* Advances in X-ray Analasis, 26, 35-44.

Pawley, G.S. (1980). *EDINP, the Edinburg powder profile refinement program.* Journal of Applied Crystallography, 13, 630-633.

Peschar, R., Schenk, H. and Capkova, P. (1995). *Preferred orientation correction and normalisation procedure for ab initio structure determination from powder data.* Journal of Applied Crystallography, 28, 127-140.

Popa, N.C. (1992). *Texture in Rietveld refinement.* Journal of Applied Crystallography, 25, 611-616.

Prince, E. (1981). *Comparison of profile and integrated-intensity methods in powder refinement.* Journal of Applied Crystallography, 14, 157-159.

Prince, E. (1985). *Precision and accuracy in structure refinement by the Rietveld method.* In structure and statistics in crystallography edited by A.J. Wilson, Adenine Press.

Prince, E. (1993). *Mathematical aspects of Rietveld refinement.* In the Rietveld method, edited by R.A. Young, Oxford University Press, Great Britain, 43-54.

Rietveld, H.M. (1967). *Line profile of neutron powder diffraction peaks for structure refinement.* Acta Crystallography, 22, 151-152.

Rietveld, H.M. (1969). *A profile refinement method for nuclear and magnetic structures*. Journal of Applied Crystallography, 2, 65-71.

Roe, R.J. (1965). *Description of crystallite orientation in polycrystalline materials. III. General solution to pole figure inversion*. Journal of Applied Physics, 36, 2024-2031.

Ruer, D. (1976). *Methode vectorielle d'analyse de la texture*. PhD Thesis, University of Metz. [Originil reference unavailable - cited by Matthies and Wenk (1985) in the textbook *Preferred Orientation in Deformed Metals and Rocks*, edited by H.-R. Wenk. Orlando: Academic Press].

Ruer, D. and Baro, R. (1977). *A new method for the determination of the texture of materials of cubic structure from incomplete reflection pole figures.* Advances in X-ray Analysis, 20, 187-200.

Sakata, M. and Cooper, M.J. (1979). *An analysis of the Rietveld profile refinement method.* Journal of Applied Crystallography, 12, 554-563.

Sasa, Y. and Uda, M. (1976). *Structure of stoichiometric* USi_2. Journal of Solid State Chemistry, 18, 63-68.

Siemens (1986). *X-ray spectrometers and diffractometers*. Catalogue MP 42, 1986, Federal Republic of Germany, order number E86060-K6042-A101-A2-7600.

Sitepu, H. (1991). *Characterisation of preferred orientation in crystalline materials by x-ray powder diffraction*. Master of Applied Science Thesis. Curtin University of Technology.

Sitepu, H., O'Connor, B.H. and Li, D.Y. (1996). *Preferred orientation in powders and influence on Rietveld x-ray powder diffraction pattern-fitting*. Physics Journal of the Indonesian Physical Society, 1, 73-80.

Smith, D.K. and Barrett, C.S. (1979). *Special handling problems in x-ray diffractometry*. Advances in X-ray Analysis, 22, 1-12.

Suortti, P. and Jennings, L.D. (1977). *Accuracy of structure factors from x-ray powder intensity measurements*. Acta Crystallography, A33, 1012-1027.

Toraya, H. and Marumo, F. (1981). *Preferred orientation correction in powder pattern-fitting*. Mineralogical Journal, 10, 211-221.

Uda, M. (1967). *The structure of synthetic* Fe_3S_4 *and the nature of transition to FeS.* Zeitschrift fur Anorgnische und Allgemeine Chemie, 350, 105-109.

Vadon, A. (1981). *Generalisation et optimisation de la methode vectorielle d'analyse de la texture.* PhD Thesis, University of Metz, France.

Valvoda, V. (1986). *Texture correction in phase analysis and thin film studies.* Powder Diffraction, 1, 28-32.

Valvoda, V. (1987). *Correction of integrated x-ray intensities for preferred orientation in quantitative phase analysis.* Journal of Applied Crystallography, 20, 453-456.

Valvoda, V. (1992). *Preferred orientation effects.* In Accuracy in Powder Diffraction II: Proceedings of the International Conference, Gaithersburg, USA, May 26-28, 1992. Edited by E.Prince and J.K. Stalick. NIST Special Publication 846, 127-135.

Von Dreele, R.B. (1997). *Quantitative texture analysis by Rietveld refinement.* Journal of Applied Crystallography, 30, 517-525.

Weiss, L.E. and Wenk, H.-R. (1985). *An Introduction.* In Preferred Orientation in Deformed Metals and Rocks, edited by H.-R. Wenk, pp. 1-10. Orlando: Academic Press.

Wenk, H.-R. (1985). *Measurements of pole figures.* In Preferred Orientation in Deformed Metals and Rocks, edited by H.-R. Wenk, pp. 11-47. Orlando: Academic Press.

Wenk, H.-R. (1991). *Standard project for pole-figure determination by neutron diffraction.* Journal of Applied Crystallography, 24, 920-927.

Wenk, H.-R., Kern, H., Schaefer, W. and Will, G. (1984). *Comparison of neutron and x-ray diffraction in texture analysis of deformed carbonate rocks.* Journal of Structural Geology, 6, 687-692.

Wenk, H.-R., Matthies, S. and Lutterotti, L. (1994). *Texture analysis from diffraction spectra.* Materials Science Forum, 157-162, 473-480.

Will, G., Bellotto, M., Parrish, W. and Hart, M. (1988). *Crystal structures of quartz and magnesium germanate by profile analysis of synchrotron-radiation high-resolution powder data.* Journal of Applied Crystallography, 21, 182-191.

Will, G., Parrish, W. and Huang, T.C. (1983). *Crystal-structure refinement by profile fitting and least-squares analysis of powder diffraction data.* Journal of Applied Crystallography, 16, 611-612.

Williams, R.O. (1968). *The representation of the textures of rolled copper, brass, and aluminum by biaxial pole figures.* Trans. Met. Soc. AIME, 242, 104-115.

Word, D.S. and Oertel, G. (1980). *Deformation in cambrian slate belt of Wales.* Journal of Geology, 88, 309-326.

Young, R.A. (1993). *Introduction to the Rietveld method.* In the Rietveld method, edited by R.A. Young, International Union of Crystallography, Oxford University Press, Great Britain, pp. 1- 38.

APPENDIX 1

DERIVATION OF MARCH MODEL EXPRESSION

March Theory of the Reorientation of Tabular Marker by Homogeneous Strain

March's (1932) theory, models the reorientation of tabular grains in a material under compression. The theory considers the movement of planes passing through the center of the sphere. This mapping of the grains into the unit sphere neglects their detailed shapes and their positions.

Let the original rock have a uniform distribution of marker grain orientations. Consider only those grains and planes in the unit sphere that have their poles in a small circular area with a diameter of the elemental size, d. Designate the center of that area as the pole of the sphere. Then all traces of the planes with poles inside the elemental area lie in a narrow equatorial zone of width d, and planes with poles at the boundary of the elemental area have traces tangent with the two boundaries of the elemental zone. Now apply a strain at constant volume to the unit sphere, keeping in mind that the strain affects the planes themselves but not the poles.

An axial symmetric strain shortens the polar axis and enlarges the equator, thus transforming the sphere into an oblate spheroid. The strain not only makes the equatorial zone thinner but it also moves it to a greater distance from the center of the spheroid. Both effects influence the orientation of the marker planes. Because the most strongly inclined planes of the original set must remain tangent to both boundaries, the thinning of the equatorial zone reduces the maximum angle possible between planes belonging to the set. The stretching of the distance from the center in each of two principle directions further reduces this angle. Thus the elemental area occupied by the poles of the deformed planes on the surface of an undistorted unit sphere serving for reference is reduced by three factors. The number of planes and thus of poles occupying the elemental area, on the other hand, remains unchanged, and the pole density increases accordingly.

Axial symmetry was here introduced only for conceptual simplicity; symmetry does not alter the effect of strain on the density distribution near one of the principle axes.

Actually, original and final densities of poles can be compared in any direction, but this requires care with the choice of an appropriate coordinate system. It will, therefore, be sufficient to follow March's (1932) example and to give the formula relating the final pole densities in the principal directions of the strain to an original unitary and uniform density. The relationship is :

$$\varepsilon_i = \rho_i^{-1/3} - 1 \qquad \text{(A1)}$$

where ρ_i is a principal pole density, normalised by dividing it by the average pole density for all orientations, and where ε_i is a principal strain, expressed in the standard way as the change of length divided by the original length. The March (1932) model of the reorientation of tabular marker by homogeneous strain as shown in equation (A1) can be mathematically derived by using geometrical relationships approach as shown below.

March Model Derivation Using Geometrical Principles

(i) Linear Markers Approach

Consider a spherical portion of the specimen of radius r_o containing numerous linear markers. Each marker represents a vector directed outward from the sphere centre, and the markers are assumed to have a uniform distribution of orientations prior to deformation - see Figure (A1). After deformation due to a stress applied along axis x_i, the original sphere becomes a triaxial ellipsoid with principal semi-axes r_i'.

In order to model the deformation, a conical element subtending a small solid angle $\partial\omega_o$ on the undeformed sphere is considered. The axis of the conical element x_1, and ∂r_1 is the radius of the circular base of the conical element. The solid angle subtended by the circular base is :

$$\partial w_o = \frac{\pi(\partial r_1)^2}{r_o^2} \qquad \text{(A2)}$$

After deformation, the base of the conical element will then be an ellipsoid, with the solid angle subtended by the base of the deformed cone being given by :

$$\partial\omega' = \frac{r_1' r_2' r_3'}{(r_1')^3}\partial\omega_o \qquad \text{(A3)}$$

If the specimen undergoes dilatation D (*i.e.* a change in volume) during the deformation, then D is the ratio of final volume $(r_1' r_2' r_3')$ to initial volume (r_o^3):

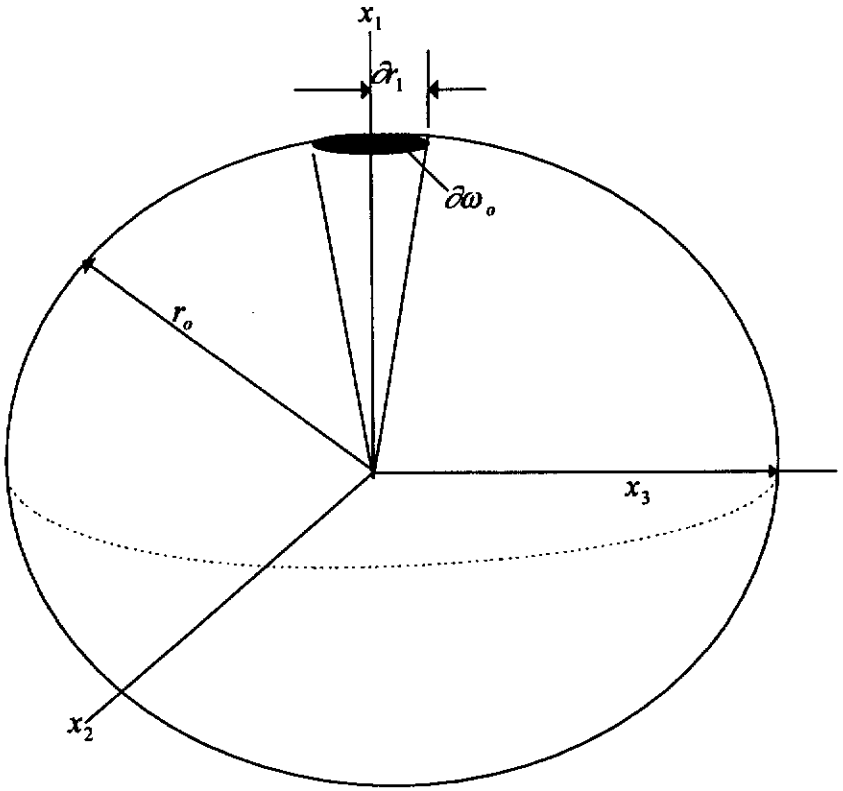

(a)

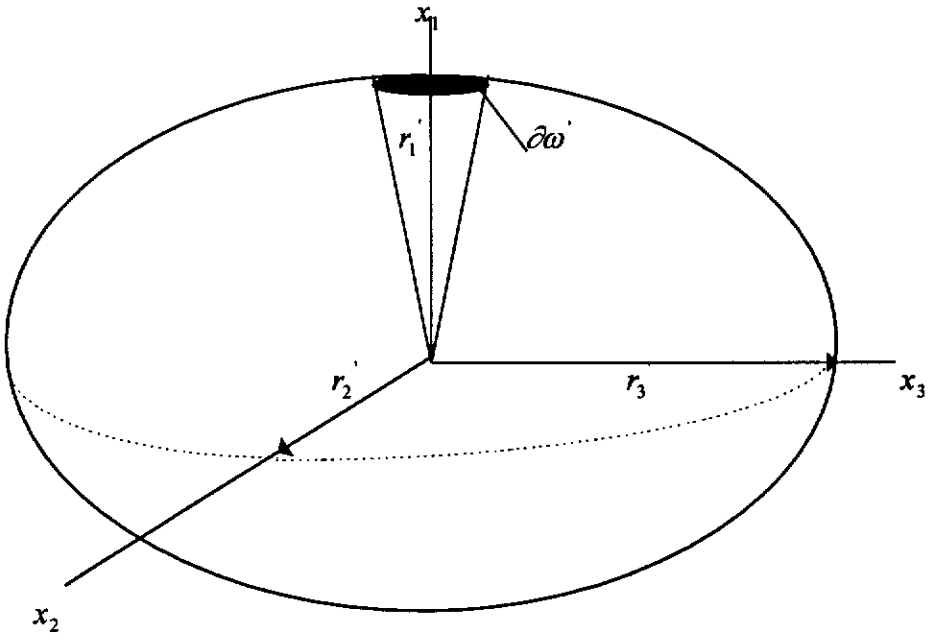

(b)

Figure A1. Rotation of linear markers during deformation. (a) Sphere of specimen before deformation. (b) Same specimen, deformed into triaxial ellipsoid. Strain is homogeneous.

$$D = \frac{r_1' r_2' r_3'}{r_o^3} \tag{A4}$$

Equation (A3) then becomes :

$$\frac{\partial \omega_o}{\partial \omega'} = \frac{1}{D} \cdot \left(\frac{r_1'}{r_o}\right)^3 \tag{A5}$$

The total number of marker orientation vectors within any conical volume element of powder is equal to the product of the angular density distribution ρ and the solid angle $\partial\omega$ subtended by each conical element. This number is conserved under deformation, such that,

$$\rho_o \partial \omega_o = \rho' \partial \omega' \tag{A6}$$

where ρ_o and ρ' are the initial and final angular density values, respectively.

Substitution of equation (A6) into (A5) gives :

$$\frac{\rho'}{\rho_o} = \frac{1}{D}\left(\frac{r_1'}{r_o}\right)^3 \tag{A7}$$

The angular density of the marker population after deformation in terms of a uniform distribution can be written as :

$$\rho_i = \frac{\rho'}{\rho_o} \tag{A8}$$

Also note that :

$$\frac{r_i'}{r_o} = 1 + \varepsilon_i \tag{A9}$$

where ε_i is the elongation strain in the direction of the principle radius vector r_i'. Substitutions of equations (A8) and (A9) into equation (A7) gives :

$$\rho_i^{1/3} D^{1/3} = (1 + \varepsilon_i) \tag{A10}$$

The relationship between the strain and the orientation distribution becomes

$$\varepsilon_i = \rho_i^{1/3} - 1 \tag{A11}$$

if the volume is conserved.

(ii) Planar Marker Approach

For the case of passive platy markers, represented by particles of planar arrays in the medium, consider the same sphere of specimen of initial radius r_o in which a large

number of planar markers are embedded. Let the each marker orientation be represented by a plane passing through the sphere center and having a pole vector directed outward from the sphere center.

Figure (A2) shows the material sphere which are deformed by a general strain, as in the linear markers case, and those the coordinate directions, x_i, to coincide with the principal strain directions. The sphere is a triaxial ellipsoid with principal semi-axes of r_i' in the x_i directions after deformation.

Consider all planar markers having great-circle projections that are contained within a zone of width $\partial s_2 = \partial s_3$, centered about the x_2x_3 plane, on the surface of the undeformed material sphere. These planar markers orientations about the x_2x_3 plane range across an angle of $\partial\theta_2 = \partial\theta_3$, where

$$\partial\theta_2 = \frac{\partial s_2}{r_o} \tag{A12}$$

and

$$\partial\theta_3 = \frac{\partial s_3}{r_o} \tag{A13}$$

A cone with its axis in the x_1 direction would be defined by the poles of these planar markers. Suppose the diameter of the circular area subtended by the cone on the sphere surface is ∂s_1. Figure (A2) shows that in the undeformed sphere :

$$\partial s_1 = \partial s_2;\quad \partial s_1 = \partial s_3;\quad \partial\theta_1 = \partial\theta_2 \text{; and } \partial\theta_1 = \partial\theta_3 \tag{A14}$$

The part of the surface of sphere subtended by the angle can be assumed to be a planar surface because the conical element is taken to be arbitrarily small. The area, A_o, of this circular surface is

$$A_o = \frac{\pi}{4}(\partial s_1)^2 \tag{A15}$$

The solid angle, $\partial\omega_o$, subtended by the conical element is

$$\partial\omega_o = \frac{A_o}{r_o^{\,2}} = \frac{\pi}{4}(\frac{\partial s_1}{r_o})^2 \tag{A16}$$

After deformation, the zone containing the planes under consideration has a width :

$$\partial s_2' = \partial s_3';\ \partial s_2' = \partial s_2(\frac{r_1'}{r_o}) \text{; and } \partial s_3' = \partial s_2(\frac{r_1'}{r_o}) \tag{A17}$$

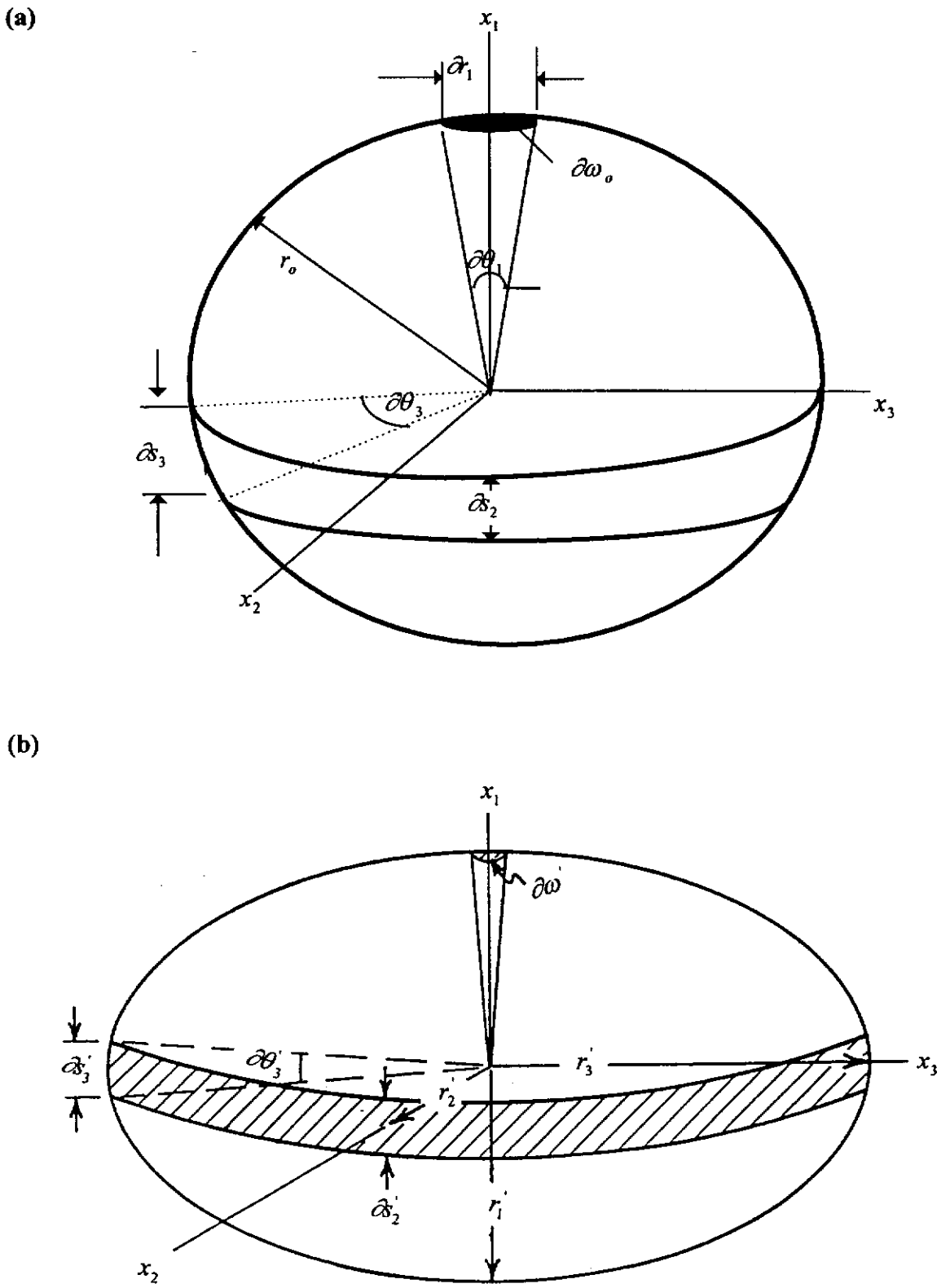

Figure A2. Rotation of the planar markers during deformation. (a) Sphere of specimen before deformation. (b) Same specimen, deformed into triaxial ellipsoid. Strain is homogeneous.

Because the change in width is a strain function only in the x_1 direction and is independent of any strains in the x_2 and x_3 directions, the deformed zone width is uniform around the entire material ellipsoid. This results from the strain homogeneity in the material. The markers planes orientations around the x_2 x_3 plane range across angles of $\partial\theta_2'$ in the x_2 direction and $\partial\theta_3'$ in the x_3 direction, where using equations (A17)

$$\partial\theta_2' = \frac{\partial s_2'}{r_2'} = \frac{\partial s_2}{r_o}\left(\frac{r_1'}{r_2'}\right) \tag{A18}$$

and

$$\partial\theta_3' = \frac{\partial s_3'}{r_3'} = \frac{\partial s_2}{r_o}\left(\frac{r_1'}{r_3'}\right) \tag{A19}$$

The planar markers poles under consideration lie within a cone that subtends an elliptical area on the surface of the materials ellipsoid about the x_1 direction after deformation. The elliptical area principal axes, A', are

$$A' = \frac{\pi}{4}(r_1'\partial\theta_2')^2 \tag{A20a}$$

and

$$A' = \frac{\pi}{4}(r_1'\partial\theta_3')^2 \tag{A20b}$$

Substitution of equations (A18) and (A19) into equations A20(a) and (b) gives :

$$A' = \frac{\pi}{4}\left(\frac{\partial s_2}{r_o}\right)^2 \frac{(r_1')^4}{r_2'r_3'} \tag{A20c}$$

The solid angle, $\partial\omega'$, subtended by conical element can be written as below :

$$\partial\omega' = \frac{A'}{(r_1')^2} \tag{A21a}$$

Substitution of equation (A20c) into equation (A21a) yields :

$$\partial\omega' = \left[\frac{\pi}{4}\left(\frac{\partial s_2}{r_o}\right)^2 \frac{(r_1')^2}{r_2'r_3'}\right] \tag{A21b}$$

As it has shown in equation (A14) that $\partial s_1 = \partial s_2$ then equation (A16) can be substituted into equation (A21b) to give :

$$\partial\omega' = \partial\omega_o \frac{(r_1')^3}{r_1' r_2' r_3'} \tag{A22}$$

Substitution of equation (A4) into equation (A22) gives :

$$\frac{\partial\omega_o}{\partial\omega'} = D(\frac{r_1'}{r_o})^{-3} \tag{A23}$$

The planar markers number within the zone under consideration remains constant throughout the deformation process. Therefore, equation (A6) also describes the poles conservation within conical elements that subtend solid angles of $\partial\omega_o$ and $\partial\omega'$ before and after deformation, respectively. Substitution of equation (A6) into (A23) gives :

$$\frac{\rho'}{\rho_o} = D(\frac{r_1'}{r_o})^{-3} \tag{A24a}$$

After deformation, $$\rho_i = \frac{\rho'}{\rho_o} \tag{A24b}$$

where ρ_i be the angular density in the x_i coordinate direction of the markers population, expressed as multiples of a uniform population distribution. Substitution of equation (A24a) into (A24b) yields :

$$\rho_i = D(\frac{r_1'}{r_o})^{-3} \tag{A25a}$$

Substitution of equation (A9) into (A25a) gives :

$$\rho_i = D(\varepsilon_i + 1)^{-3} \tag{A25b}$$

Equation (A25b) is the generalised relationship in principal coordinates between planar markers poles PO, ρ_i, and strain, ε_i. The equation of March for strain as a function of poles PO can be written as :

$$\varepsilon_i = D^{1/3}\rho_i^{-1/3} - 1 \tag{A26}$$

It can be seen that equation (A26) is analogous to equation (A10) which gives the March relationship for strain as a function of poles PO for linear markers orientation. If volume is conserved equation (A26) can be written as below:

$$\varepsilon_i = \rho_i^{-1/3} - 1 \tag{A27}$$

Equation (A27) is the most commonly used formulation of the March (1932) theory where ε_i is a principal strain at constant volume, defined as a ratio of length change of a material line to its original length, and ρ_i is the normalised frequency of poles of the

basal planes of the strain markers in one of the principal directions. March considered the geometry of passive markers, originally oriented at random, and allowed to deform homogeneously within a matrix taken to have experienced no volume change. To apply March model, one must make the untested assumption that the only mechanism by which markers respond to the deformation is passive rotation. Etheridge and Oertel (1979) showed other possible mechanisms of PO such as intracrystalline deformation, recrystallisation or preferred crystallisation which must be excluded.

It is useful to understand the March's simple theory geometric foundations because the theory has proved to be adequate for many purposes. Such understanding is needed to judge whether the theory is applicable in a particular instance or not. Lipshie (1984) provided the most complete derivation of the March model and demonstrated how its application works. Oertel (1985) developed a procedure to estimate March strain in rock from the degree of phyllosilicate PO by combining March (1932) theory and transmission XRD technique. Oertel's experimental results showed that the March model has been highly successful in describing, in detail, the textures found in natural and synthetic deformed materials and in quantitative relating deformation to PO. Oertel (1985) indicated also that the formula for rod-shaped markers finds application more rarely because a rodlike crystal habit is uncommon among the rock-forming minerals and also because those minerals that have such a habit, like the amphiboles, do not diffract x-rays sufficiently strongly from the crystallographic plane normal to the long dimension of the grains to allow their use on the x-ray pole figure goniometer. This apparatus, however, is usually the most convenient tool for the estimation of the orientations distributions of large number of grains in a materials [see Section (3.3)].

Extended March (1932) Equations

Owens (1973) derived a generalised March equation relating the angular distribution frequency (ADF) of planar elements to the strain in a rock. Chen (1991) used XRPD method to obtain the ADF data and determined the stretch tensor from the ADF by taking advantage of today's powerful personal computer. The strain results obtained by Chen from the Cambrian Slate Belt, North Wales, from Dorothea Quarry that consists of

muscovite and chlorite with quartz and minor albite and hematite specimens were [0.77±0.05, 0.30±0.04, -0.57±0.00]. These results were in good agreement with that measured directly from ellipsoidal strain indicators, the so-called "reduction spots", *i.e* [0.80, 0.31,-0.57], respectively (Wood and Oertel; 1980).

Based on the theory given by March (1932), Owens (1973) derived the modification of an angular density distribution [ADD] (*i.e.*, number of lines divided by the solid angle) of linear elements under strain. The concept used by Owens was that the number of lines contained within a material cone, defining an element of solid angle, remains constant during deformation. As a result, the ADD will alter under strain only in so far as the solid angle alters. March (1932) used the geometrical approach to derive the variation in solid angle. Following March [equation (A4)], the relationship between the volume of the cone after and before strains can be written as :

Volume after strain = Dilatation × Volume before strain

$$\frac{1}{3}r_f^3\partial w_f = |\vec{S}| \times \frac{1}{3}r_i^3\partial\omega_i \tag{A28a}$$

$$\partial w_f = |\vec{S}|(\frac{r_i}{r_f})^3\partial\omega_i \tag{A28b}$$

$$\partial w_f = |\vec{S}|(\lambda)^3\partial\omega_i \tag{A28c}$$

The relationship between the initial (f_i) and final (f_f) angular densities can be obtained by substitution of equation (A28c) into equation (A6), *i.e.*

$$f_f = f_i(\frac{\partial\omega_i}{\partial\omega_f}) = \frac{1}{|\vec{S}|}\lambda^{3/2}f_i \tag{A29}$$

If f_i has a uniform density, ρ, then equation (A29) can be written as :

$$f_f(\theta_f,\theta_f) = \frac{1}{|\vec{S}|}\rho\lambda^{3/2}f_i(\theta_f,\theta_f) \tag{A30}$$

This is the expression given by March (1932) which the angular density expressed in a direction (θ_f,θ_f) as a function of (θ_f,θ_f).

Owens (1973) generalised equation (A30) to cover any varying, initial distribution, $f_i(\theta_i,\phi_i)$ which explicitly required the relationship between (θ_i,θ_i) and (θ_f,θ_f) as shown below :

$$f_f(\theta_f,\phi_f)=\frac{1}{|\bar{S}|}\lambda^{3/2}(\theta_f,\phi_f)f_i(\theta_i,\phi_i) \tag{A31}$$

or $$r_f(\theta_f,\phi_f)=\bar{S}r_i(\theta_i,\phi_i) \tag{A32}$$

It can be seen from equations (A31) and (A32) that if the angular density, $f_i(\theta_i,\phi_i)$, is known, in direction before and after strains according to equation (A32) which a vector oriented along (θ_i,ϕ_i) moves to (θ_f,ϕ_f), then the angular density after strain in the direction (θ_f,ϕ_f) can be calculated from equation (A31).

Owens (1973) showed that, after a constant-volume deformation, the poles have the frequency distribution described by equation (A31). Chen (1991) modified equation (A31), *i.e.* the frequency distribution, F, in an arbitrary direction into the following equation :

$$F=(\lambda^2)^{3/2}f \tag{A33}$$

where f is the initial pole distribution frequency which is assumed to have been uniform for all orientation, and λ is the elongation in that arbitrary direction. The distribution frequencies F and f can be replaced by x-ray intensities, I and q, and B is augmented by a certain background noise level because the diffracted x-ray intensity is linearly proportional to the pole distribution frequency of strain markers. Equation (A33) can be written as follows :

$$I=(\lambda^2)^{3/2}q+B \tag{A34}$$

As shown in Figure (2.1) in Section (2.1.2) that equation (A34) can be extended in (i) sample coordinates, ${}^{S}X_i$ and (ii) reference coordinates, ${}^{R}X_i$, which coincide with principal axes, S_i, of a strain, ε. The Euler angles $(\varphi_1,\phi,\varphi_2)$ relates these two coordinates in which the coordinates transformation was shown in the text of the Figure (2.1) above. However, the symbols used in Figure (2.1) such as E_1,E_2 and E_3 are changing to S_1, S_2 and S_3 in following discussion. Following the transformation in Figure (2.1) which is equivalent to Figure (2.6) and equations 2.27(a), (b) and (c) in Chapter 2 Section (2.2.1); it can be seen immediately that the initial sample coordinates and the final sample coordinates are related by an orthogonal transformation matrix, **A**, which has three independent coefficients. As indicated by Bunge (1982), the three

rotations of equations 2.27(a), (b) and (c) may be expressed in matrix form [equations (2.29) and (2.30)].

The orientation $g[\varphi_1 \phi \varphi_2]$ of two coordinate systems with respect to each others can be written also in the form a_{ij}. As a result, the orientation of the reference coordinate system ${}^{R}X_i$ with respect to the sample coordinate system ${}^{S}X_i$ may be illustrated as if a moveable coordinate system is brought at first into coincidence with ${}^{S}X_i$ and then rotated through a_{ij} to come into coincidence with ${}^{R}X_i$ according to the following equation :

$$ {}^{R}X_i = a_{ij}\,{}^{S}X_j \tag{A35} $$

The inverse transformation from reference to sample coordinate is :

$$ {}^{S}X_j = \left[a_{ij}\right]^{-1}\,{}^{R}X_i \tag{A36} $$

The inverse of the matrix a_{ij} is equal to its transpose :

$$ \left[a_{ij}\right]^{-1} = \left[a_{ji}\right] \tag{A37} $$

The components of the matrix are not independent. They must obey the orthonormality relations :

$$ a_{ij} \cdot a_{ik} = \delta_{jk} \tag{A38} $$

and

$$ a_{ij} \cdot a_{kj} = \delta_{ik} \tag{A39} $$

where δ_{ij} is the Kronecker symbol

$$ \delta_{ik} = \begin{cases} 1 \; for \; i = k \\ 0 \; for \; i \neq k \end{cases} \tag{A40} $$

Equations (A38) and (A39) expresses the fact that the rows and columns of the matrix are unit vectors that are mutually perpendicular. That the components of the matrix are not independent is a drawback of this representation, especially when considering continues ODFs, which one wants to express in terms of independent variables. An advantage of the matrix representation of rotation is that the resultant rotation of two or more rotations can easily be expressed by matrix multiplication.

The condition of volume constancy implies that the principal stretches are by :

$$ S_i = (\varepsilon_i + 1) \tag{A41} $$

and

$$S_1 \cdot S_2 \cdot S_3 = 1 \tag{A42}$$

Thus the stretch tensor in reference coordinates is :

$$\left[{}^{R}S_{ij} \right] = \begin{bmatrix} S_1 & 0 & 0 \\ 0 & \dfrac{1}{S_1 S_3} & 0 \\ 0 & 0 & S_3 \end{bmatrix} \tag{A43}$$

Let in reference coordinates, ${}^{R}S$, having two independent coefficients, be the matrix notation for the stretch $\left[{}^{R}S_{ij} \right]$. In sample coordinates, the tensor, ${}^{S}S$, is related to ${}^{R}S$ by a transformation with the matrix, **A**, as a operator :

$${}^{S}S = A^{T}\ {}^{R}S\ \ A \tag{A44}$$

The components of the tensors in sample coordinates, are combinations of five coefficients, $(\varphi_1, \phi, \varphi_2)$ from A, (S_1, S_2) and ${}^{R}S$ as shown in equation (A44). The reciprocal relation of equation (A44) can be written as :

$${}^{R}S = A^{S}\ S\ \ A^{T} \tag{A45}$$

Let a material line be represented by a vector in the sample coordinates, ${}^{S}r$, which is deformed to a unit vector, ${}^{S}R (|{}^{S}R| = 1)$ by a stretch ${}^{S}S$:

$${}^{S}R = {}^{S}S\ {}^{S}r \tag{A46}$$

The deformed state has to taken into account then deduce from it the shape of the original as given below :

$${}^{S}r = {}^{S}S^{-1}\ {}^{S}R \tag{A47}$$

The square length of ${}^{S}r$ is given by :

$$\left| {}^{S}r \right|^2 = {}^{S}r^{T}\ {}^{S}r \tag{A48}$$

Substituting equation (A47) into equation (A48) yields :

$$\left| {}^{S}r \right|^2 = ({}^{S}S^{-1}{}^{S}R)^{T}({}^{S}S^{-1}{}^{S}R) = {}^{S}R^{T}\ {}^{S}S^{-1}\ {}^{S}S^{-1}\ {}^{S}R \tag{A49}$$

and substituting equation (A44) into equation (A49) gives :

$$\left| {}^{S}r \right|^2 = {}^{S}R^{T}(A^{T}\ ({}^{R}S^{-1})^2\ A){}^{S}R \tag{A50}$$

In the direction of ${}^{S}R$, the elongation direction, λ^2, defines by

$$\lambda^2 = \frac{\left| {}^{S}R \right|^2}{\left| {}^{S}r \right|^2} \tag{A51}$$

According to Owens (1973), a material plane deformed by the stretch, ${}^{S}S$, the marker pole in the initial state, l, is related to its deformed counterpart, L, by $({}^{S}S^{-1})^{T}$. Hence, the quadratic elongation in the direction of L, parallel to R, is :

$$\lambda^2 = \left(\frac{1}{{}^{S}R^{T}(A^{T}({}^{r}S)^{2}A)\ {}^{S}R} \right)^{3/2} \cdot q + B \tag{A52}$$

There are seven coefficients in the equation (A52); in addition to q and B, five are embedded in the $(A^{T}({}^{r}S)^{2}A)$ terms.

One can express the equation (A52) in principal reference coordinates to reduce the coefficients to four. To describe orientation, a set of angular variables, $({}^{r}\theta, {}^{r}\phi)$, related to the reference coordinates was described such as :

$$\tan({}^{R}\theta) = \frac{{}^{R}X_2}{{}^{R}X_1} \tag{A53a}$$

and

$$\tan({}^{R}\phi) = \frac{({}^{R}X_1{}^{2} + {}^{R}X_2{}^{2})^{1/2}}{{}^{R}X_3} \tag{A53b}$$

Hence :

$${}^{R}X_1 = \sin({}^{R}\theta)\cos({}^{R}\phi) \tag{A54a}$$

$${}^{R}X_2 = \sin({}^{R}\theta)\sin({}^{R}\phi) \tag{A54b}$$

$${}^{R}X_3 = \cos({}^{R}\theta) \tag{A54c}$$

Let a powder line be represented by a vector, ${}^{R}r$, and be deformed

$${}^{R}R\left|{}^{R}R\right| = 1 \tag{A55}$$

by the stretch ${}^{R}S$. In analogy with equations (A46), (A47), (A48) and (A51):

$${}^{R}R = {}^{R}S\ {}^{R}r \tag{A56}$$

$${}^{R}r = {}^{R}S^{-1}\ {}^{R}R \tag{A57}$$

$$\left|{}^{R}r\right| = {}^{R}R^{T}\ {}^{R}r \tag{A58}$$

and

$$\lambda^2 = \frac{\left|{}^{R}R\right|^2}{{}^{R}\left|r\right|^2} \tag{A59}$$

With equations (A56), (A57), and (A58), equation (A52) can be written as :

$$\lambda^2 = \left(\frac{1}{{}^R R^T ({}^r S)^2 A \; {}^R R} \right)^{3/2} \cdot q \qquad \text{(A60)}$$

Let the unit vector, ${}^R R$, have an orientation $({}^R\theta, {}^R\phi)$ and thus components :

$$[R_i] = [\sin {}^R\theta \cos {}^R\phi, \sin {}^R\theta \sin {}^R\phi, \cos {}^R\theta] \qquad \text{(A61)}$$

Expand the matrix notation of equations (A60) by substituting equations (A43) and (A61), then the observed x-ray intensities, I_I, with orientations $({}^R\theta_I, {}^R\phi_I)$ becomes:

$$I_I({}^R\theta_I, {}^R\phi_I) = \left[S_1^2 \sin^2 {}^R\theta_I \cos^2 {}^R\phi_I + \frac{\sin^2 {}^R\theta_I \sin^2 {}^R\phi_I}{S_1^2 S_3^2} + S_3^2 \cos^2 {}^R\theta_I \right]^{-3/2} \cdot q \qquad \text{(A62)}$$

The March-Dollase PO Correction Factor for Powder Diffraction

Consider a planar powder diffraction sample formed by a volume conserving, cylindrically-symmetric compression such that the initial sample thickness d_o is reduced to d. As the samplecompression is axially symmetric the stretch tensor axial lengths in the sample plane are equal,

$$S_1 = S_2 \qquad \text{(A63)}$$

and the stretch tensor axial length along the sample normal is defined as the March PO parameter,

$$S_3 = \frac{d}{d_o} = r \qquad \text{(A64)}$$

Furthermore, as sample volume is conserved, the product of the stretch tensor axial length is unity.

$$S_1 S_2 S_3 = 1 \qquad \text{(A65)}$$

Substitution of equations (A63) and (A64) into equation (A65) yields :

$$S_1 = S_2 = r^{-1/2} \qquad \text{(A66)}$$

Substitution of equations (A64) and (A66) into equation (A62) gives :

$$I_I({}^R\theta_I, {}^R\phi_I) = \left[r^{-1} \sin^2 {}^R\theta_I \cos^2 {}^R\phi_I + \frac{\sin^2 {}^R\theta_I \sin^2 {}^R\phi_I}{r^{-1} r^2} + r^2 \cos^2 {}^R\theta_I \right]^{-3/2} \cdot q \qquad \text{(A67)}$$

which simplifies to

$$I_I({}^R\theta_I, {}^R\phi_I) = \left[r^{-1} \sin^2 {}^R\theta_I + r^2 \cos^2 {}^R\theta_I \right]^{-3/2} \cdot q \qquad \text{(A68)}$$

or

$$I_I({}^R\theta_I, {}^R\phi_I) = P_I \cdot q \tag{A69}$$

where :

$$P_I = \left[r^{-1} \sin^2 {}^R\theta_I + r^2 \cos^2 {}^R\theta_I \right]^{-3/2} \tag{A70}$$

where θ_I is the angle between the diffracting plane normal and the sample normal.

APPENDIX 2

POLE-FIGURE DATA FOR MOLYBDITE AND CALCITE

A2.1. XRPD Molybdite

(a)

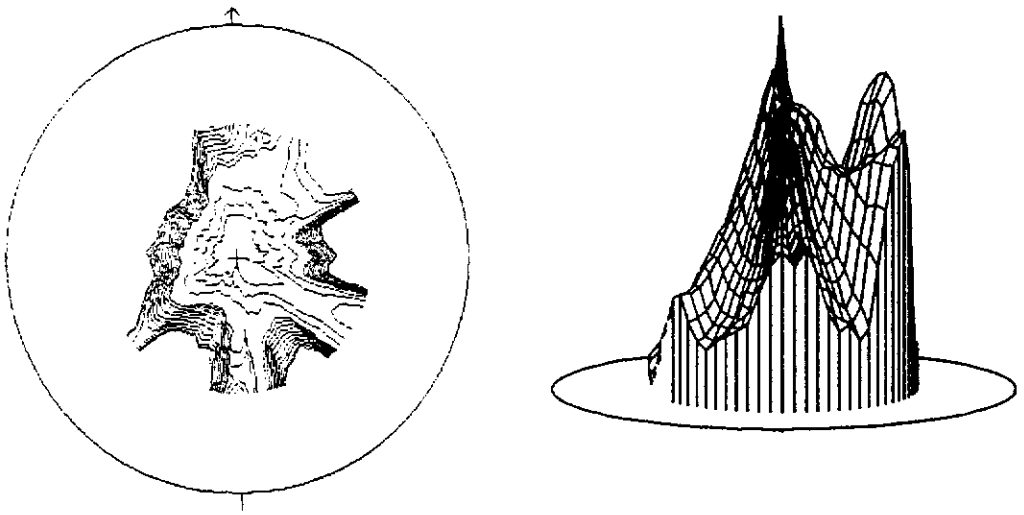

(b)

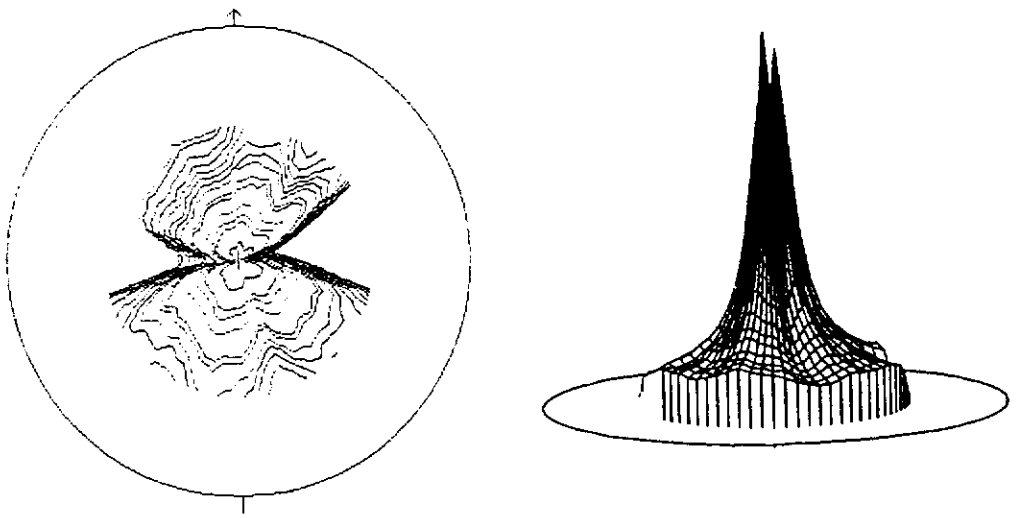

Figure A2.1.1(a). 2D and 3D representations of the molybdite <020> XRPD pole-figures: (a) side drifted - M0X and (b) briquetted for 44MPa - M2X. The contour levels are in random density units.

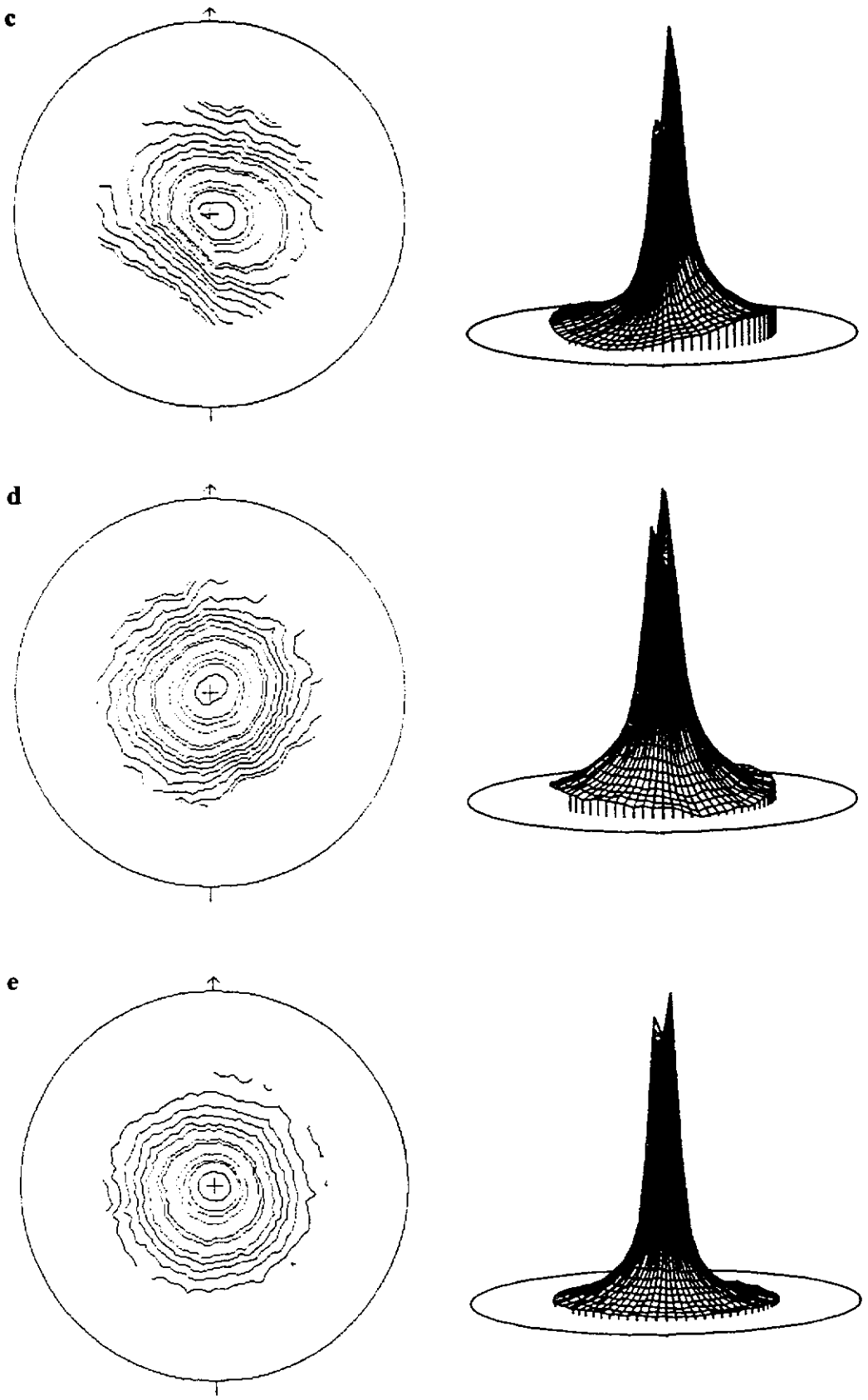

Figure A2.1.1(b). 2D and 3D representations of the molybdite <020> XRPD pole-figures: (c) briquetted for 66MPa - M3X, (d) briquetted for 88MPa - M4X and (e) briquetted for 110MPa - M5X. The contour levels are in random density units.

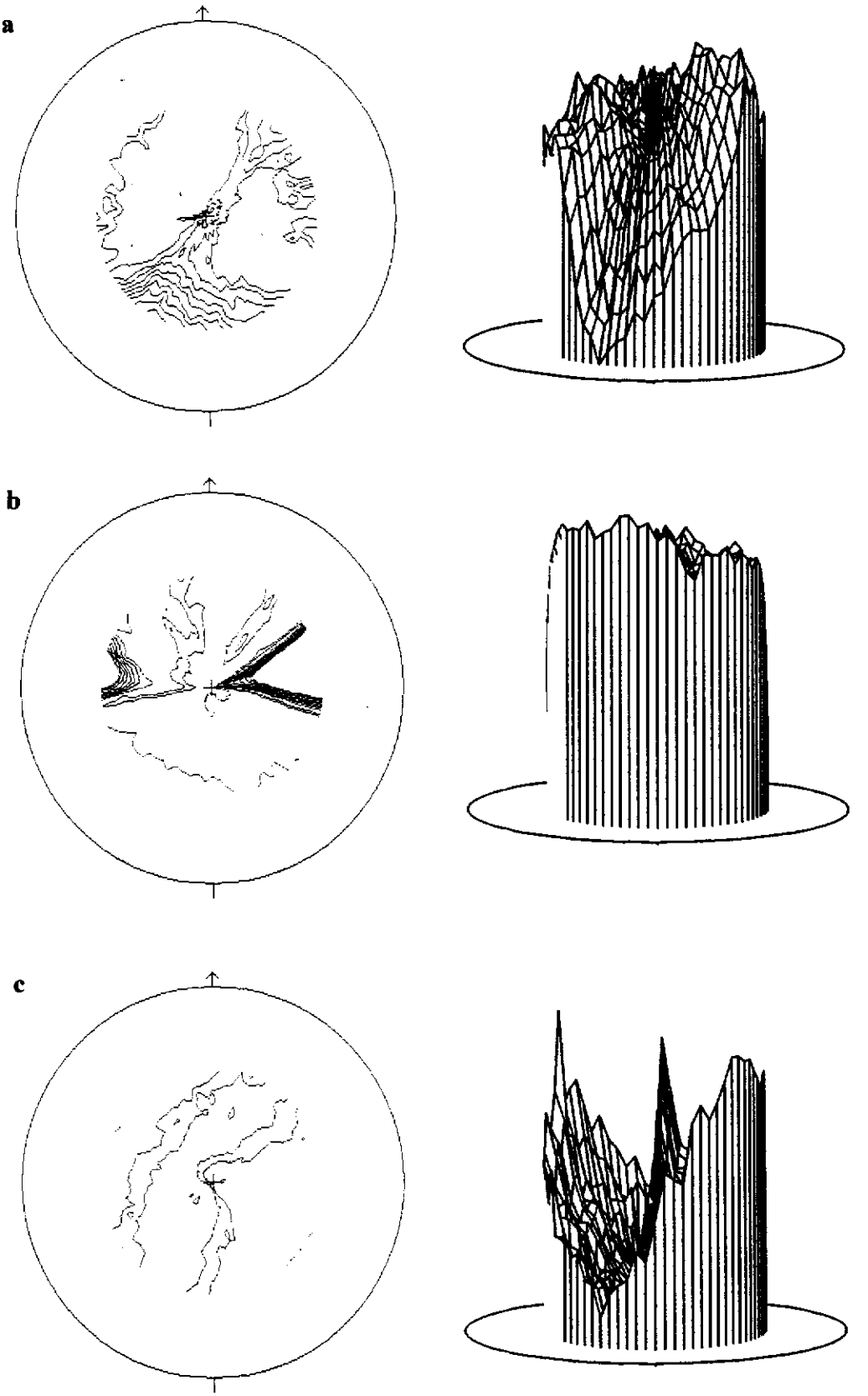

Figure A2.1.2(a). 2D and 3D representations of the molybdite <110> XRPD pole-figures: (a) side drifted - M0X, (b) briquetted for 44MPa - M2X, and (c) briquetted for 66MPa - M3X. The contour levels are in random density units.

d

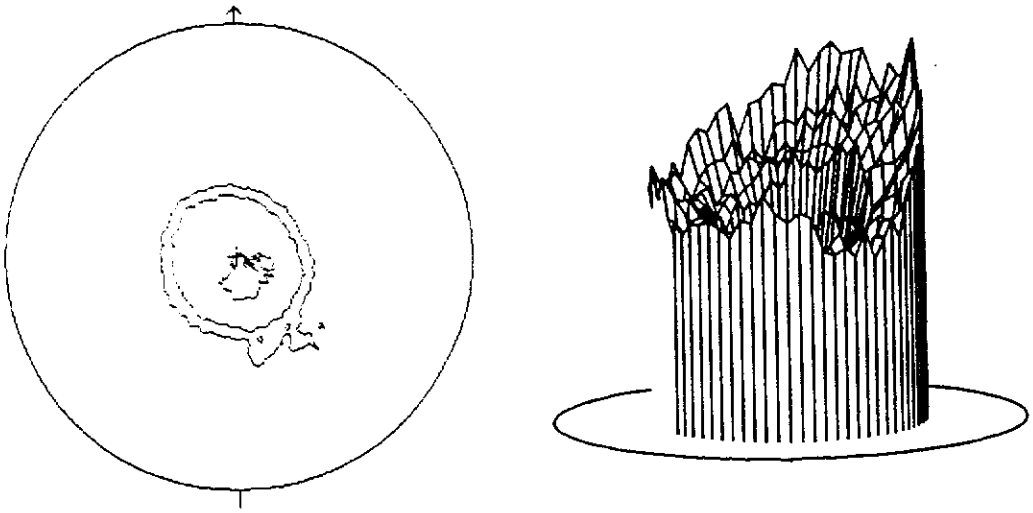

e

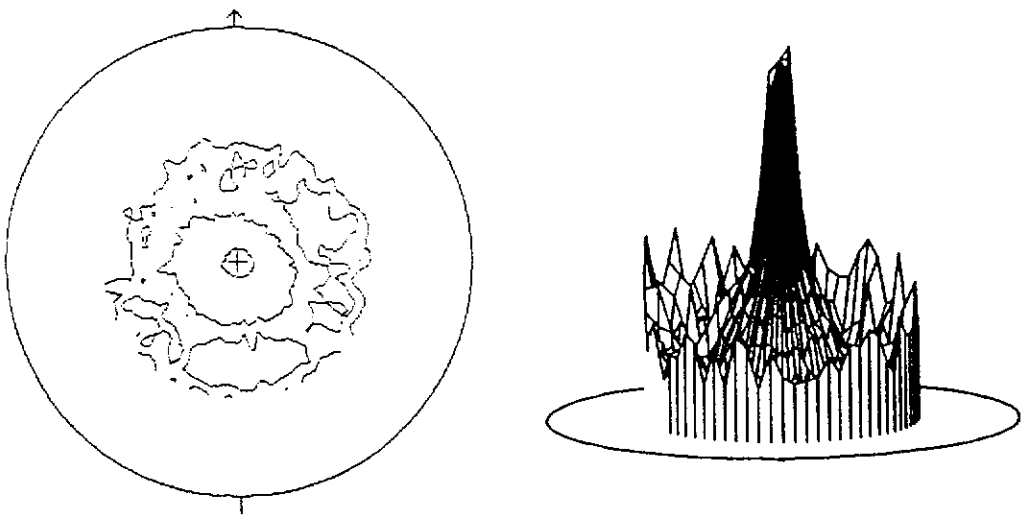

Figure A2.1.2(b). 2D and 3D representations of the molybdite <110> XRPD pole-figures: (d) briquetted for 88MPa - M4X and (e) briquetted for 110MPa - M5X. The contour levels are in random density units.

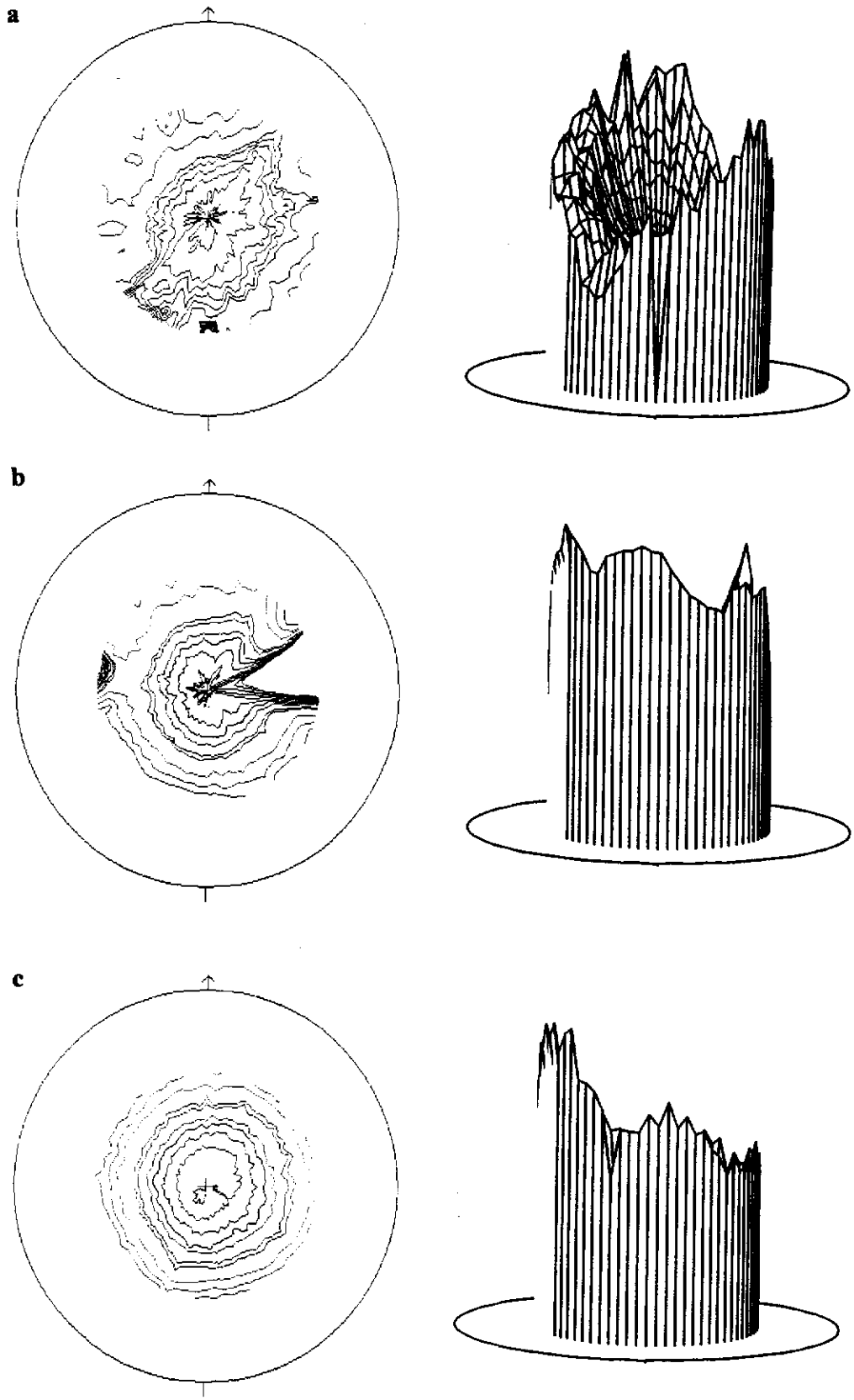

Figure A2.1.3(a). 2D and 3D representations of the molybdite <021> XRPD pole-figures: (a) side drifted - M0X, (b) briquetted for 44MPa - M2X, and (c) briquetted for 66MPa - M3X. The contour levels are in random density units.

d

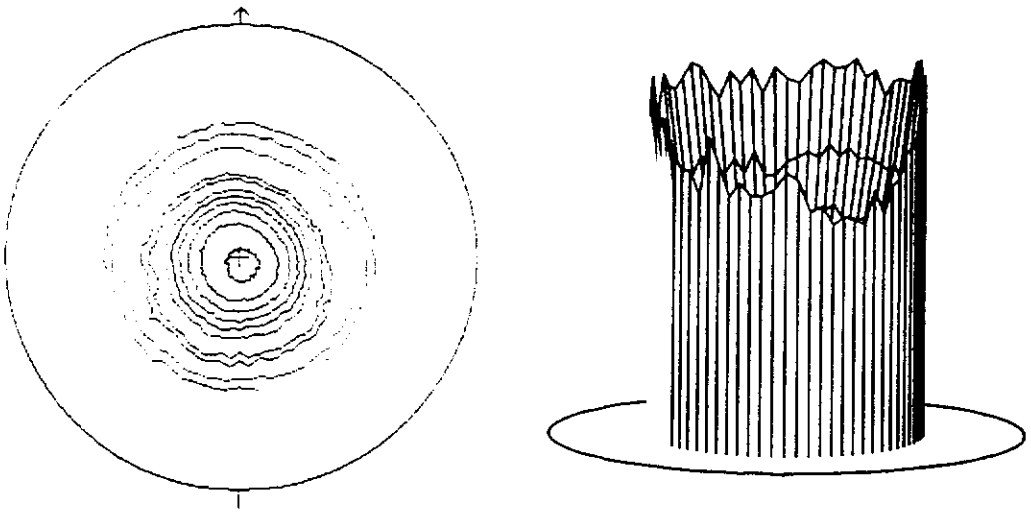

e

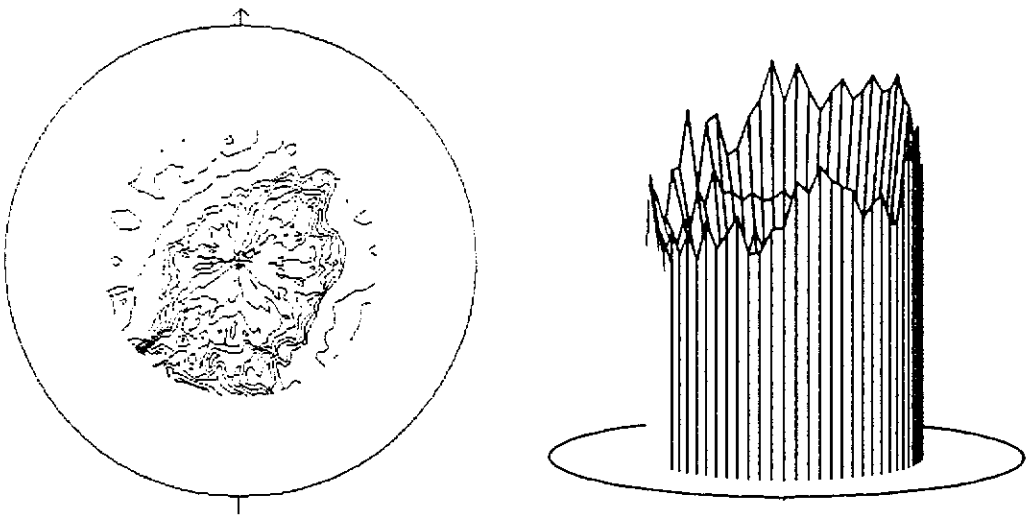

Figure A2.1.3(b). 2D and 3D representations of the molybdite <021> XRPD pole-figures: (d) briquetted for 88MPa - M4X and (e) briquetted for 110MPa - M5X. The contour levels are in random density units.

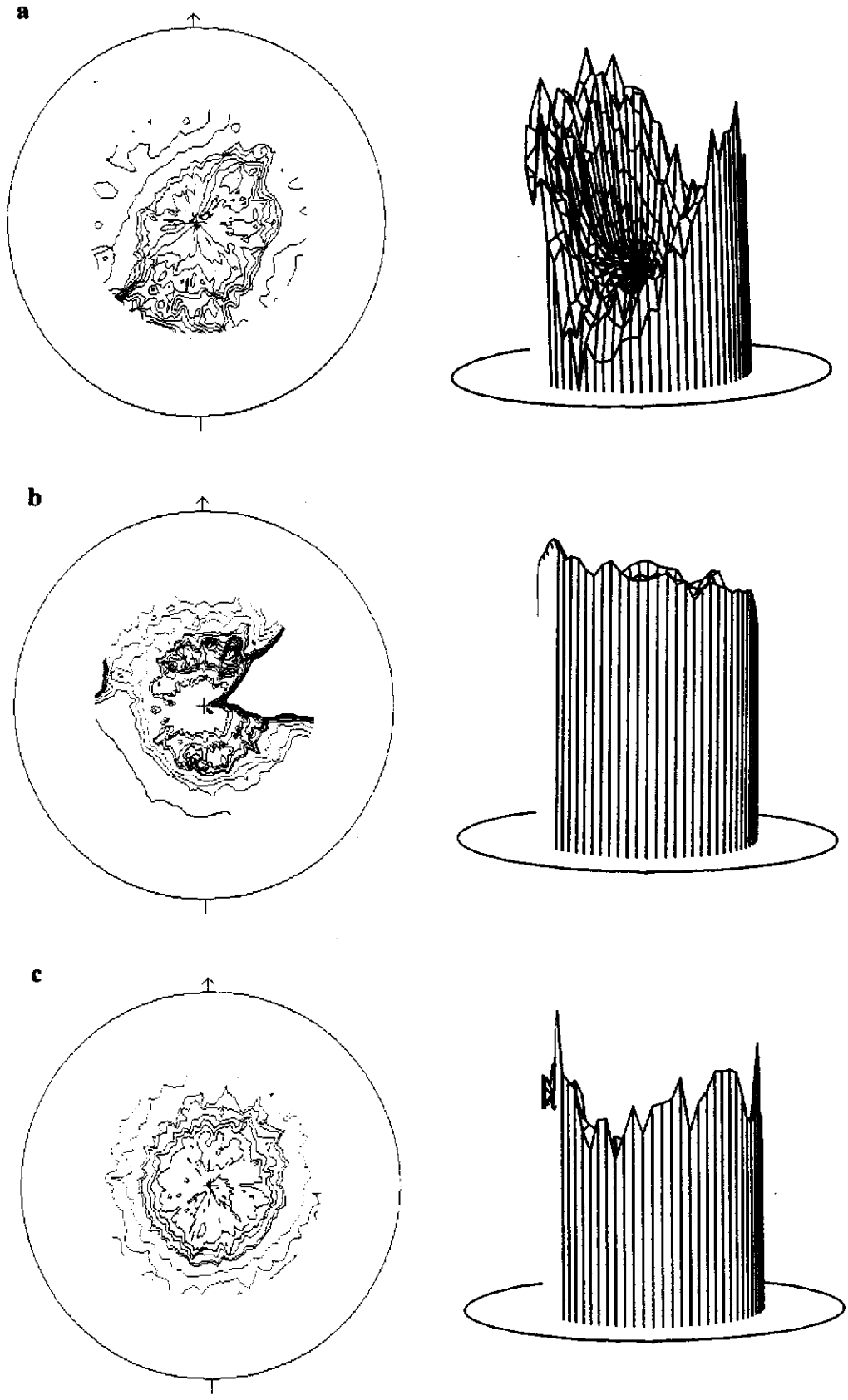

Figure A2.1.4(a). 2D and 3D representations of the molybdite <111> XRPD pole-figures: (a) side drifted - M0X, (b) briquetted for 44MPa - M2X, and (c) briquetted for 66MPa - M3X. The contour levels are in random density units.

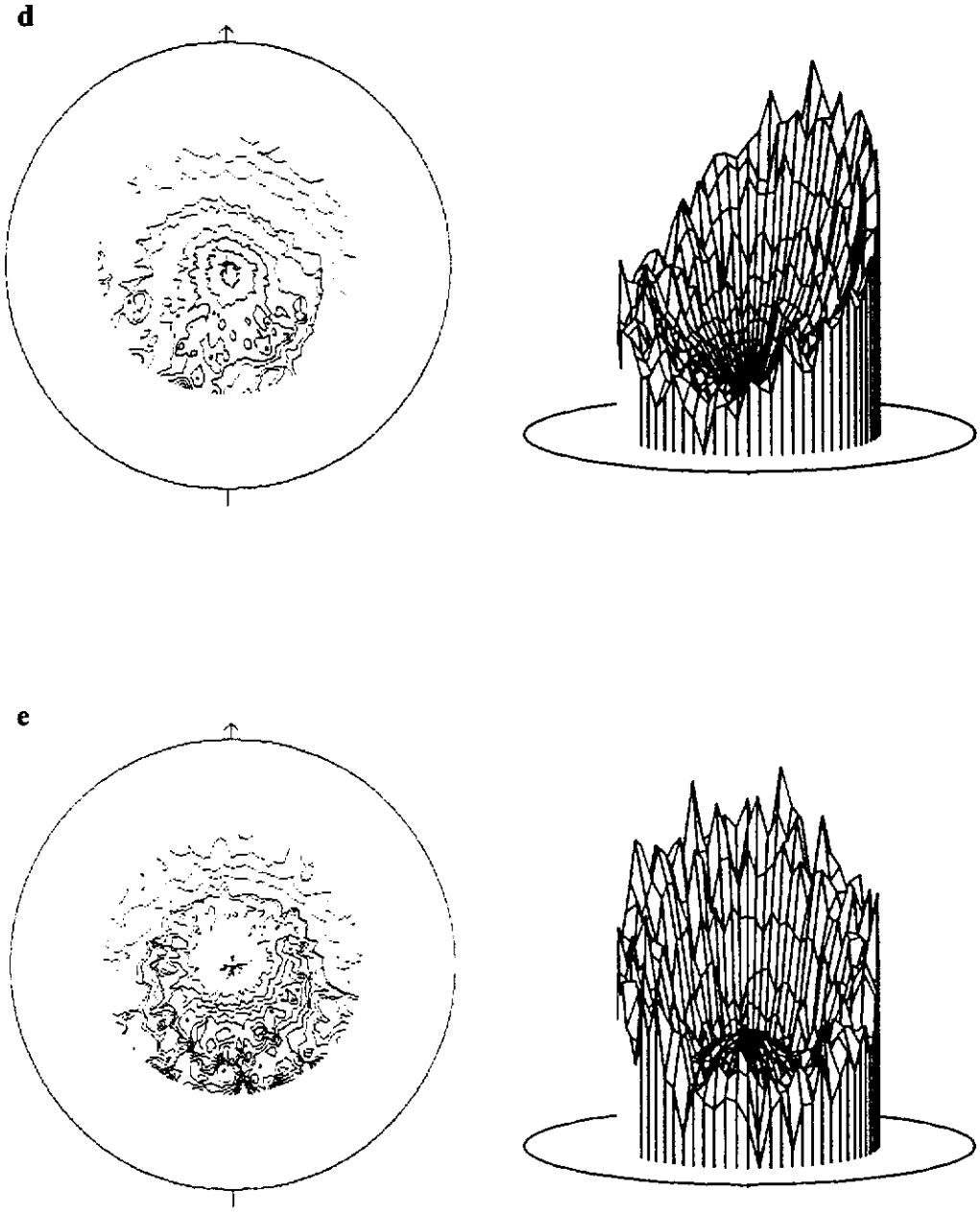

Figure A2.1.4(b). 2D and 3D representations of the molybdite <111> XRPD pole-figures: (d) briquetted for 88MPa - M4X and (e) briquetted for 110MPa - M5X. The contour levels are in random density units.

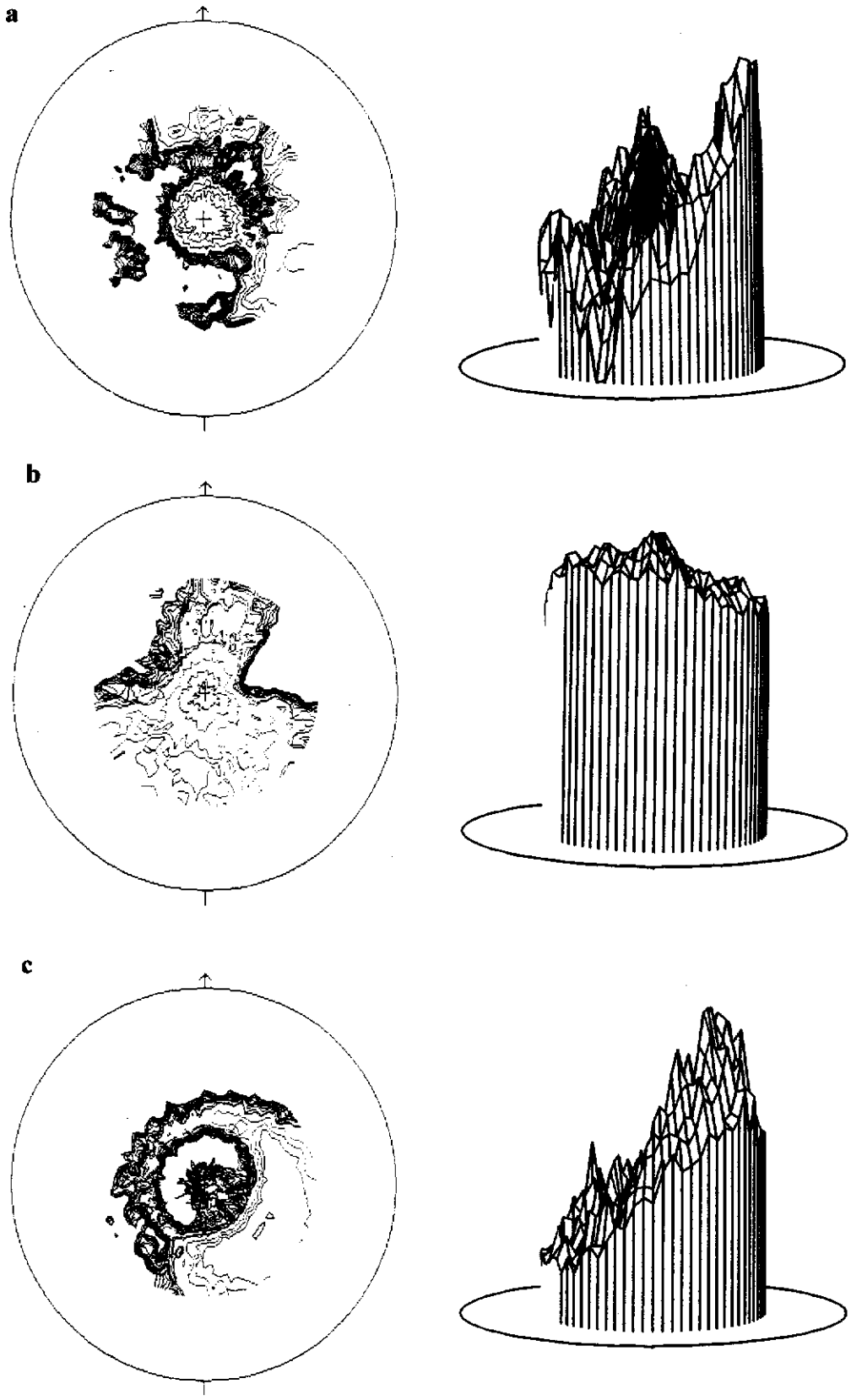

Figure A2.1.5(a). 2D and 3D representations of the molybdite <150> XRPD pole-figures: (a) side drifted - M0X, (b) briquetted for 44MPa - M2X, and (c) briquetted for 66MPa - M3X. The contour levels are in random density units.

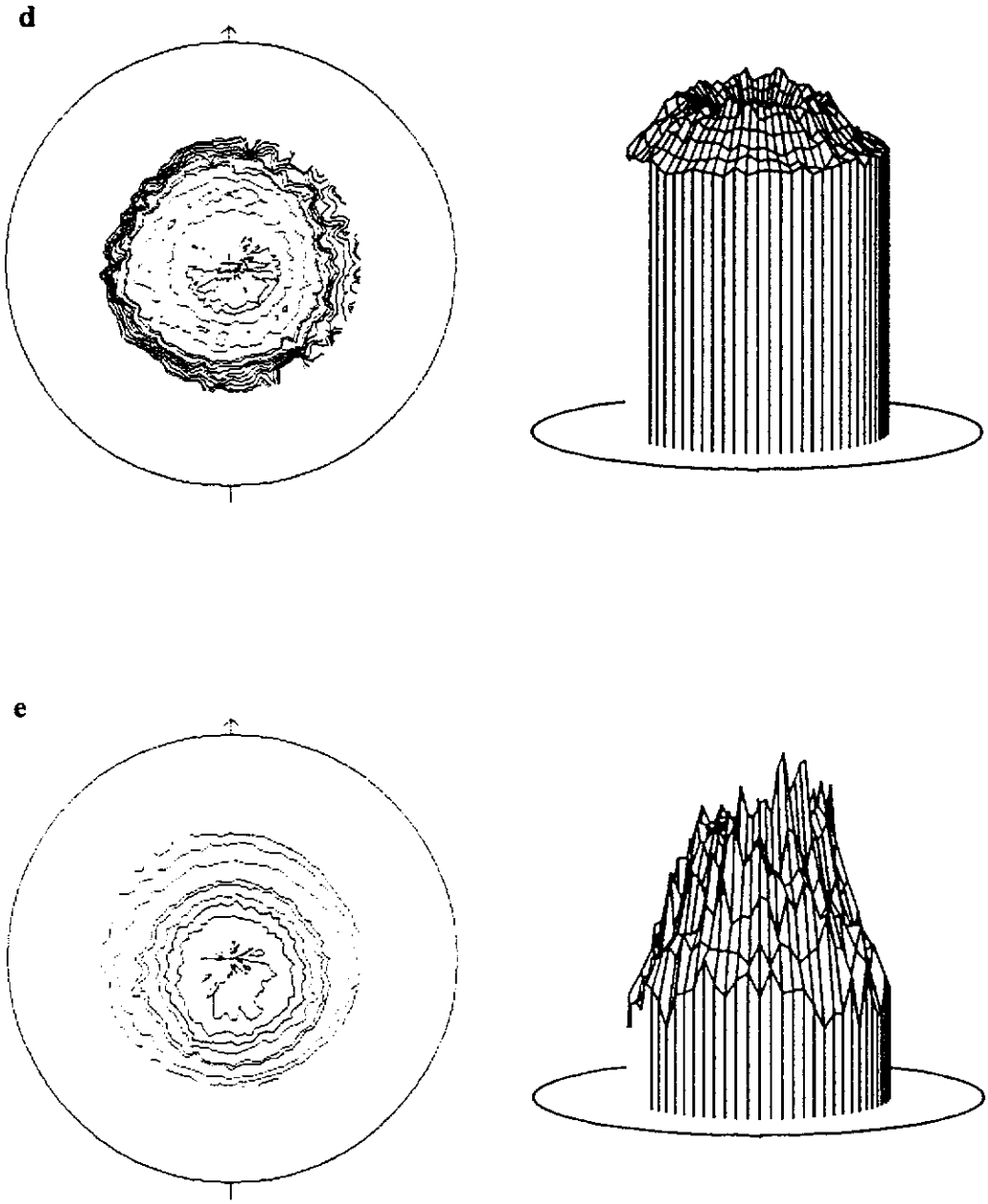

Figure A2.1.5(b). 2D and 3D representations of the molybdite <150> XRPD pole-figures: (d) briquetted for 88MPa - M4X and (e) briquetted for 110MPa - M5X. The contour levels are in random density units.

A2.2. XRPD Calcite

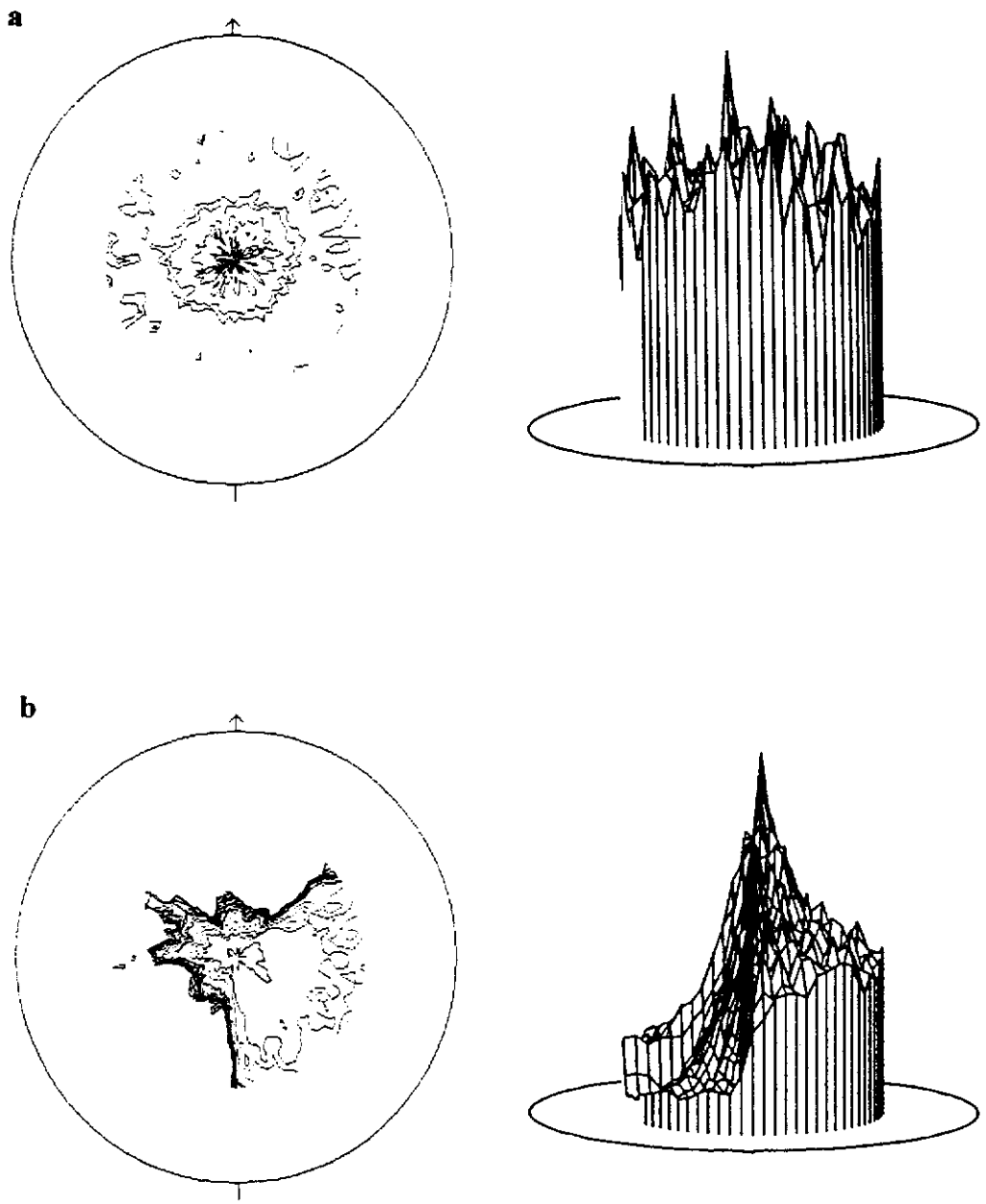

Figure A2.2.1(a). 2D and 3D representations of the calcite <104> XRPD pole-figures: (a) side drifted - C0X and (b) briquetted for 44MPa - C2X. The contour levels are in random density units.

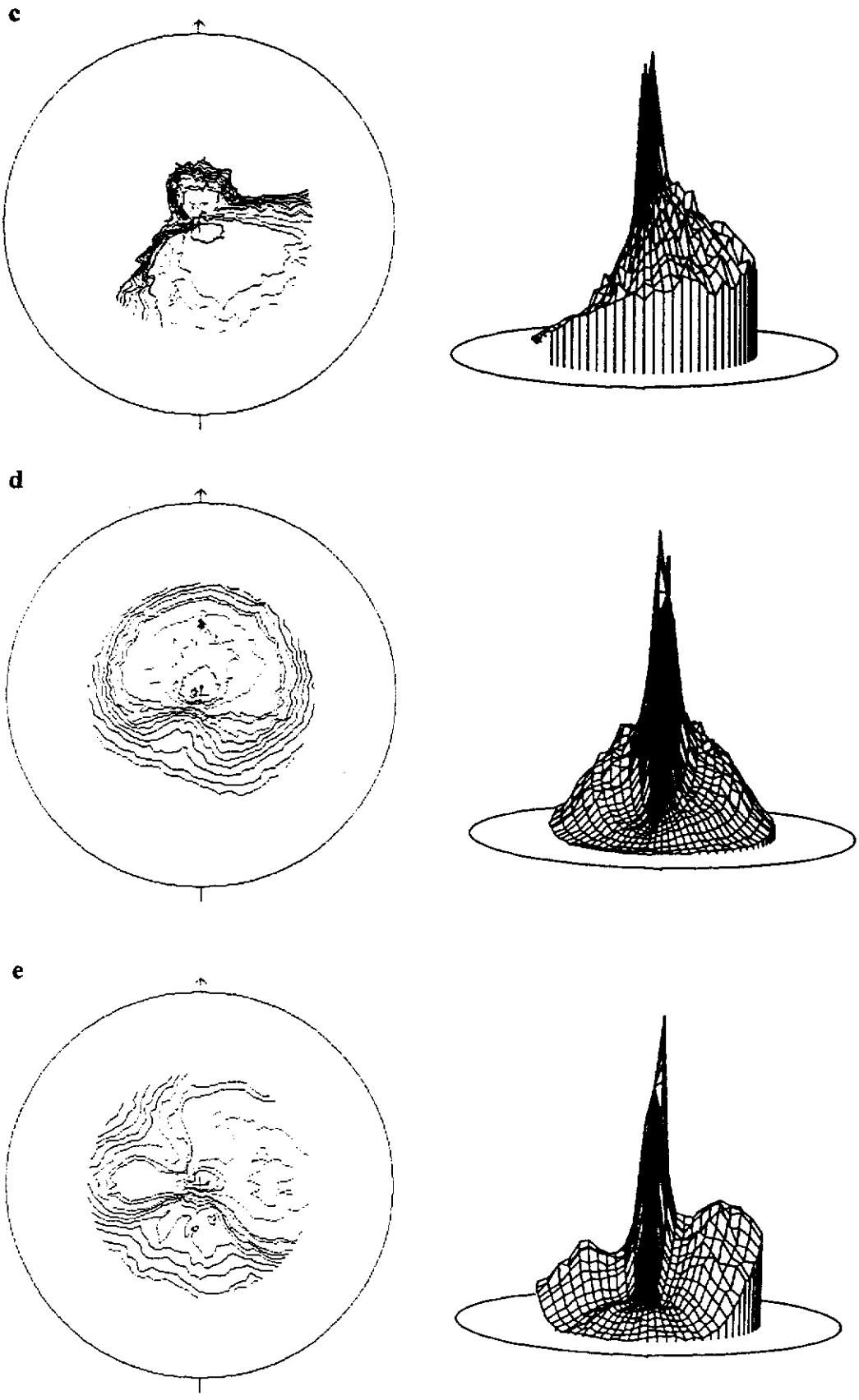

Figure A2.2.1(b). 2D and 3D representations of the calcite <104> XRPD pole-figures: (c) briquetted for 88MPa - C4X, (d) briquetted for 132MPa - C6X and (e) briquetted for 176MPa - C8X. The contour levels are in random density units.

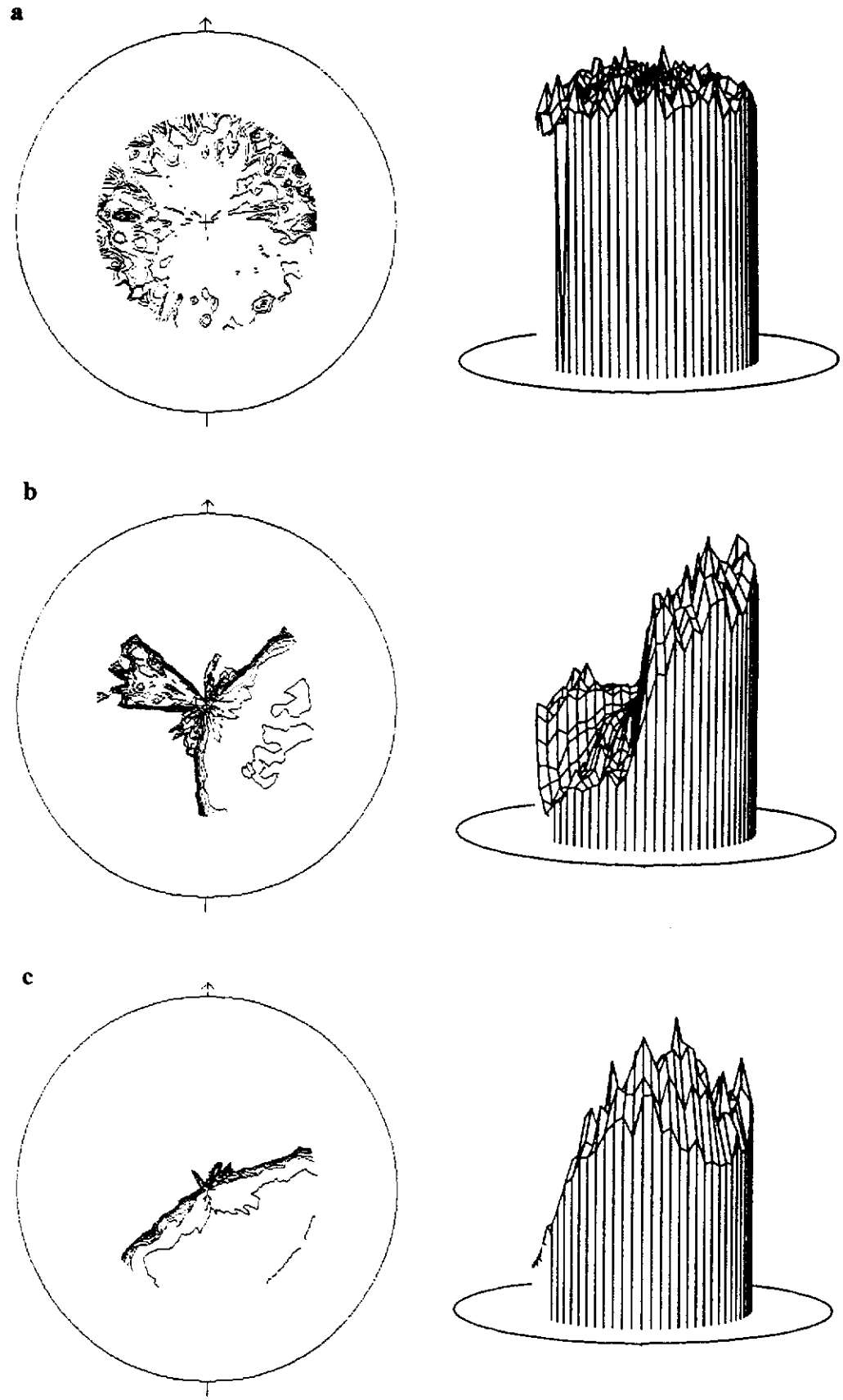

Figure A2.2.2(a). 2D and 3D representations of the calcite <012> XRPD pole-figures: (a) side drifted - C0X, (b) briquetted for 44MPa - C2X and (c) briquetted for 88MPa - C4X. The contour levels are in random density units.

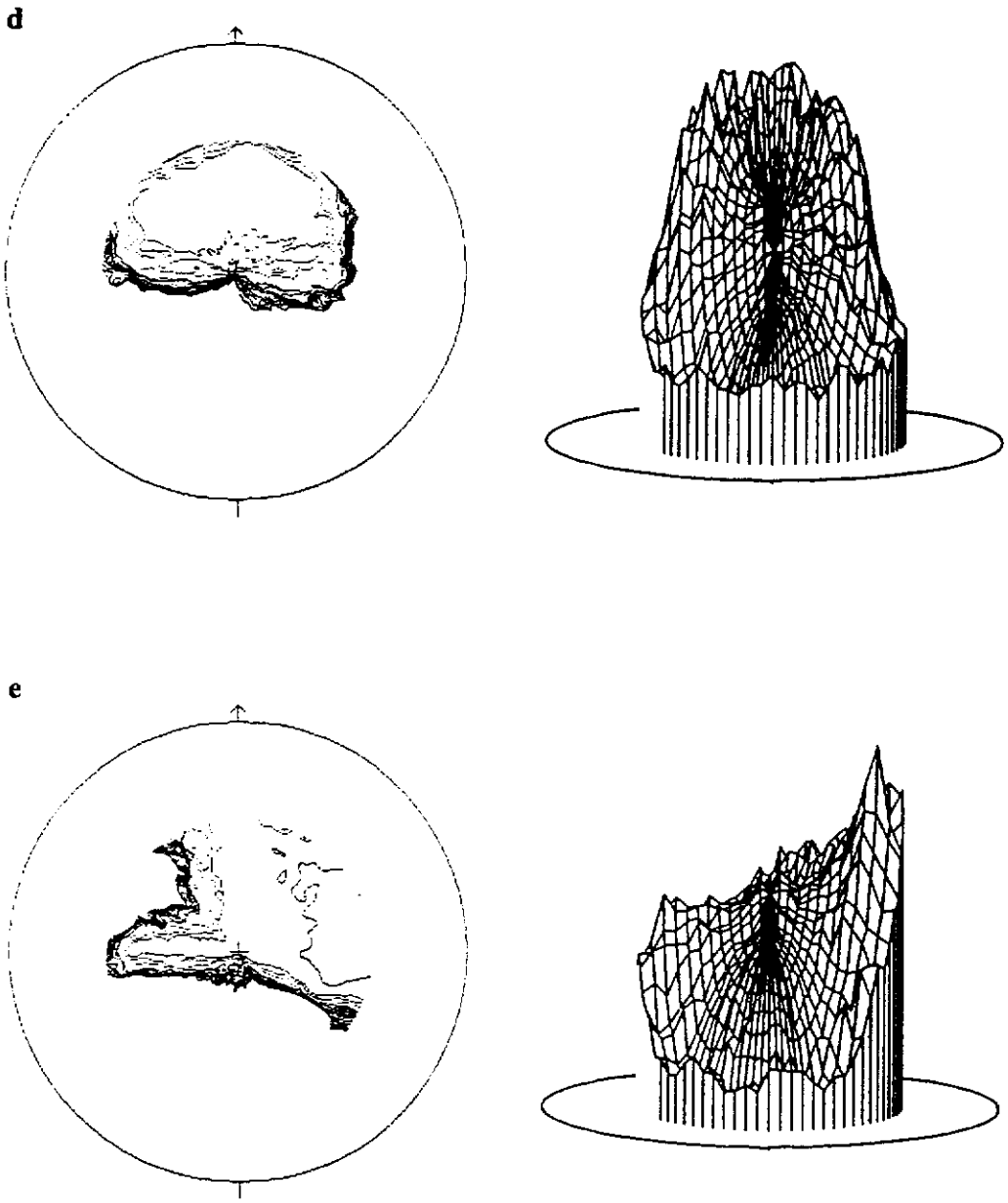

Figure A2.2.2(b). 2D and 3D representations of the calcite <012> XRPD pole-figures: (d) briquetted for 132MPa - C6X and (e) briquetted for 176MPa - C8X. The contour levels are in random density units.

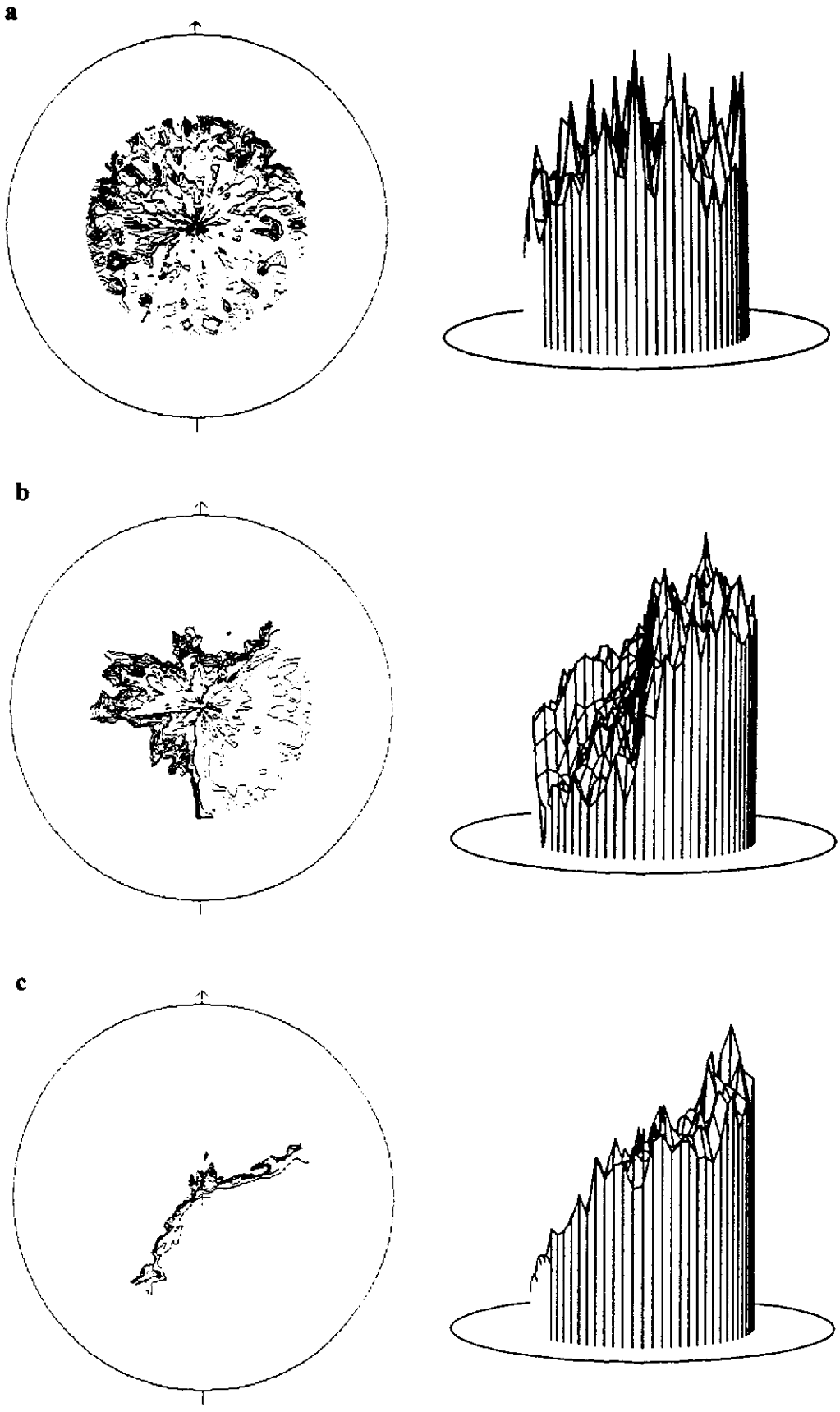

Figure A2.2.3(a). 2D and 3D representations of the calcite <006> XRPD pole-figures: (a) side drifted - C0X, (b) briquetted for 44MPa - C2X and (c) briquetted for 88MPa - C4X. The contour levels are in random density units.

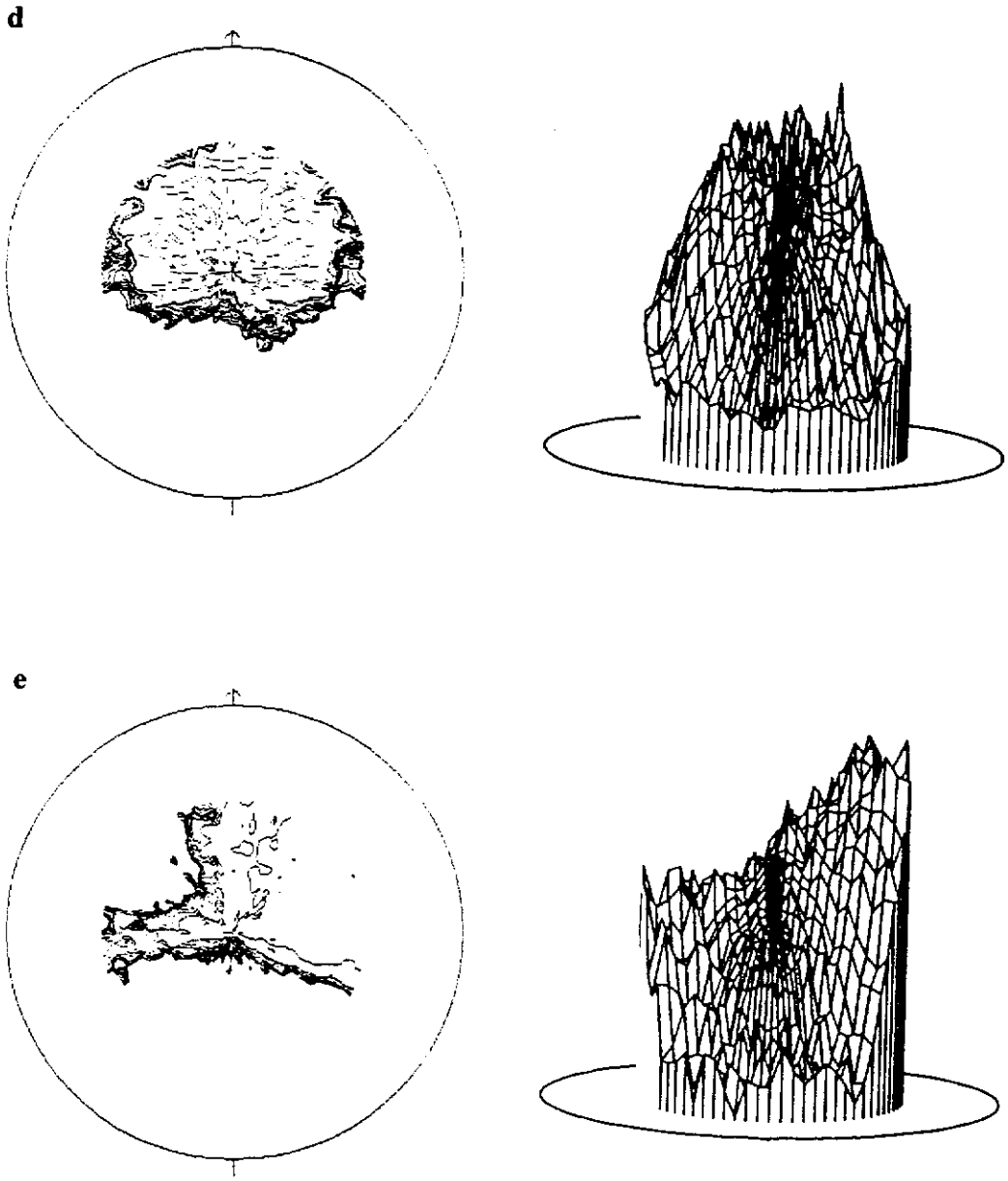

Figure A2.2.3(b). 2D and 3D representations of the calcite <006> XRPD pole-figures: (d) briquetted for 132MPa - C6X and (e) briquetted for 176MPa - C8X. The contour levels are in random density units.

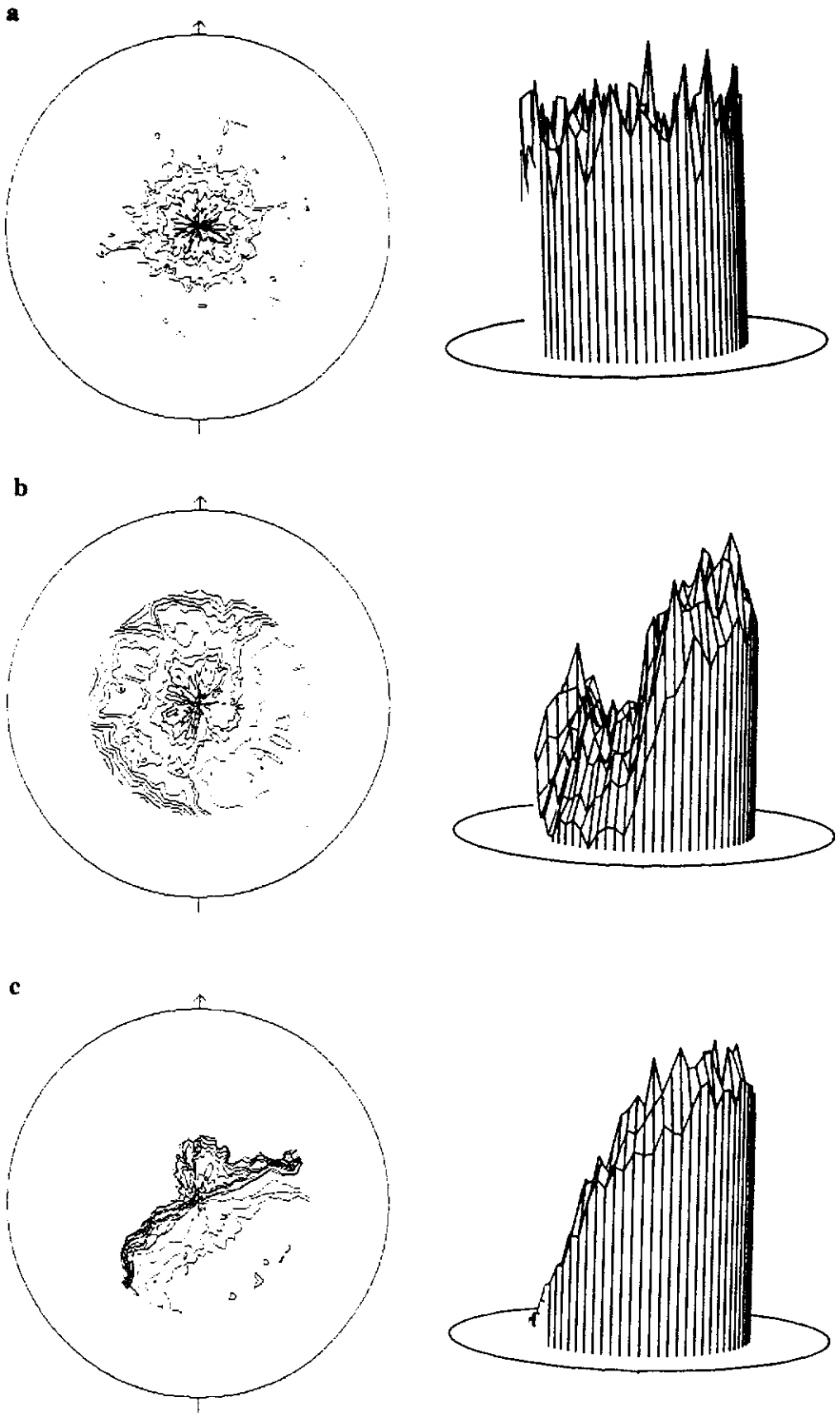

Figure A2.2.4(a). 2D and 3D representations of the calcite <110> XRPD pole-figures: (a) side drifted - C0X, (b) briquetted for 44MPa - C2X and (c) briquetted for 88MPa - C4X. The contour levels are in random density units.

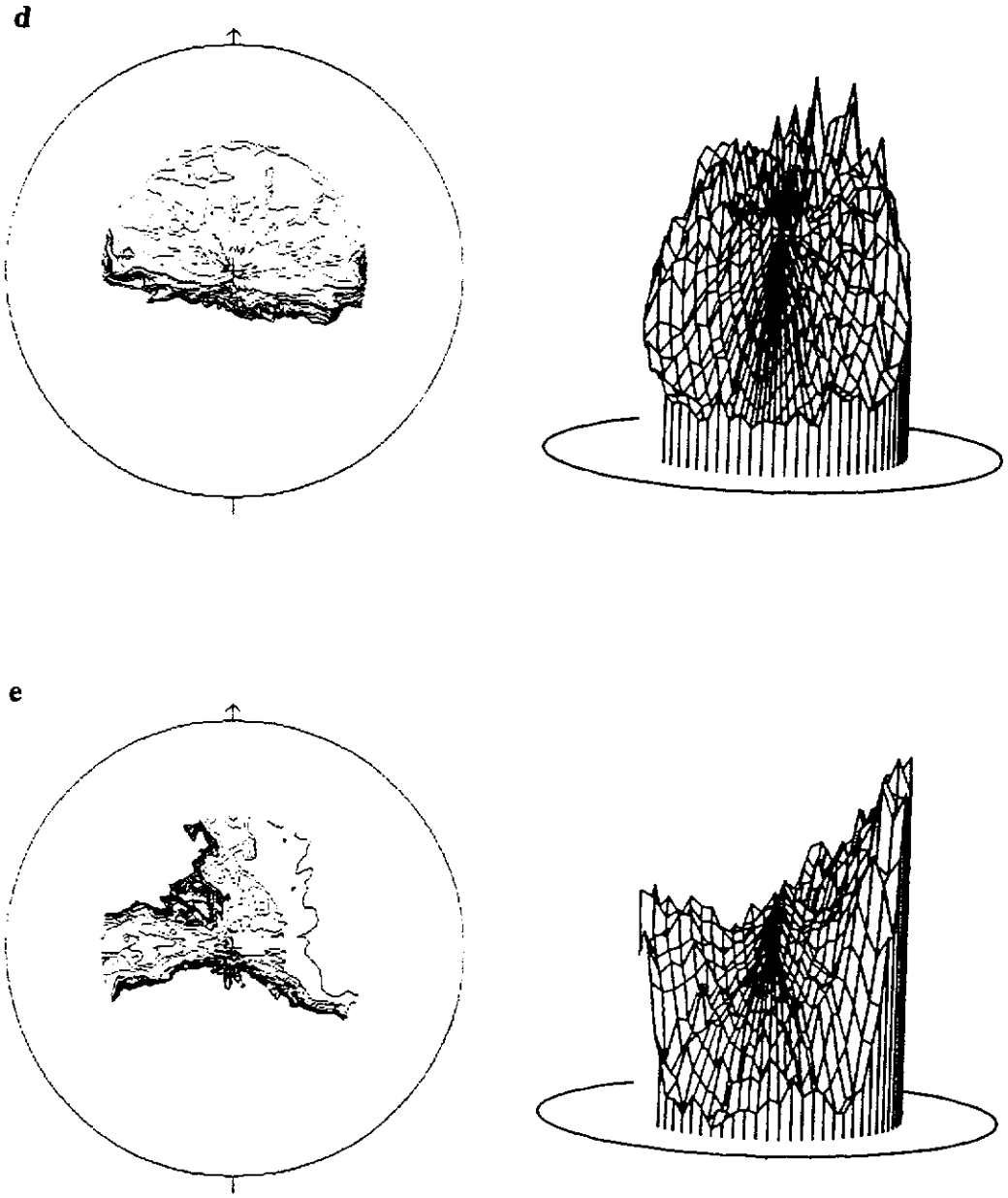

Figure A2.2.4(b). 2D and 3D representations of the calcite <110> XRPD pole-figures: (d) briquetted for 132MPa - C6X and (e) briquetted for 176MPa - C8X. The contour levels are in random density units.

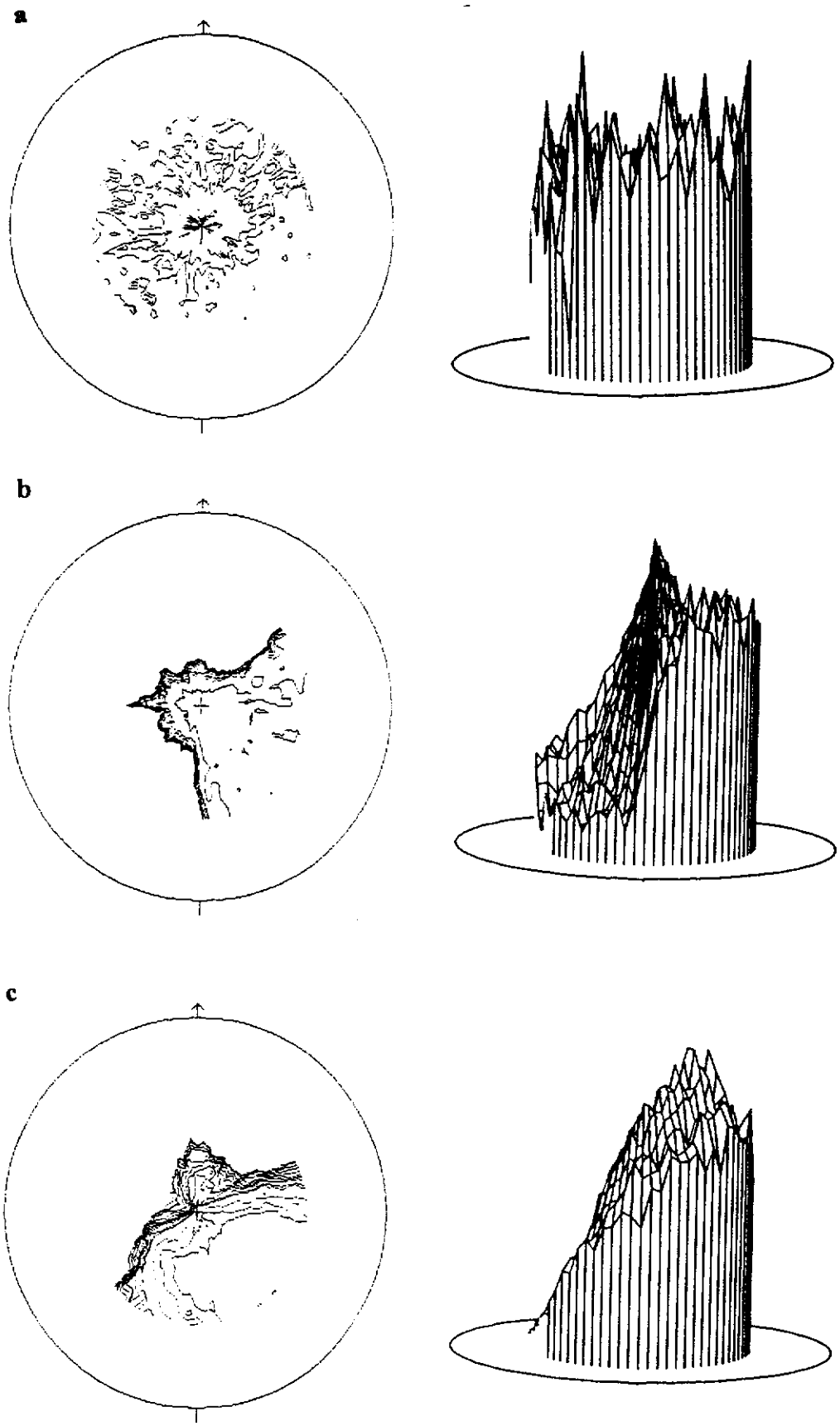

Figure A2.2.5(a). 2D and 3D representations of the calcite <113> XRPD pole-figures: (a) side drifted - C0X, (b) briquetted for 44MPa - C2X and (c) briquetted for 88MPa - C4X. The contour levels are in random density units.

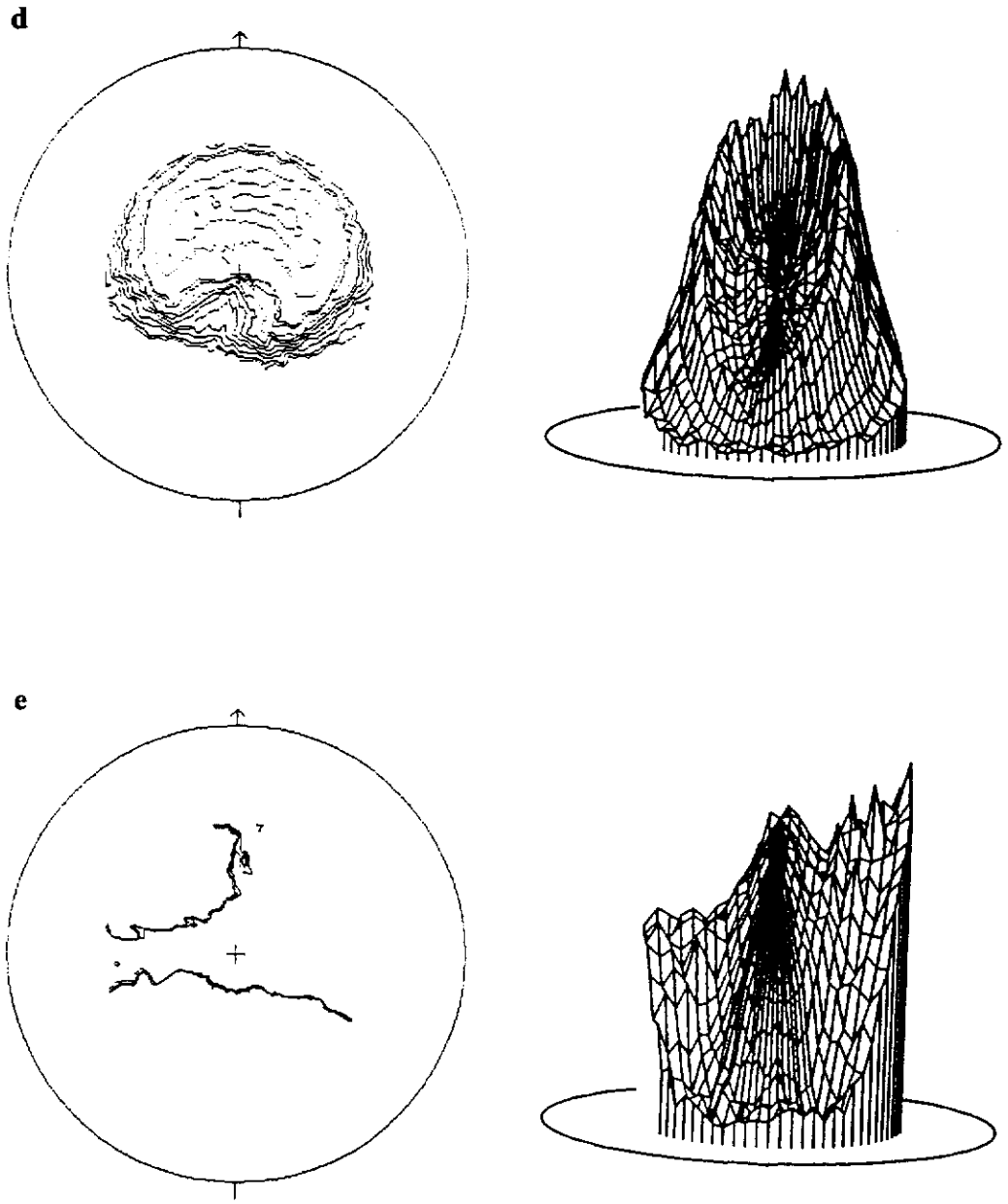

Figure A2.2.5(b). 2D and 3D representations of the calcite <113> XRPD pole-figures: (d) briquetted for 132MPa - C6X and (e) briquetted for 176MPa - C8X. The contour levels are in random density units.

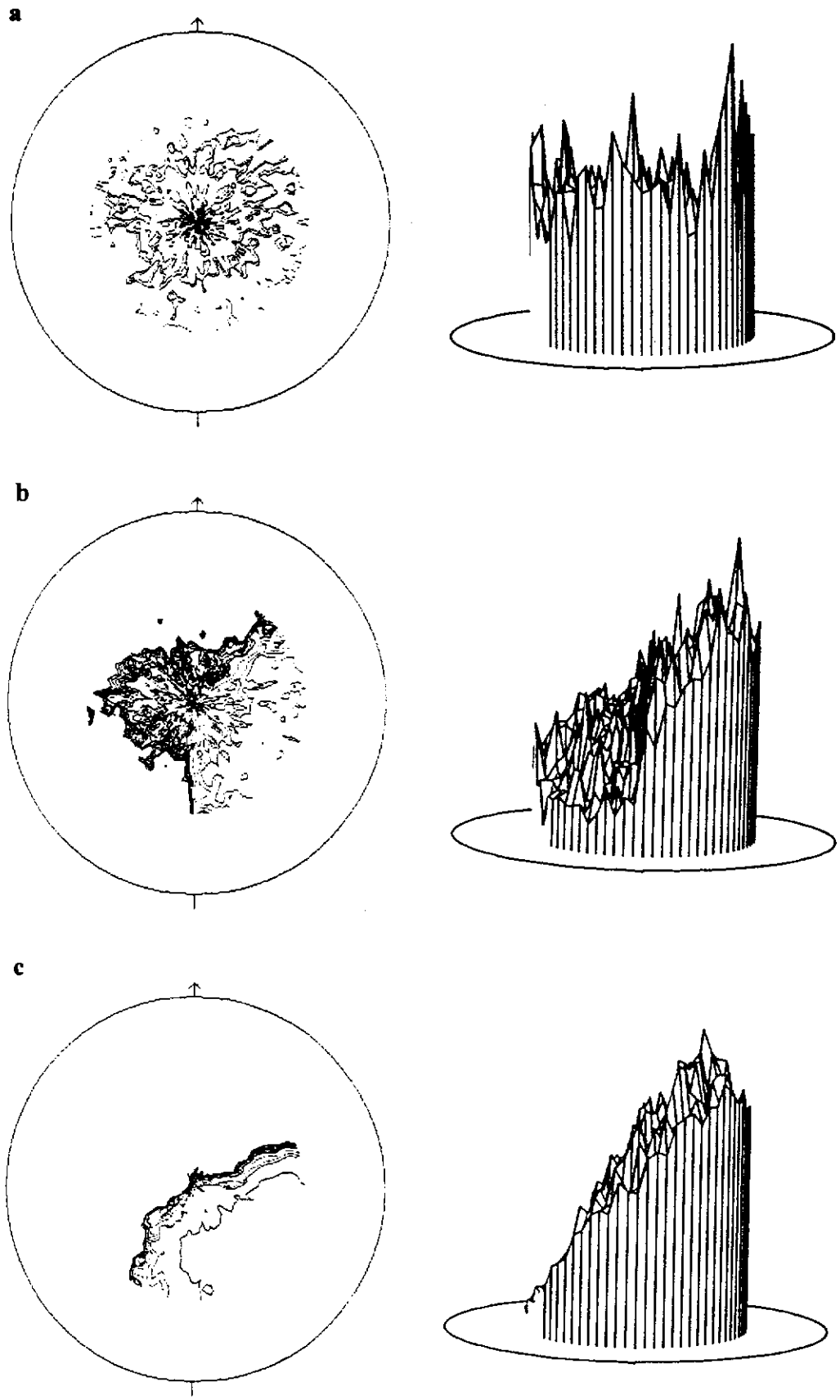

Figure A2.2.6(a). 2D and 3D representations of the calcite <202> XRPD pole-figures: (a) side drifted - C0X, (b) briquetted for 44MPa - C2X and (c) briquetted for 88MPa - C4X. The contour levels are in random density units.

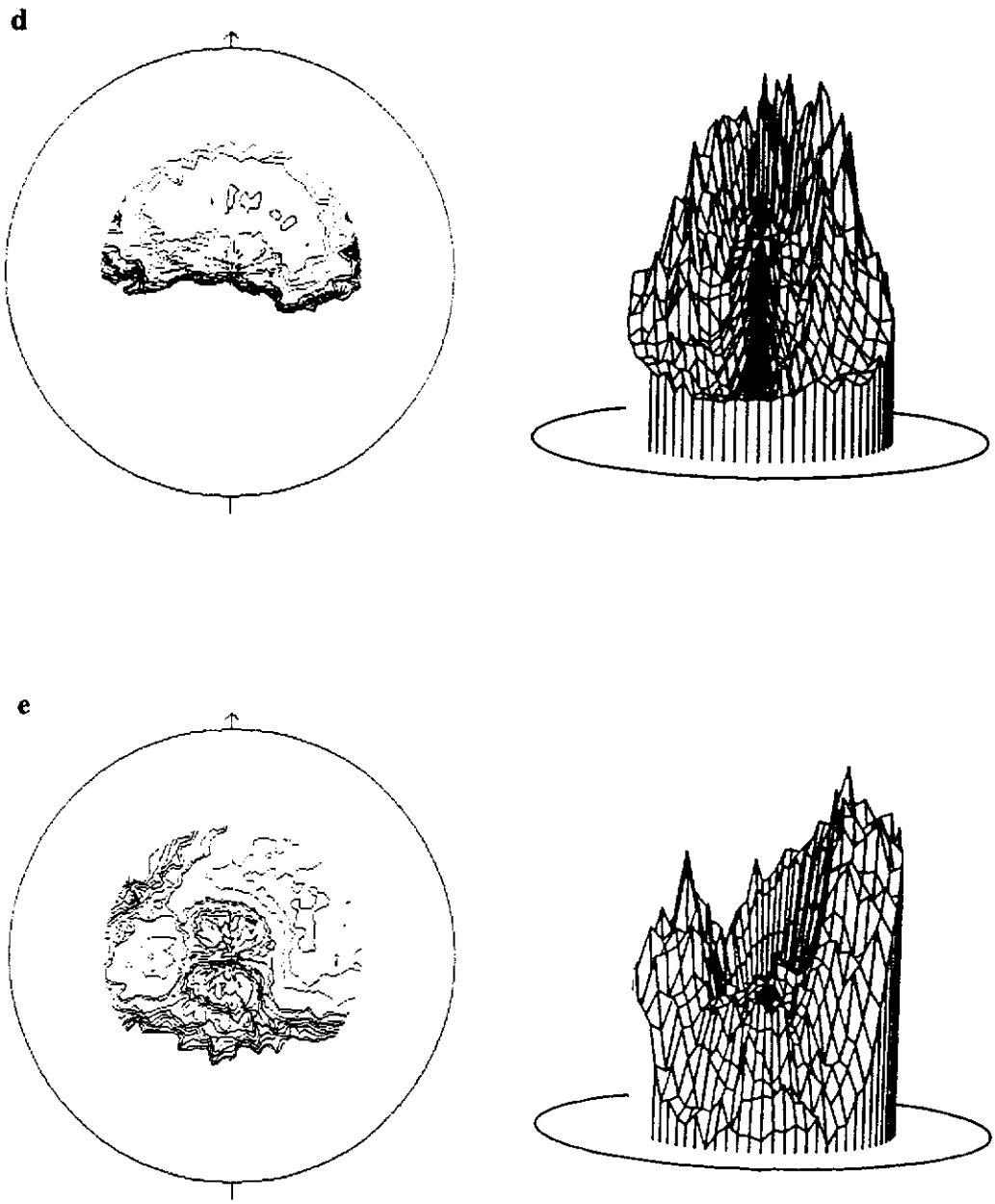

Figure A2.2.6(b). 2D and 3D representations of the calcite <202> XRPD pole-figures: (d) briquetted for 132MPa - C6X and (e) briquetted for 176MPa - C8X. The contour levels are in random density units.

A2.3. NPD Calcite

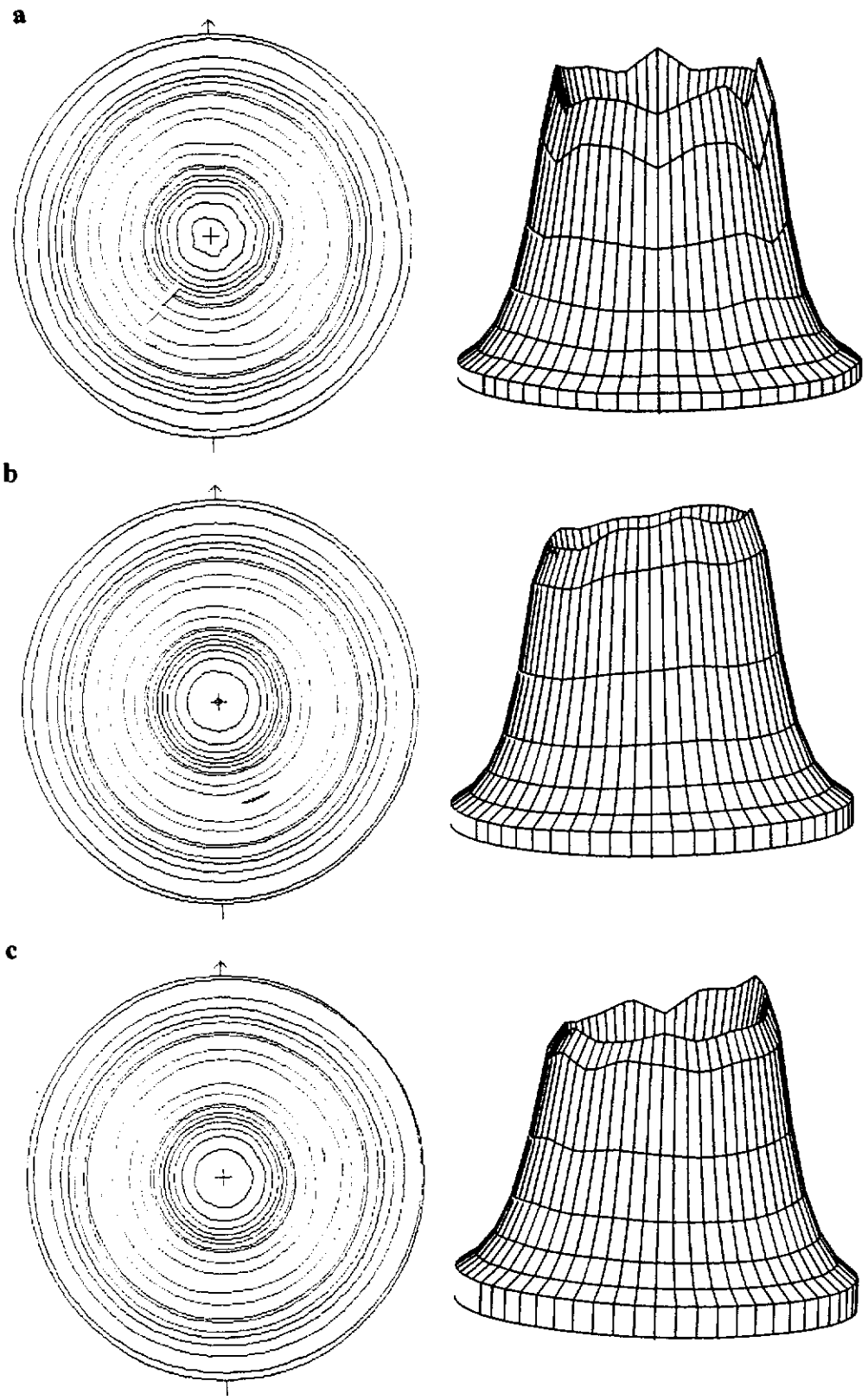

Figure A2.3.1. 2D and 3D representations of the calcite <104> NPD pole-figures: (a) side drifted - C0N, (b) briquetted for 88MPa - C4N and (c) briquetted for 176MPa - C8N. The contour levels are in random density units.

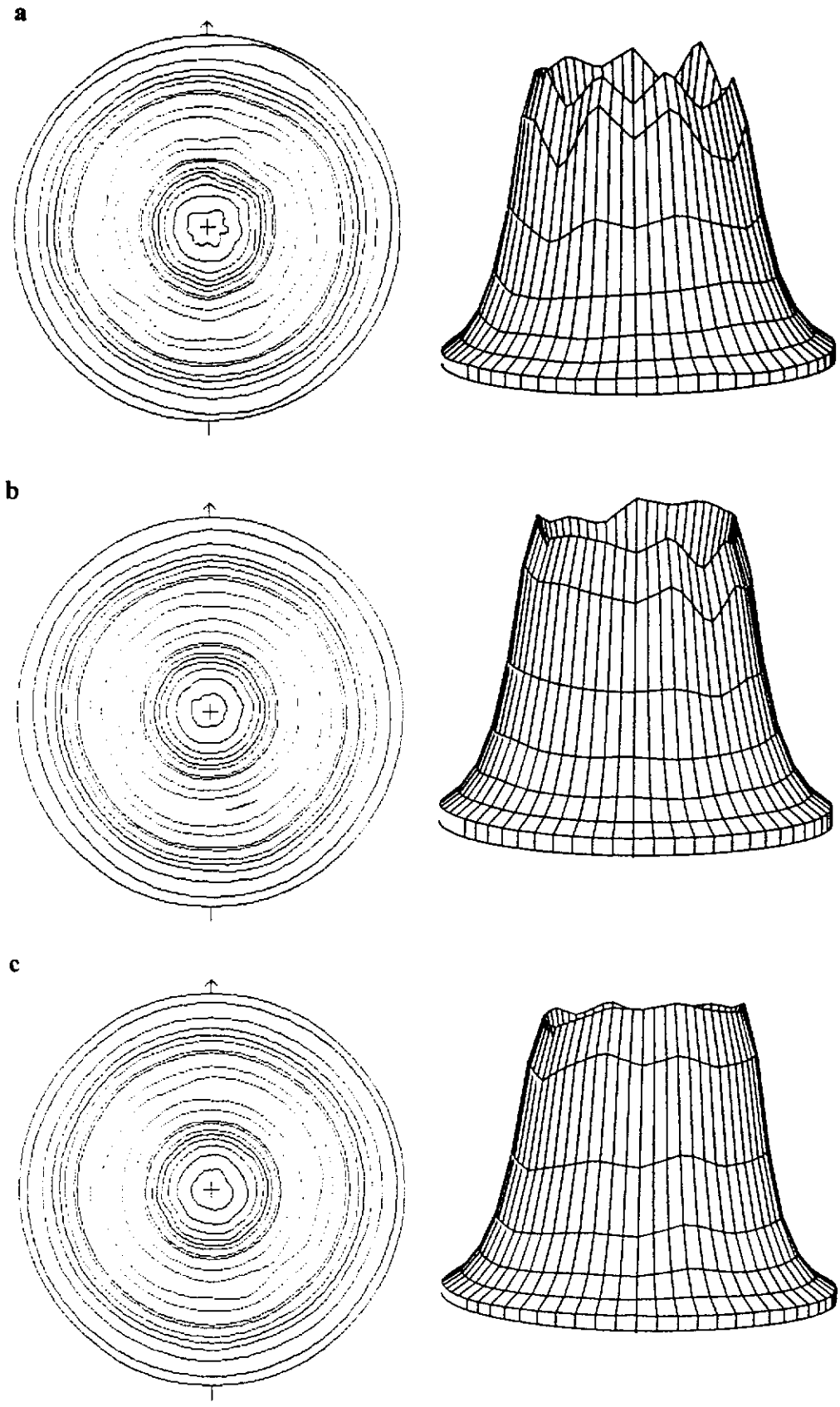

Figure A2.3.2. 2D and 3D representations of the calcite <012> NPD pole-figures: (a) side drifted - C0N, (b) briquetted for 88MPa - C4N and (c) briquetted for 176MPa - C8N. The contour levels are in random density units.

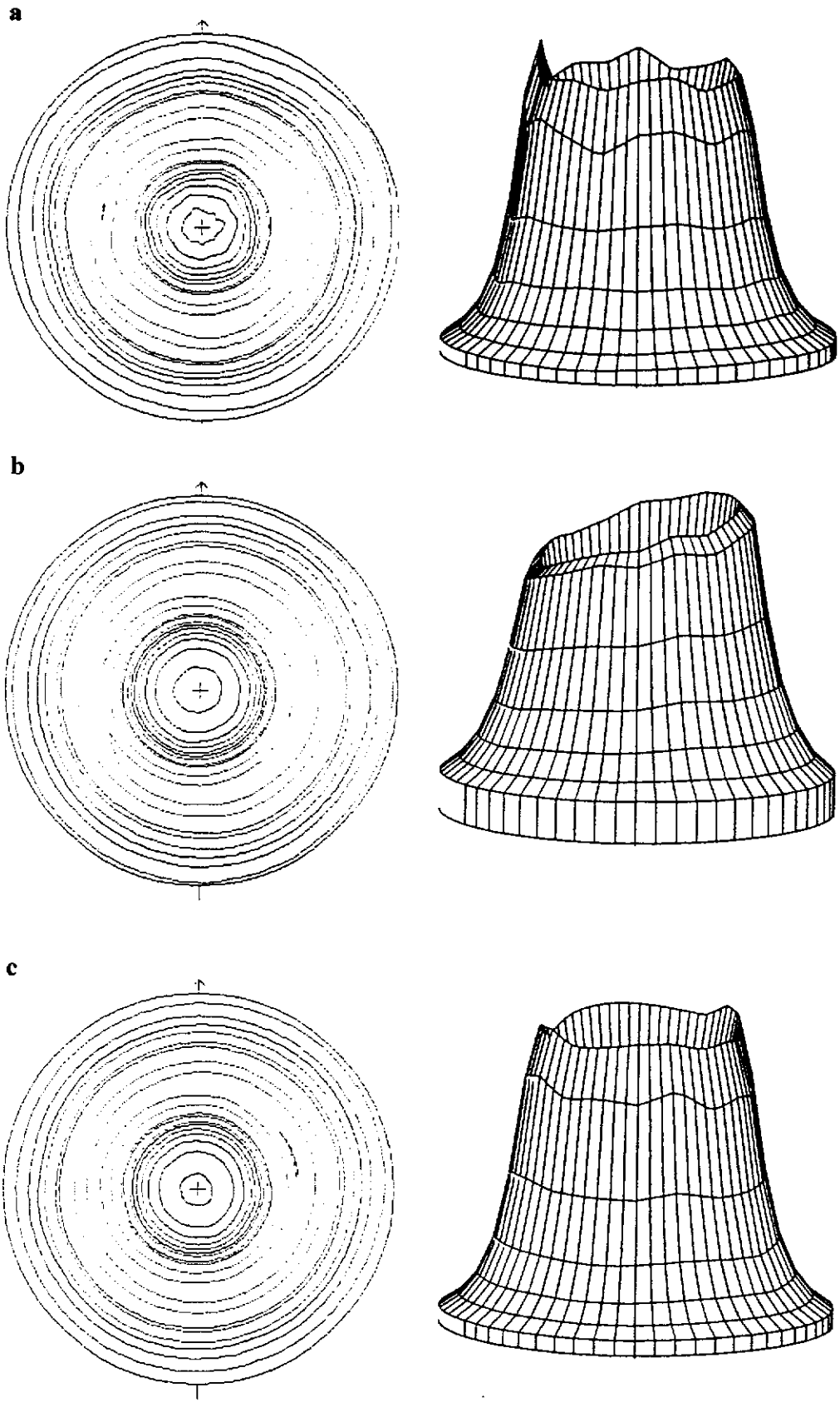

Figure A2.3.3. 2D and 3D representations of the calcite <006> NPD pole-figures: (a) side drifted - C0N, (b) briquetted for 88MPa - C4N and (c) briquetted for 176MPa - C8N. The contour levels are in random density units.

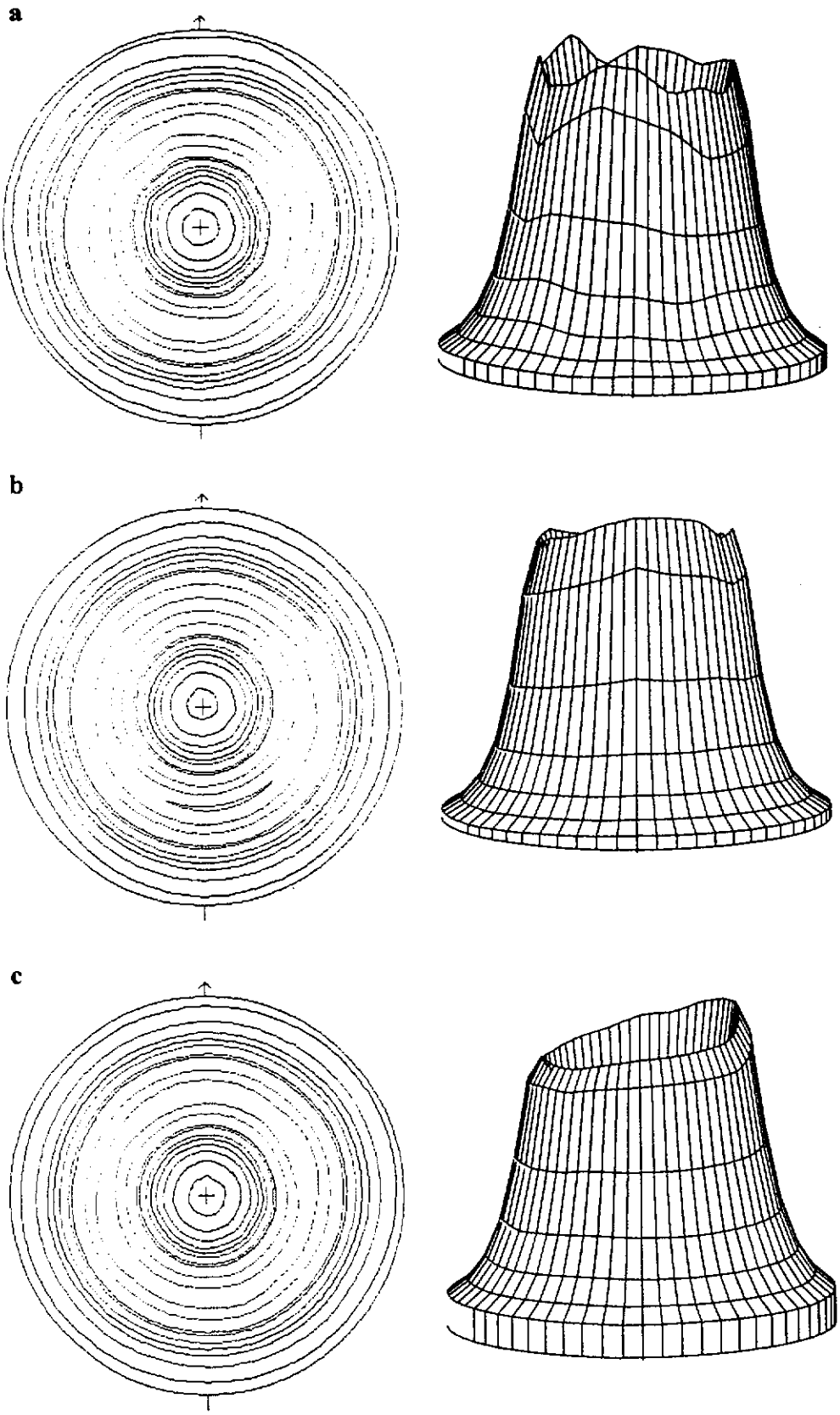

Figure A2.3.4. 2D and 3D representations of the calcite <113> NPD pole-figures: (a) side drifted - C0N, (b) briquetted for 88MPa - C4N and (c) briquetted for 176MPa - C8N. The contour levels are in random density units.

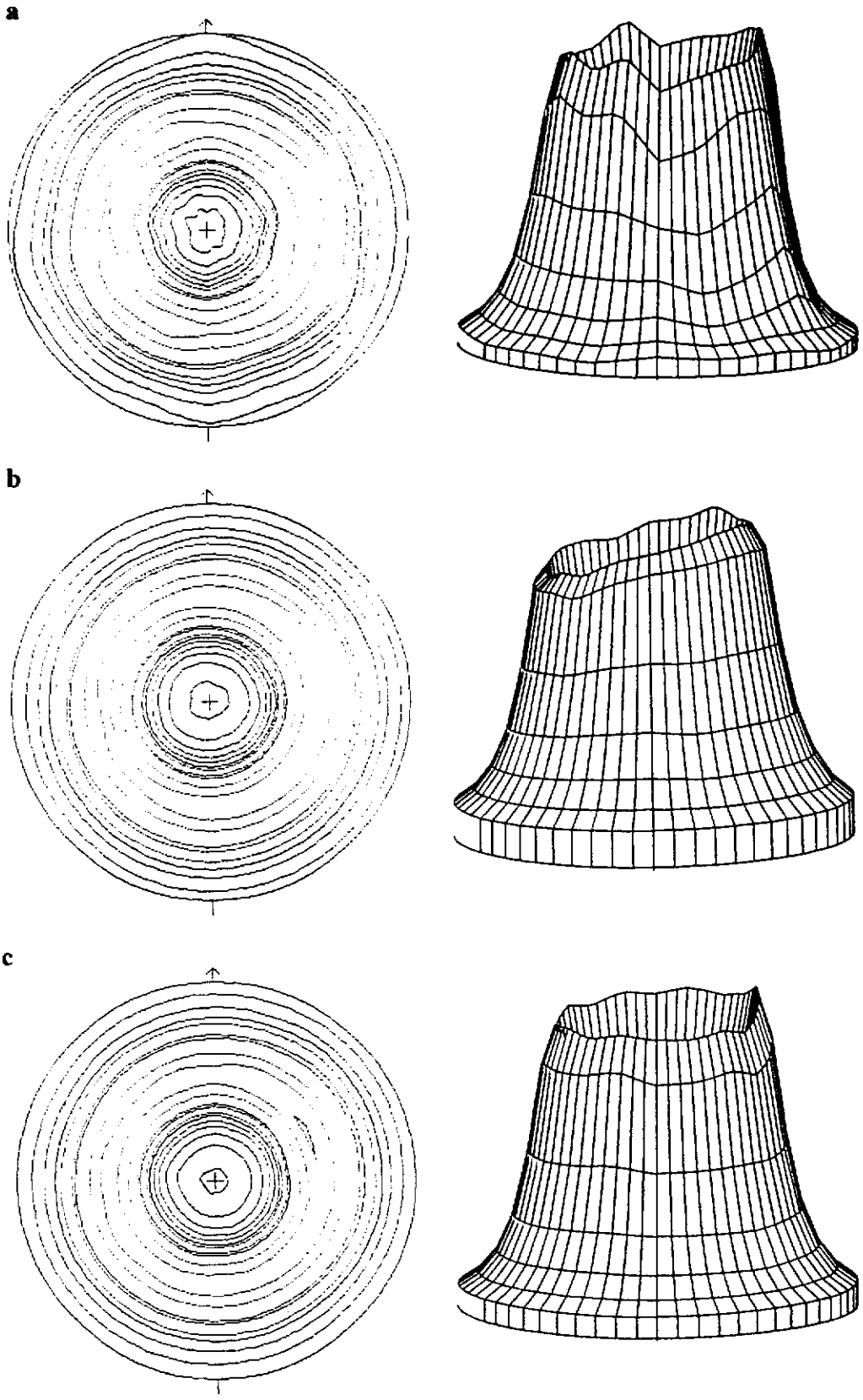

Figure A2.3.5. 2D and 3D representations of the calcite <018> NPD pole-figures: (a) side drifted - C0N, (b) briquetted for 88MPa - C4N and (c) briquetted for 176MPa - C8N. The contour levels are in random density units.